

Investigation of the seismic and seismological structure of the Alboran Sea, Western Mediterranean

Dissertation

zur Erlangung des Doktorgrades
der Mathematisch-Naturwissenschaftliche Fakultät
der Christian-Albrechts-Universität zu Kiel

vorgelegt von
Wiebke Leuchters

Kiel, 2014

Erster Gutachter:

Prof. Dr. Ingo Grevemeyer

Zweite Gutachterin:

Prof. Dr. Heidrun Kopp

Tag der mündlichen Prüfung:

18.11.2014

Zum Druck genehmigt:

18.11.2014

gez. Prof. Dr. Wolfgang J. Duschl, Dekan

Abstract

The understanding of the formation history of the Alboran Sea is investigated using seismic wide-angle refraction data in the East Alboran Basin in transition to the Algerian Basin and as second dataset using seismological data of the Alboran region and the surrounding onshore domains.

The seismic wide-angle refraction data result in a velocity profile showing a transition from thinned continental crust to oceanic crust. The profile is trending with a length of 250 km from West to East and can be divided in three segments. The westernmost segment consists of crust where the velocity structure clearly mimics continental crust. With a thickness of 6 - 7 km is this crust extremely thinned compared to typical continental crust. The second segment in the central part of the analysed profile describes the transition from the continental to oceanic crust. The crustal thickness of the segment is up to 12 km which is due to the crossing of a topographic high, the Maimonid Ridge. The main part of this segment has a crustal velocity structure of continental crust. The transition from continental crustal velocities to oceanic crustal velocities emerge in the last few kilometers of the central segment. In the East, the third segment of the profile is identified with a crustal velocity structure typical for oceanic crust. The thickness of this segment is also in the range for typical oceanic crust with 6 - 7 km.

The upper mantle velocity in the two western segments is with respect to typical continental crustal velocities with ~ 7.0 km/s extremely low. Also beneath the oceanic crust low upper mantle velocities of ~ 7.6 km/s result from the seismic modeling. These low velocities are comparable to upper mantle velocities in some arc-back-arc regions (e.g. Mariana Arc and Tonga Arc). This indicates that the Alboran Basin is a back-arc basin formed while slab rollback like the Mariana Arc where the low upper mantle velocities are a result of the formation history.

The transition from thinned continental crust in the East Alboran Basin to oceanic crust in the Algerian Basin and the low upper mantle velocities in the oceanic lithosphere are a support for the Alboran Basin as back-arc basin. The transition from extremely thinned continental to oceanic crust describes the Alboran Basin as back-arc basin formed while westward slab rollback.

The local seismicity in the Alboran region shows a thinning of the lithosphere from West to East. In the West, lithospheric earthquakes occur down to a depth of 30 km. The East Alboran Basin has a maximum hypocenter depth of 15 km. However, much deeper earthquakes with a depth of up to 100 km are located mostly in the western part of the West Alboran Basin. Those can be associated to the remnant slab of an extinct subduction zone.

Lithospheric seismicity occurring in the Alboran Basin are mainly rupturing close to topographic

features in two clustering regions. Those topographic features are the Alboran Ridge in the East of the West Alboran Basin where the hypocenters are down to 30 km and the Carboneras Fault in the East Alboran Basin with hypocenter depths down to 15 km.

Both datasets, the wide-angle refraction data and the seismological data, show a crustal thinning from West to East. Additionally to the seismic velocity structure and the lithospheric seismicity, the deep earthquakes in the West of the West Alboran Basin provide further information for the Alboran Basin as it was available before. The slab rollback theory as formation history of the basin is supported by the datasets.

Zusammenfassung

Das Verständnis der Entstehungsgeschichte der Alboran See wurde mittels geophysikalischer Methoden untersucht. Hierzu wurden seismische Weitwinkel-Refraktionsdaten im östlichen Alboran Becken im Übergang zum Algerischen Becken und ein zweiter Datensatz bestehend aus seismologischen Daten der Alboran Region und umgebenden Landregionen verwendet.

Die seismischen Weitwinkel-Refraktionsdaten ergeben ein krustales Geschwindigkeitsmodell in dem der Übergang von ausgedünnter kontinentaler Kruste zu ozeanischer Kruste dargestellt wird. Das Profil ist mit einer Länge von 250 km von West nach Ost ausgerichtet und kann in drei Segmente unterteilt werden. Der westlichste Teil des Profils besteht aus Kruste in der die Geschwindigkeitsstruktur klar kontinentale Kruste abbildet. Im Vergleich zu typischer kontinentaler Kruste ist diese Kruste mit 6 - 7 km Dicke extrem ausgedünnt. Das zweite Segment welches den zentralen Teil des seismischen Profils beinhaltet beschreibt den Übergang von kontinentaler zu ozeanischer Kruste. Dieses Segment weist eine krustale Dicke von bis zu 12 km auf, wobei die hohe Dicke seine Ursache in der auf dem Profil liegenden topographischen Erhebung, dem Maimonid Rücken, hat. Hauptsächlich beträgt die krustale Geschwindigkeit des zentralen Segments die von kontinentaler Kruste. Der Übergang von kontinentalen Geschwindigkeiten zu ozeanischen Geschwindigkeiten entwickelt sich innerhalb weniger Kilometer im östlichsten Teil des zentralen Segment. Das dritte Segment besteht aus dem östlichsten Teil des seismischen Profils. Ein krustales Geschwindigkeitsprofil, welches typische ozeanische Kruste abbildet ergibt sich hier aus der Modellierung. Die krustale Dicke von 6 - 7 km ist ebenfalls typisch für ozeanische Kruste.

In den beiden westlichen Segmenten ist die seismische Geschwindigkeit im oberen Mantel mit 7 km/s extrem niedrig. Unterhalb der ozeanischen Kruste im östlichen Segment ergibt sich aus der Modellierung ebenfalls eine niedrige seismische Geschwindigkeit des oberen Mantels mit 7.6 km/s. Beide niedrigen Geschwindigkeiten lassen sich zu Geschwindigkeiten im oberen Mantel von einigen Arc-Backarc-Strukturen vergleichen (z.B. Marianen Bogen und Tonga Bogen). Dieses deutet an, daß das Alboran Becken ein Backarc-Becken ist welches wie der Marianen Bogen durch Zurückweichen der abtauchenden ozeanischen Platte ("slab rollback") entstand. Die niedrigen seismischen Geschwindigkeiten im oberen Mantel sind ein Ergebnis aus der Formationsgeschichte des Backarc-Beckens.

Der Übergang von dünner kontinentaler Kruste im östlichen Alboran Becken zu ozeanischer Kruste im Algerischen Becken und die niedrigen oberen Mantelgeschwindigkeiten unterstützen die Interpretation des Alboran Beckens als Backarc-Becken. Der Bereich entlang des seismischen

Profils mit extrem ausgedünnter kontinentaler Kruste zu ozeanischer Kruste beschreibt das Alboran Becken als Backarc-Becken welches durch das westwärtige Zurückweichen der abtauchenden ozeanischen Platte gebildet wurde.

Die lokale Seismizität in der Alboran Region stellt eine Ausdünnung der Lithosphäre von West nach Ost dar. Lithosphärische Beben im westlichen Alboran Becken treten in einer Tiefe von bis zu 30 km auf. Im östlichen Alboran Becken wurden Beben mit einer maximalen Tiefe von 15 km lokalisiert. Die tiefsten Beben in der Alboran Region mit einer Tiefe bis 100 km treten hauptsächlich im westlichen Teil des westlichen Alboran Beckens auf. Diese Erdbeben können auf die Reste der Lithosphärenzunge der früheren Subduktionszone zurückgeführt werden.

Die lithosphärische Seismizität des Alboran Beckens tritt hauptsächlich nahe von topographischen Strukturen auf. Diese verteilen sich in zwei Bereiche. Zum einen entlang des Alboran Rückens im Osten des westlichen Alboran Beckens mit bis zu 30 km tief liegenden Hypozentren und zum anderen nahe der Carbonera Verwerfung im östlichen Alboran Becken mit Beben in bis zu 15 km Tiefe.

Beide Datensätze, die seismischen Weitwinkel-Refraktionsdaten und die seismologischen Daten, zeigen eine krustale Verdünnung von West nach Ost. Zusätzlich zu der seismischen Geschwindigkeitsstruktur und der lithosphärischen Seismizität werden mit den tieferen Erdbeben im westlichen Teil des westlichen Alboran Beckens weitere Informationen für das Alboran Becken bereitgestellt als bisher vorhanden waren. Diese Daten unterstützen das westwärtige Zurückweichen der abtauchenden ozeanischen Platte als Formationsgeschichte des Alboran Beckens.

Contents

Abstract	i
Zusammenfassung	iii
1 Introduction	1
1.1 The Western Mediterranean Sea: Tectonic Evolution	2
1.1.1 The two Plates in the Mediterranean Region	2
1.1.2 Formation of the Western Mediterranean Sea	3
1.2 The Alboran Sea: Tectonic Evolution	9
1.2.1 Geology of the Alboran Sea	9
1.2.2 Formation of the Alboran Sea	12
1.3 Related Work	15
1.3.1 Active Seismics	15
1.3.2 Seismology	16
1.4 Motivation of this Study	17
2 Tools for Seismic Analysis	19
2.1 Seismic Refraction Analysis	19
2.1.1 Phase Picking	19
2.1.2 Rayinvr	20
2.1.3 Tomo2D	21
2.1.4 Amplitude Modeling	25
2.2 Earthquake Analysis	26
2.2.1 SEISAN	26
2.2.2 VELEST	27
3 Seismic Data	29

3.1	Seismic Refraction	29
3.1.1	Profile Location	29
3.1.2	Data Acquisition	29
3.1.3	Data Pre-Processing	32
3.1.4	Phase Picking	34
3.2	Earthquake Dataset	36
3.2.1	The Project	36
3.2.2	Data Acquisition	36
3.2.3	Data Pre-Processing	37
3.2.4	Phase Picking	39
4	Seismic Refraction Analysis	43
4.1	Forward Modeling	43
4.1.1	Modeling Strategy	43
4.1.2	Resulting Forward Model	43
4.2	Inversion	48
4.2.1	Modeling Strategy	48
4.2.2	Modeling Results	55
5	Synthetic Modeling of the Seismic Refraction Data	63
5.1	Modeling Procedure	63
5.2	Synthetic Seismogram	64
6	Modeling Results and Discussion of the Seismic Refraction Data	67
6.1	Velocity Structure	67
6.2	Formation of the analysed Profile in the Alboran Sea	73
7	Seismicity	77
7.1	Recorded Earthquakes in the Alboran Region	77
7.2	Minimum 1D Model	78
7.2.1	Minimum 1D P-Velocity Model	80
7.2.2	Inversion with P- and S-Phases	85
7.2.3	Final Minimum 1D Velocity Model	86
7.3	Results of the Seismological Analysis	88

8 Conclusion	97
A Enlarged Plots	101
B Data Fit and Seismograms of the Recorded Seismic Refraction Data	103
Abbreviations	127
List of Figures	129
List of Tables	137
Bibliography	139
Acknowledgements	149
Eidesstattliche Erklärung	151
Curriculum Vitae	153

Chapter 1

Introduction

More than 40 years before the theory about plate tectonic was accepted and propagated by natural scientists in the 1960s, Alfred Wegener had the idea of the continental drift. Observation of the coastlines of different continents far away from the other looked like a puzzle and geological parallels between Africa and South America inspired Alfred Wegener to the theory of continental drift which he first published in "*Die Entstehung der Kontinente*" in 1912. His assumption was of one supercontinent that broke in parts which drifted away, plowing through the oceanic crust. With the assumption of one supercontinent Wegener was right. But the way how the shells of the continent diverged and floated over the earth was not correct. The supercontinent now is named Pangaea and was the origin of all now existing continents.

Magnetic anomalies were discovered in the Atlantic which form a symmetric pattern lined parallel to the Mid Atlantic Ridge. This pattern gave the idea for *Dietz* (1961) and *Hess* (1962) to establish a theory about formation of oceanic crust by sea floor spreading at mid ocean ridges. And when crust is formed somewhere it has to be consumed at another place when there is no extension of the earth or compression of existing crust. This was the origin of plate tectonics which had its onset in Wegeners idea about continental drift. The main plates of the present are displayed in figure 1.1.

Plate tectonics comprise three different types of plate boundaries. The constructive plate boundary where sea floor spreading forms new crust and the plates diverge, the destructive plate boundary known as subduction zones where plates converge and old crust is consumed and the conservative plate boundaries, the transform boundary, where the plates slide along the other.

For the evolution of the Alpine system and therewith the gross structure of the Mediterranean region plate tectonics were responsible. *Dewey et al.* (1973) reconstructed the evolution of this region by defining the initial positions of continental fragments, beginning with seafloor spreading of the Atlantic ocean. Rotation of the African and Eurasian plates and the relative motion towards each other are described by *Dewey et al.* (1973) from 180 Ma until present. This results in the gross structure of the Mediterranean region.

The seismic and seismological structure of the Alboran Sea in the Western Mediterranean is investigated in this study to gain insights into the complex structure of the basin. This

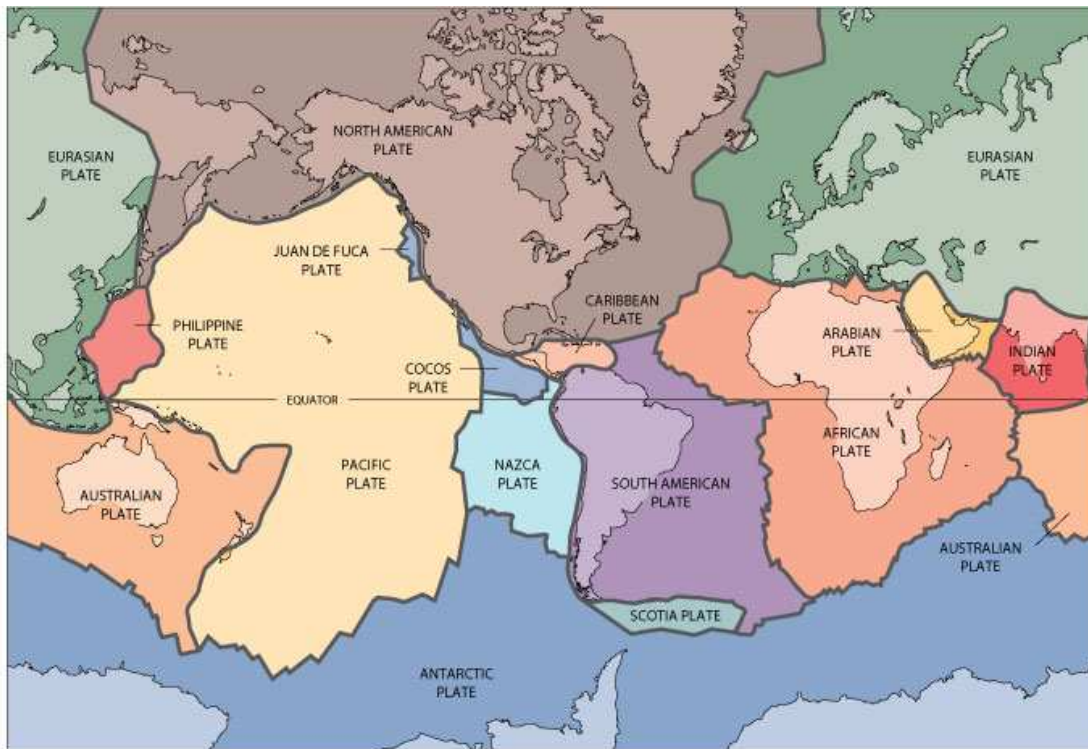


Figure 1.1: Tectonic map of present plate boundaries of the main plates (<http://pubs.usgs.gov/gip/dynamic/slabs.html>).

results gives more information to support a hypothesis of the formation history of this region.

1.1 The Western Mediterranean Sea: Tectonic Evolution

The Western Mediterranean Sea is part of the Alpine System and started to form its present structure in Oligocene. The Alboran Sea at the westernmost End of the Mediterranean Sea is topic of this study. Therefore an introduction to the Mediterranean Sea and its formation history is given in this chapter.

1.1.1 The two Plates in the Mediterranean Region

In the western mediterranean region are two plates converging. These are the Eurasian and the African plate (figure 1.1).

The Eurasian Plate

The Eurasian plate includes most of the Eurasian continent and is one of the biggest tectonic plates. The main part of the Eurasian plate is of continental lithosphere. In the

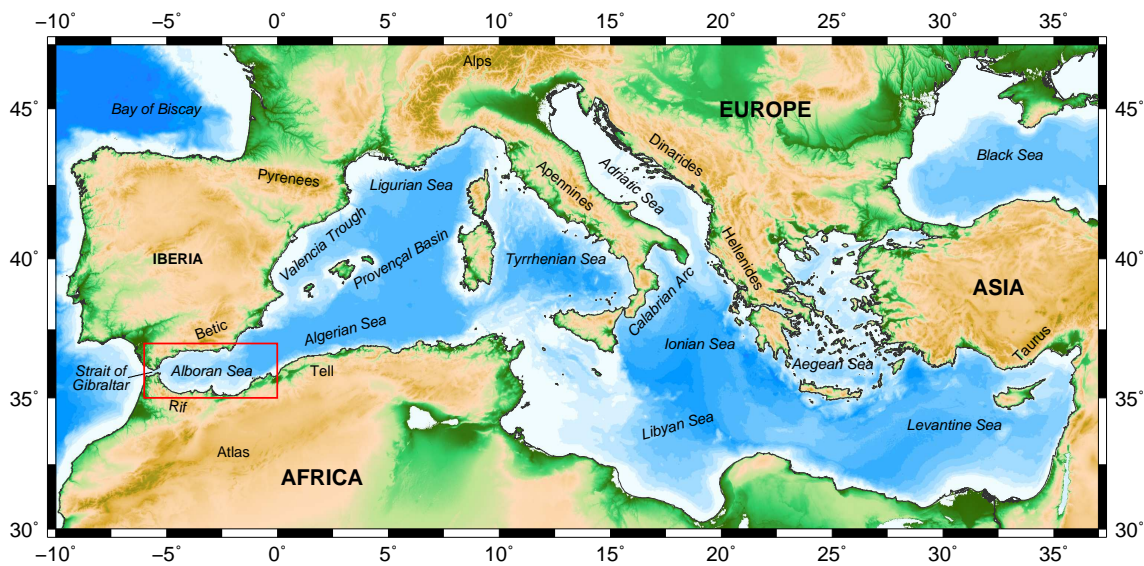


Figure 1.2: Map of the Mediterranean Sea. The red rectangle denotes the Alboran Sea.

West and in the North the boundaries are of oceanic origin with divergent plate boundaries where new oceanic crust is formed at mid ocean ridges. Most of the southern and eastern margin of the Eurasian plate are in a convergent setting. In South-East Asia are present subduction zones whereas the southern and the southwestern part of the plate is in convergent mode but has not a clear subduction zones because of continent-continent collisions.

The northern half of the Eurasian continent is neighboured by the North-American plate whereas the southern part is bordered from east to west by the Philippine, Australian, Indian, Arabian and African plates (figure 1.1).

The African Plate

The African plate contains the whole African continent and has a percentally higher amount of oceanic lithosphere compared to the Eurasian plate. Oceanic crust surrounds the continental crust in the East, South and West (figure 1.1). In the North it is bordered by the Eurasian plate in a convergent regime. East, South and West are in divergent regime with production of new oceanic crust. The bordering tectonic plates are the Arabian, Indian, Australian, Antarctic, South American and North American plates (clockwise enumeration).

1.1.2 Formation of the Western Mediterranean Sea

The Mediterranean Sea is located between the European and the African continent. It was formed while the convergent motion of the tectonic plates of Africa and Europe. Simultaneously with the plate convergence some basins evolved. These new evolved basins are in the western part of the Mediterranean Sea the Alboran Sea, the Algerian-Provençal Basin, the Valencia Trough, the Ligurian Sea and the Tyrrhenian Sea (from West to East).

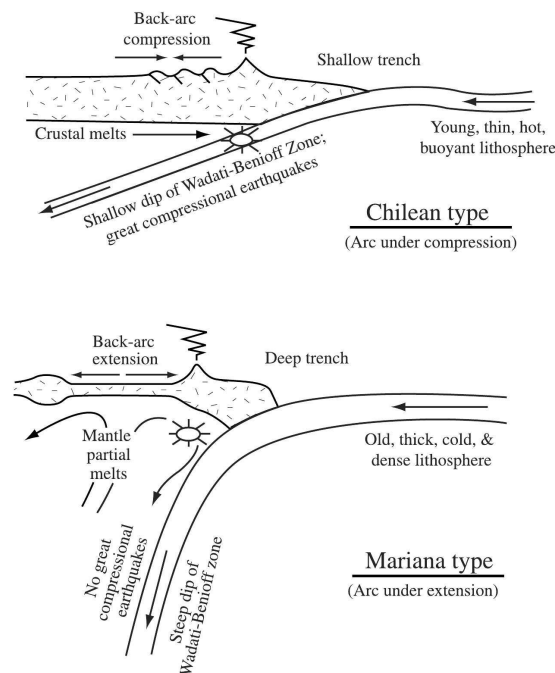


Figure 1.3: Two types of subduction: the Chilean or Andean subduction in a compressional regime (top) and the Mariana type subduction with an extensional back-arc basin (bottom). The figure is taken from Stern (2002) after Uyeda and Kanamori (1979).

The eastern Mediterranean Sea includes from West to East the Adriatic Sea, the Ionian Sea and the Aegean Sea. These basins form the Mediterranean Sea (figure 1.2).

Before Oligocene (> 35 Ma)

In the Mediterranean area, the average convergence between the African and the Eurasian plate is about 0.5-2 cm/yr in NNW-SSE direction increasing from the western (~0.5 cm/yr) to the eastern Mediterranean (~1 cm/yr) (DeMets *et al.*, 1990; Faccenna *et al.*, 2004). A decrease in convergence rate appeared during Late Paleogene / Early Neogene due to collision of both plates (Bailey, 1992; Burke, 1996; Jolivet and Faccenna, 2000; Rosenbaum *et al.*, 2002). A slower convergence continued into reduction of subduction and an increase of slab retreat which ends in an opening of back-arc basins (Jolivet and Faccenna, 2000). This stage delineates a change from compressional Andean-type to an extensional Mariana-type subduction (figure 1.3) (Jolivet *et al.*, 1999; Jolivet and Faccenna, 2000).

The Andean- or Chilean-type of a subduction zone subducts young lithosphere (< 50 million years old) which is thin, hot and not so dense like the underlying asthenospheric mantle because of a thin lithospheric mantle below the crust. The slab has a small dipping angle because of the buoyancy of the subducted material. Consequently in the back-arc region compression appears because the slab tries to resist to be subducted and compresses the overriding plate. Contrary to that, the Mariana-type of subduction experiences extension in the back-arc region. Cold and thick lithosphere is subducted which

is relatively old (> 100 million years old). The thickness of mantle lithosphere can be estimated by $thickness_{lith. mantle} (in km) = 10 \sqrt{age \text{ in } 10^6 \text{ years}}$ because it cools down and gets thicker through time. Crustal thickness stays constant over the whole time. The average density of old crust and old and thick lithospheric mantle is higher than in the underlying asthenosphere and therefore the subducted lithospheric slab sinks with a high angle into the asthenosphere. The slab is pulled down and due to a developed convection cell in the asthenosphere, the subducted slab is pulled further down and the back-arc region extends. The amount of earthquakes is lower in Mariana-type subduction compared to Andean-type subduction because of weak coupling between the two plates and therefore lower resistance against subduction (Uyeda and Kanamori, 1979; Stern, 1998, 2002). Further trench retreat and a rollback of the slab in SE direction continued in the western Mediterranean Sea due to subduction of cold and old lithospheric material. Extension started in the overriding plate and a rifting system initiated. This was the initiation for formation of basins which later formed the western Mediterranean (Rosenbaum et al., 2002).

Oligocene (ca. 34 Ma to 23 Ma)

After the change of subduction type from Chilean- to Mariana-type subduction (compressional to extensional subduction zone) extensional basins started to evolve. The western rift was formed at ca. 35 Ma with evolution of the Gulf of Lion (Jolivet et al., 1999). The subduction system has changed from a SE dipping subduction zone to a NW dipping subduction system in the southern part of the western European continent in Oligocene time (ca. 34 Ma to 23 Ma) (Rosenbaum et al., 2002). This results in a production of calc-alkaline volcanism in nowadays Provençal and Sardinian area (Wilson and Bianchini, 1999; Rosenbaum et al., 2002; Faccenna et al., 2004) which ceased ca. 13 Ma ago. The magmatism was due to seafloor spreading in the back-arc basin of a northwestward dipping subduction zone in the area of Sardinia, Corsica and the Provence (Wilson and Bianchini, 1999). The extensional “front” was during this period more than 1500 km long (Faccenna et al., 2004).

With the beginning of extension and therefore counterclockwise rotation of about 30° in the area of Corsica and Sardinia the formation of all basins in the western Mediterranean had its initiation in the Gulf of Lion (Jolivet et al., 1999; Rosenbaum et al., 2002). Blocks were separated from the European continent and started to rotate together with the Corsica-Sardinia block (figure 1.4 (a) and (b)). With rotation of the Corsica-Sardinia block the Liguro-Provençal Basin started to open from ca. 30 Ma onward. This rifting of the block and the opening of the basin continued until ca. 21 Ma (Jolivet and Faccenna, 2000; Rosenbaum et al., 2002; Faccenna et al., 2004; Brun and Faccenna, 2008).

During Oligocene time back-arc extension migrated further southward from the Liguro-Provençal Basin to the Valencia Trough. The Valencia Trough was opened by rotation of the Balearic block since ca. 26 Ma (Rosenbaum et al., 2002).

Burdigalian (ca. 21 Ma to 16 Ma)

During the extension of the Liguro-Provençal Basin seafloor spreading formed new crust. This ceased together with the end of counterclockwise rotation of the Corsica-Sardinia block and hence at the end of opening of the Ligurian Sea during Burdigalian time (ca. 21 Ma to 16 Ma) (*Burrus, 1984; Jolivet et al., 1999; Jolivet and Faccenna, 2000; Rosenbaum et al., 2002; Faccenna et al., 2004; Brun and Faccenna, 2008*). Because of collision of the Corsica-Sardinia block with the Apennines the opening of the basin ceased (figure 1.4 (c) and (d)). The slab rollback stopped and terminated further extensional processes in this basin (*Rosenbaum et al., 2002*).

During 26 - 16 Ma a clockwise rotation of the Balearic block started to open the the Valencia Trough (*Rosenbaum et al., 2002; Faccenna et al., 2004*). Subsequently, the rifted block split into the Balearic and the Kabylies blocks. A new basin, the Algerian Basin, was formed, opening between these two blocks. The Algerian Basin started to grow because of slab rollback and extension. Due to fast rollback seafloor spreading started to form new oceanic crust in the Algerian-Provençal Basin (*Rosenbaum et al., 2002*).

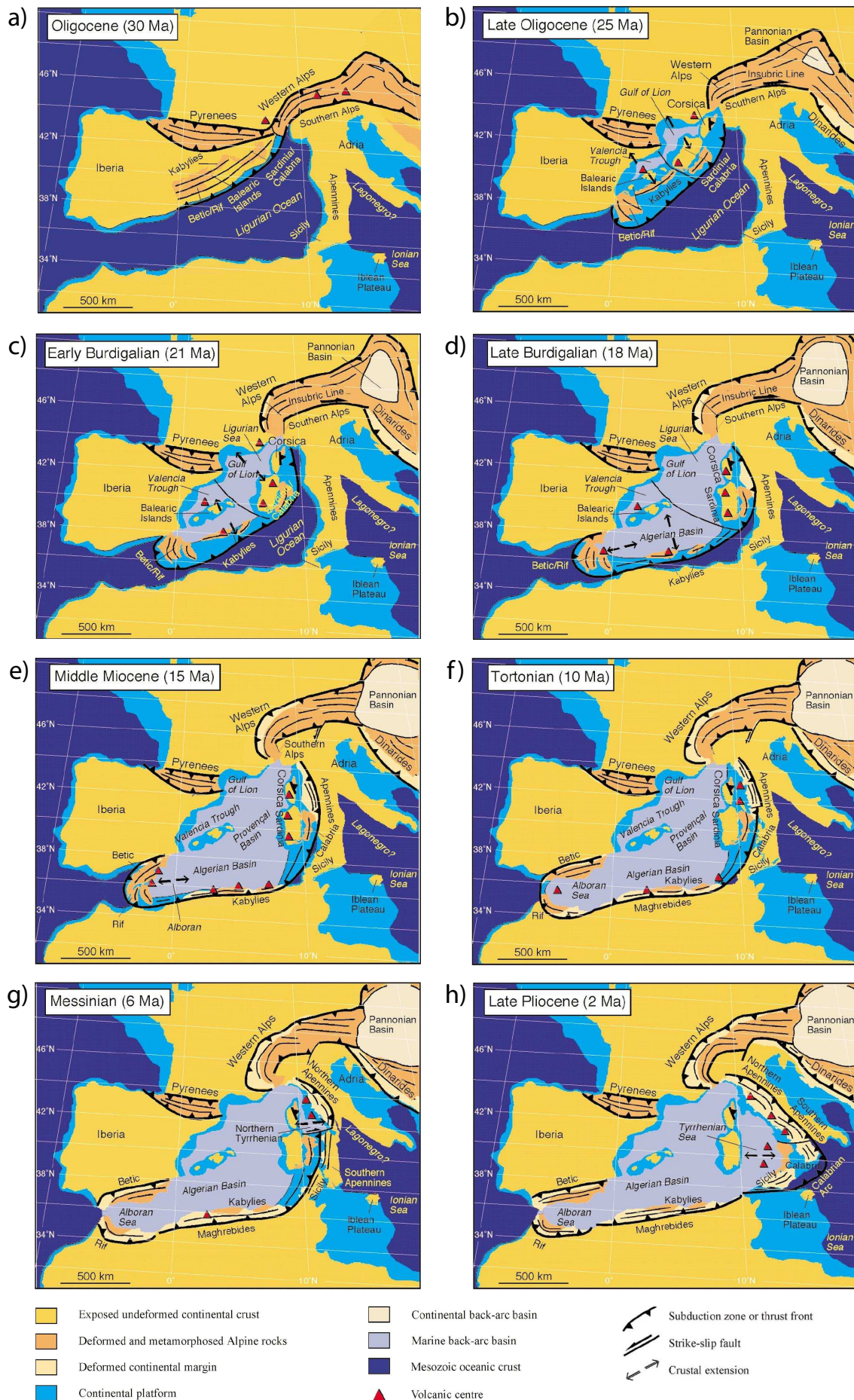
A clockwise rotation of the Betics block during Burdigalian and a coeval counterclockwise rotation of the Rif defines the beginning of the opening of the Alboran Sea (section 1.2.2).

Magmatism of calcalkaline type was spread in the western Mediterranean during entire Burdigalian time in Liguro-Provençal Basin, Valencia Trough and in the Sardinian area which migrated southeastward to the Tyrrhenian region and along the north African coast (*Wilson and Bianchini, 1999; Faccenna et al., 2004*). Also in Morocco and northwestern Algeria subduction related magmatism was present.

Middle Miocene (around 15 Ma)

During Middle Miocene the oceanic lithosphere of Mesozoic age between Kabylies block and the African continent was completely subducted. The Kabylies block migrated further southward until it collided and was accreted at the northern African margin (figure 1.4 (e)). This resulted in the end of southward rollback and extension of the Algerian

Figure 1.4: *Compilation of figures of Rosenbaum et al. (2002) for the evolution of the western Mediterranean. (a) Beginning of the evolution of the western Mediterranean in Oligocene. (b) First stage of extension and formation of the Valencia Trough and the Gulf of Lion in Late Oligocene. (c) Formation of the Provençal Basin in Early Burdigalian. (d) Opening of the Algerian Basin in Late Burdigalian. (e) Collision of the Kabylies Block with the African margin and first stage of opening the Alboran Basin in Middle Miocene. (f) Accretion of Betic and Rif on Iberia and Africa (respectively) in Tortonian. (g) Start of formation of the Northern Tyrrhenian Sea in Messinian. (h) Further opening of the Tyrrhenian Sea in the South in Late Pliocene.*



Basin. Thrusting started in the External Maghrebides (*Wilson and Bianchini, 1999; Rosenbaum et al., 2002*). The collision of the Kabylies block with the African continent divided the subduction zone in two segments. The western segment with a eastward and the eastern segment with a westward dipping subduction zone (*Loneragan and White, 1997; Wilson and Bianchini, 1999; Rosenbaum et al., 2002*).

The eastern part of the subduction zone continued in the Tyrrhenian Sea while the western part delineated the beginning of the formation of the Alboran Basin and the Gibraltar Arc. Clockwise rotation of the Betics block and counterclockwise rotation of the Rifian block created this region (*Rosenbaum et al., 2002; Faccenna et al., 2004*). Contrary to the formation of the Algerian Basin with an extension in N-S direction, this region experienced an E-W directed opening of a new basin. The retrograde migration of the slab of the western Mediterranean subduction zone stopped and caused the end of formation of the Valencia Trough/Balearic Basin during Middle Miocene (ca. 15 Ma) (*Wilson and Bianchini, 1999; Faccenna et al., 2004*).

Magmatism during Middle Miocene appeared in the entire western Mediterranean region and was of calcalkaline type, related to subduction processes (*Wilson and Bianchini, 1999; Faccenna et al., 2004*).

From Tortonian (ca. 12 Ma to 7 Ma) to present

During Tortonian (ca. 12 Ma to 7 Ma), the Alboran Sea developed in the western part of the western Mediterranean Sea and in the eastern part the Tyrrhenian Sea was generated (figure 1.4 (f), (g) and (h)).

A further clockwise rotation of the Betics block and counterclockwise rotation of the Rifian block formed the Gibraltar arc connected to the formation of the Alboran Sea which is described in section 1.2.2.

The Tyrrhenian Sea started to form since approximately 9 Ma (Middle Tortonian). Prior there was probably a calm phase of back-arc extension in this region and during Tortonian a new extension between Corsica and Sardinia in the West and the Apennines in the East developed (*Jolivet et al., 1999; Rosenbaum et al., 2002; Faccenna et al., 2004*). This worked in two steps. First the northern Tyrrhenian Sea started to open during 9 Ma to 5 Ma. At the same time the crust of the Apennines was shortened and thrust and a counterclockwise rotation took place. During the second phase (5 Ma to present) the southern part of the Tyrrhenian Sea opened, controlled by slab rollback of oceanic Ionian lithosphere beneath Calabrian arc. This was accompanied by counterclockwise rotation of the Apennines during Tortonian to Pliocene (ca. 5.3 Ma to 2.6 Ma) in the northern region and from Pliocene until now in the southern Tyrrhenian Sea. After rifting until 5 Ma in the Tyrrhenian Basin seafloor spreading to SE occurred until ca. 1 Ma and formed new oceanic crust (*Jolivet et al., 1999; Wilson and Bianchini, 1999; Faccenna et al., 2004; Brun and Faccenna, 2008*).

The subduction slab in the Sicily Channel broke into two pieces. One slab with further southward rollback to the northern African region and the other slab retreated in the Calabrian region to the SE (*Faccenna et al., 2004*). Together with a 15° to 25° clockwise rotation

of Calabria during Pliocene and Pleistocene (ca. 2.6 Ma to 12000 a) and clockwise rotation of the Sicily block the Calabrian arc formed simultaneously to the formation of the Tyrrhenian Basin (*Rosenbaum et al.*, 2002; *Faccenna et al.*, 2004).

During Early Tortonian alkaline volcanism appeared in the Valencia Trough and calcalkaline volcanism in the whole Algerian Basin. In the southern Alboran region alkali-basalt magmatism was present (*Faccenna et al.*, 2004). Between 10 Ma and 5 Ma alkali-basalts erupted in northern Tunisia, Sardinia and the southern Tyrrhenian Basin. In the Tyrrhenian Basin it changed to calcalkaline volcanism and rested after 5 Ma.

The solely left subduction zone in the Western Mediterranean is in the Calabrian region and partly in the northern Appenines (*Faccenna et al.*, 2004).

1.2 The Alboran Sea: Tectonic Evolution

The Alboran Sea is the westernmost part of the Mediterranean Sea (figure 1.2) and lies between the convergent plates of Europe and Africa. It is bordered in the West by the Strait of Gibraltar and in the East it continues into the Algerian Sea and the Southern Balearic Basin. The northern and southern borders of the Alboran Sea are mountain chains formed during the formation of the Mediterranean Sea. In the North on the Iberian Peninsula are the Betic mountains and in the South on the African plate the Rifian mountains. Together with Gibraltar, the mountain chains form an arc.

The formation of the Alboran Sea is until now still under investigation. There exist different hypotheses for the formation, e.g. the subduction related back-arc basin, the Mediterranean type back-arc basin, a basin related to mantle diapir, a basin related to convective removal of lithospheric root or a basin related to asymmetric delamination of lithospheric mantle (*Polyak et al.*, 1996). The main hypotheses are explained in section 1.2.2.

1.2.1 Geology of the Alboran Sea

The geology of the Alboran Sea is a result of the geodynamic evolution of the Mediterranean. The convergence between the African and the Eurasian continent played a big role in the formation of this region.

Onshore the main pre-Neogene crustal domains of the Gibraltar Arc are the External Zone, the Internal Zone and the Flysch Trough (figure 1.5 (a)). The External Zone comprises the South Iberian cover on the Iberian Peninsula and the Maghrebian cover on the African continent (figure 1.5 (a)). Sedimentary rocks of Mesozoic to Tertiary age represent the passive paleomargin of Iberia and Africa which were deformed by thrusting and folding during the Alpine orogenesis. The sediments consist of autochthonous, parautochthonous and allochthonous non-metamorphic rocks (*Coward and Dietrich*, 1989; *Lonergan and White*, 1997; *Comas et al.*, 1999; *Rosenbaum et al.*, 2002; *Cavazza et al.*, 2004; *Frizon de Lamotte et al.*, 2004).

A separation of the External and the Internal Zones is done by the Flysch Trough (figure 1.5 (a)). This unit consists of Cretaceous to Early Miocene marine sediments of nappes

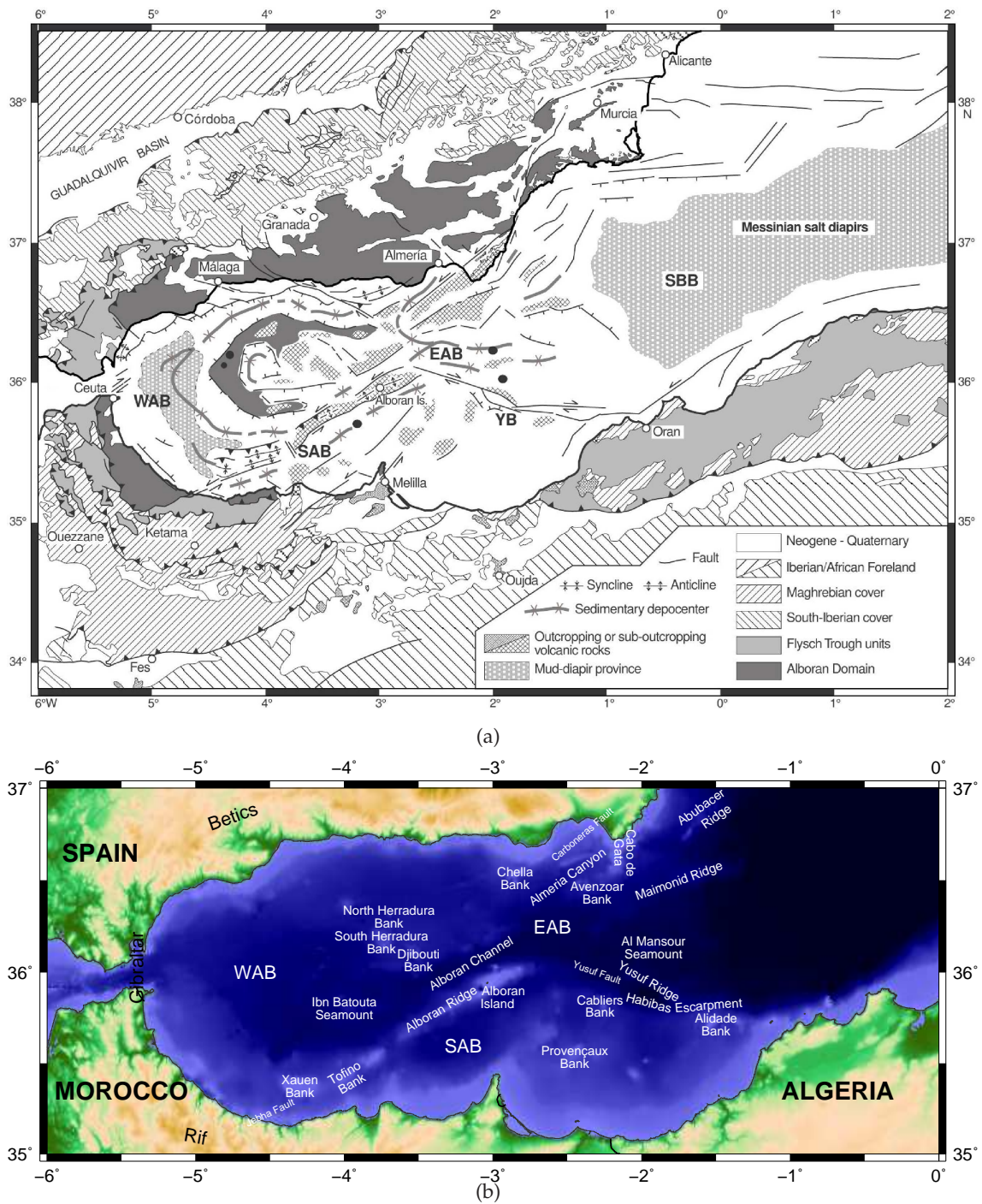


Figure 1.5: (a) Geological map of the Alboran Sea and surrounding onshore (after Comas *et al.* (1999)). Black circles show location of ODP Leg 161 sites and DSDP Site 121. (b) Topographic map of the Alboran Sea. Main structural features are shown. EAB = East Alboran Basin; SAB = South Alboran Basin; SBB = South Balearic Basin; WAB = West Alboran Basin; YB = Yusuf Basin.

which were highly deformed and deposited in a trough on oceanic or very thin continental crust (Comas *et al.*, 1999; Cavazza *et al.*, 2004).

The Internal Zone is also known as Alboran Domain (figure 1.5 (a)). It is made of Paleozoic and Mesozoic marine sediments thrust onto the External Zone during Miocene. Deformation and partly high-pressure low-temperature metamorphism influenced the structure. Parts of the Internal Zone are (from bottom to top) the Nevado-Filábride, Alpujarride and Maláguide complexes (Lonergan and White, 1997; Comas *et al.*, 1999; Rosenbaum *et al.*, 2002; Cavazza *et al.*, 2004; Frizon de Lamotte *et al.*, 2004).

Magmatism in the arcuate Betic-Gibraltar-Rif mountain belt is mainly of calc-alkaline series and occurred during Miocene (Duggen *et al.*, 2008).

The Alboran Sea itself has different structural features like margins, subbasins and structural highs (figure 1.5 (b)) (Maldonado and Comas, 1992; Ballesteros *et al.*, 2008). The main subbasins are the West Alboran Basin (WAB), South Alboran Basin (SAB) and East Alboran Basin (EAB). In the WAB are different topographic highs where the prominent features are the Xauen Bank, Tofino Bank, Ibn Batouta Seamount, South Herradura bank, North Herradura Bank and Djibouti Bank (from West to East). Djibouti Bank, North and South Herradura Bank are also called the 36°10' High (Ballesteros *et al.*, 2008). At the boundary to the SAB are the Alboran Channel and the Alboran Ridge with Alboran Island on top. The Cabliers Bank, Provençaux Bank and Alidade Bank are the main topographic highs in the SAB (West to East). In the easternmost part of the SAB is the Habibas Escarpment which forms the boundary to the EAB and the Algerian Basin. In the EAB are the Chella Bank, Almeria Canyon, Avenzoar Bank, Maimonid Ridge, Al Mansour Seamount and Yusuf Ridge (Northwest to Southeast).

The basins of the Alboran Sea are covered by Miocene to present sediments with a thicker sequence in the west (up to 7 - 8 km) compared to the east (less than 4 km). This sedimentary cover is of syn-rift deposits and post-rift sediments (Comas *et al.*, 1992, 1999).

In the transition to the South Balearic and Algerian Basin an evaporitic layer is present, developed due to the Messinian salinity crisis (Duggen *et al.*, 2003; Booth-Rea *et al.*, 2007; Govers, 2009).

Strike-slip, normal and reverse faults cut the Alboran Basin (e. g. Maldonado *et al.*, 1992). Parallel to the Almeria Canyon runs the Carboneras Fault in NE-SW direction, a strike slip fault. Other major faults are also strike slip and are the Jebha Fault which also trends NE-SW and continues on land Morocco and the Yusuf Fault with an NW-SE trend, running parallel to the Yusuf Ridge (Maldonado *et al.*, 1992).

Until Miocene volcanism influenced the morphology of the Alboran Sea, occurring mainly in the central and eastern part (Comas *et al.*, 1999). Magmatic style was tholeiitic (LREE¹-depleted) to calc-alkaline (LREE¹-enriched) (Hoernle *et al.*, 1999; Duggen *et al.*, 2004, 2008) which formed the different structural features like Alboran Island (tholeiitic) or Xauen Bank (calc-alkaline). Tholeiitic volcanism occurs mainly in the central Alboran Sea (keel-shaped) and calc-alkaline volcanism subparallel to the arcuate Betic-Gibraltar-Rif mountain belt.

¹LREE = Light Rare Earth Element

1.2.2 Formation of the Alboran Sea

The Alboran Sea is an extensional basin formed during a compressional regime where the continental plates of Africa and Eurasia collide. How the Alboran Sea formed during this compressional regime is until now under discussion. There exist different hypotheses to explain the processes until present. The main hypotheses are enumerated by e. g. *Rosell et al.* (2011):

- convective removal of thickened lithospheric root that caused uplift and extension (*Platt and Vissers, 1989; Platt et al., 1998*)
- lithospheric delamination caused by gravitational collapse of thickened lithosphere (*Seber et al., 1996; Mezcuca and Rueda, 1997; Calvert et al., 2000*)
- westward to southwestward rollback of oceanic slab that generated back-arc extension (*Royden, 1993; Lonergan and White, 1997; Gutscher et al., 2002*)
- south-eastward rollback of an oceanic slab attached to African plate (*Doglioni et al., 1997*)
- south-eastward delamination of subcrustal lithospheric slab (*Docherty and Banda, 1995*)
- slab detachment: vertical broken-off piece of a previously subducting lithospheric slab (*Zeck, 1996, 1997*)

Mainly represented theories are explained and summarized in the following sections.

Convective Removal Theory

A schematic view of convective removal is shown in figure 1.6. Figure 1.6 (a) is the state with an initial thickness of the lithosphere. While plate convergence between the African and Eurasian plate the lithosphere thickened when the two continental plates collided (figure 1.6 (b)). The thermal gradient in the lithosphere decreased. Convection removes the lower part of the thickened lithosphere, which is colder and hence denser compared to the underlying asthenosphere, (figure 1.6 (c)) and results in a step of the thermal gradient (*Platt and England, 1993; Turner et al., 1999*). This step occurs because asthenosphere replaces the removed lithosphere and the asthenosphere is hotter compared to the lithosphere. The thinning of the lithosphere is accompanied by an increase of elevation because of removed dense lithosphere and an increase of the potential energy which involves stress differences and are caused by differences in potential energy of different rocks. The differences in potential energy triggers the extension of the region of thinned lithosphere (figure 1.6 (d)). Lithospheric thinning increases the thermal gradient and shallower parts are getting hotter. At last the thermal gradient decreases by re-establishing the thermal equilibrium (*Platt and England, 1993*).

Convective removal is associated by magmatism through partial melting in the lower crust (*Turner et al., 1999*). This volcanism is of calc-alkaline style.

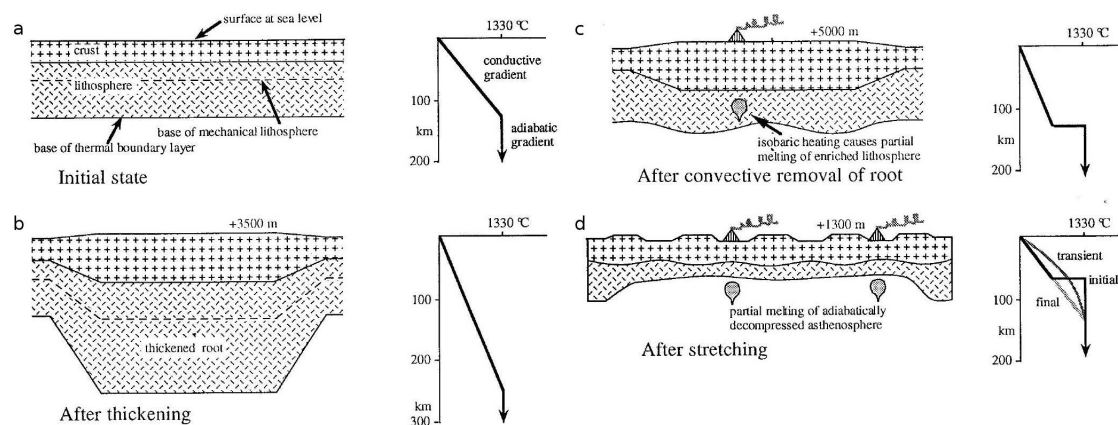


Figure 1.6: Sketch of convective removal (after Platt and England, 1993). (a) The initial state with the initial thermal profile in equilibrium. (b) Thickened lithosphere with a reduced thermal gradient. (c) Convective removal thinned the lithosphere and replaced removed lithosphere by asthenospheric mantle. The thermal gradient was induced with a step at the lithosphere-asthenosphere boundary. (d) Extension results and the thermal gradient due to lithospheric thinning increases. Through time the thermal gradient gets back to its equilibrium.

The results of e.g. Platt and Vissers (1989); Platt et al. (1998); Turner et al. (1999) support convective removal as the theory for the formation of the Alboran region.

Lithospheric Delamination Theory

Lithospheric delamination is similar to convective removal. During the plate convergence between Africa and Eurasia, the lithosphere in the Alboran region thickened. Lithospheric mantle started to detach from the crustal lithosphere and peels away. The removed lithosphere is replaced by hot asthenospheric material. Uplift followed the delamination of lithosphere and resulted in an extensional regime (Seber et al., 1996). Volcanism was the result of the hot asthenosphere which replaced the delaminated slab and accompanied the extensional regime.

Low seismic velocities in the upper mantle is one result which would follow lithospheric delamination (Seber et al., 1996).

In the Alboran region it is thought to be a complex structure where the Iberian lithosphere delaminates to the north, the Moroccan Lithosphere to the south and the lithosphere beneath the Gulf of Cadiz to the west beneath the Atlantic (Seber et al., 1996).

Westwards Slab Rollback Theory

After Royden (1993) and Lonergan and White (1997) the Alboran region has its beginning in the Alpine orogenic belt. The blocks of the Betics and the Rif originate like the Corsican, Sardinian, Calabrian and Kabylies block from the Alpine area and were formed during high-pressure metamorphism of the Alpine orogenesis (Rosenbaum et al., 2002). These blocks broke away from the European continent and rotated and migrated away from the European continent due to subduction rollback and therewith linked back-arc exten-

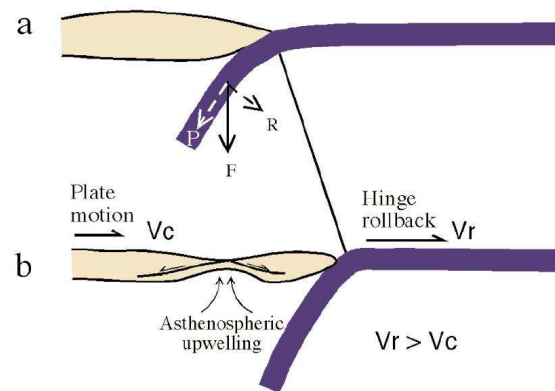


Figure 1.7: Sketch of the evolution of slab rollback (Rosenbaum *et al.*, 2002 after Lonergan and White, 1997). (a) The vertical negative buoyant force F of the subducting slab has the two components P (slab pull) and R (slab retreat). If R is big enough and the asthenospheric mantle cannot support the overlying cold and dense slab anymore, the slab starts to retreat. (b) Extension starts and opens a back-arc basin when the velocity of the retreating slab v_r exceeds the velocity of the plate convergence v_c .

sion (figure 1.4 (a) and (b) and section 1.1.2 (“Before Oligocene (> 35 Ma)” and “Oligocene (ca. 34 Ma to 23 Ma)”)). At 30 Ma in the Gulf of Lion extension started with first stages of opening of the Liguro-Provençal, the Alboran and the Tyrrhenian basins (Jolivet *et al.*, 1999). During Burdigalian the clockwise rotation of the Betics and the counterclockwise rotation of the Rif began. These rotations lasted until ca. 10 Ma and were in the Betic area about 130° to 200° and in the Rif $\sim 100^\circ$ (Lonergan and White, 1997; Rosenbaum *et al.*, 2002). A curvature in the western end of the subduction zone in the Mediterranean Sea produced a westward rollback of the subduction hinge, separating the new formed Alboran Basin from the Algerian Basin. This rollback migrated further to the SW until the subduction zone reaches the African margin in the south. From there on the rollback continued simply westward further into the area with oceanic lithosphere of the Atlantic (figure 1.4 (e)). Rapid westward rollback thinned the continental crust to approximately 15 km during the period from Early Burdigalian to Early Tortonian (Wilson and Bianchini, 1999; Lonergan and White, 1997; Rosenbaum *et al.*, 2002; Faccenna *et al.*, 2004). The end of back-arc extension was when the rollback of the subduction slab reaches Gibraltar and accretion of the continental blocks of the Betics onto the Iberian margin and of the Rif onto the northern African margin occurred during Middle to Late Tortonian (Lonergan and White, 1997; Rosenbaum *et al.*, 2002; Faccenna *et al.*, 2004) (figure 1.4 (f)). The Betic and Rif block form the External Zone in these areas.

Its origin has the slab rollback in old oceanic lithosphere which is colder and dense compared to the underlying asthenosphere and therewith can sink into the asthenosphere. A sketch of subduction rollback is shown in figure 1.7. Back-arc extension occurs when subduction rollback exceeds the plate convergence. Slab rollback ends when all oceanic lithosphere is subducted (Lonergan and White, 1997).

Over the whole time of formation of the Alboran Basin about 210 km crust was extended (Faccenna *et al.*, 2004). Observations in the Betics and the Rifian cordillera like the rotation analysis support the slab rollback model (Rosenbaum *et al.*, 2002). Thrusting in the External Zone and coeval extension in the Internal Zone of the Betic, Rif, Gibraltar and Alboran regions approve the theory of slab rollback (Gutscher *et al.*, 2002). Lonergan and White (1997) depicted that the diffusely located volcanism also supports the slab rollback theory in an eastward dipping subduction zone with westward rollback of the slab. Also the types of volcanism of calcalkaline, alkaline and basaltic style can be due to slab rollback because extensional volcanism and volcanism associated to a formation of an arc occur in regions which are formed during slab rollback and which are present in the Alboran region.

1.3 Related Work

1.3.1 Active Seismics

The *Working Group for Deep Seismic Sounding in the Alboran Sea 1974* (1978) performed a seismic sounding experiment in 1974 where onshore stations in Spain and Morocco recorded seismic data from offshore shots with the goal to determine the run of the Moho depth. They found a shallow Moho in the Alboran Sea with a depth of ~16 km and low mantle velocities.

Seismic studies close to the coast were analysed by Comas *et al.* (1992) for the Spanish and Bourgois *et al.* (1992) for the Moroccan coast. Both analysis are based on industrial multichannel seismic studies (MCS) and analyse the sequences above the basement to gain an insight into the formation history of this region.

In 1992 a survey to gain multichannel deep seismic data called ESCI-Alb was conducted in the Alboran Sea. First interpretation is published by Comas *et al.* (1995). ESCI-Alb is a subproject of the Spanish national program "ESCI¹ project: Seismic Studies of the Iberian Crust". The onshore part is the subproject ESCI-Béticas (García-Dueñas *et al.*, 1994).

ESCI-Alb contains two profiles with altogether ~400 km of multichannel deep seismic data. ESCI-Alb 1 is running in NNE-SSW direction from the northern margin of the Alboran Sea to the center. The interpretation together with ESCI-Béticas 2 is published by Gallart *et al.* (1995). ESCI-Alb 2 trends in WSW to ENE and provides information of the upper structure of the central Alboran Sea to the Algero-Balearic basin. A reinterpretation of further processed data of two parts of the ESCI-Alb 2 profile (ESCI-Alb 2b and ESCI-Alb 2c) was done by Booth-Rea *et al.* (2007). They interpreted the structure of the crust as tripartite. The westernmost part is continental crust modified by arc magmatism, changing to a magmatic arc crust and altering the structure to oceanic crust in the eastern part of the profile.

¹ESCI = Estudios Sísmicos de la Corteza Ibérica

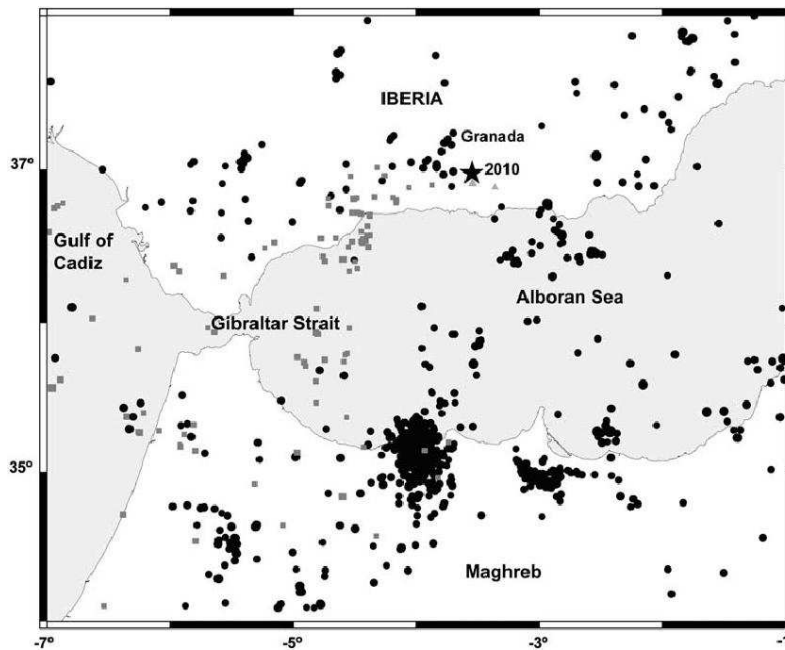


Figure 1.8: Seismic map of Bufo *et al.* (2011). Epicenters in the Alboran region from 1990-2010 with a magnitude larger than 3.0 (catalog of Instituto Geográfico Nacional (IGN), Spain). Circles: earthquake shallower than 40 km, squares: earthquakes between 40 and 150 km depth, triangles: earthquakes deeper than 150 km and star: 2010 Granada earthquake.

1.3.2 Seismology

Different studies were conducted by using earthquake data to model the deeper structure beneath the Alboran region (e. g. *Serrano et al.*, 1998; *Gurría and Mezcuca*, 2000; *Bufo *et al.**, 2004; *Thiebot and Gutscher*, 2006; *Fernández-Ibáñez and Soto*, 2008). The different studies used earthquake data from several years to obtain a sufficient amount of data. Stations were only onshore and therewith the interpretation of the offshore structure contained an error due to runtime errors of an earthquake (*Serrano et al.*, 1998; *Gurría and Mezcuca*, 2000; *Fernández-Ibáñez and Soto*, 2008).

In other studies earthquake data were used to specify the focal mechanism of earthquakes and performed a seismotectonic interpretation (*Bufo *et al.**, 2004). The seismotectonic structure of the Alboran region is diffuse and the stress is released by continuous seismic activity with moderate magnitude. The plate boundary between Africa and Eurasia is not outlined by the hypocenters.

Figure 1.8 shows a map of *Bufo *et al.** (2011) of the Alboran region with shallow, intermediate and deep earthquakes. Shallow earthquakes (< 40 km) occur in the eastern part of the Alboran region. Earthquakes in the intermediate depth (40-150 km) occur in the western part of the Alboran Sea which could indicate the remaining slab of the subducted crust. Deep earthquakes rarely occur in this region. One of the deep earthquakes is the magnitude 6.2 earthquake in 2010 close to Granada in a depth of 650 km (*Bufo *et al.**, 2011). Stronger earthquakes are also rare in this region. The Granada event was the recent strong event. In 1954, a magnitude 7.8 event ruptured also beneath Granada in a depth of 630 km (*Chung and Kanamori*, 1976). A historic event with a magnitude of 6.1 ruptured in 1910 offshore Adra (~16 km deep) (*Stich et al.*, 2003b).

1.4 Motivation of this Study

The geophysical investigation in the Alboran Sea has its aim to gain a structural model of the lithosphere. Refraction analysis is done with wide-angle data collected in 2006. The dataset is used to model the crustal structure and depth of the Moho (chapter 4). Deeper structure below the Alboran Sea is modeled with the usage of earthquake data to develop a 1D-velocity model (chapter 7). The motivation for both studies is summarized in a good way by *Maldonado and Comas (1992)*:

A general consensus was reached at the workshop² to recognize the importance of the Alboran Sea and surrounding mountain belts, not only for the analysis of the geodynamics of the African and Eurasian plates, and probably for the evolution of the adjacent continental margins of the central North Atlantic, but also to understand mechanisms of creation of small seas and oceans interior to orogenic inland arcs.

By modeling the structure of the Alboran Sea, a base for the interpretation of the formation of the region is provided. The resulting models make it possible to determine which formation hypothesis enumerated in section 1.2.2 is plausible and which one is implausible.

Main questions which are the goal to be answered by an analysis of available data are:

- Which kind of crust is present in the eastern Alboran Sea?
- Which kind of crust is present in the transition from the Alboran Basin to the Algero-Balearic Basin?
- Which formation history has the Alboran Basin?
- How is the structure of the mantle along the analysed seismic refraction profile defined?
- How is the seismicity distributed in the Alboran Sea (especially for shallow and deep events)?

²CIESM, XXXI Congress and Plenary Assembly 1988 (International workshop in Athens, Greece)

Chapter 2

Tools for Seismic Analysis

In this thesis seismic refraction and wide-angle data are used for the study of the crustal structure and recordings of local earthquakes to delineate a simple 1D model for the structure of the mantle.

For the interpretation of seismic data recorded traveltimes and amplitudes need to be interpreted. In active seismics, traveltime data are inverted for seismic velocities, imaging the crustal and upper mantle structure. Similar approaches can be applied to passive data, i.e. earthquakes.

In this chapter, tools and inversion techniques will be briefly outlined.

2.1 Seismic Refraction Analysis

The aim of the seismic refraction and wide-angle profiling is to gain a 2D velocity structure by using traveltimes of reflected and refracted acoustic waves. Therefore two different approaches are used: a forward method and tomographic inversion. Each method is done with a distinct program. The forward modeling was done with the ray tracing program *rayinvr* (Zelt and Ellis, 1988; Zelt and Smith, 1992). For the inversion of the traveltimes the *Tomo2D* code from Korenaga was used (Korenaga *et al.*, 2000, 2001).

For the validation of the resulting 2D velocity structure an amplitude modeling approach was used. Therewith resulting amplitudes of the velocity structure are compared to recorded data (section 2.1.4).

2.1.1 Phase Picking

Phase picking for the refraction analysis is done with the *zplot* program (Zelt, 1997). Collected data are converted with *segy2z* into the *z* format which is used for the program *zplot*. Interactive plotting, picking, filtering and data editing are the main usage of the program. Different phases which are identified while picking are related to a number for further usage with other programs. The number is a phase ID and makes it possible to distinguish between for example Pg-, PmP- and Pn-phases ¹.

¹Pg = seismic refraction from crust; PmP = seismic reflection from Moho; Pn = mantle diving

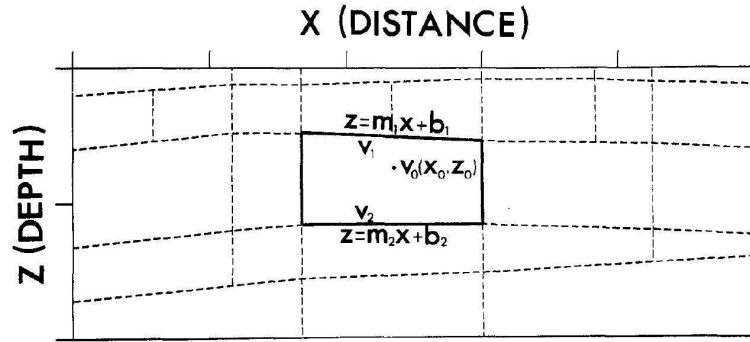


Figure 2.1: Example for a model layering from rayinvr (Zelt and Ellis, 1988).

With the small program headup the picked phases are stored in a file together with the phase relating ID. For usage with rayinvr (section 2.1.2) these picks are converted to a tx.in file which is ascii-format. Tomo2D (section 2.1.3) needs a different kind of format which can be produced out of the tx.in file.

2.1.2 Rayinvr

Rayinvr is a program for ray tracing via forward and inverse modeling by Zelt and Ellis (1988). The forward modeling method (which is used in this study) is based on a 2D trial-and-error forward modeling approach with a simple, layered, large-block velocity model parameterisation and uses the converted output of the zplot output file (section 2.1.1). The parameters of the model are quasi horizontal layers where the depths of the separating boundaries and the velocities in this layers are defined in a simply to change file. The depth values of one boundary are defined at different x-positions of the model. The velocities are defined at top and bottom of a layer for x-coordinates. This results in a model with trapezoidal blocks (figure 2.1). The velocities in the trapezoidal blocks are linear interpolated between the upper and lower velocity values.

To test the constructed model the ray tracing equations are solved numerically. When the raypaths are near-horizontal,

$$\frac{dz}{dx} = \cot \Theta \quad \text{and} \quad \frac{d\Theta}{dx} = \frac{(v_z - v_x \cot \Theta)}{v} \quad (2.1)$$

and for near-vertical raypaths

$$\frac{dx}{dz} = \tan \Theta \quad \text{and} \quad \frac{d\Theta}{dz} = \frac{(v_z \tan \Theta - v_x)}{v} \quad (2.2)$$

are solved, where Θ is the angle between the tangent to the ray and the z-axis.

Through the model Snell's law has to be satisfied for each ray at every point of the model. Each ray is divided into several small segments (Δ) where the length of each segment is dependent on the velocity gradient in the velocity model and therewith the ray bending. Is the velocity gradient in a layer large, the length of a ray segment is small. Is the velocity

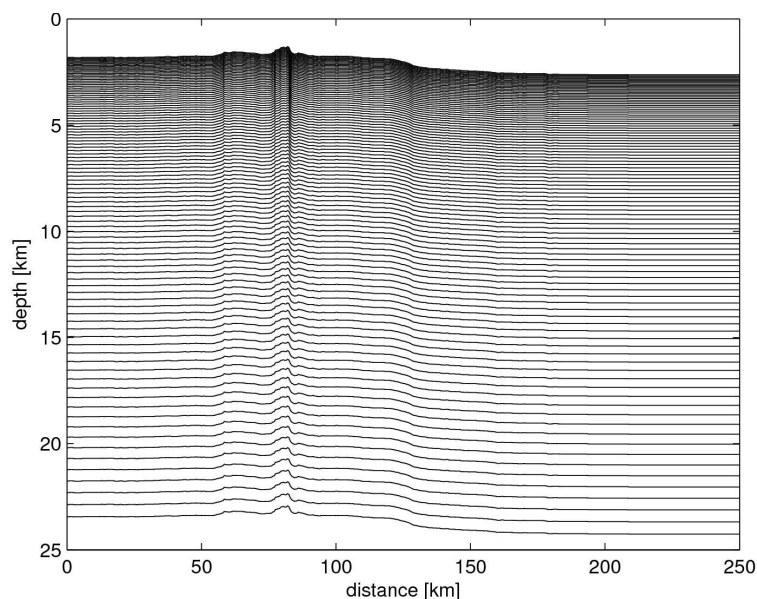


Figure 2.2: Grid structure of a velocity model. A mesh is hanging below the seafloor with a spacing increasing with depth. The used grid spacing of the x-axis for this study is 0.5 km, which is due to distinguishability not visualised in this grid.

gradient small, the length of a segment is large:

$$\Delta = \frac{\alpha v}{|v_x| + |v_z|}. \quad (2.3)$$

α is a parameter for the step length and is chosen after consideration of RMS traveltimes error and computational time.

More complex structures of a velocity model can be constructed with pinch-out layers. These layers have in some blocks of the model a thickness of 0 km and are needed to model a subduction zone or just an isolated block.

Rays are traced through the model as ray families. These ray families are turning rays, reflections or head waves. The endmodel is constructed after trial-and-error forward modeling when the RMS traveltimes error of the computed traveltimes is small compared to the observed data.

2.1.3 Tomo2D

The tomographic inversion of the 2D seismic traveltimes data is done with the Tomo2D-code from *Korenaga et al.* (2000). It is a jointly inversion of refracted and reflected phases which are identified and picked in the program *zplot* (section 2.1.1).

The parameterisation of the starting 2D velocity model is a sheared mesh hanging beneath the seafloor and/or land surface (*Korenaga et al.*, 2000). Therefore designated x-coordinates are chosen which can differ in distance to the next node. The finer the node-spacing, the finer the resolution of the velocity model. But with an increasing number of nodes the computational time increases and a too coarse node spacing can result in

inaccuracy. The node spacing of the z-coordinate can be equidistant or differ in depth. A finer spacing in the upper parts of a model is useful to resolve stronger variations in the velocity structure which is due to geological settings. In the lower parts of a model a wider spacing of the depth nodes is good enough because the structure is not as good resolved in the dataset as in the upper part where more rays are passing through and defining this domain. The resulting grid has the topography as its top and each layer of the mesh is parallel to the topography (figure 2.2). This mesh is balanced in resolution of geological structures and computational effort.

A further input file can be a reflector file. This reflector can be the crust-mantle boundary which is used to model the PmP phases. It is defined as a simple x-z-file where the first column contains the x-coordinates and the second column the corresponding z-coordinate. The number of coordinates is arbitrary.

Forward Problem

Tomo2D includes a forward and an inverse approach for a velocity model. The forward approach is a combination of two methods: the graph method, which is also known as shortest path method, and the ray bending method. The combination of these two methods has its purpose in efficiency of memory and computational time (*Korenaga et al., 2000*). *van Avendonk et al. (2001)* tested if the shortest path method on a finer grid can decrease the error efficiently in a calculation or if a combination of the shortest path method with ray bending is more efficient. A mix of both methods is useful during similar computational time and results in higher accuracy and a lower error.

The graph method after *Moser (1991)* which is based on *Nakanishi and Yamaguchi (1986)* uses the traveltimes of a seismic wave as the traveled distance through a mesh. The principles of Huygens and Fermat and Snell's law are the basis for this: each point is a point source which propagates in 360 degrees around the source, a seismic waves uses the fastest way through a medium and that the angle of incidence at a boundary between two media with different seismic velocities defines the emergent angle ($\frac{\sin \Theta_1}{\sin \Theta_2} = \frac{v_1}{v_2}$).

In refraction tomography the graph method computes the shortest path from one node to the next and through the whole mesh from the source to the receiver. The resulting path is a good approximation to the global minimum of traveltimes and the associated path (*Moser, 1991*). To compute the rays for the approximation, a mixed fifth/tenth forward star is used like in *Korenaga et al. (2000)* where the nodes which are connected to the cur-

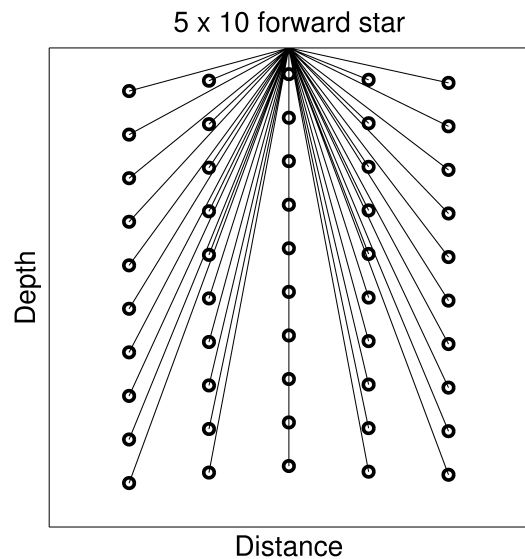


Figure 2.3: Forward star of 5 x 10 nodes used in the graph method. Circles mark grid nodes of the used mesh.

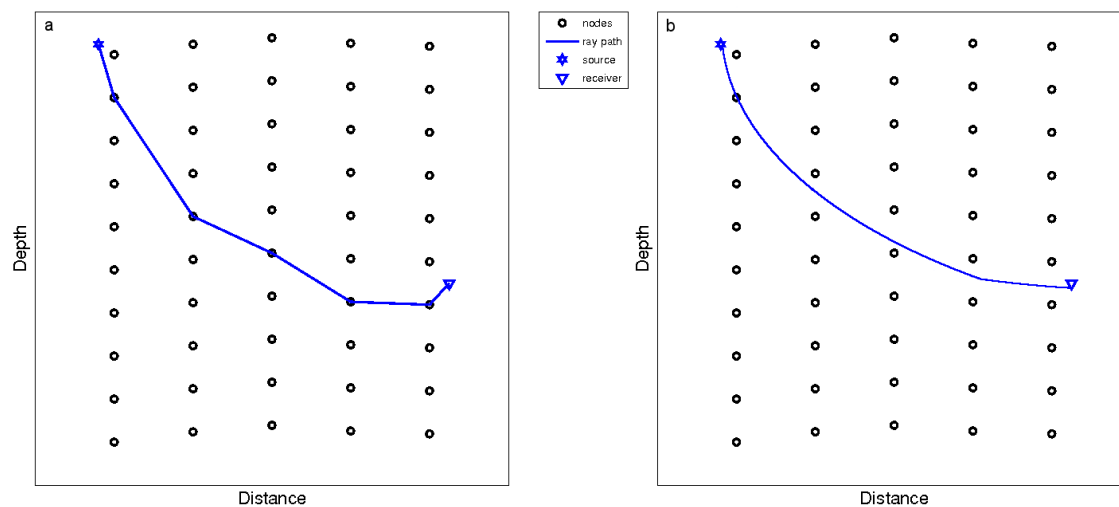


Figure 2.4: Comparison of a ray path with the graph method (a) and with a combination of graph method and ray bending (b). A hybrid method results in a smoother ray and higher accuracy of traveltimes with a lower RMS error.

rent source of the ray are defined (figure 2.3). This means, that a node is only connected with nodes in its neighbourhood and not to all nodes in the mesh to minimize the computational time and to gain a good approximation to the first arrivals. A higher order of the forward star with finer grid spacing would result in a better approximation of the traveltimes through a mesh with a much longer computational time. Instead of this, a combination with the ray bending method is used. Applying the graph method for solving the ray path, a number of points is connected with straight lines (figure 2.4 (a)). Using additionally the ray bending method it results in a lower RMS error and smoother rays (figure 2.4 (b)).

Moser *et al.* (1992) developed a ray bending method which is introduced by Korenaga *et al.* (2000) in their Tomo2D code. A good initial guess is needed for the ray bending method to result faster in the global minimum because otherwise it is not definite if the traveltimes result in a local or the global minimum. Therefore the output of the graph method is used as an initial guess which is close to the global minimum of traveltimes. The computational time of the ray bending method is proportional to the number of rays (Korenaga *et al.*, 2000) and much lower than the computational time of a solution with the graph method with the same resolution.

By using the conjugate gradient method the traveltimes of rays are minimized. This is done iteratively. The stopping criterium is a threshold value for the calculated traveltimes. Rays which define the path through a mesh are interpolated as beta-splines which are curves that are defined by a small number of controlling points. With the small number of controlling points, the minimization of traveltimes through a mesh is more efficient than the graph method through the same mesh. Or it is much more accurate than just the graph method.

Inverse Problem

For inversion an initial reference model is needed. The traveltime residual along a path of a refracted ray is described by

$$\delta T_j = \int_{\Gamma_j} \delta u \delta \Gamma \quad (2.4)$$

with δT_j as traveltime residuals, δu as slowness perturbations and Γ_j as ray paths (Korenaga *et al.*, 2000). Reflections can be described by

$$\delta T_j = \int_{\Gamma_j} \delta u \delta \Gamma + \left. \frac{\delta T}{\delta z} \right|_{x=x_j} \delta z(x_j) \quad (2.5)$$

with x_j as reflecting point of the j th ray. The equations 2.4 and 2.5 can be expressed in one equation with \mathbf{d} as the traveltime residual vector, \mathbf{G} as the Fréchet derivative matrix and $\delta \mathbf{m}$ as the unknown model perturbation vector. The resulting matrix equation is

$$\mathbf{d} = \mathbf{G} \delta \mathbf{m}. \quad (2.6)$$

The Fréchet derivative matrix contains the information about the path length distribution of rays to relevant velocity nodes which describes the velocity sensitivity and the depth sensitivity which is given by the reflectors dip, incident angle of a ray and the velocity at a reflecting point (Bishop *et al.*, 1985). Equation 2.6 defines the beginning of Korenagas traveltime tomography.

A fast convergence of equation 2.6 is only possible when the starting model is not far away from a true model. Otherwise more iterations have to be applied to result in a convergence of the model.

Through the traveltime tomography an error of the picked phases can be assessed to correlate them to some extent. An application of horizontal and vertical smoothness constraints for depth and velocity perturbations is used to gain a unique solution of the undetermined equation 2.6. The correlation lengths are two 1D smoothness constraints, for horizontal and vertical directions, with less memory storage compared to one 2D smoothing constraint with a dense matrix (Toomey *et al.*, 1994). A Gaussian smoothing with one decay length is applied on all smoothing matrices (horizontal (\mathbf{L}_{H_v}) and vertical (\mathbf{L}_{V_v}) smoothing matrix for slowness perturbation and smoothing matrix for depth perturbation (\mathbf{L}_d)) (Toomey *et al.*, 1994). Additionally a depth kernel weighting parameter w is adapted for the weighting of depth sensitivity in the Fréchet matrix. A regularized linear system of equation 2.6 is

$$\begin{bmatrix} \mathbf{d} \\ 0 \\ 0 \\ 0 \end{bmatrix} = \begin{bmatrix} \mathbf{G}_v & w \mathbf{G}_d \\ \lambda_v \mathbf{L}_{H_v} & 0 \\ \lambda_v \mathbf{L}_{V_v} & 0 \\ 0 & w \lambda_d \mathbf{L}_d \end{bmatrix} \begin{bmatrix} \delta \mathbf{m}_v \\ \frac{1}{w} \delta \mathbf{m}_d \end{bmatrix} \quad (2.7)$$

with subscripts v for velocity and d for depth components (Korenaga *et al.*, 2000). With respect to the resolution of the data weights for the slowness (λ_v) and reflector depth (λ_d)

perturbations control the relative importance of the smoothing constraints.

Equation 2.7 is solved with LSQR (*Paige and Saunders, 1982*). If the starting model is far away from a solution some residuals can be large and make the inversion unstable because of large outliers. To keep the inversion stable, additional damping is introduced in equation 2.7 (*Korenaga et al., 2000*):

$$\begin{bmatrix} \mathbf{d} \\ 0 \\ 0 \\ 0 \\ 0 \\ 0 \end{bmatrix} = \begin{bmatrix} \mathbf{G}_v & w\mathbf{G}_d \\ \lambda_v\mathbf{L}_{H_v} & 0 \\ \lambda_v\mathbf{L}_{V_v} & 0 \\ 0 & w\lambda_d\mathbf{L}_d \\ \alpha_v\mathbf{D}_v & 0 \\ 0 & w\alpha_v\mathbf{D}_d \end{bmatrix} \begin{bmatrix} \delta\mathbf{m}_v \\ \frac{1}{w}\delta\mathbf{m}_d \end{bmatrix} \quad (2.8)$$

with the velocity damping matrix \mathbf{D}_v , the depth damping matrix \mathbf{D}_d and the damping controlling parameters α_v and α_b . \mathbf{D}_v and \mathbf{D}_d are similar to the damping of *van Avendonk et al. (1998)* derived from the penalty function for the magnitude of the model perturbation.

Four weighting parameters, two for smoothing and two for damping, have to be selected before solving equation 2.8. *Korenaga et al. (2000)* suggest to first test the two smoothing parameters with a single inversion run and then fix each parameter to the best value. The decision for a parameter is dependent on the constraints (like model roughness) of the user.

Resulting velocity models of the joint refraction and reflection tomography are non-unique. This non-uniqueness is observable in the depth of the during inversion computed reflector and the velocity field. Lower crustal velocities are primarily resolved by traveltimes of reflections and not by refracted rays. The depth kernel weighting parameter w has large influence on the resulting velocity profile for regions with low resolution. A value of 1 for w characterizes an equal weighting of depth and velocity nodes. A higher value w specifies higher depth perturbation and a lower velocity perturbation. Regions with a sparse ray coverage better recover the velocity structure with a higher depth kernel weighting parameter than a low w which compensates insufficient recovery of the velocity model with velocity perturbations, even when the traveltimes of both are nearly the same (*Korenaga et al., 2000*). The range of possible velocity models for different values of w can be tested by using this parameter as a single controlling parameter and the result shows the velocity-depth ambiguity (*Bickel, 1990*).

The choice of parameters for the analysis in this study is described in section 4.2.1.

2.1.4 Amplitude Modeling

Amplitude modeling is done with the reflectivity method. With the reflectivity method synthetic seismograms are computed to compare the results with recorded data. The goal is to model seismograms which look like a reproduction of the measurements.

While computation of seismograms a velocity profile is the input and different parameters can be set. The combination of velocity profile and parameters have to be adjusted to

gain the best fit to the data. The method is used as a helping tool for the interpretation of amplitudes. Base for the reflectivity method is the work of *Fuchs and Müller (1971)* which is an extension of *Fuchs (1968)*. A detailed description is published by *Müller (1985)*. Calculation of the reflectivity method is based on the ray theory with included transmission and reflection coefficients. This method integrates wavenumber or slowness to compute a seismogram. The model is of a number of homogeneous layers where an inhomogeneous layer is divided into several homogeneous layers. For the reflectivity method all reflections and multiple reflections above and below a layer are summed up to result in a synthesis of wave-fields (*Müller, 1985*). In each layer reflection and transmission for hundreds of slownesses and, because of the frequency dependency, a number of frequencies are computed. This is the most time consuming part of this computational method. Several input parameters and the model setting are defined in one model file. Parameters are amongst others the size of the window with the step size, reduction velocity and minimum time of the seismogram, the minimum and maximum phase velocities, frequency range, time increment and duration of a signal. Specifications of each single homogeneous layer are made for depth, P- and S-velocity, a quality factor Q for P- and S-waves and the density. The quality factor Q is defined as loss of energy by damping compared to the residual maximal energy per period:

$$Q = \frac{2\pi A_{max}}{\delta A}. \quad (2.9)$$

A high Q represents a low damping and a low Q a high damping, thus Q^{-1} is the damping parameter.

Usage of the reflectivity model is for regions with little three-dimensional effects because the input model is a one-dimensional velocity profile. A comparison to measured three-dimensional affected data and therewith interpretation of those is impracticable.

2.2 Earthquake Analysis

For earthquake analysis two software packages are used. SEISAN comprises a program for phase picking of events. With VELEST an inversion of a 1D velocity profile is done to compute a minimum 1D velocity model. The aim of the computation is to find a good velocity model for the research area to locate the hypocenters of the events.

2.2.1 SEISAN

SEISAN is a SEISMic ANalysis software package for earthquake analysis (*Havskov and Ottemöller, 1999; Ottemöller et al., 2010*). It is freeware which is upgraded continuously by the developers and users of the software with improvements of the existing software package or new programs.

SEISAN can process different data formats. The standard formats are SEISAN waveform file format (*Ottemöller et al., 2010, Appendix B*), GSE (GSE = Group of Scientific Experts, GSETT-3 (1997)), SEED/MINISEED (SEED = Standard for the Exchange of Earthquake

Data, *IRIS Consortium* (1993)) and SAC binary and SAC ASCII (SAC = Seismic Analysis Code, *Goldstein* (1999)). The supported data formats of original digital waveform data files of the identified events (section 3.2.3) are stored in a folder which is accessed by the SEISAN programs. Earthquake readings and full epicenter solutions of each event are written in a treelike subdirectory structure of the experiment after date (yearly and monthly subdirectories). These files are S-files in Nordic format (*Ottmöller et al.*, 2010, Appendix A), include phase readings and source information and direct to the waveforms of the experiment. The used database is for a simple organization of several events recorded on a number of stations and for an easy use of this dataset with the software.

SEISAN and the subprograms can be used under EEV, a program to work interactively with the dataset. Out of this programs many SEISAN subprograms can be started. The program HYP is a modification from the HYPOCENTER program (*Lienert and Havskov*, 1995) and is used for location of the events, if these are local, regional or global events. It uses specified velocity models to calculate the hypocenter. Plotting of the location of the hypocenter with the location error is also part of HYP. MULPLT is used for trace plotting, phase picking and spectral analysis. The location of the theoretical phases can also be done out of this program for a quick location as reference for further phase identification. An epicenter of an event can be plotted with the EPIMAP program. It uses a file in Nordic format which can be the output of HYP, SELECT or COLLECT. SELECT searches in the database for events with distinct criteria and stores these in Nordic format. COLLECT just collects S-files of events from the database in a Nordic format file. The output files of HYP, SELECT and COLLECT can be used for SPLIT to split the Nordic format files into single S-files of events into the database or a specified folder. For the final location of the events the database is updated with the UPDATE program. The S-files are updated with the picks and the location of each event.

These are the main programs of the SEISAN software package which are used in this study. There exist more programs for displaying a Wadati diagram, calculating a fault plane solution, the magnitude ect., which is too extensive to list and describe in a compact way. For further information look at *Ottmöller et al.* (2010).

2.2.2 VELEST

VELEST is a software to work out a minimum 1D velocity model (*Kissling*, 1995; *Kissling et al.*, 1994). The aim of the resulting model is for a better earthquake location or as a reference model for further seismic tomography. To gain the final minimum 1D velocity model the with the SEISAN software package (section 2.2.1) picked phases of events are converted from the file with the picks in Nordic format to a CNV format used in VELEST. Further to the input file with the picked phases, a file with listed stations which recorded the events, a model file with the starting velocity model and a command file with several input parameters for VELEST are needed. The station file comprises the name of a station, the coordinates, depth or height of the situation and possibly a time correction for the station which compensates differences to a reference station in subsurface geology and height. The input model defines the layering of the model with the starting veloci-

ties and can include a damping value. In the VELEST command file different parameters can be set like number of earthquakes in the CNV file, a v_p/v_s -ratio, damping values, number of iteration of the inversion etc. (for further information see *Kissling (1995)*). With the command file the inversion of the starting velocity model is defined by the included parameters. The inversion of the starting velocity model runs for the assigned number of iterations and a reduction of the RMS error is the goal. Layering stays the same during inversion and the hypocenter location and velocities are inverted and a station correction for runtime correction of the differences of the geology below a station are computed. Results are summarized in an output file with the calculated velocity profile and the associated RMS error. A file with the hypocenters calculated with the resulting velocity profile and a station list completed with the runtime corrections are further output files. The usage of VELEST demands to test a number of different starting models and parameters to recognize the differences of the results and find a good endmodel. The definition of an endmodel needs a comparison of several models to find one model with a low RMS error and a reasonable velocity structure. There is not the one correct solution. For a good result a good starting model is needed.

Chapter 3

Seismic Data

The structure beneath the Alboran Sea is, as mentioned before, still under investigation. Different types of data were collected and analysed in this study to gain more information about the structure of the lithosphere and therewith find evidences for a formation theory of this region (hypotheses presented in section 1.2.2). Different datasets and different modeling methods are used to define the present structure below the Alboran region. Therefore active seismics for seismic refraction analysis are used to model the crustal structure (section 3.1) and passive data are recorded over a time period to gain information of the deeper structure below the Alboran Sea (section 3.2).

3.1 Seismic Refraction

3.1.1 Profile Location

The Alboran Sea is the westernmost part of the Mediterranean Sea. Until now the formation of the Alboran Sea during the formation of the whole Mediterranean Sea is not well understood. There are some hypotheses for the formation of the Alboran Sea which could explain its main features (section 1.2.2). For getting a better understanding of the Alboran Sea Basin, seismic refraction and wide-angle data were collected. These data were acquired during a cruise of the german research vessel FS Meteor from 29th of August to 20th of September 2006. Profile 02 of this cruise is WSW - ENE oriented and is located in the eastern part of the Alboran Basin in transition to the Algerian Basin (figure 3.1). It is oriented like this because Multichannel Seismic data were acquired along this profile in 1992, analysed by *Comas et al.* (1995) and reprocessed and analysed by *Booth-Rea et al.* (2007) (section 1.3.1). The profile starts at height of Melilla, a spanish exclave in North Morocco, circa 65 km off the coast in the Alboran Trough, north of the Alboran Ridge. It continues 250 km in ENE direction and ends north of Mostaghanem in Algeria.

3.1.2 Data Acquisition

During the cruise M69-2 with FS Meteor 25 Ocean Bottom Seismometer (OBS) and Ocean Bottom Hydrophone (OBH) stations were deployed on profile 02. In the East, there are 5

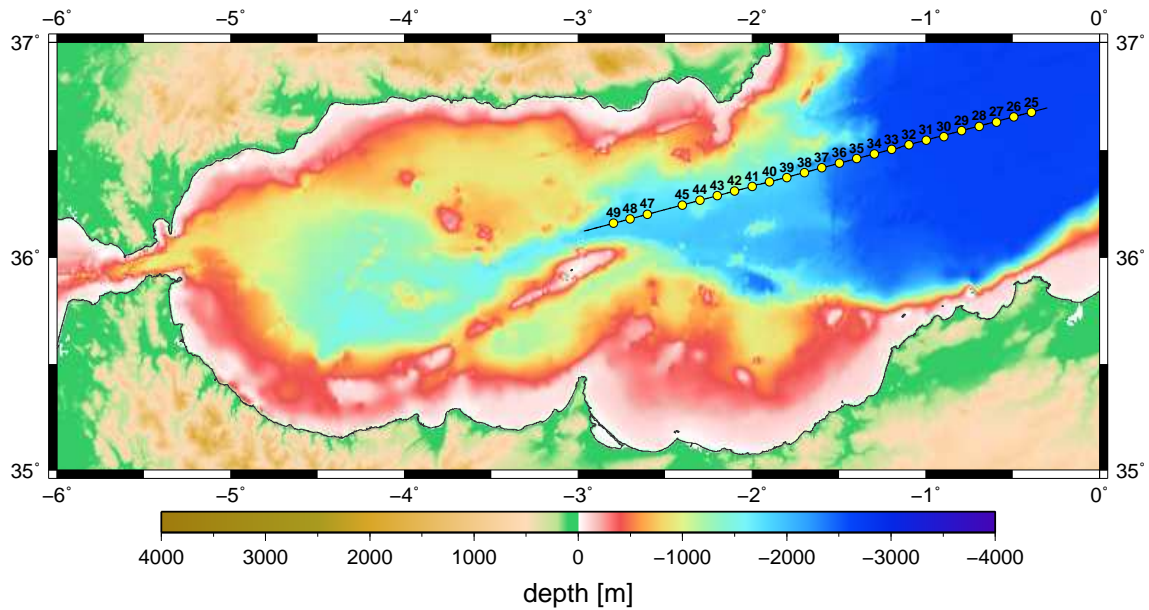


Figure 3.1: Location of profile 2 of the Meteor cruise M69-2. Yellow circles are the OBH and OBS positions.

OBS stations equipped with a hydrophone and a three-component seismometer (figure 3.2 left). Continuing to the West are 20 OBH stations deployed, just equipped with a hydrophone (figure 3.2 right). Each station has a distance to the next one of around 5 nm. The 25 stations were deployed in a 135 nm long profile line which is 250 km in a 75° angle from ENE to WSW.

Instruments

Ocean Bottom Hydrophones and Ocean Bottom Seismometer Ocean Bottom Hydrophones (OBHs) are equipped with a HTI hydrophone of the High Tech Inc. company¹ or an OAS hydrophone of the Optimum Allied Systems company². Additional to a HTI or OAS hydrophone there are Owen geophones on a OBS station with 4.5 Hz.

For storing the data of the instruments, there is a recorder from SEND Off-Shore Electronics GmbH³. This recorder is of the type Marine Longterm Seismocorder (MLS) or Marine Broadband Seismocorder (MBS) which save the data on compact flash disks. The recorder has an inner clock synchronized with the GPS signal and is stored during operation in a titanium cylinder together with a power supplying battery. This cylinder is attached to the flotation and connected to the measuring hydrophone and geophone (figure 3.2: pressure tube).

Main part of an OBH or OBS is the flotation and is designed like the titanium cylinders and the releasers by K.U.M. Umwelt- und Meerestechnik Kiel GmbH⁴. For deployment it

¹<http://www.hightechincusa.com>

²<http://www.oas-inc.com>

³<http://www.send.de>

⁴<http://www.kum-kiel.de>

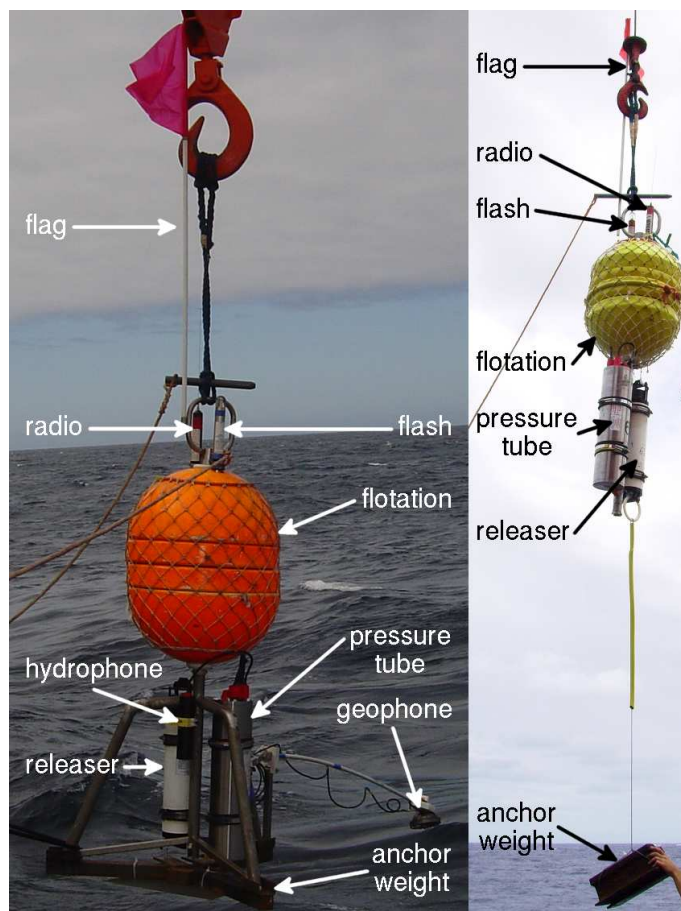


Figure 3.2: An OBS (left) and OBH (right) while deployment. The hydrophone on the photo with the OBS is not visible.

is connected to an anchor weight in order that the instrument sinks to the seafloor (figure 3.2). It can be recovered when an acoustic signal is sent to the releser of the station. The releser drops the anchor weight and the OBH/OBS rises back to the seafloor.

Seismic Signal For creating a seismic signal two BOLT⁵ airguns were used with a volume of 32 litres each. The airguns are triggered to shoot every 60 s by a speed of approximately 4 knots. This results in a ~123.5 m spacing of shots.

The guns operate at 150 bar to generate a seismic signal. The air gets compressed in the chamber of the airgun. A trigger signal gives the impulse to release the air out of the pressure chamber. This generates a pressure wave which propagates through the water column to the seafloor and penetrates into the subsurface (section 3.1.2 “*Seismic Wave*”). Along the 250 km long profile, more than 2200 shots were fired.

Seismic Wave

The seismic wave generated by two BOLT airguns (section 3.1.2 “*Seismic Signal*”) is reflected and refracted along seismic interfaces in the ground and recorded from OBH and

⁵<http://www.bolt-technology.com>

OBS as motion of hydrophone and geophone. A traveltime of a wave from the source to the receiver is gained from the shooting time compared to the time the wave is recorded from the stations recorder. The time the wave uses to reach the receiver depends on the speed of the seismic wave through the subsurface.

There exist different types of seismic waves: compressional wave, shear wave and surface waves. Compressional waves are longitudinal waves and are also called P-waves or primary waves because they travel faster than the secondary waves and are registered first. Secondary waves (S-waves) are shear waves which can travel only through solid material because liquids are not shearable. A surface wave travels, as the name says, like a water wave along the earth's surface.

The seismic speed depends on physical properties: density of the material ρ and elasticity due to shearing μ and compression κ of the material. The speed of a P-wave is defined by

$$v_p = \sqrt{\frac{\kappa + \frac{4}{3}\mu}{\rho}}. \quad (3.1)$$

The velocity of S-waves depends on shear modulus and density

$$v_s = \sqrt{\frac{\mu}{\rho}}. \quad (3.2)$$

3.1.3 Data Pre-Processing

First Steps

After recovering the OBH/OBS, the recorders are stopped and synchronized again with the GPS time to gain the time shift of the recorders inner clock during the whole operation. This is important to get the correct traveltimes of seismic waves. The next step is to copy the data of each OBH/OBS from the flash cards to a linux computer for further processing.

The recorded data is in a format specific from recorders manufacturer SEND. These raw data are converted to a s2x-format, resampled and converted into a pseudo SEG-Y format (steps in figure 3.3). Resampling corrects time slips on MTS or MLS recorders which occur due to temperature dependencies of the recorders GPS clock. The conversion to a pseudo SEG-Y format is done with seg-ywrite and produces for each channel one continuous data file. With the Pascal Quick Look (PQL) program⁶ a fast check of the data can be done. Each channel of the recorded data (one hydrophone channel for OBH plus three geophone channels for OBS) is displayed in this program as amplitude over time.

To cut the pseudo SEG-Y data into traces, the ukooa file is used. The ukooa file is separated in four parts. The first part is the header which contains information about the cruise like which survey it is, the date of the survey and the contractors. The second part contains information about the synchronization times before starting and after ending the recorder of each OBH/OBS and the skew time. The third part contains coordinates and

⁶<http://www.pascal.nmt.edu/category/related-topics/pql>

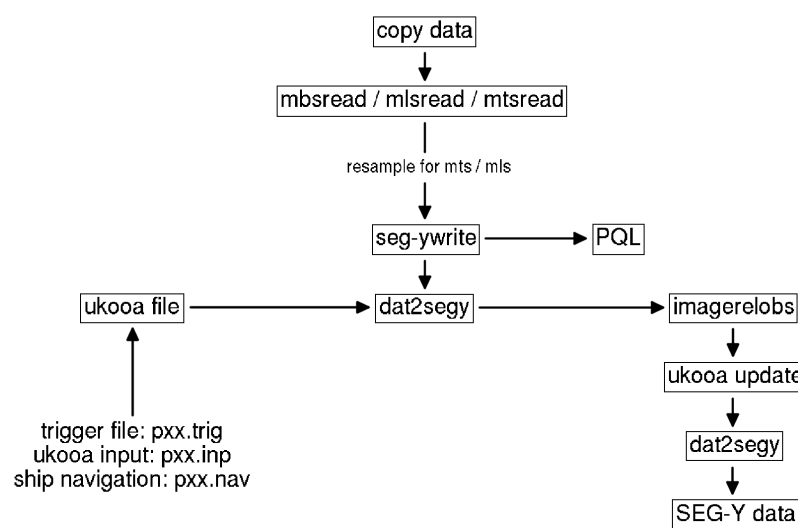


Figure 3.3: This diagram illustrates the steps for data pre-processing. The steps are run on board the vessel. The final output is a dataset in SEG-Y format which is used to pick the phases of the seismic waves (section 3.1.4).

depth of each OBH/OBS. And the last part contains information about each shot: GPS-time, shot number, GPS-coordinates and water depth. All parts are merged to one ukooa file out of three files containing an ukooa input file, trigger information of the shots and the ships navigation. This ukooa file is used to get the correct position of each airgun shot of the SEG-Y traces. Dat2segy uses the ukooa file to convert the pseudo SEG-Y traces into SEG-Y traces with the right geometry and correcting the output by taking the skew time into account.

To correct the position of the OBH/OBS, a relocalization has to be done. An exact positioning of the station is important for exact traveltimes of a seismic wave and further modeling. Due to few differences in OBH/OBS position because of drifting and/or little error in deployment position a slightly wrong position is logged and wrong traveltimes and an asymmetry in the data are the result. The relocalization is done with the relobs program which outputs a new OBH/OBS position after picking a few phases of the water wave. Afterwards an update of the ukooa file with the new position has to be done to ensure a correct geometry of the SEG-Y data files. New SEG-Y files are generated with the new ukooa file which contain the corrected geometry.

Filtering

To gain better data quality, the recorded data have to be debiased, filtered and deconvoluted before usage. The signal-to-noise ratio will be improved by the use of these steps. The filtering procedure uses a high-pass-filter to remove noise and improve the signal generated by the airguns. Deconvolution has the goal to get the raw signal of the earth in the SEG-Y data. Therefore the signal of the wavelet will be removed and a the Wiener filter (Wiener, 1949) is used.

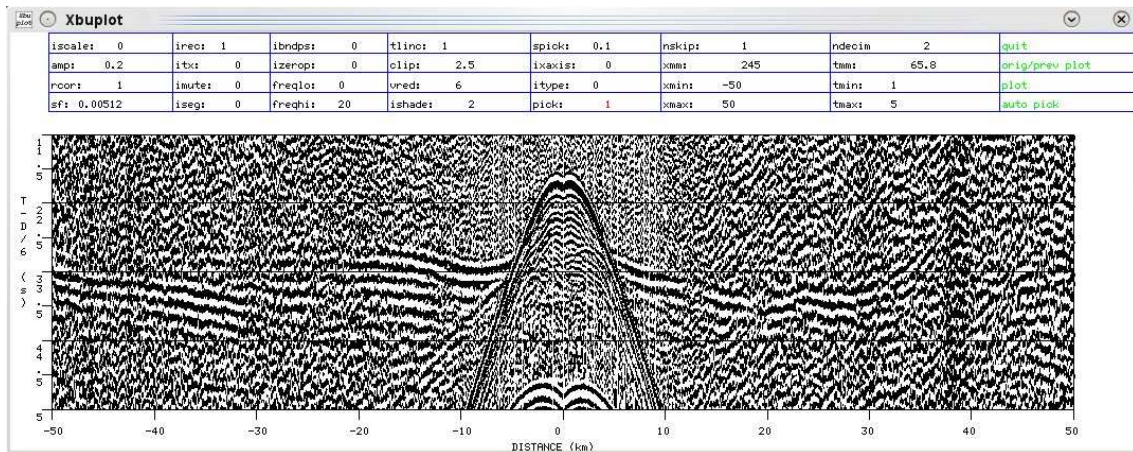


Figure 3.4: Data of OBH 36 in the program *zplot*. In this program for phase picking, different parameters can be adjusted for a better view on the data and therewith better picks of phases.

3.1.4 Phase Picking

For phase picking of seismic refraction data the program *zplot* is used (section 2.1.1; *Zelt* (1997)). Therefore the SEG-Y data are converted into a z-format.

While using *zplot*, different parameters like a zoom into the data, an additional filtering in the program or others can be adjusted to improve the view on the data for a better picking result. In figure 3.4 seismic data of OBH 36 is displayed in the *zplot* program.

Phase identification is done in *zplot* by considering changes in slope angle and/or amplitude. The different phases are marked by colors where each color stands for one number (like a phase ID) that is stored with each pick in a picking file (x-coordinate, traveltime, estimated picking error and phase ID). This makes it possible to assign a pick to a phase for programs which are used for later modeling.

On the 24 OBH and OBS stations which recorded data, 13685 picks are made on a 250 km long profile with a maximum offset of 60 km for the most stations. Identified phases are refractions and reflections. Refractions are picked from the sedimentary layer (abbreviation is Ps), upper (Pu) and lower crust (Pg) and the Moho (Pn). Reflections are identified at the Moho (PmP), but also in the sedimentary layer between layers with a sharp contrast of the P-wave velocity.

Pick uncertainties are applied on each picked phase by estimating the errors of the picks from the signal to noise ratio. These uncertainties are important to estimate the error of the resulting velocity model compared to the recorded data.

For the forward modeling of the picks with the *rayinvr* program (section 2.1.2), the file with the picks is converted to a tx-format. In the Tomo2d inversion (section 2.1.3) a further conversion from the tx-format to a suitable format is made.

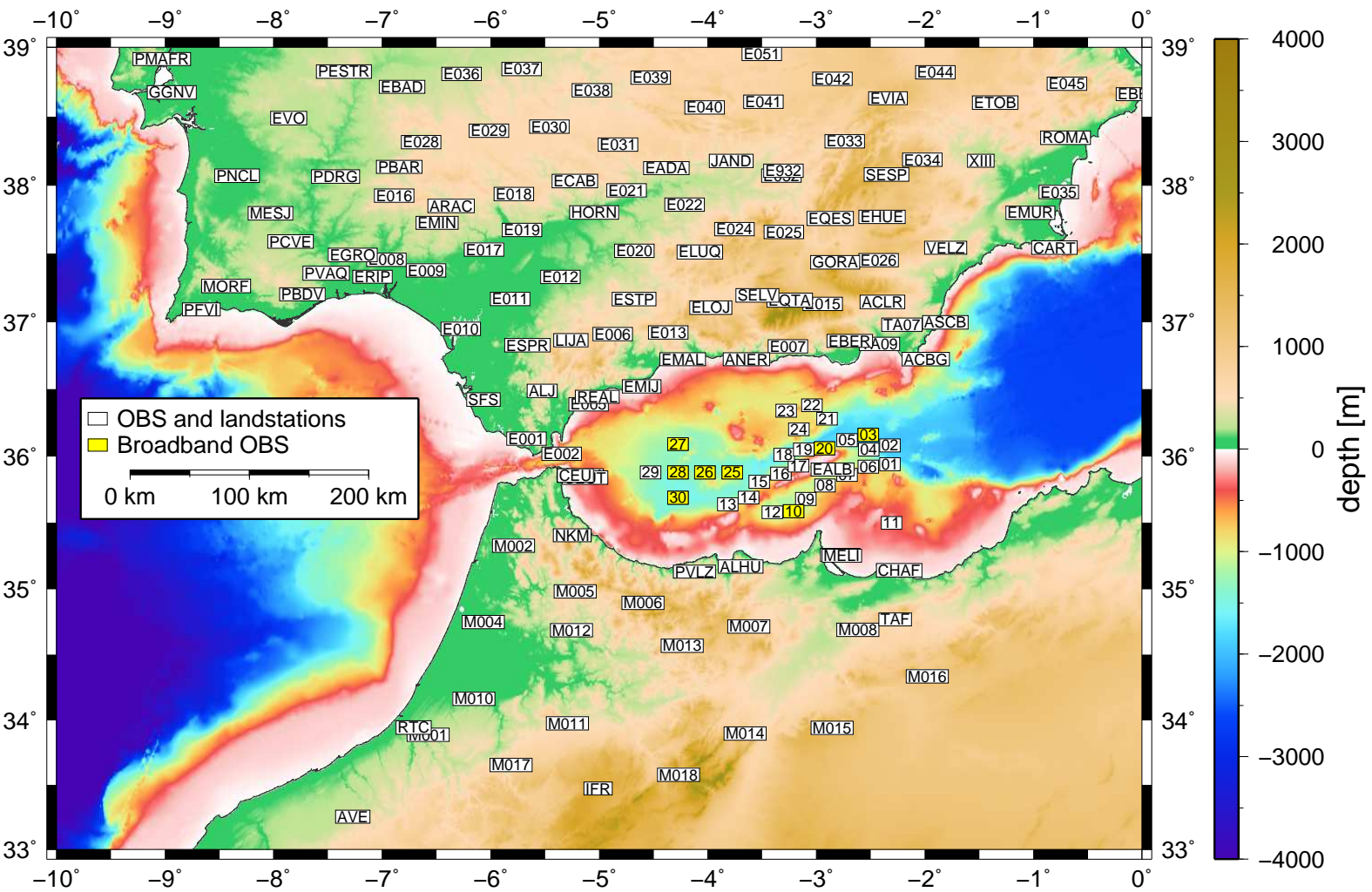


Figure 3.5: Location of the OBS, LOBSTER and landstation of the seismic network from August 2009 to January 2010. OBS and LOBSTER are marked with numbers and landstations with name shortcut of the station.

3.2 Earthquake Dataset

For additional information about the structure below the Alboran Sea a project called TOPO-MED⁷ was set up in this region. It is a subproject of the TOPO-EUROPE⁸ project, which has the purpose to map the structure of Europe. With geosciences uplift and subsidence of parts of the European continent is mapped for the present state. Further uplift and subsidence could trigger geohazards like erosion or desertification (by declining sealevel or uplift) and flooding (by rising sealevel or subsidence). The influences of topography on possible geohazards is a reason for the investigation of the European continent with the TOPO-EUROPE project. To map the present state and the changes of the continent gives the possibility of a forecast for the evolution and possible geohazards. The subproject TOPO-MED contains the Mediterranean region. The aim is to investigate the present structure of this region. In section 1.1.2 the evolution of the western Mediterranean is described. The last stage is the end of the subduction zone from the Gibraltar to the Calabrian Arc. The TOPO-MED project investigates the last stage of the subduction zone and the evolution of the Mediterranean Sea and a possibility of a new subduction zone along the north African margin. These investigations are an analysis for possible geohazards in the future.

3.2.1 The Project

From August 2009 to January 2010 seismic data were recorded in the Western Mediterranean as part of the TOPO-MED project. Therefore 30 OBS and LOBSTER (section 3.2.2) were deployed in August 2009 for longtime recording. Additionally to these instruments landstations in the southern part of the Iberian Peninsula and in northern Morocco were available for a larger dataset (figure 3.5).

The offshore data were collected in combination of two cruises with the German research vessel FS Poseidon. In August 2009 while the FS Poseidon cruise POS389, the 30 OBS and LOBSTER were deployed for the longtime recording. The recovery of the station was conducted while the cruise POS393 in January 2010. A first report of this project is published as IFM-GEOMAR Report (*Grevemeyer, 2011*).

Most times the seismic activity in the Alboran region and the surrounding area is of low to moderate magnitude. The aim of this part of the TOPO-MED project is to record the seismic activity and use the records for a modeling of the crustal and upper mantle seismic velocities.

3.2.2 Data Acquisition

Instruments

For the recording of earthquakes different instruments are used. Offshore and onshore instruments have different requirements.

⁷<http://www.esf.org/activities/eurocores/running-programms/topo-europe/the-crps/topomed.html>

⁸<http://www.esf.org/activities/eurocores/running-programms/topo-europe.html>

Offshore Offshore instruments are OBS and LOBSTER⁹. The OBS are described in section 3.1.2 “*Ocean Bottom Hydrophones and Ocean Bottom Seismometer*”. A LOBSTER is a “Longterm OBS for Tsunami and Earthquake Research” designed like the OBS by K.U.M. Umwelt- und Meerestechnik Kiel GmbH. Because of the possibility to equip a LOBSTER for a longterm experiment (a second battery tube for extra power supply of the recorder), four additional floating disks can be added for a higher buoyancy compared to an OBS. The sensors on a LOBSTER are a hydrophone and a broadband seismometer. The Hydrophone is of the type HTI like the hydrophone used for OBS. Guralp systems provide the CMG-40T broadband seismometer¹⁰. It has three components and can afford 30 s to 50 Hz bandwidth output. For long periods it can supply 1 s, 2 s, 10 s or 60 s and a high frequency option with 100 Hz.

The recorder for a LOBSTER is a MCS, a Marine Compact Seismocorder, from SEND Off-Shore Electronics GmbH. Data are stored on a harddrive inside the recorder box and the inner clock is more stable compared to other models of SEND recorders (e. g. those which are used for recording seismic wide-angle data in section 3.1.2 “*Ocean Bottom Hydrophones and Ocean Bottom Seismometer*”). The power supply for the recorder is done by a battery pack, which is stored together with the recorder in a titanium cylinder. This cylinder is fixed to a frame on the LOBSTER and connected to the sensors.

Deployment and recovery of a LOBSTER is similar to the OBS (section 3.1.2 “*Ocean Bottom Hydrophones and Ocean Bottom Seismometer*”).

Onshore For the onshore network a system from Nanometrics Inc. is used. The seismometer is the Trillium 120¹¹. It is a three component broadband seismometer with a low noise level and has a working field in a broad temperature range ($\pm 45^{\circ}C$). The bandwidth is 120 s to 145 Hz. Taurus¹² is the used datalogger which is also a product of Nanometrics Inc.. It contains a precise GPS clock for accurate time recordings and has a long operating time. Data are stored on a removable hard disk drive up to a size of 64 GB. Power supply is provided by two 18 W solar panels.

Additional to these stations, permanent onshore stations are used for this study. Those are part of the permanent network of Spain.

3.2.3 Data Pre-Processing

Resulting data of the offshore stations are downloaded from the flash cards or hard drives of the recorders and converted to SEG-Y data format. During the recording time a time shift of the recorders inner clock has occurred which is assumed to be a linear shift. This has to be corrected on the data time series.

Time corrected data are triggered with an algorithm to recognise seismic events in the records of a station. The algorithm detects possible earthquakes by applying different

⁹http://kum-kiel.de/eng/pdf/Lobster_eng.pdf

¹⁰<http://www.guralp.com/products/40T>

¹¹<http://www.nanometrics.ca/products/trillium-120-ppa>

¹²<http://www.nanometrics.ca/products/taurus>

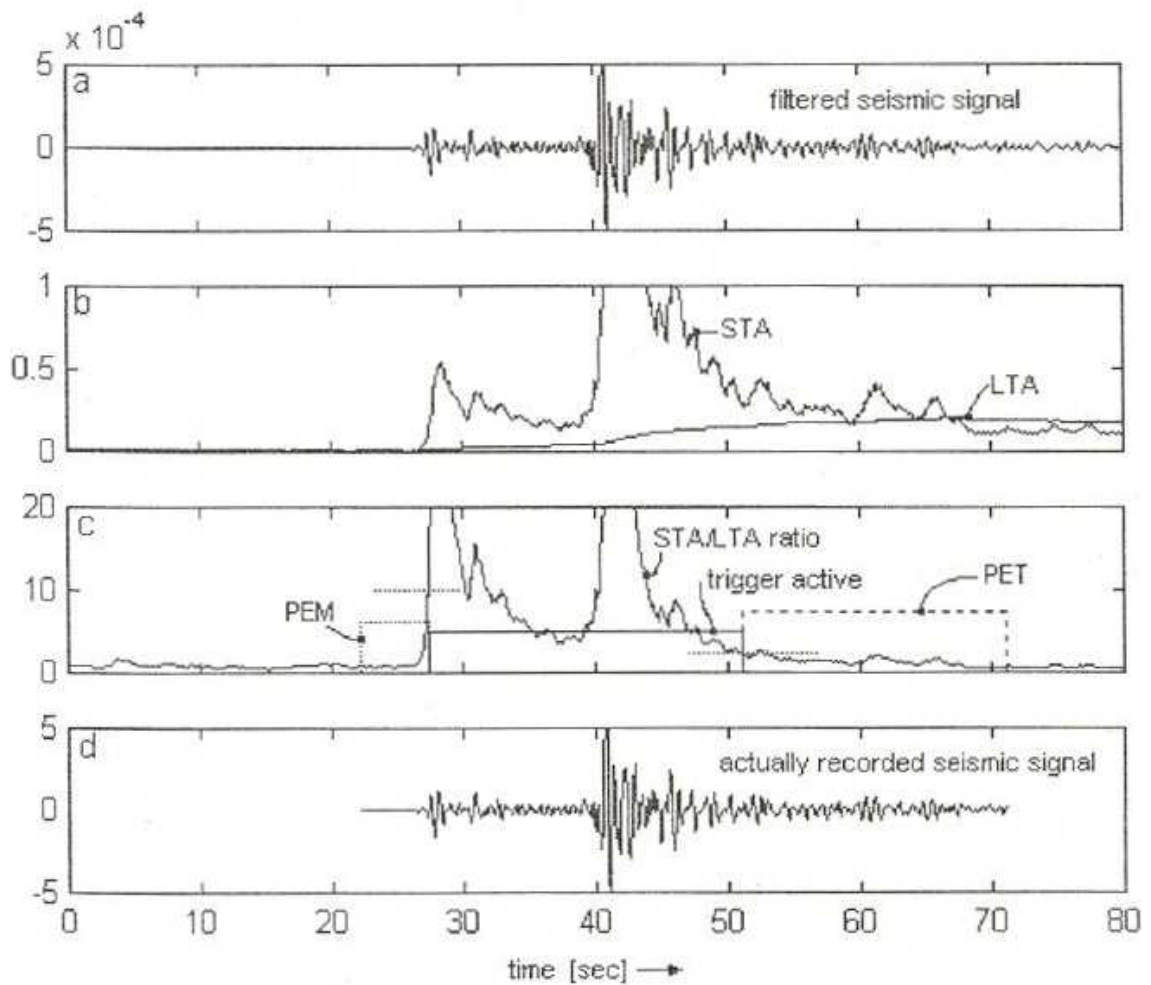


Figure 3.6: An example of the STA/LTA trigger algorithm: (a) The filtered seismic signal. (b) STA and LTA average amplitude of the seismic signal. (c) STA/LTA ratio with the window of trigger activity between the trigger ratio (left dotted line) and the de-trigger ratio (right dotted line). The pre-event time (PEM, dotted rectangle) and the post-event time (PET, dashed rectangle) complete the by this algorithm selected event. (d) The selected seismic signal of the event. From Trnkoczy (2002).

parameters on the timeline. Before adopting the trigger algorithm, the data have to be filtered. The filter is a band-pass filter to reduce the background noise and results in a signal where even small events are detectable by the trigger algorithm.

Short Time Average over Long Time Average (STA/LTA, Trnkoczy (2002)) is the used algorithm (figure 3.6) where the average amplitude of a short time window (STA) is compared to the average amplitude of a long time window (LTA) by dividing STA by LTA. The length of the STA time window is commonly used between 0.3 s and 2 s for local and regional events (used value is parameter s in table 3.1). Is this value too low, false signals like spikes can also be detected as an event. Is it too high, small events are not detected. For the LTA time window a common value is 60 s (l in table 3.1). A too low value can

result in no triggering because the threshold for triggering is not reached. Therefore a too high value is better but can result in triggering of a non seismic signal. The threshold for triggering is the trigger ratio, a STA/LTA value (t in table 3.1). A common value is 4. 8 or higher is for an unquiet site of the instrument with seismic signals made by humans. Sites with a low noise value can work with a trigger ratio below 4 without detecting too many wrong events. The end of triggering is set by a de-trigger ratio, also a STA/LTA value (d in table 3.1). This threshold is commonly set between 2 and 3 for relatively quiet seismic sites and higher for sites with high noises. A lower value would cause a later de-triggering. Additionally to the trigger interval defined by the trigger and de-trigger ratio pre-event time (PEM for pre-event memory) and post-event time (PET) are added to the detected event. PEM is set to a value which includes maximum time between P- and S-wave arrival to assure that also the P-wave is part of the selected timewindow plus a noise timeline before the event. The resulting PEM window depends on the size of the network and is for example for a network with 200 km radius 40 s. PET has to be as long as the end of the event is reached to get the whole seismic signal and do not cut off the end of an event. An appropriate value for local events is 30 s and for regional events 60 to 90 s.

An example of the STA/LTA trigger algorithm and the parameters is displayed in figure 3.6 and table 3.1.

For a better possibility of the earthquake analysis a minimum number of stations on which an event is detected can be set. For the analysis of the events the detected time windows are cut out of the timeline and each event is stored in a single file. The SEG-Y traces are converted for further processing with the SEISAN software package (section 2.2.1) into a SEISAN waveform and listed in a SEISAN database.

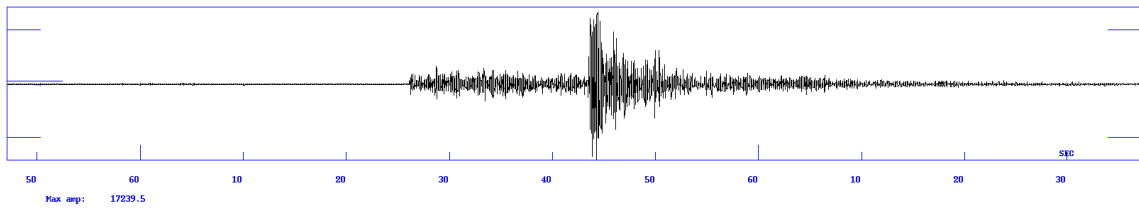
Parameter	s	l	m	t	d	S	M
Value	1.0 s	60 s	250 s	4.6	1.0	3	30 s

Table 3.1: STA/LTA parameter used in this study. s = length of short term window, l = length of long term window, m = mean removal window length, t = trigger ratio, d = de-trigger ratio, S = minimum number of stations with detected events, M = network trigger time window length. S and M are typical used values. The other parameters are determined for this study.

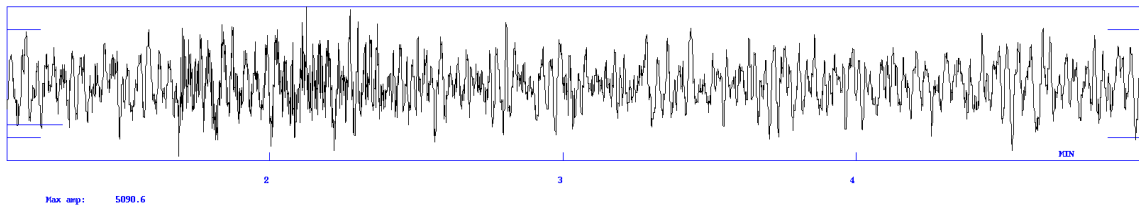
3.2.4 Phase Picking

The identification of phases of a seismic event is done with the MULPLT program of the SEISAN software package (section 2.2.1). By the STA/LTA trigger algorithm detected events are read in the program. The aim is to identify P- and S-phases on as many stations as possible.

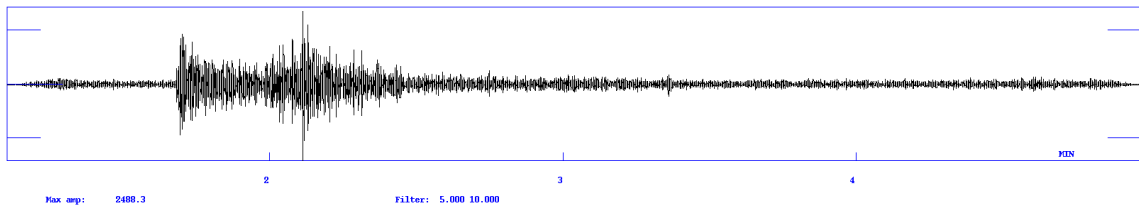
Because of noises the identification of P-phases can be difficult. A S-phase identification can get difficult due to noises and interference with parts of earlier phases. Examples of waveforms are shown in figure 3.7. The examples are from the event on 30 October 2009 at 07:01 am and show two different kinds of waveforms. The upper one (figure 3.7(a)) is



(a) Record of an event on a station (OBS08) with high signal to noise value.

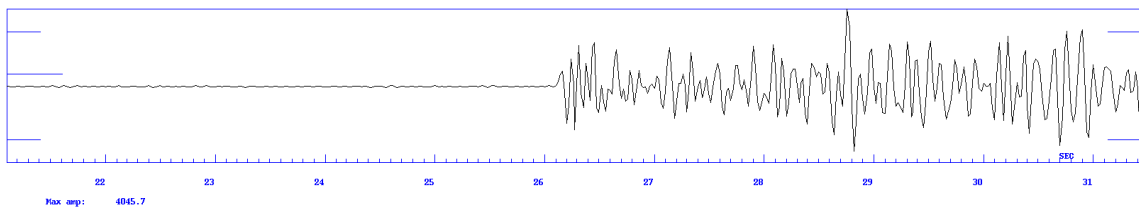


(b) Record of another station (M004) of the same event with much noise.

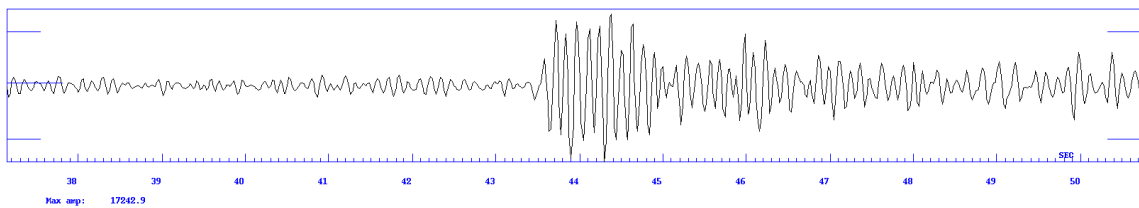


(c) Filtered record of station M004.

Figure 3.7: Examples of records of an event for (a) good and (b) bad data quality. Filtering while picking can help to identify phases which are hidden in the noise. (c) is the filtered record of (b).



(a) Zoom into P-arrival.



(b) Zoom into S-arrival

Figure 3.8: The waveforms show a zoom into a P- and a S-arrival on OBS08 for the event on 30 October 2009 at 07:01 am. (a) A clear P-arrival is shown with low noise on the station. (b) The S-arrival is also well identifiable.

a clear waveform with a low noise value. A zoom into the P- and the S-arrival is shown in figure 3.8 where the phases are well identifiable. In figure 3.7(b) a record of a station

with a low signal to noise ratio is shown. Without a filter the P- and S-arrivals are not to identify. Applying a filter on the waveform (figure 3.7(c)) makes some phases easier to identify but can also cause an error by phase shifting. While applying a filter on the record it is important to compare the picked phases afterwards with the unfiltered arrival to make sure that a phase shift does not lead to a wrong pick. Therefore also an error assessment can be included into the picking. Picks can be weighted by defining the picking uncertainty and adding a weight factor. Addressing a 4 to the picked phase, the weight of the pick is 0 and it will not be used for hypocenter determination and traveltime inversion. An addressed 3 on the pick weighs it with 0.25, a 2 with 0.5 and a 1 with 0.75. If no weighting value is assigned to a pick, it will be weighted with 1. The weighting factors are assigned when an uncertainty in picking has to be estimated. Relatively to other readings of the same earthquake the weighting factors are added to a pick. No clear time frame of uncertainty can therefore be assigned to one weighting factor because in each earthquake this time frame can vary.

During the recording time of over five months between August 2009 and January 2010, 229 analysable events were detected. Altogether 6446 picks of P- and S-phases are made for these 229 events on 155 stations.

Chapter 4

Seismic Refraction Analysis

Collected seismic data are picked and modeled to analyse the structure of the lithosphere beneath the eastern Alboran Sea (for location of the seismic profile see figure 3.1). The modeling is done with two different strategies. The first phase is a forward modeling (section 4.1) where the resulting model is used as an input model for the second phase, an inversion (section 4.2).

4.1 Forward Modeling

4.1.1 Modeling Strategy

Forward modeling is done with the program rayinvr (section 2.1.2). The picks (section 3.1.4) are converted into the tx-format, an ascii-format, which is used in this program. The approach for the forward modeling is interactively from top to bottom.

The starting model for the forward modeling is a flat layered model with the during the cruise M69-2 recorded bathymetry along the profile as the top layer, the seafloor.

Depth and velocity nodes are adjusted to fit the traveltimes which are picked. The number of nodes is relatively low with a spacing along the profile of 3 to 10 km for the depth nodes and a velocity node spacing of 30 km (figure 4.1). Spacing of the nodes is defined by necessity of a change in topography of a layer or a change in velocity along the defined layer. The resulting model is interactively defined until the best fit is gained.

4.1.2 Resulting Forward Model

While forward modeling some basic structures occur in the velocity model (figure 4.2) in the eastern Alboran Sea (for profile location see figure 3.1). In the central to eastern part of the velocity model a low velocity zone (LVZ) is modeled. The existence of this structure is consolidated by reflections from the bottom of the low velocity zone and reflections from the bottom of the basement, recorded and visible on seismograms (example displayed in figure 4.3) and by an MCS study where data were recorded along this profile in 1992, the interpretation published by *Comas et al.* (1995) and reinterpreted by *Booth-Rea et al.* (2007). Below the basement a crust consisting of an upper and a lower crust is existent. The up-

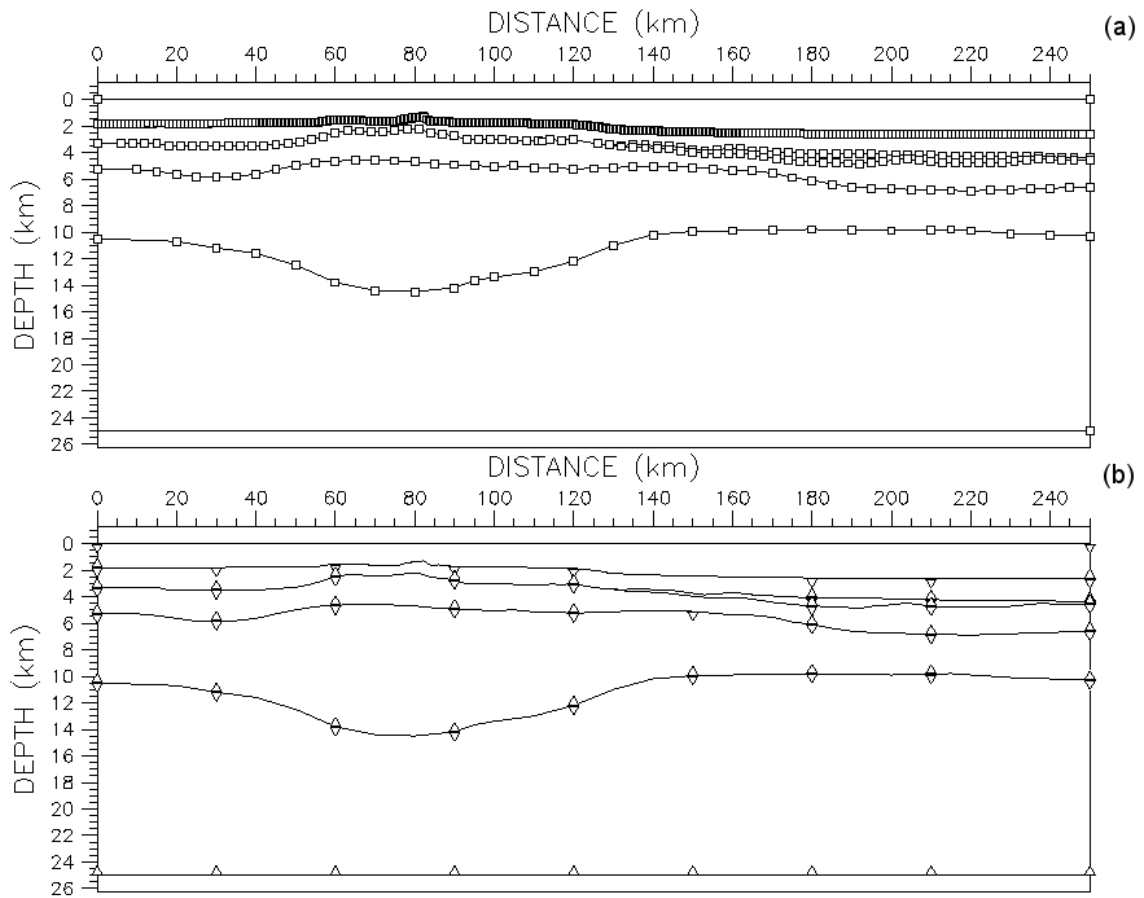


Figure 4.1: Distribution of the (a) depth nodes and (b) velocity nodes in the forward model. (a) Squares define the position of depth nodes. The upper layer, which simulates the seafloor, has a fine spacing of 0.5 km because of measured bathymetry data. Below the seafloor a spacing of 3 to 10 km is defined through the modeling phase. (b) Triangles define the velocity nodes. Those triangles with apex down are velocity nodes which define the velocity at the top of a layer. Apex up triangles show the position of nodes which define the velocity at the bottom of a layer. The distance between velocity nodes is 30 km.

In addition to the node spacing the layering of the final forward model is illustrated (left = West, right = East).

per crust is thinnest in the eastern central part of the profile (ca. km 135 - 180, thicknesses listed in table 4.1). The lower crust has three different parts with different thickness: the westernmost part of the profile (ca. km 0 - 40) has a lower crustal thickness of 5 to 6 km. Thickening to the center of the profile appears in a distance of few kilometers to a maximum thickness of 9.8 km. In the easternmost part of the profile a thin lower crust is present with a thickness of 3 to 4 km.

More detailed thickness structure of the resulting model is summarized in table 4.1.

The final forward velocity model (figure 4.2) is separated in three parts, like the layering indicates from the different crustal thicknesses (also visible in figure 4.1): the westernmost part of the profile from ca. km 0 to 40, the western to central part from ca. km 40 to 140 and the eastern part from ca. km 140 to 250.

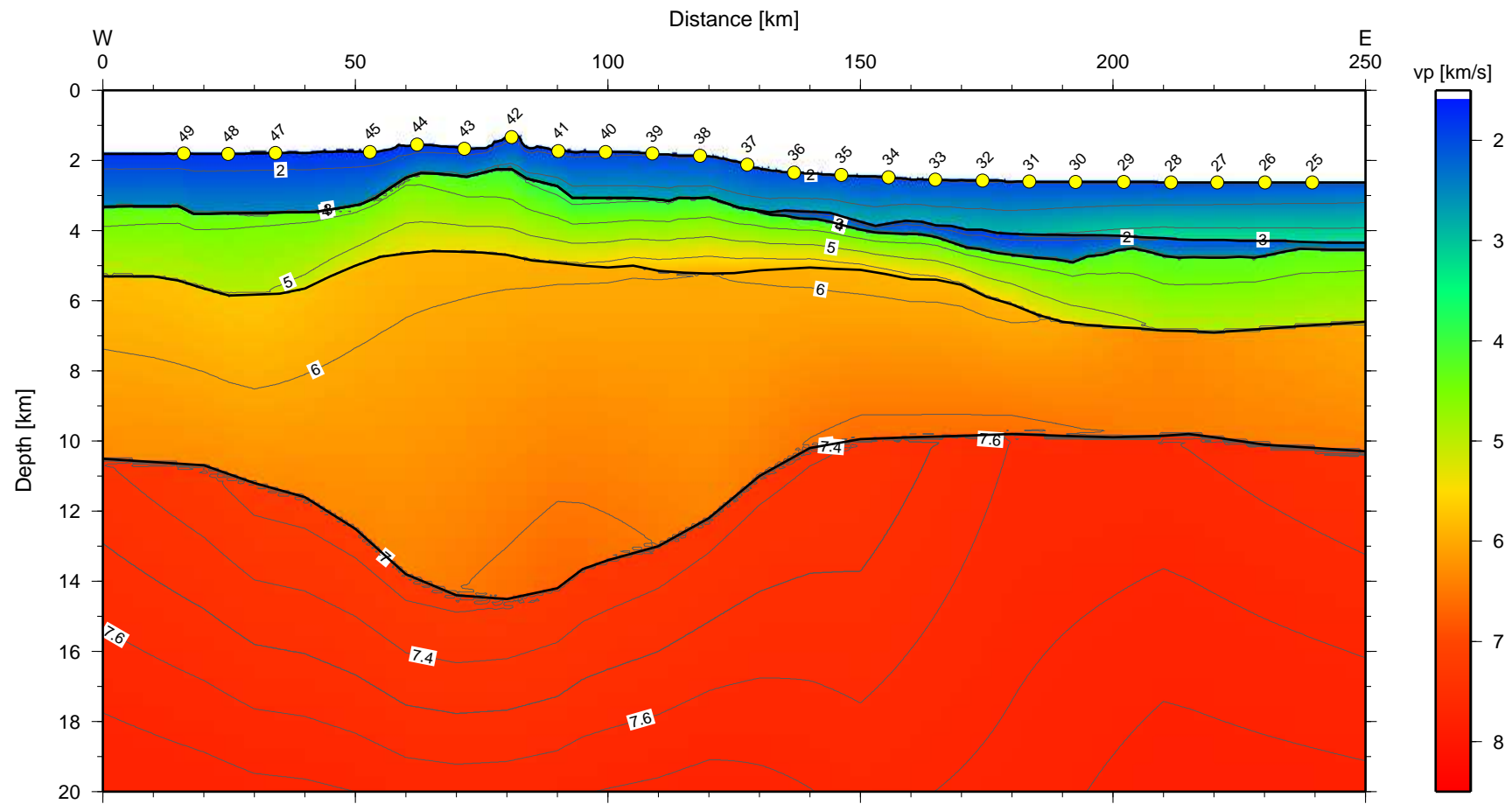


Figure 4.2: The final forward model. Isolines are every 0.5 km/s between 2 and 7 km/s and every 0.1 km/s between 7 and 8 km/s. Left = West, right = East.

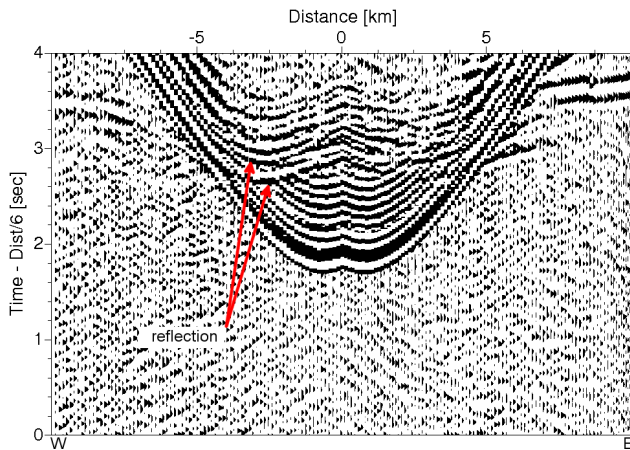


Figure 4.3: Closeup of the seismogram of OBH33. Reflections of the bottom of the low velocity zone and the bottom of the basement are recorded (red arrows).

distance along profile [km]	water depth [km]	sediment thickness [km]	upper crust thickness [km] (depth at top [km])	lower crust thickness [km] (depth at top [km])	mantle depth
10	1.81	1.50	1.99 (3.31)	(5.30)	
20	1.81	1.71	2.13 (3.52)	5.05 (5.65)	10.70
30	1.80	1.70	2.33 (3.50)	5.37 (5.83)	11.20
40	1.78	1.70	2.17 (3.48)	5.95 (5.65)	11.60
50	1.76	1.49	1.75 (3.25)	7.50 (5.00)	12.50
60	1.59	0.90	2.16 (2.49)	9.15 (4.65)	13.80
70	1.62	0.79	2.19 (2.41)	9.80 (4.60)	14.40
80	1.34	0.91	2.45 (2.25)	9.80 (4.70)	14.50
90	1.73	1.00	2.19 (2.73)	9.28 (4.92)	14.20
100	1.75	1.31	1.99 (3.06)	8.35 (5.05)	13.40
110	1.83	1.30	2.02 (3.13)	7.85 (5.15)	13.00
120	1.88	1.17	2.18 (3.05)	6.97 (5.23)	12.20
130	2.23	1.18	1.72 (3.41)	5.87 (5.13)	11.00
140	2.38	1.29	1.38 (3.67)	5.15 (5.05)	10.20
150	2.45	1.52	1.15 (3.97)	4.83 (5.12)	9.95
160	2.55	1.54	1.29 (4.09)	4.52 (5.38)	9.90
170	2.56	1.92	1.07 (4.48)	4.30 (5.55)	9.85
180	2.61	2.09	1.40 (4.70)	3.70 (6.10)	9.80
190	2.61	2.21	2.04 (4.82)	3.25 (6.60)	9.85
200	2.62	1.94	2.19 (4.56)	3.15 (6.75)	9.90
210	2.63	2.09	2.13 (4.72)	3.00 (6.85)	9.85
220	2.63	2.14	2.13 (4.77)	3.00 (6.90)	9.90
230	2.63	2.07	2.10 (4.70)	3.30 (6.80)	10.10
240	2.63	1.90	2.17 (4.53)	3.50 (6.70)	10.20

Table 4.1: Thickness and depth of the layers in the final forward velocity model.

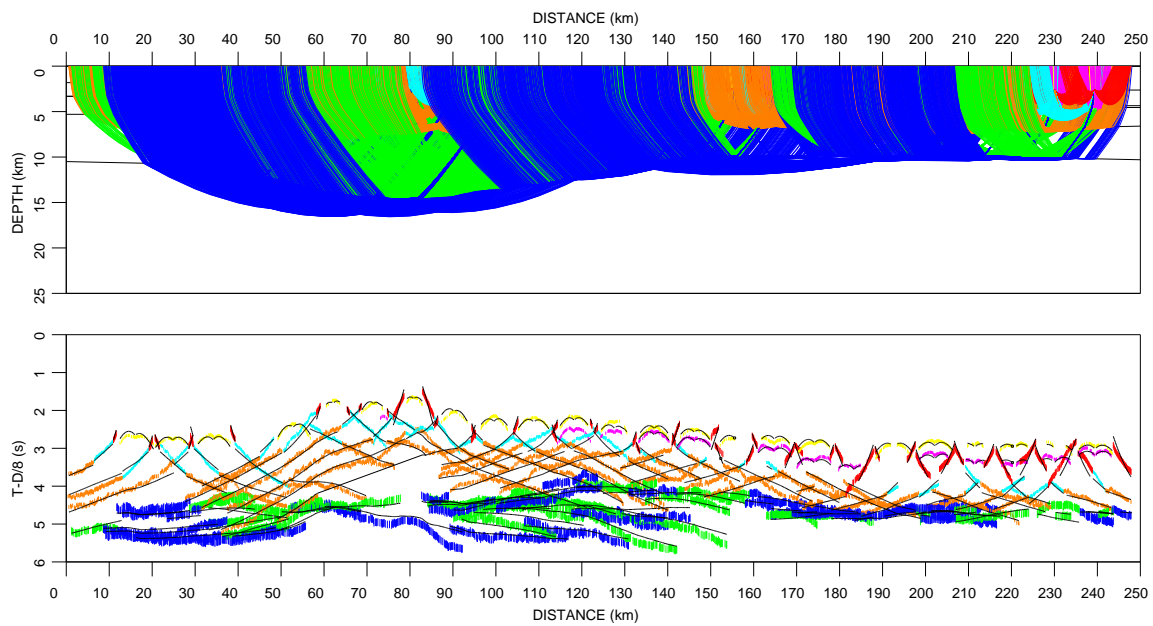


Figure 4.4: Top: Coverage of the resulting model with the forward modeling method. Bottom: Fitting of the data (colored bars are the error bars for the different phases) on the resulting velocity model. Left = West, right = East.

In the first 40 km of the profile a sedimentary thickness of ~ 1.8 km with a P-wave velocity of 1.8 km/s at top and 2.5 km/s at bottom of this layer. The crustal thickness is 7 to 8 km. v_p increases from 4.4 to 5 km/s at the border between upper and lower crust and from 5.8 to 6.3 km/s in the lower crust. The mantle velocities are relatively low with ~ 7.3 km/s directly at the Moho.

Between km 40 and 140, the crust is the thickest along the profile. This is the part of the profile where the topographic feature Maimonid Ridge is crossed (for location see figure 1.5(b) and 3.1). Sedimentary thickness is ~ 800 m to 1.5 km, thinnest at top of the topographic high. The velocity is slightly increasing from west to east in this part: from 1.8 to 2 km/s at the top and from 2.5 to 2.7 km/s at the bottom of the sedimentary layer. In the thicker crust the velocity increases from ~ 4 km/s in the upper crust to 6.7 km/s at the deepest part of the profile with a upper mantle velocity of ~ 7.3 km/s.

From km 140 to the end of the profile the crust thins to 5 to 6 km with v_p increasing from ~ 4.2 km/s at top of the upper crust to 6.6 to 6.4 km/s at the Moho. Ontop the crust a sedimentary layer of ~ 2 km thickness is existent. This layer comprises a low velocity zone (LVZ) with velocities of ~ 2 to 2.6 km/s below sediments with v_p of 2 km/s right below the seafloor increasing with depth to 3 to 3.3 km/s. The upper mantle velocity is ~ 7.6 km/s.

In figure 4.4 (top) the coverage of rays traced forward through the modeled velocity profile is illustrated. The resolution of the velocity profile is until a depth just under the Moho. Error estimation is displayed in figure 4.4 (bottom). Color bars denote the error assessment of picks for first arrivals, which is assigned to the picks while phase picking. Fitting to the picks (black lines in figure 4.4 bottom) was improved while forward mode-

ling. The RMS traveltimes residual of all traced rays is 0.118 s.

The resulting velocity model has an abrupt transition of P-wave velocities at layer boundaries. This is not close to a possible reality where a slight change of velocities would be realistic. Therefore an inversion is used and described in the following section with the rayinvr velocity model used as a starting model.

4.2 Inversion

An inversion of seismic data is used to gain a velocity model of the researched profile (figure 3.1) which has a good fit to the recorded data and could be a plausible subsurface structure.

4.2.1 Modeling Strategy

The modeling strategy for the inversion is to use the forward model which is provided after fitting the recorded data to a discrete layered model with the rayinvr program (section 4.1). The used program for inversion is Tomo2D (section 2.1.3).

	Ps	Pu	Pg	PmP	Pn
Lht	1	1	1	1	1
Lhb	1	1	1	1	1
Lvt	0.1	0.1	0.5	0.4	0.6
Lvb	1	1	5	5	4
LhR	1	1	1	1	4
SV	20	20	40	30	100
SD	10	10	10	10	20
DV	10	20	40	80	50
DD	20	20	20	20	40
Q	10^{-4}	10^{-4}	10^{-6}	10^{-4}	10^{-6}

Table 4.2: Chosen parameters for different phases. The tested modeling steps are named after the last added phase (e.g. parameter test for sedimentary layer, upper and lower crust refractions and mantle reflections (Ps, Pu, Pg and PmP) is named PmP). Parameter abbreviations are explained in the text.

Parameter Adjustment for Tomo2D

The grid size for the model is set to 501 x 92 (figure 2.2), which is every 500 m along the profile and an increasing grid size with depth (~50 m at the seafloor and ~550 m in a depth of 22 km). A fine grid size is needed to suffice an accurate traveltimes modeling. A too coarse grid would not fit the data with an acceptable error and a very fine grid would increase the computational time and result in a finer velocity model but not improve the data fit.

For Tomo2D different parameters have to be chosen for further modeling:

- Lht = horizontal correlation length (at top of model)
- Lhb = horizontal correlation length (bottom)

- Lvt = vertical correlation length (top)
- Lvb = vertical correlation length (bottom)
- LhR = correlation length for the reflector
- SV = velocity smoothing
- SD = depth smoothing
- DV = velocity damping
- DD = depth damping
- Q = tolerance for LSQR algorithm

The choice for parameters is made after some tests with the rayinvr model and different values for each parameter. Parameters with a low error and low to moderate roughness are chosen as further modeling parameters (summarized in table 4.2). Parameters are determined for each modeling step:

1. sedimentary layer refractions (Ps)
2. sedimentary layer and upper crust refractions (Ps and Pu)
3. sedimentary layer, upper and lower crust refractions (Ps, Pu and Pg)
4. sedimentary layer, upper and lower crust refractions and mantle reflections (Ps, Pu, Pg and PmP)
5. sedimentary layer, upper and lower crust and mantle refractions and mantle reflections (Ps, Pu, Pg, PmP and Pn)

When one parameter is varied while it is tested, the other parameters are kept fixed to the values of

Lht	Lhb	Lvt	Lvb	LhR	SV	SD	DV	DD	Q
4	10	0.1	3	2	100	100	10	10	10^{-3}

The starting model is for each tested parameter the same: the final model of the forward modeling (figure 4.2).

The correlation length is defined in four parameters: horizontal and vertical correlation length for the top and the bottom of the model. Low horizontal and vertical roughness and a low error is gained with a low horizontal correlation length at top and bottom of 1 for all inversions. The vertical correlation length differs for the different modeling steps. At the top the parameter with the best error/roughness ratio is between 0.1 to 0.6 and at the bottom between 1 and 5 (table 4.2).

For the reflector which is included in the modeling for the modeling steps with Pn- and PmP-phases a correlation length of 1 respectively 4 (included Pn phases) is the best parameter.

Smoothness of the model is determined by the velocity and depth smoothing parameter (SV and SD). Velocity smoothing uses higher parameters for phases which penetrate

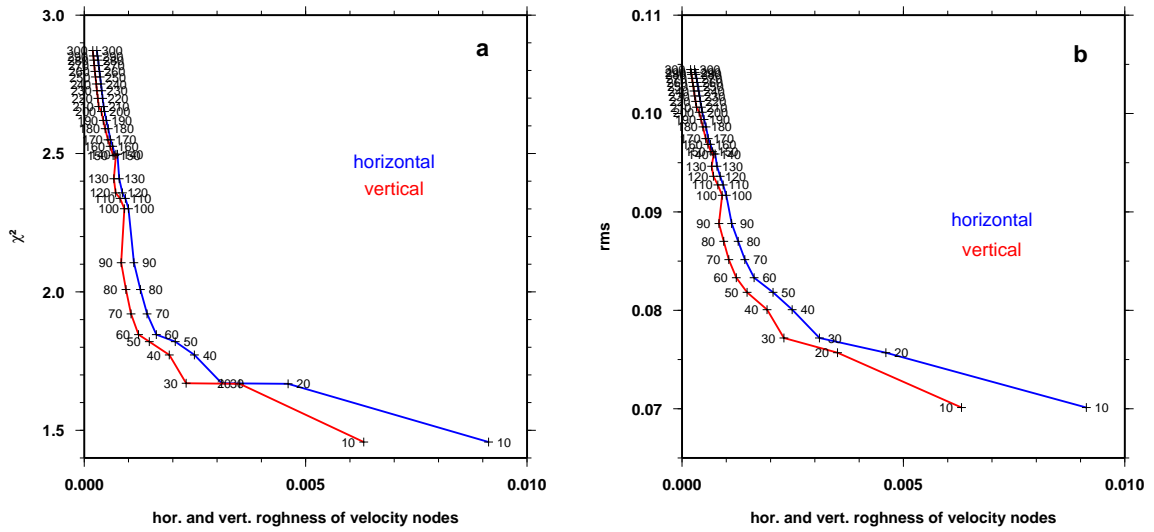


Figure 4.5: Testing of the velocity smoothing (SV) for the modeling step with PmP-phase. (a) χ^2 and corresponding horizontal and vertical roughnesses for different SV values. (b) RMS and corresponding horizontal and vertical roughnesses for different SV values. Chosen parameter was for the PmP-phase the value 30 because of a low error and low roughness.

deeper into the model. For Ps and Pu a value of 20 is chosen, for Pg a 40, for PmP a 30 and for Pn a 100. In figure 4.5 the error and roughnesses for tested values of SV are plotted for the PmP modeling step. A low error and coeval low horizontal and vertical model roughness is gained with a SV parameter of 30.

For depth smoothing the best tested parameter is 20 for the Pn modeling step and 10 for the others.

Damping values for velocity increases from 10 for the Ps modeling step to 80 for the PmP modeling step. The Pn modeling step gains best results with a DV value of 50.

Depth damping values are determined to be 40 for the Pn modeling phase and 20 for the Ps, Pu, Pg and PmP modeling phases.

The tolerance for the LSQR algorithm gains best parameter test results with 10^{-4} for the Ps, Pu and PmP modeling steps and 10^{-6} for the two other modeling steps.

These determined parameters are used for the following inversion to gain a good velocity model with low errors and not to intense horizontal and vertical roughness.

After some models correlation lengths are changed due to too fine structures to values of

Lht	Lhb	Lvt	Lvb	LhR
4	10	0.5	2	6

This results in a little higher error for the velocity models but a smoother structure. Too fine structures are not resolved by the inversion. Those would be artefacts made by the inversion and not reasonable fine structures which image the real subsurface structure and are recorded by the data.

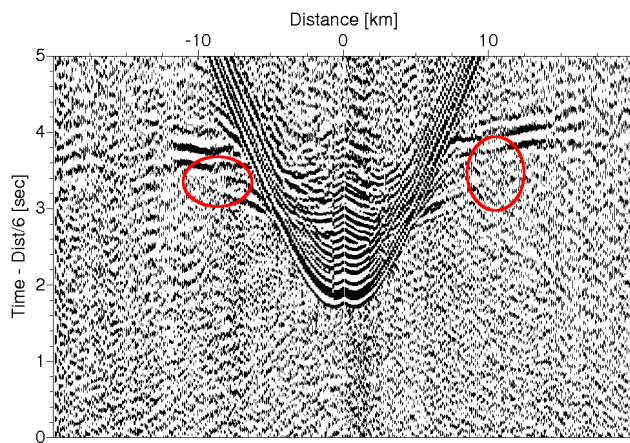


Figure 4.6: An example for the “step” in the refraction arrivals of OBH32 as indication of a LVZ (red circles).

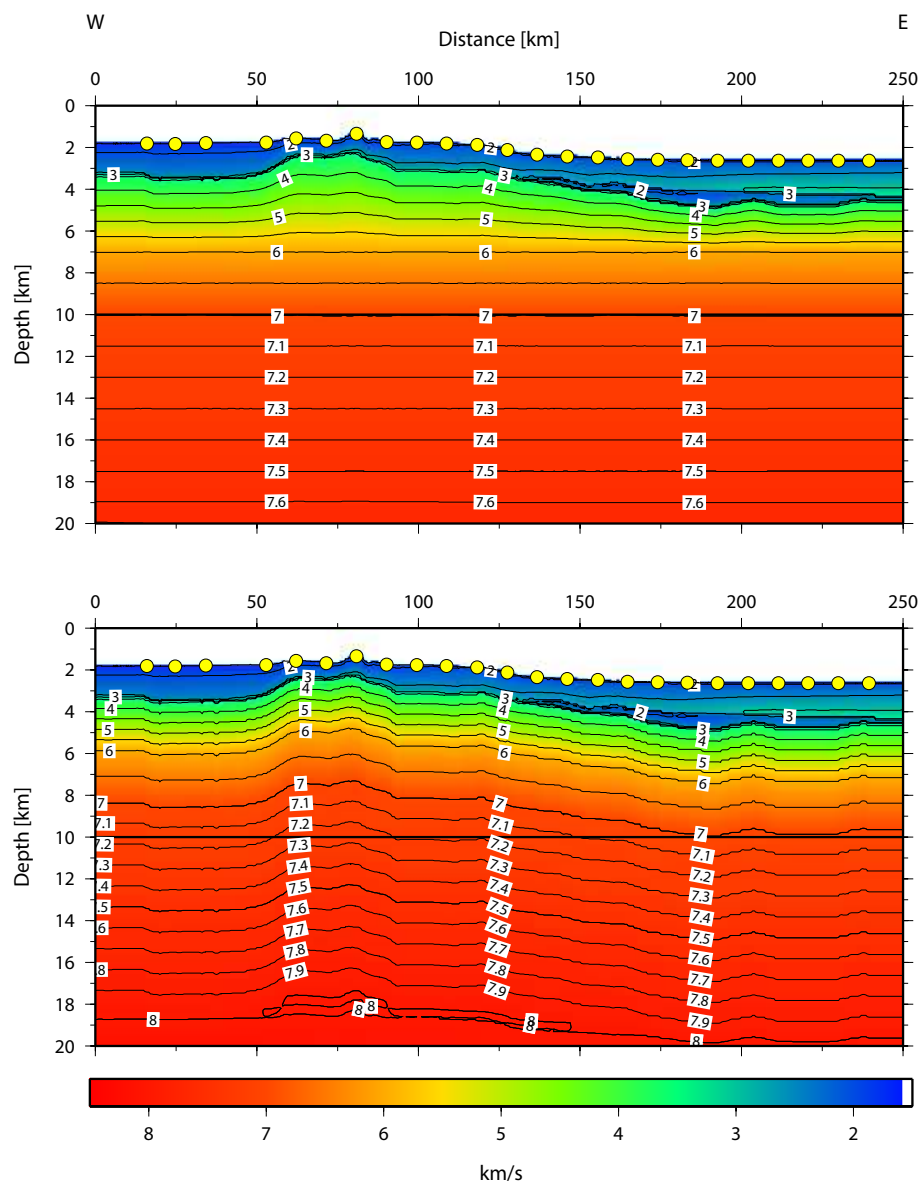


Figure 4.7: Different starting models with a velocity gradient below the basement. Iso-lines are every 0.5 km/s and from 7 km/s onward every 0.1 km/s. The thick black line shows one of different tested Mohos inverted with this starting model.

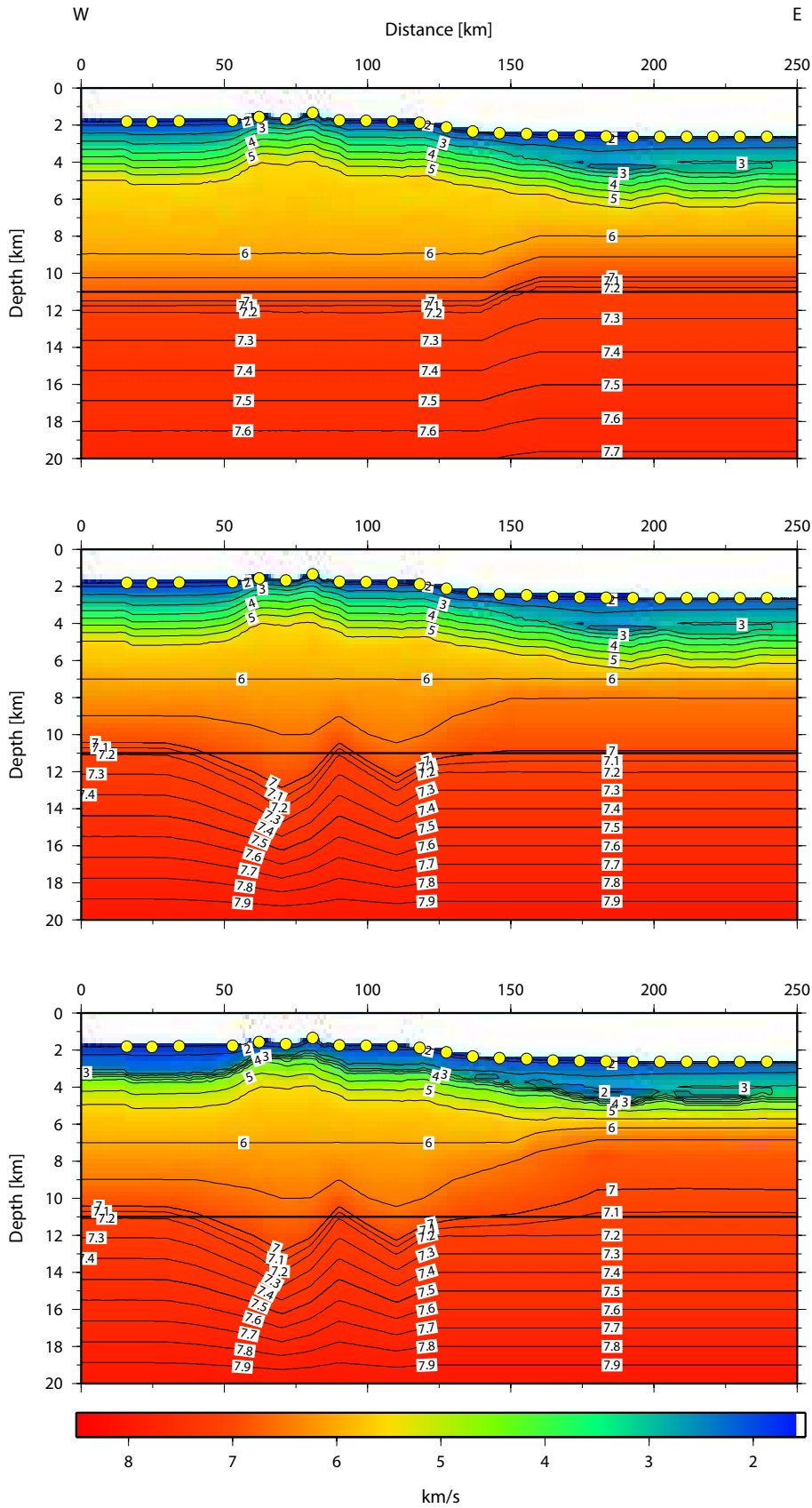


Figure 4.8: Different starting models with a velocity structure below the basement. Iso-lines are every 0.5 km/s and from 7 km/s onward every 0.1 km/s. The thick black line shows one of different tested Mohos inverted with this starting model.

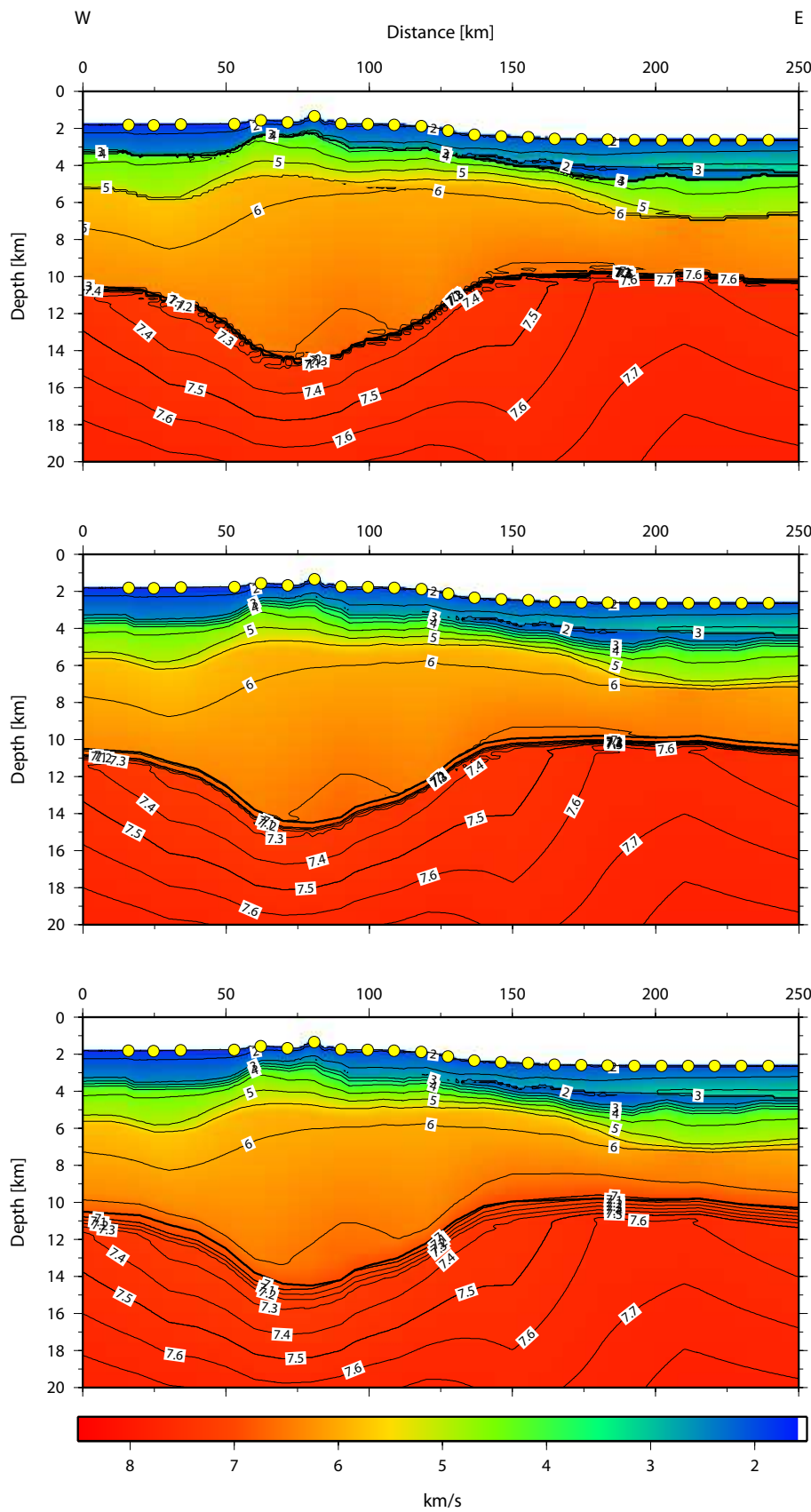


Figure 4.9: Different starting models. Top: Result of the forward modeling. Center: Forward model with a 0.5 km thick velocity transition zone between layers. Bottom: Forward model with a 2 km thick velocity transition zone between crust and mantle and a 0.5 km thick velocity transition zone between other layers. Iso-lines are every 0.5 km/s and from 7 km/s onward every 0.1 km/s. The thick black line shows one of different tested Mohos inverted with this starting model.

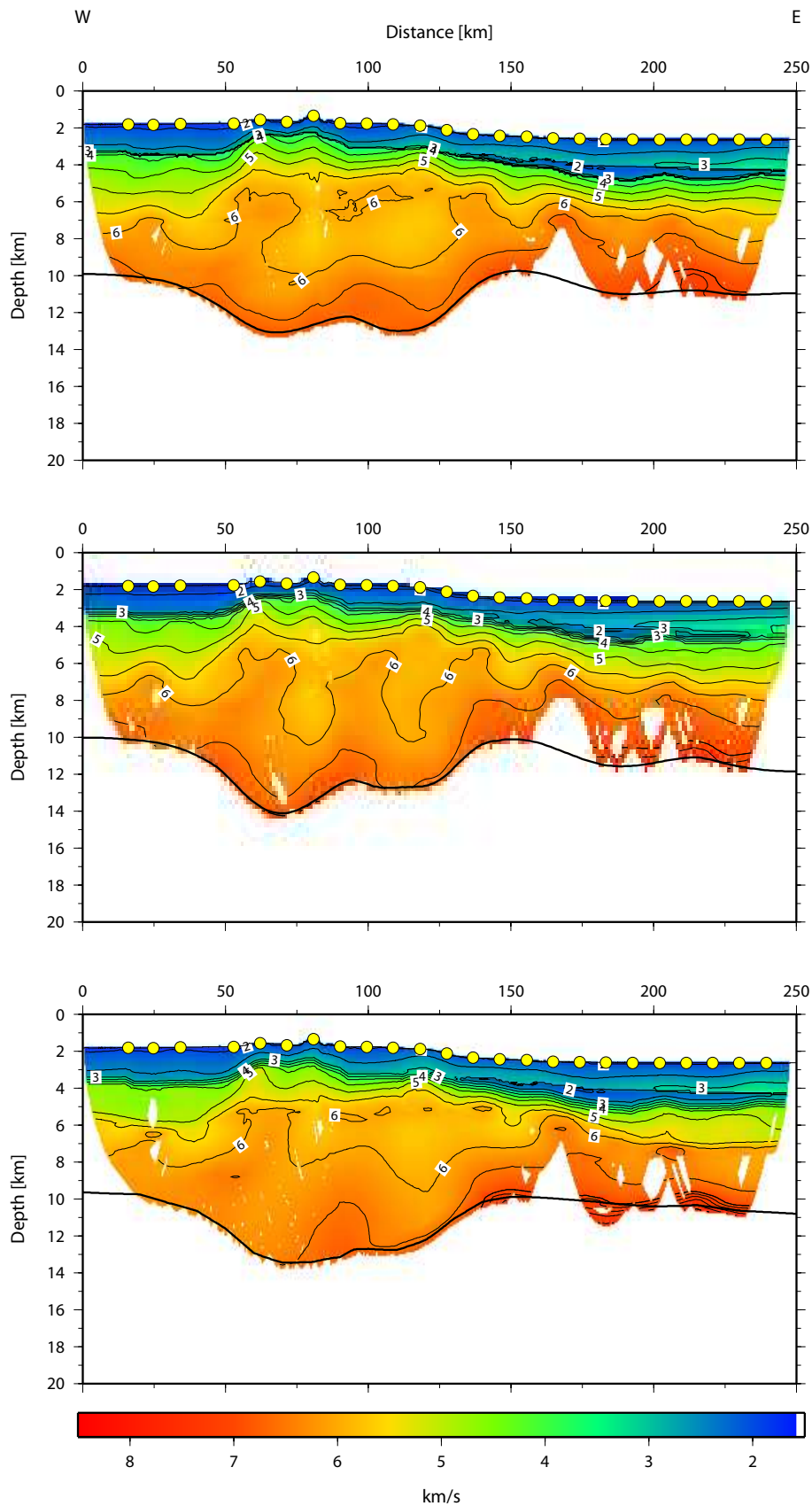


Figure 4.10: Resulting models after inversions of different starting models. Top: Inversion result with a starting model with a velocity gradient below the basement (figure 4.7, top). Center: Inversion result of a starting model with structure below the basement (figure 4.8, bottom). Bottom: Inversion result with the forward model result as starting model (figure 4.9, bottom). Iso-lines are every 0.5 km/s and from 7 km/s onward every 0.1 km/s. The thick black line shows the resulting Moho.

4.2.2 Modeling Results

With the determined parameters different starting models have been tested (examples are shown in figure 4.7, 4.8 and 4.9).

Tomo2D is not made for modeling a low velocity zone (LVZ). Therefore the LVZ which is forward modeled with rayinvr based on reflections (see section 4.1.2) is included into the different starting models. The existence of a LVZ is also supported by the “steps” of the refraction arrivals in seismograms (example in figure 4.6) which supports the decision of inclusion of the LVZ in the different starting models.

The tested starting models differ in most parts in the sub-basement structure. Some starting models are for example with different velocity gradients below the basement (examples in figure 4.7) and others are with different structures below the basement (examples in figure 4.8). One model is the result of the forward modeling. The model is tested with an abrupt velocity transition between layers (figure 4.9, top) and with a velocity gradient at layer boundaries (figure 4.9, center and bottom).

Resulting velocity models show similar structures, if the starting model was the result of the forward modeling, a model with structure or a model with a onedimensional velocity gradient below the basement (figure 4.10). An inversion of Ps, Pu, Pg and PmP results in a flat Moho in a depth between ~9.5 and 11 km for the western part of the profile. Between km 40 and 140 of the profile, a thicker crust is present. In the eastern part of the profile the Moho is thinner and lies for most models in a depth between ~10 and 11 km. At the edges of the profile, the Moho depth is massive influenced by the depth of the Moho before inversion. These first and last kilometers of the profile are only resolved in the upper few kilometers of the velocity model and not in the depth which would be needed to model the Moho depth.

The velocity structure of the inversions are as well similar. The sedimentary cover is composed of velocities of ~2 to 2.6 km/s with a LVZ in the eastern part of the profile. In the different starting models the LVZ was included which, after inversion, is confirmed because it is not removed in any inversion. This LVZ lies beneath a layer of higher velocities of up to ~3.6 km/s. The thickness of the sedimentary cover is 1 to 1.3 km at the topographic high, 1.5 - 1.7 km in the West and ~2 km in the East.

The upper crust has a higher velocity gradient compared to the lower crust. Below the topographic high, the gradient is higher compared to the parts of the profile east and west of this feature. An increasing velocity from ~4 km/s to ~5.5 km/s in a layer of 1.5 to 2 km thickness is followed by a ~4 to 9 km thick lower crust with a small velocity gradient. Below the topographic high the crust is thickest with a ~9 km thick lower crust. This part has a structure in the velocity model with a shallowing and deepening 6 km/s isoline, varying slightly between different inversions. The westernmost part and the eastern half of the profile has a more layered structure in the crust. Velocities directly above the Moho are 6.5 to 7 km/s.

Structure of the Moho is in all inversions similar with most differences in the eastern half where the resolution is getting worse due to availability of fewer PmP arrivals. The depths of the Moho in this part is driven by the depth of the Moho before inversion. Es-

pecially between ca. km 160 and 210 the Moho differs. The Moho depth is successively deepening until the profile end or deepens relatively abrupt in a few kilometers and continues until the end of the profile more or less horizontal (figure 4.10).

For inversion of Pn phases, a resulting model of inversion of Ps, Pu, Pg and PmP phases is used with an included high velocity gradient at the Moho. Without changing the velocity model in the upper mantle, the inversion with Tomo2D does not result in a reasonable structure. The gradient at the crust-mantle transition is reduced while inversion which results in steeply through the velocity model traced rays. The error gets worse compared to a velocity model where the crust-mantle boundary velocity is influenced after inversion of Ps, Pu, Pg and PmP and before inversion of Pn phases.

An average of models is calculated to show the average inversion result for the crust (figure 4.11, top). The structure is as described above. In figure 4.11 (bottom) the standard deviation of the averaged models is shown. The highest standard deviation is in the transition from the sedimentary layer to the crust. In some parts it is as high as 0.5 km/s. This is due to the differences in the starting models. The averaged inversion includes models with an abrupt velocity transition from the sedimentary layer to the crust as starting model and models with a narrow transition zone at this boundary. During inversion the velocity structure does not change so much that the extreme differences of these two different kinds of starting models results in nearly the same velocities. A starting model with an abrupt velocity transition keeps after inversion a high velocity gradient in this part of the profile where a model with a transition layer between sedimentary layer and crust results in a lower velocity gradient. The standard deviation of the velocity structure is in most parts of the rest of the profile smaller than 0.2 km/s.

The Moho depth differs in the West up to ± 0.5 km (grey shaded in figure 4.11). The thickest part of the crust has a standard deviation of the Moho of nearly 1 km and decreases to 0.1 km in the central part of the profile. In the most eastern part of the profile the Moho depth is modeled with ~ 0.5 km uncertainty comparing a set of inversion results.

Inversion results of Ps, Pu, Pg and PmP phases have a Gaussian distribution of travel-time misfit (figure 4.12 (b) and (d)). Maximum misfit of single rays is ± 200 ms. Before inversion the error is equally distributed for simple starting models with low similarity to the resulting model (figure 4.12 (a)). These models can have a RMS of traveltime misfit of more than 300 ms. The forward model result has residuals centered around ~ 150 ms but is not Gaussian distributed (figure 4.12 (c)). The average residual is -92 ms with an RMS of 191 ms. After inversion the residuals of both different starting models are similar: a Gaussian distribution centered around 0 ms (figure 4.12 (b) and (d)). Both have an RMS of the residuals of ~ 67 ms.

An error assessment is also done in other ways than looking at the traveltime residuals. The derivative weighted sum (DWS) is computed and a checkerboard test is carried out. The DWS describes the weighted ray length in a cell of the grid. This is a relative value. A higher DWS describes that more rays pass this cell and it is better resolved. But it does not include information of the direction of the rays which is important to estimate the quality of the model. A model with good quality would include many crossing rays. To analyse the quality of the model, a checkerboard test is performed after DWS calculation.

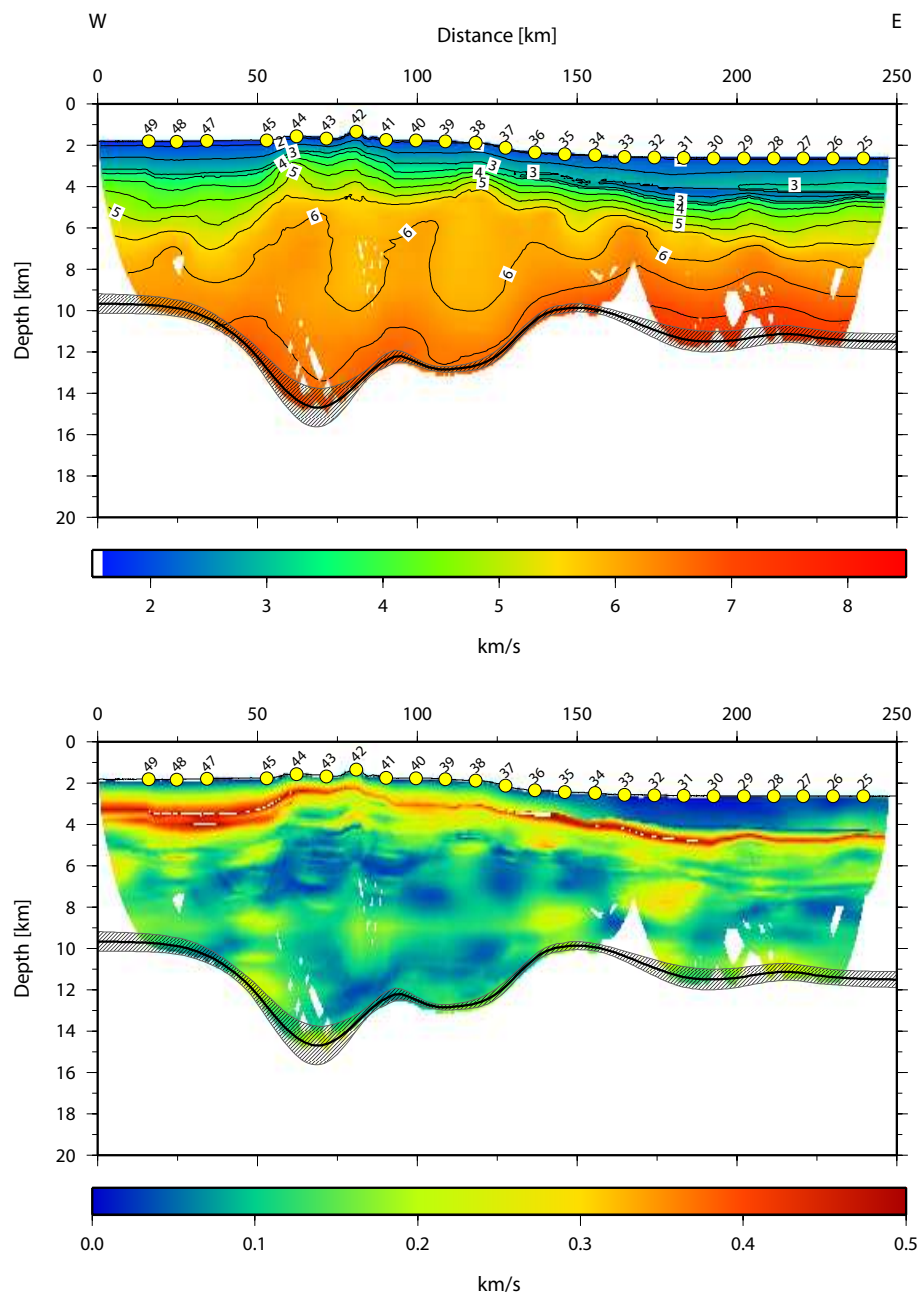


Figure 4.11:

Top: Average of Tomo2D inversions of Ps, Pu, Pg and PmP. The average Moho is shown as a black line. Grey shaded is the standard deviation of the Moho. Isolines are every 0.5 km/s. Bottom: Standard deviation of the crustal inversions.

Figure 4.13 shows the resolution of the model just with Ps, Pu, Pg and PmP phases. The western to central part of the model shows in most parts a good to acceptable resolution. In the East the PmP rays resolve the model not as a whole block. This part includes regions with no resolution (empty white spots) and with acceptable to (at some points) good resolution. The sedimentary layer and the upper crust have a good resolution over the whole model. The quality of the inversion result has to be checked with a checkerboard test which is done after inclusion of available mantle reflections.

The result of the inversion with mantle phases is shown in figure 4.14. Inversion of the averaged model of inverted Ps, Pu, Pg and PmP phases (figure 4.11) results in a gradi-

ent at the crust-mantle boundary. Directly below the Moho, the mantle velocity lies in the West around 7 km/s and in the East around 7.6 km/s. The diving rays do not dive deep in the mantle, what would be unrealistic, but relatively shallow along the Moho. Pn phases improve the ray coverage in the lower crust especially in the eastern half of the profile. Further discussion about the velocity structure follows in chapter 6.

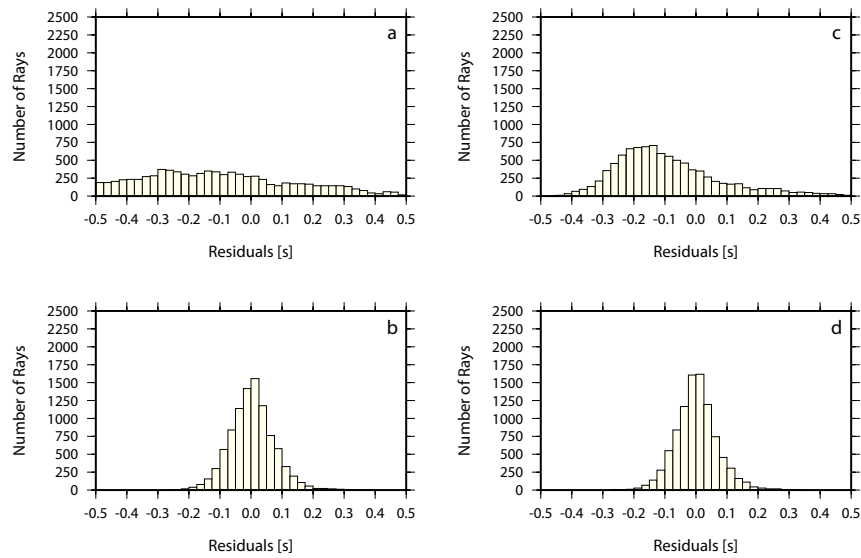


Figure 4.12: The histograms show the traveltime residuals for two different modelings. (a) Residuals for a starting model with a velocity gradient (figure 4.7, top). (b) Resulting residuals after 5 inversion iterations. (c) Residuals for the starting model of forward modeling result with an inserted velocity gradient between sedimentary layer and crust and between crust and mantle (figure 4.9, bottom). (d) Resulting residuals after 5 inversion iterations.

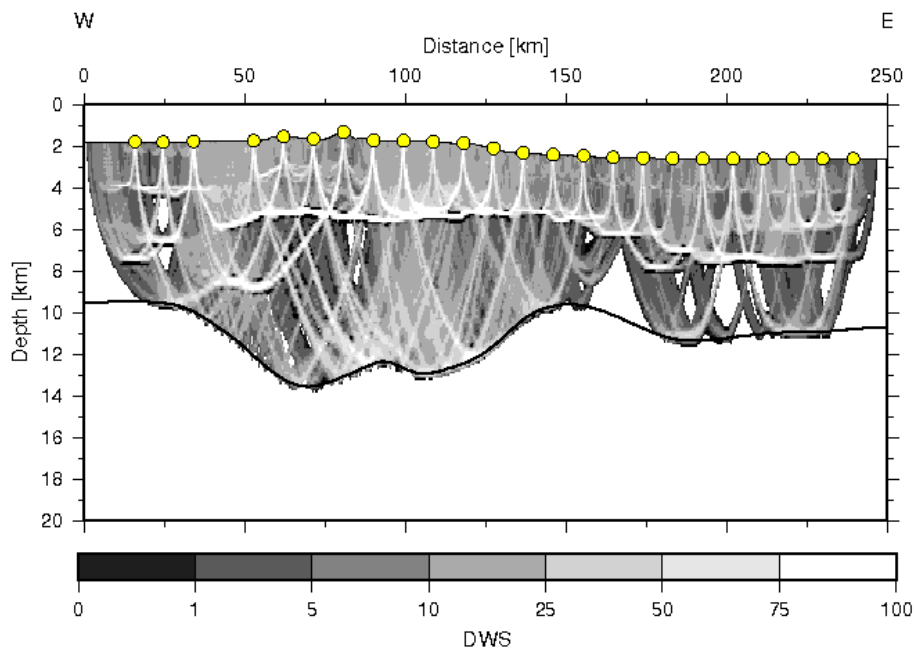


Figure 4.13: DWS of the inversion result.

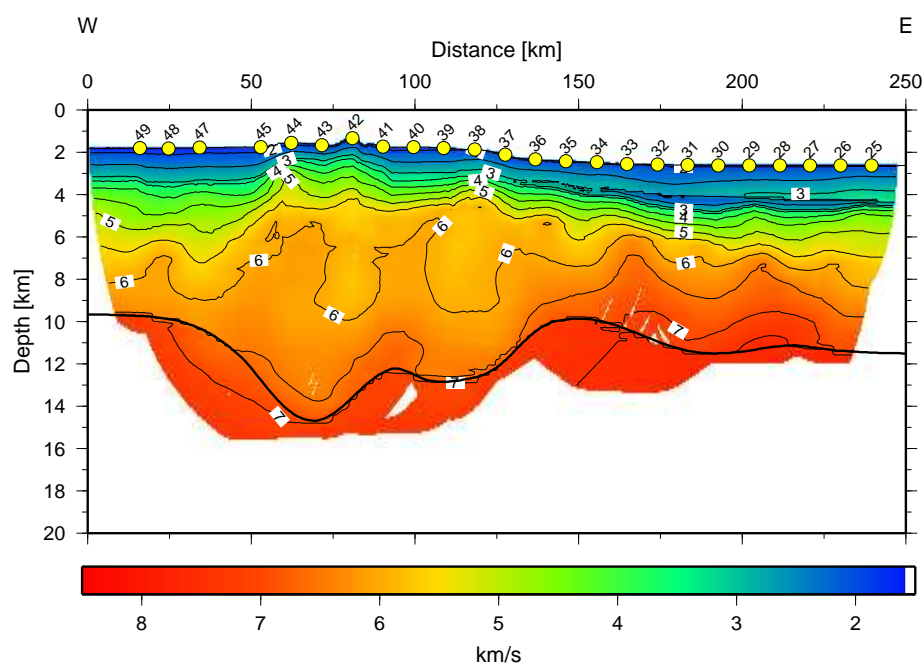


Figure 4.14: Velocity model after inversion of Ps, Pu, Pg, PmP and Pn phases. Iso-lines are every 0.5 km/s. (Enlarged plot is in the appendix: figure A.1.)

For the illustration of the data quality and data fit, the modeled phases are plotted onto the seismograms (figure 4.15). All modeled phases for all stations and their fit onto the picked data are shown in the appendix in figure B.1. The seismograms of all OBH and OBS stations and channels are shown in figure B.2 to B.40 in the appendix.

The relatively small offset of the recorded data is evident (figure 4.15). The data examples show a good fit of the modeled phases on the recorded data. It supports the low RMS of ~67 ms calculated after inversion of the seismic data (histograms in figure 4.12 (b) and (d) and explanation on page 56).

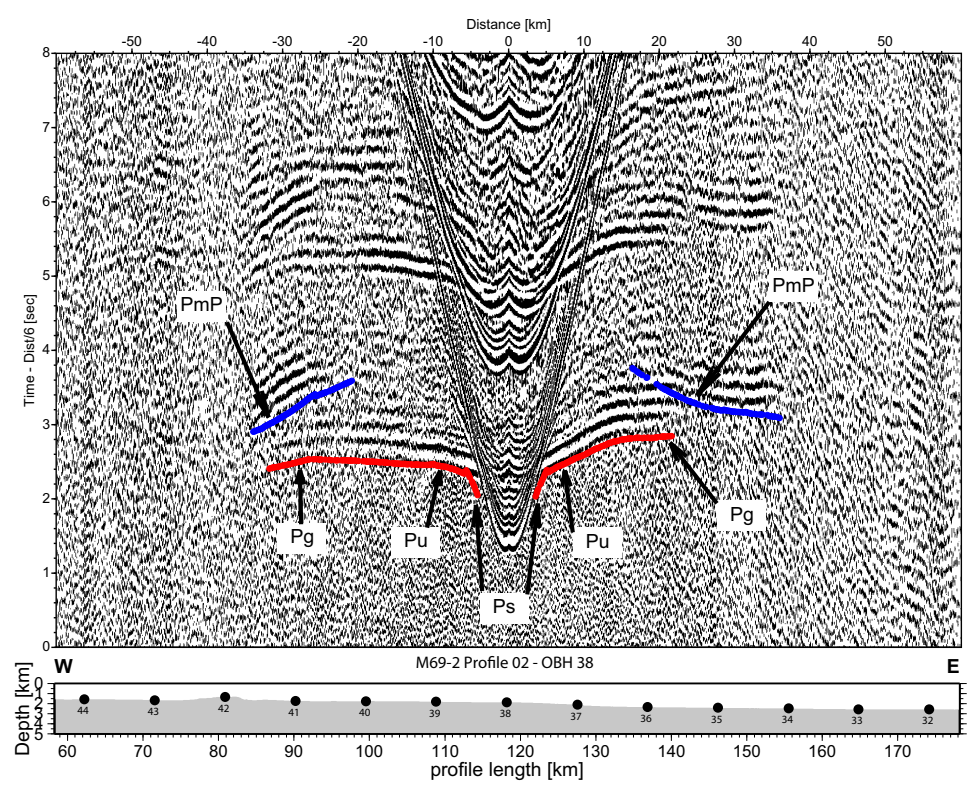
Figure 4.15(a) shows the fit for OBH 38. In the near offset of ± 60 km, no Pn phases are clearly identified. The identified PmP phases are for the resulting velocity model good recovered. Also available crustal refractions (upper and lower crust) and the Ps arrivals are recovered by the velocity model in a good way. OBH41 (figure 4.15(b)) has also a good data fit to the picked phases. For this station, also Pn are identified while data picking which also show a good recovery with the resulting velocity profile.

The resolution of the modeled velocity structure is tested with a checkerboard test. Different sizes of a checkerboard pattern are percentally added to the final velocity model. With the for this model calculated traveltimes and the final model as starting model the recovery of the checkerboard is the goal. In figure 4.16 different sizes of a checkerboard are compared. Figure 4.16 (a), (c) and (e) are the constructed checkerboards, figure 4.16 (b), (d) and (f) the recovered models.

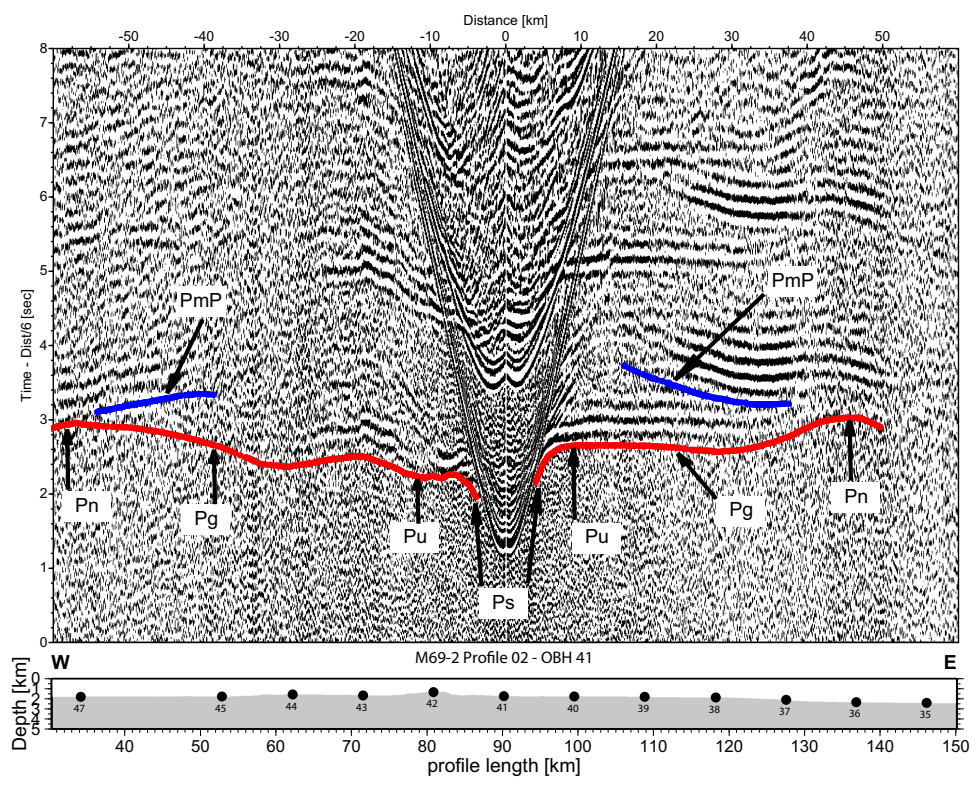
Figure 4.16 (a) and (b) show a fine checkerboard with a size of 10 km in width and 2 km in depth. The recovered model shows a good resolution in the sedimentary layer and the upper crust. Also a part of the lower crust is resolved. Just at the edges of the profile the pattern is smeared in the upper part of the profile. This result demonstrates a good resolution of the finer structure in the first ~3 to 5 km of the subsurface.

A rougher grid is shown in figure 4.16 (c) and (d). The grid size is 20×3 km. The gross structure is resolved. Just the thicker part of the crust with the root-like structure shows in the deeper parts the prefix of the checkerboard pattern without the correct intensity. The rest of the model recovers the checkerboard in a good way.

A checkerboard grid of 50×5 km (figure 4.16 (e)) is recovered good in size and intensity for the crust (figure 4.16 (f)). The result shows that very rough structures are resolved by the inversion.



(a)



(b)

Figure 4.15: Data example for (a) OBH38 and (b) OBH41.

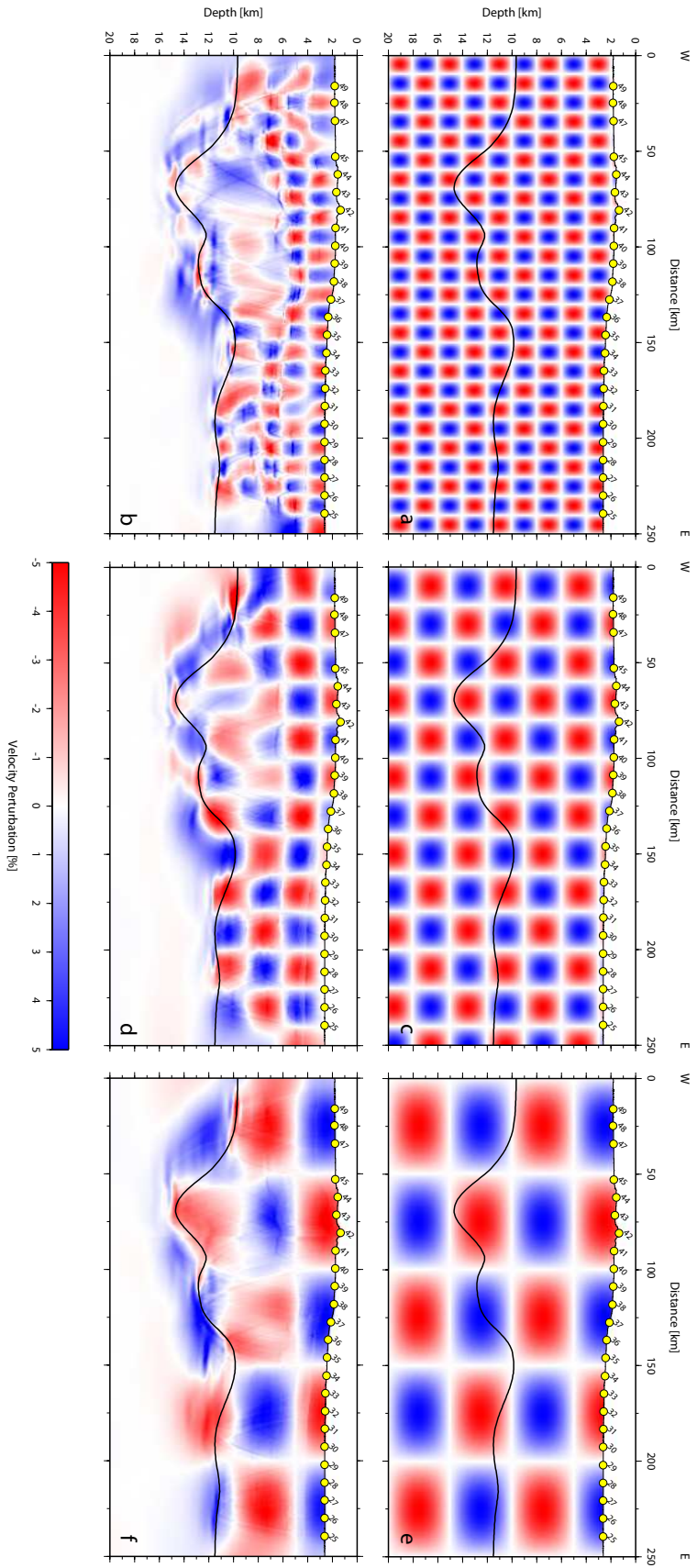


Figure 4.16: Checkerboard test with an anomaly of 5%. (a), (c) and (e) are the inserted anomalies, (b), (d) and (f) the results of the checkerboard test, respectively. (a) Checkerboard grid size of $10 \text{ km} \times 2 \text{ km}$. (b) Recovery of the $10 \text{ km} \times 2 \text{ km}$ checkerboard structure. In the upper ~ 3 to 5 km the resolution of the velocity model is fine enough to resolve the checkerboard structure. This includes the sedimentary layer and the upper crust. Only the westernmost part of the model does not resolve the checkerboard structure. (c) Checkerboard grid size of $20 \text{ km} \times 3 \text{ km}$. (d) The larger grid cells are resolved in the sedimentary layer and the crust. Only in the thicker crust the lower crust is not resolved very good. (e) Checkerboard grid size of $50 \text{ km} \times 5 \text{ km}$. (f) Huge grid cells of the checkerboard are resolved in the whole crust.

Chapter 5

Synthetic Modeling of the Seismic Refraction Data

Additionally to the forward modeling and inversion of recorded data, an amplitude modeling with the reflectivity method was carried out. The aim is to reproduce the recorded seismogram as a synthetic seismogram.

5.1 Modeling Procedure

Due to a validity for only onedimensional velocity structure, the amplitude modeling could merely be made for the eastern part of the analysed seismic profile. These are the OBS stations 25 to 29. After the modeling procedure, the synthetic seismograms are compared to the recorded data.

The velocity profile of compressional waves (v_p) is taken from the resulting tomographic inversion (chapter 4.2.2). Shear wave velocities v_s are calculated by the reflectivity program with the relation $\frac{v_p}{v_s} = \sqrt{3}$. Additional to these two parameters (v_p and v_s , see figure 5.1 continuous red line (v_p) and dashed red line (v_s)) the density ρ is also an input parameter for the calculation of synthetic seismograms with the reflectivity program. With Birch's law (Birch, 1961), an approximation of the density is made ($\rho = 0.252 + 0.3788 v_p$). Damping values are set for the different depths by the Quality Factor Q . A high Q describes a low damping and vice versa. The damping values are tested to identify the best fitting value for a synthetic seismogram which resembles the recorded data. Normal values for the Quality Factor are lower for the sediment and increase with depth to high values in the lower crust and mantle. A relation of Q_p and Q_s is used to estimate the Quality Factor for S-waves ($Q_p = 2.25 Q_s$; Müller, 1985).

For the definition of the Quality Factor of P-waves different values are tested and there-with identified for the synthetic modeling. Values of Q_p are illustrated in a Quality Factor – depth diagram in figure 5.1 (Q_p : continuous black line; Q_s : dashed black line). The sediment has a low Quality Factor which describes a high damping. In the upper crust the damping decreases a little bit while in the lower crust the Quality Factor increases rapidly (damping decreases rapidly). Damping in the upper mantle is small.

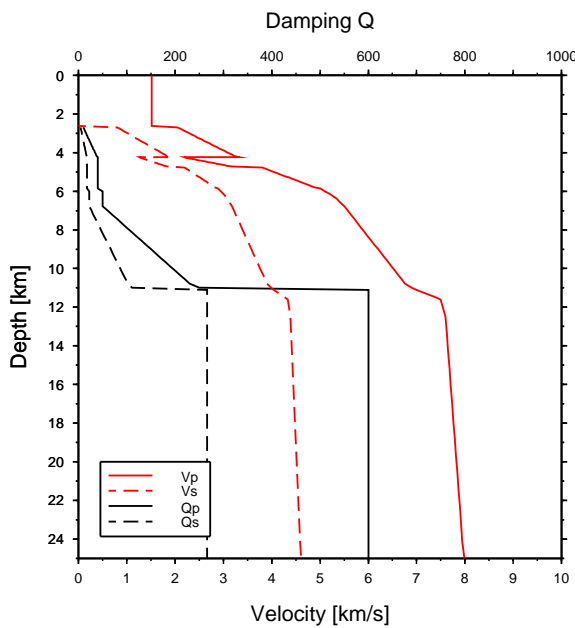


Figure 5.1: Velocity-depth profile for v_p and v_s and damping values with depth (Q_p and Q_s). A high Q describes a low damping and vice versa.

5.2 Synthetic Seismogram

After determination of the parameters for the reflectivity method, a synthetic seismogram is calculated. The seismogram of recorded data of OBS 26 is displayed in figure 5.2. Figure 5.3 shows the synthetic seismogram with the in figure 5.1 imaged values of v_p , v_s , Q_p and Q_s as input parameters. For a better comparison of the seismic records, noise is added to the synthetic data.

Complexity of the modeling were existing in the sedimentary layer and the transition from crust to mantle. In the sedimentary layer the low velocity zone (LVZ) gave the challenge to model the abrupt ending of the seismic signal with the transition to the crustal phases. This LVZ was confirmed through the modeling phase (forward modeling and inversion, chapter 4). The LVZ is needed also in the velocity profile to model a synthetic seismogram with a step-like structure at the end of P_s arrivals (figure 5.2 and 5.3). During amplitude modeling, the LVZ was introduced in the velocity profile. The abrupt end of the signal was derived by the velocity structure and, in addition, a high damping in the sedimentary layer, decreasing slightly with depth (from $Q_p = 10$ to 40). After synthetic modeling, the LVZ in the sedimentary layer is not developed as intensive as in the recorded data.

The damping in the upper crust is produced by a Quality Factor of 40 to 50. Damping decreases further with depth by an increasing value of the Quality Factor to 250 at the bottom of the crust. The mantle is modeled with a low damping.

The crustal structure around OBS 26 is not completely onedimensional. This causes especially in the upper crust slight differences of the synthetic seismogram compared to the measured data.

Crustal refractions are modeled with a higher velocity gradient in the upper crust and a lower gradient in the lower crust. This part of the crust has a high damping which leads

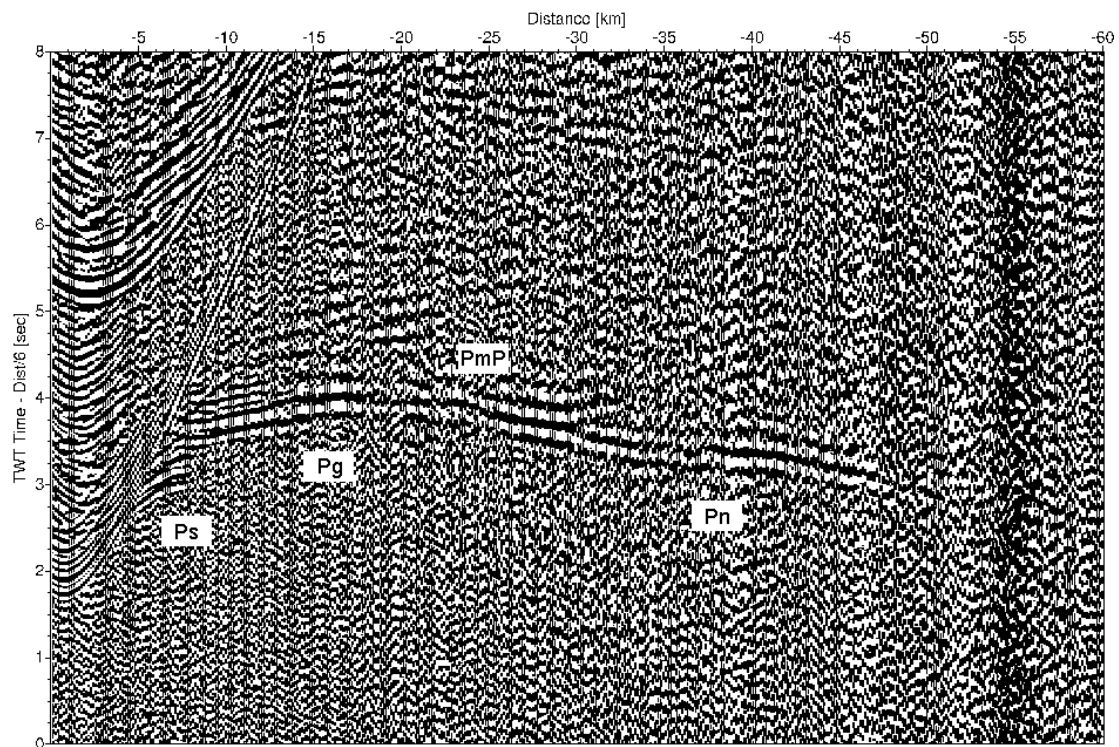


Figure 5.2: Recorded seismogram of OBS26.

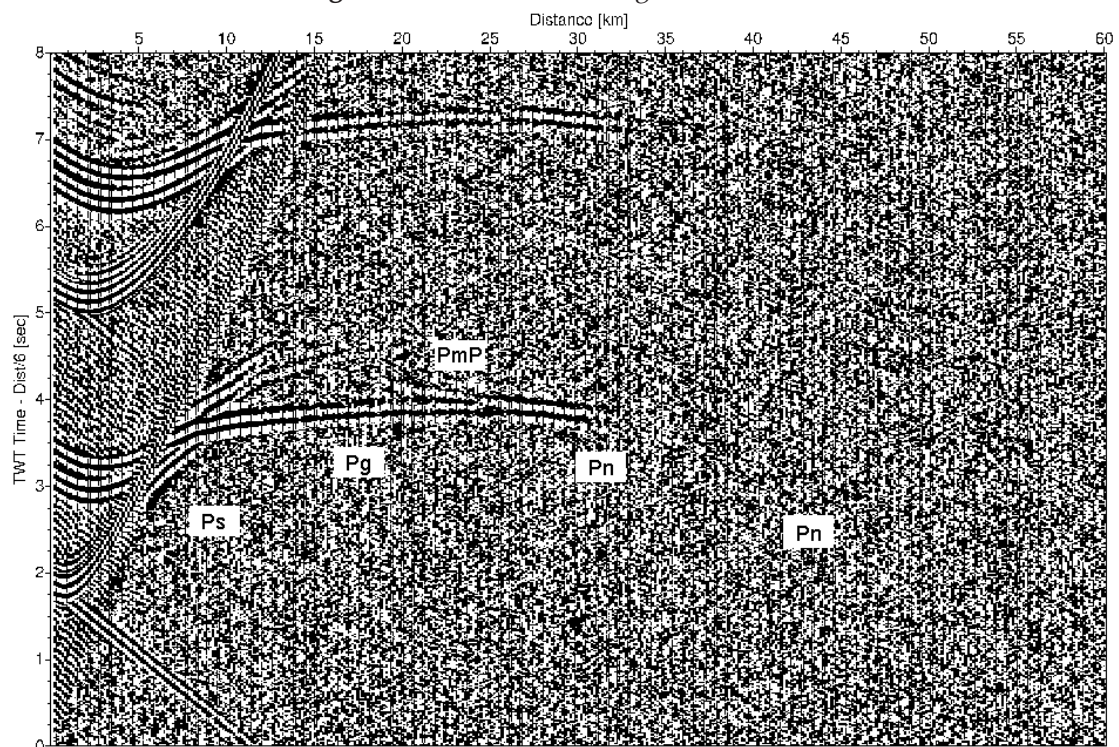


Figure 5.3: Recovered seismogram after amplitude modeling for OBS26.

to just a small rest of the signal which dives through the mantle. Hence the mantle phases are only modeled where refraction and reflection interfere (figure 5.3). The recorded data show a longer record section of mantle refractions with ≈ 50 km offset. Less noise added to the synthetic data would result in more arrivals visible with a longer offset to the OBS position but with too less noise added compared to the recorded data.

Synthetic data show, that a lot of noise is present in the Alboran Sea where the seismic data were recorded. This noise hides signals of the lower crust and the mantle. The velocity structure which was modeled with forward and inverse method was supported. With damping and added noise, the velocity structure results in a similar seismogram modeled with the reflectivity method (figure 5.3) compared to the measured data (figure 5.2).

Chapter 6

Modeling Results and Discussion of the Seismic Refraction Data

During the modeling procedure different techniques were used to gain an image of the structure below the Alboran Sea. Recorded seismic data of a profile in WSW to ENE direction (figure 3.1) were used to image the structure (chapter 4) and modeling of a synthetic seismogram (chapter 5) was made to gain information about damping in the subbottom and to support the recorded data with their relatively small offsets and their amplitudes.

6.1 Velocity Structure

The final velocity profile is displayed in figure 4.14 (enlarged view in figure A.1 in the appendix). This profile can be divided in three different sections: the westernmost part,

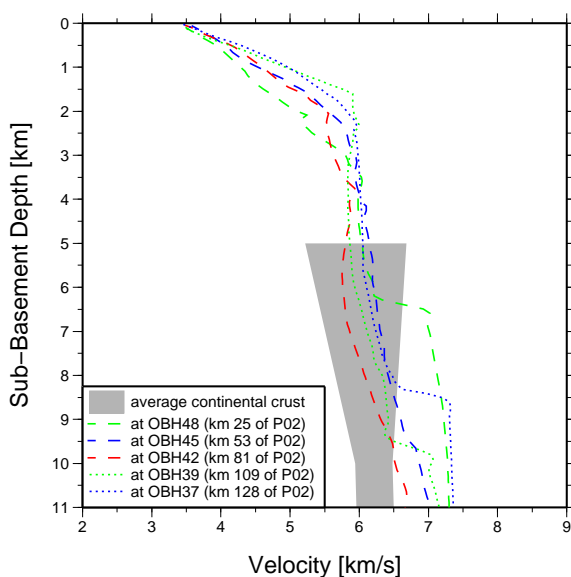


Figure 6.1: Comparison of velocity profiles of the western half of the seismic section with the velocity structure of typical continental crust after Christensen and Mooney (1995) (grey shaded).

the central part and the eastern part.

West of the Maimonid Ridge, the first 40 km of the seismic refraction profile define the westernmost domain. This part has a crustal thickness of ~6 to 7 km (see figure 4.14, A.1 and table 6.1) with seismic velocities which resemble velocities of continental crust. In figure 6.1, a velocity profile below OBH 48 (green dashed line) is displayed. Grey shaded is drawn a velocity structure for average continental crust after *Christensen and Mooney (1995)*. The crustal part of the velocity profile lies in the range of continental crustal velocities. A comparison to velocity profiles for oceanic crust would show a too slow crust in this part of the profile. Thus, the crust clearly resembles continental crust. But this crust is thinned compared to average continental crust.

Additionally to a velocity profile of the westernmost part of the seismic line, four seismic velocity profiles from km 40 to 140 of the seismic refraction profile are also shown in figure 6.1. This is the part below the Maimonid Ridge. All four velocity profiles below the Maimonid Ridge show crustal velocities in a range for continental crust. Crustal thickness is at the deepest part more than 12 km because of the root-like structure in this part of the profile. A thin sedimentary layer lies atop this topographic high with a maximum thickness lower than 1.5 km, in most parts below 1.3 km.

station	sediment thickness	crustal thickness	station	sediment thickness	crustal thickness
OBH 49	1.56	6.37	OBH 36	1.28	6.81
OBH 48	1.70	6.37	OBH 35	1.41	6.08
OBH 47	1.70	6.83	OBH 34	1.60	5.86
OBH 45	1.38	9.64	OBH 33	1.63	6.19
OBH 44	0.82	11.90	OBH 32	1.97	6.39
OBH 43	0.81	12.13	OBH 31	2.13	6.64
OBH 42	0.92	11.30	OBH 30	2.25	6.64
OBH 41	1.00	9.70	OBS 29	1.90	6.85
OBH 40	1.30	9.46	OBS 28	2.12	6.42
OBH 39	1.30	9.74	OBS 27	2.14	6.44
OBH 38	1.20	9.58	OBS 26	2.10	6.61
OBH 37	1.27	8.40	OBS 25	1.89	6.94

Table 6.1: The thicknesses of the sediment and the crust after seismic inversion are listed in this table for profiles below each seismic station. Sedimentary thickness is calculated by subtracting the water depth from the basement depth, which is taken from the forward modeling. Due to damping in the sedimentary layer while inversion with the program *Tomo2D*, the basement depth does not change between forward modeling and inversion. For the crustal thickness, the basement depth is subtracted from the Moho depth, which is a result of the inversion.

In the first 140 km of the seismic refraction profile, the sediment layer (0.8 - 1.7 km thick, see table 6.1) comprises velocities increasing from 1.8 to 3 km/s. In the upper crust, a

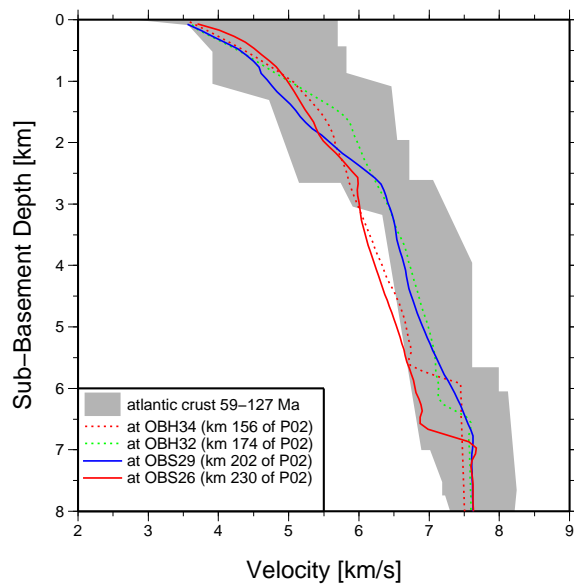


Figure 6.2: Comparison of velocity profiles of the eastern half of the seismic section with the velocity structure of typical oceanic crust in the Atlantic ocean (59 - 127 Ma old) after White et al. (1992) (grey shaded).

steep velocity gradient from ~ 3.5 km/s to 5.5 - 6 km/s with a layer thickness of 1.5 - 2 km is present. A low velocity gradient characterizes the lower crust. From the transition from the upper crust to the Moho, the velocity increases slightly to ~ 6.5 - 6.7 km/s. At the Moho in the upper mantle, low velocities of 6.9 - 7.4 km/s are completing this velocity profile. The easternmost part of the profile (km 140 - 250) shows similarities to oceanic crust. Figure 6.2 provides a comparison to 59-127 Ma old oceanic crust of the Atlantic. Four crustal velocity profiles from km 156 to 230 are shown in the diagram. The part more close to the center of the profile has an upper crust with a thickness of ~ 1.5 km. A steep velocity gradient from 3.5 to 5.5 - 6 km/s defines this part of the crust. The lower crust shows a lower gradient, increasing in ~ 4 - 5.5 km to 6.7 - 7.2 km/s. The last ~ 60 km of the profile has a thicker upper crust of ~ 2.5 km where the velocity increases to 6 - 6.4 km/s. With a lower velocity gradient in the lower crust, the seismic velocity increases to 6.9 - 7.2 km/s at the base of the crust. A lower crustal velocity up to 7.6 km/s is present beneath km 200 - 220 of the profile at the base of the crust (figure 6.2, blue line and also figure 4.14). This part of the profile shows no steep velocity gradient to the mantle. At the Moho in the upper mantle for oceanic crust relatively slow velocities of 7.5 - 7.6 km/s are present.

In the sedimentary layer velocities increase from ~ 2 to 3 km/s. This part of the profile includes a low velocity zone between \sim km 150 eastward to the end of the profile starting in a depth of ~ 1.5 km below the seafloor. This LVZ is attributed to a layer of evaporites existent in this region in the sedimentary layer. It was seen in the MCS data collected by spanish scientists in 1992. An interpretation of the MCS data was published by Comas et al. (1995) and Booth-Rea et al. (2007). In figure 6.3, the MCS data and the interpretation of Booth-Rea et al. (2007) are plotted onto the resulting velocity profile of this study.

The evaporites are deposited in the Messinian salinity crisis (e.g. Govers, 2009). They are defined by higher velocities compared to other parts of the sedimentary layer. Due to this

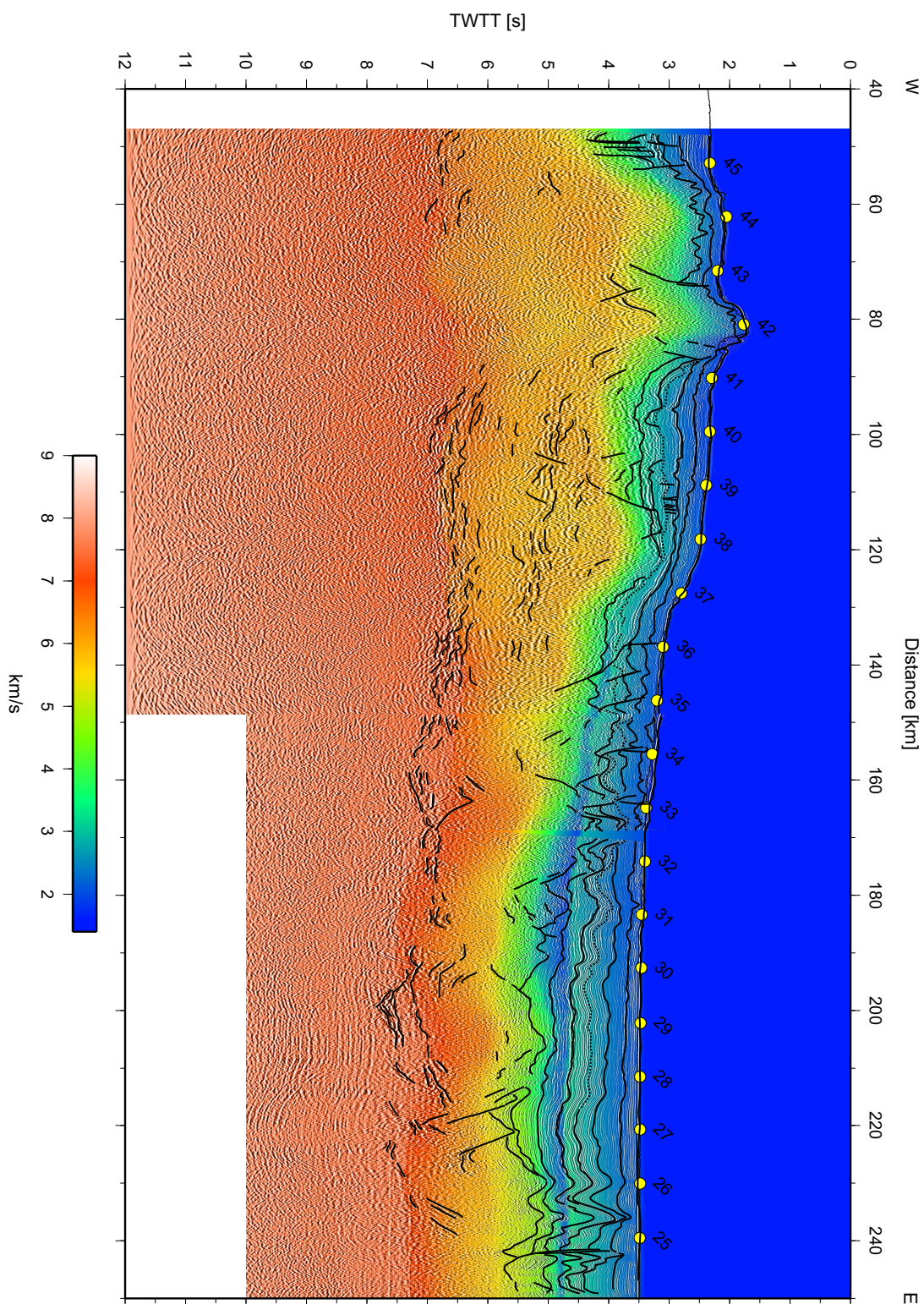


Figure 6.3: The interpretation of Booth-Rea *et al.* (2007) of the in 1992 recorded MCS data plotted over the resulting velocity profile of this study (figure 4.14 / A.1), illuminated with the MCS data.

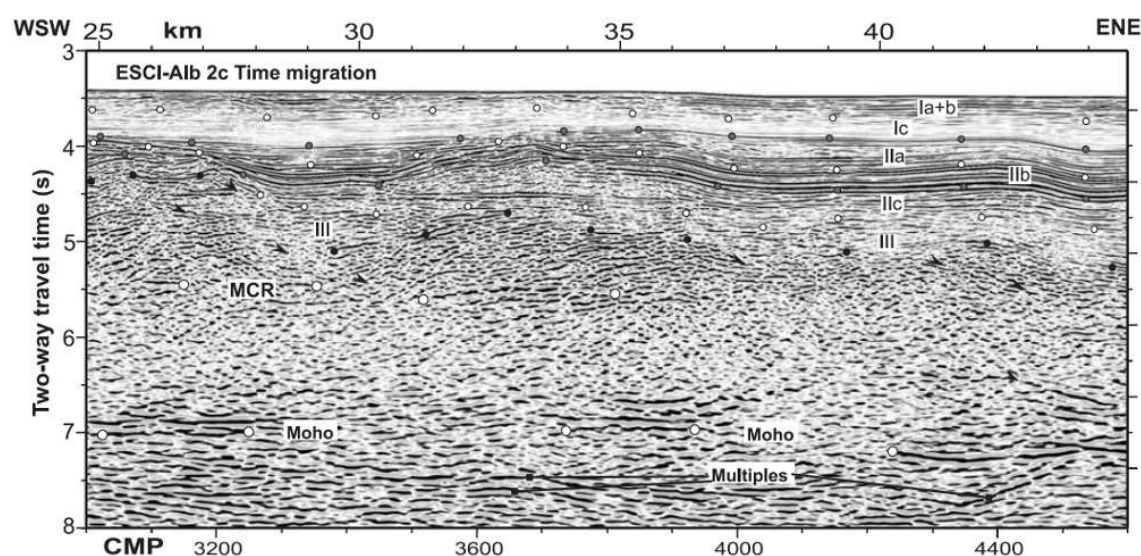


Figure 6.4: Section of the by Booth-Rea *et al.* (2007) analysed MCS profile. Arrows denote identified faults. I to III are the defined sedimentary units and MCR is the mid crustal reflector. White and grey dots define the unit boundaries and black dots the acoustic basement. (Booth-Rea *et al.*, 2007)

layer of higher velocities, a LVZ compared to the overlying sediments is present below the evaporites. In the MCS data evaporites are in the easternmost part of the profile in the reflections visible as a diapiric structure (figure 6.3).

A relation from the LVZ to the amplitude modeling is seen in the step-like structure of the refraction arrivals in the seismograms in the easternmost part of the profile (example in figure 5.2 and 5.3). A break-off of the Ps arrivals is an evidence for the LVZ in the seismograms. In the amplitude modeling, a LVZ is needed to model this break-off of the Ps arrivals (figure 5.3).

Over the whole seismic profile an undulating 6 km/s isoline is found. This is not a feature of the inversion but attributed to the formation of this region. The 6 km/s isoline is a robust feature and appears in all inversions made in this study. It can be explained as normal faults in the crust. Booth-Rea *et al.* (2007) also mentioned in their interpretation of the MCS data that there are evidences for normal faults in the crust along this profile. In figure 6.4, a section of the by Booth-Rea *et al.* (2007) analysed MCS data with marked faults (arrows) is shown. This part of analysis of the MCS data is not the main goal of their study. They found no evidence for major faults. But identified faults fit to the in this study modeled block structure. The westernmost part shows little evidence for normal faulting, to the East more faults are seen in the MCS data.

The existing faults and the undulating isoline in the crustal velocity structure mark a block structure in the crust. This block structure is a remnant of the extension in this region.

Another possible source for the undulating 6 km/s isoline could be magmatic intrusions. Samples collected in the Alboran Sea show historic volcanic activity (e.g. Duggen *et al.*, 2004). The sampled volcanic rocks are analysed and indicate similarities of the magmatic

styles found in this region to lavas of a volcanic front and rear-arc lavas from the Izu Bonin Arc (*Duggen et al.*, 2004).

A combination of both possible sources for the 6 km/s isoline could also be the explanation of the structure along the seismic refraction profile. Beneath the Maimonid Ridge, an intrusion causes higher velocities in the crust. In the easternmost part of the profile, normal faults due to extension as remnants of the formation history of the region result in small undulations of the 6 km/s isoline (see figure 4.14 or A.1).

Examining the Moho, Moho reflections analysed by *Booth-Rea et al.* (2007) coincide with the resulting Moho of this seismic refraction analysis (figure 6.3: Moho reflections identified by *Booth-Rea et al.* (2007) coincide with the in this study identified Moho (transition from yellowish to red color).).

Tomographic inversion results in a Moho with a root-like structure (figure 4.14, enlarged in figure A.1). This structure is part of the Moho and no midcrustal reflection. The origin of this structure in the Moho can be associated to the topographic feature, the Maimonid Ridge. An analysis of this structure as Moho is supported by the by *Booth-Rea et al.* (2007) analysed Moho reflections.

The analysis of the root-like structure as Moho is supported by PmP reflections recorded at stations along the whole profile (see reflections in figure B.1). The upper mantle velocities beneath the as Moho analysed reflector are compared to typical upper mantle velocities relatively low. In the easternmost part of the profile, velocities of 7.5 to 7.6 km/s are modeled. The crustal velocities are similar to oceanic crust but upper mantle velocities are lower compared to typical upper mantle velocities for oceanic lithosphere.

Also in the westernmost and central part of the profile, the upper mantle velocities are low. With 6.9 to 7.4 km/s, those velocities are much lower compared to upper mantle velocities of typical continental lithosphere which this part of the profile resembles in crustal velocities.

Considering the modeled reflections especially in the central part of the profile as mid-crustal reflections, the modeled velocities of 6.9 - 7.4 km/s must be lower crustal velocities. This would be too high for the lower crust compared to typical values in continental crust.

Deliberating both possibilities, the reflector as Moho or as mid-crustal reflector, the analysis of the reflector as Moho is supported. A mid-crustal reflector would not have continuous reflections as strong along the whole profile as they exist in the data. And the modeled velocities below the reflector are too high for the crust. The continuous over the whole profile existing reflections are PmP reflections of the Moho with relatively low upper mantle velocities.

Both methods, MCS data and seismic refraction data, consistently show similar structural features. The MCS data resolve the layering in the sedimentary layer and show some midcrustal and Moho reflections while the refraction data show the crustal structure. With the resulting velocity profile of the refraction analysis, the structure of the crust and therewith the evolution of this crust can be analysed.

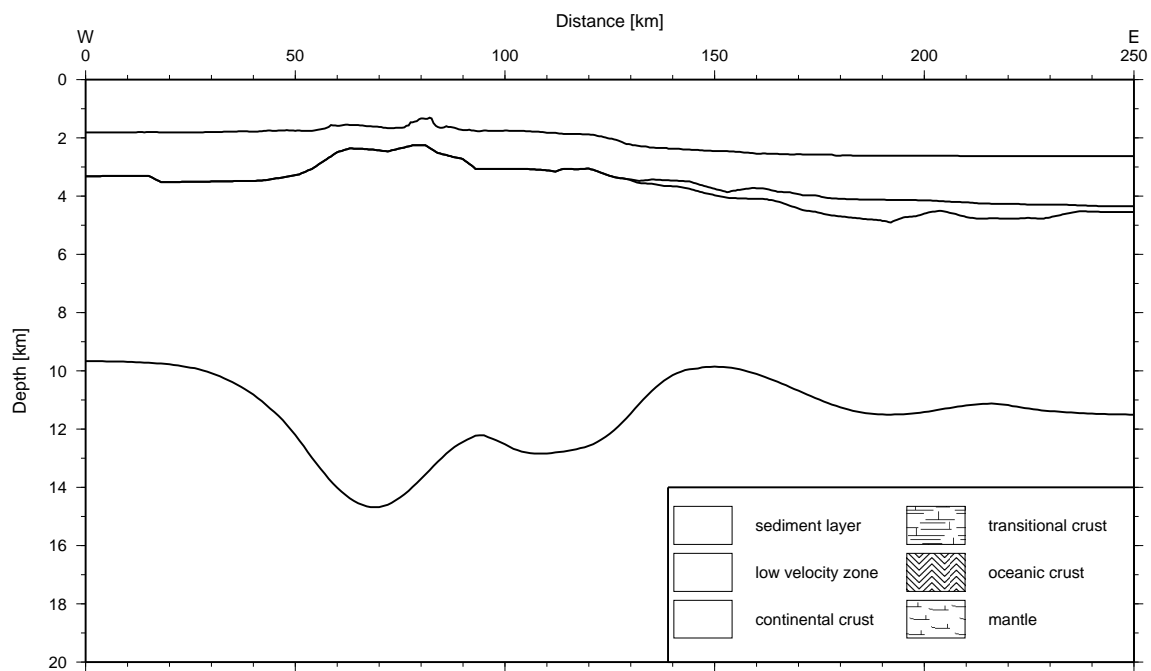


Figure 6.5: Illustration of the resulting velocity profile. The crust can be separated in three different parts. From West to East the crustal styles are of continental crust, transitional crust with more similarities in the crustal velocities to continental crust and oceanic crust.

The two westernmost segments can also be seen as one part because both have a crustal velocity structure similar continental crust. The transition to oceanic crustal velocities is relatively abrupt at the end of the central segment (km 40 - 140).

6.2 Formation of the analysed Profile in the Alboran Sea

The resulting velocity structure along the profile in the eastern Alboran Sea makes it possible to yield insights into the formation history of this region.

In the easternmost part of the profile, crust with a velocity structure of oceanic crust is present. Continuing to the West, there is crust which closely resembles continental crust as it is expressed in seismic velocities. This is the region where the Maimonid Ridge is crossed. The westernmost part of the seismic profile is crust of continental style which is, compared to typical continental crust, very thin. This style of separation of the crust along the seismic profile is plotted in an illustration in figure 6.5.

The two segments in the West (km 0 - 40 and km 40 - 140 along the profile) can also be analysed as one part. Both have crustal velocities similar to continental crust and differ mainly in their crustal thicknesses. This is due to the crossing of the topographic feature, the Maimonid Ridge. A transition from the segment with the Maimonid Ridge to the easternmost segment is relatively abrupt. The velocity structure changes in a few kilometers from continental crustal style to typical values for oceanic crust.

Convective removal (section 1.2.2 "Convective Removal Theory") as formation history for the Alboran Sea would result in thinned continental crust. After removal of thickened lithosphere due to the convergence of the African and European plate, the region would

result in an extensional phase due to no equilibrium in potential energy. Extension continues until an equilibrium in potential energy, and therewith in the thermal gradient in the lithosphere is gained. This extension would result in thinned continental crust. A thinned continental crust is present in the westernmost part of the analysed profile. But in the East, oceanic crust is present. This part of the seismic profile from the easternmost Alboran Sea in transition to the Algerian Basin would not be a result of convective removal, because crustal thinning stops before continental crust is thinned until it breaks and oceanic crust would start to form.

Lithospheric delamination (section 1.2.2 "*Lithospheric Delamination Theory*") also results in an extensional regime. In the convergent stage between Africa and Europe, a thickened continental lithospheric mantle starts to detach from the crust. Asthenosphere replaces the detached lithosphere. As result of the thermal gradient, extension starts until an equilibrium is reached. This results, similar as for convective removal, in thinned continental crust. Oceanic crust would not be a result of lithospheric delamination because extension stops before the crust breaks and oceanic crust starts to form.

Slab rollback (section 1.2.2 "*Westwards Slab Rollback Theory*") thins, due to the pulling force of an old subducted slab, the crust of the overriding continental plate. An end of slab rollback and therewith extension of the overriding plate is gained when all oceanic crust of the subducted plate is consumed. This makes it possible to form a new back-arc basin on the overriding plate in the extended crust. During the formation of a back-arc basin, continental crust of the overriding plate is extended until seafloor spreading starts and forms new oceanic crust.

The analysed seismic refraction data show in the westernmost part of the profile a velocity structure of thin continental crust which is merely 6 to 7 km thick. The transition to oceanic crust occurs in the region of the profile where the Maimonid Ridge is crossed. East to the Maimonid Ridge the back-arc basin with oceanic crust is present. Further to the East, there were data collected for other profiles of the project. These refraction seismic data result after modeling in oceanic crust (unpublished data). One profile which lies in the Algerian Basin is about 50 km away from the eastern end of the analysed profile. This describes the to the East continuing back-arc basin with its velocity structure of oceanic crust.

A further support for the westward slab rollback of the subducted slab is the extension from East to West where an indication for this style of extension is the undulating 6 km/s isoline (see e.g. figure 4.14 and A.1). This isoline indicates an existence of a block structure marked by normal faults along the profile, which are characteristics of an extensional crust. Faults are also seen in the MCS data interpreted by *Booth-Rea et al.* (2007) (figure 6.4 and explanation to it on page 71).

Also the interpretation of the 6 km/s isoline beneath the Maimonid Ridge caused by intrusions support the slab rollback theory. Sampled volcanic outcrops of the Alboran Sea analysed by *Duggen et al.* (2004, 2008) refer to a volcanic front and rear-arc lavas.

Duggen et al. (2004) analysed the Alboran region with geochemical methods. Occuring magmatism is associated to subduction of oceanic lithosphere and slab rollback. Lithospheric delamination can not be the source for the geochemistry of the analysed igneous

rocks. Volcanic activity and the transition from tholeiitic and calc-alkaline to shoshonitic and lamproitic volcanism is the result of westward slab rollback (*Duggen et al.*, 2004). The tholeiitic and calc-alkaline volcanism is referred by *Duggen et al.* (2004) to occurrence in a back-arc setting. Their resulting analysis of the igneous rocks and the age dating of those showed an end of slab rollback because no subduction related volcanism is seen in their data after Messinian (*Duggen et al.*, 2003, 2004).

Duggen et al. (2008) analysed the rock samples and separated the Alboran region in zones of different styles of lava. This zonation resulted in a North-South symmetry and an East-West asymmetry of the studied region. The styles of the igneous rocks in the different zones and the zonation itself support the slab rollback theory as formation history of the Alboran Basin.

Comparing the results of this study to other regions in the world, the very low upper mantle velocities are supported by studies of *Takahashi et al.* (2007, 2008) and *Contreras-Reyes et al.* (2011). In the Izu-Bonin-Mariana Arc region and Tonga, the arc-back-arc system is accompanied by slow upper mantle velocities.

Takahashi et al. (2007) and *Takahashi et al.* (2008) analysed seismic refraction data in region of the Mariana arc-back-arc system. A first analysis of the velocity in the Mariana arc-back-arc system shows slow velocities in the lower crust (≤ 7.3 km/s) and in the upper mantle (~ 7.7 km/s) for the arc (*Takahashi et al.*, 2007). Especially the upper mantle velocity is significantly lower than the global average of 8.1 km/s. In the back-arc basin, the Mariana Trough, the velocity structure differs to that of the Mariana Arc. Crustal velocities are up to 7.4 km/s fast. This crust is in thickness and velocity structure indistinguishable to oceanic crust. The upper mantle beneath the Mariana Trough has velocities of ~ 7.9 km/s (*Takahashi et al.*, 2008). Those mantle velocities are still low compared to the global average.

In the Tonga Arc, the by *Contreras-Reyes et al.* (2011) analysed wide-angle data show slow upper mantle velocities. The upper mantle velocities of 7.5 km/s beneath the arc are significantly lower than the average (~ 8.1 km/s). *Contreras-Reyes et al.* (2011) refer those slow velocities to hydration or magmatic underplating.

A comparison to arc-back-arc systems shows, that slow velocities in the upper mantle are present in these systems. The velocities modeled in this study are also low compared to those arc-back-arc regions. In the upper mantle, consistently lower velocities are present. The westernmost two segments of the analysed seismic refraction profile have with ~ 7.0 km/s an extremely slow upper mantle. This is comparable to extrem slow velocities found by *Contreras-Reyes et al.* (2011) in the Tonga Arc. But also the not so extremely slow velocities in the Mariana Arc are comparable to the in this study found seismic upper mantle velocities. The upper mantle velocities of ~ 7.6 km/s in the easternmost part of the analysed profile are comparable to the slower upper mantle velocities in the back-arc basin in the Mariana Arc and Tonga Arc. The crustal structure in back-arc regions are like typical oceanic crust. This is similar to the easternmost part of the in this study analysed seismic profile.

The comparison to the Izu-Bonin-Mariana Arc and the Tonga Arc shows similarities of

the analysed seismic data to the seismic velocity structure of arc-back-arc systems and supports the interpretation of the Alboran Sea as a back-arc basin formed by slab rollback.

The results of this study support the slab rollback theory as formation theory of the Alboran Sea. Those results are one more piece of the puzzle in the Alboran Sea to explain the formation history of the region. When the blocks which nowadays are the Betic and Rif blocks, thrust onto Iberia and Africa respectively, broke away from the European continent, back-arc extension began with the opening of the Gulf of Lion (*Rosenbaum et al., 2002*). Slab rollback continued during Miocene (*Rosenbaum et al., 2002*) and started to open the Alboran Sea. The slab nowadays must lie further in the West of the location of the seismic profile.

Chapter 7

Seismicity

Additionally to the seismic refraction data, seismological data were analysed in this study. In this chapter, the seismological data are discussed. Therefore stations which recorded earthquakes for a longtime period were deployed in the Alboran Sea while the cruise POS389 of the german research vessel FS Poseidon and recovered while cruise POS393 to gain an analysable dataset for a seismological analysis.

7.1 Recorded Earthquakes in the Alboran Region

TOPO-EUROPE is a project for the understanding of the european continent and is divided into several subprojects. One of these subprojects is TOPO-MED which has the goal to investigate the crustal structure and the mantle below the Gibraltar Arc and the Alboran region. Data of the Alboran region were recorded between August 2009 and January 2010. During this time 30 OBS were deployed in the western part of the Alboran Sea. For additional information landstations in Morocco and on the Iberian Peninsula were used for the location of the hypocenters of the recorded earthquakes. Altogether 155 stations were available.

The arrivals of the primary wave (P-wave) of an earthquake and the secondary waves (S-wave) were picked on stations where this information was provided (section 3.2.4). During the studied time 229 earthquakes with available P- and/or S-waves were detected. The picking of the arrivals were done with the SEISAN software package (section 2.2.1). These earthquakes had in general a low magnitude ($M_W \leq 3$).

The determination of a minimum 1D velocity model was done with the VELEST software (section 2.2.2). Due to reliability different criteria must be fulfilled by each recognised earthquakes. The criteria are

- minimum depth of 2 km
- recording on minimum 6 stations
- GAP between 0° and 180° .

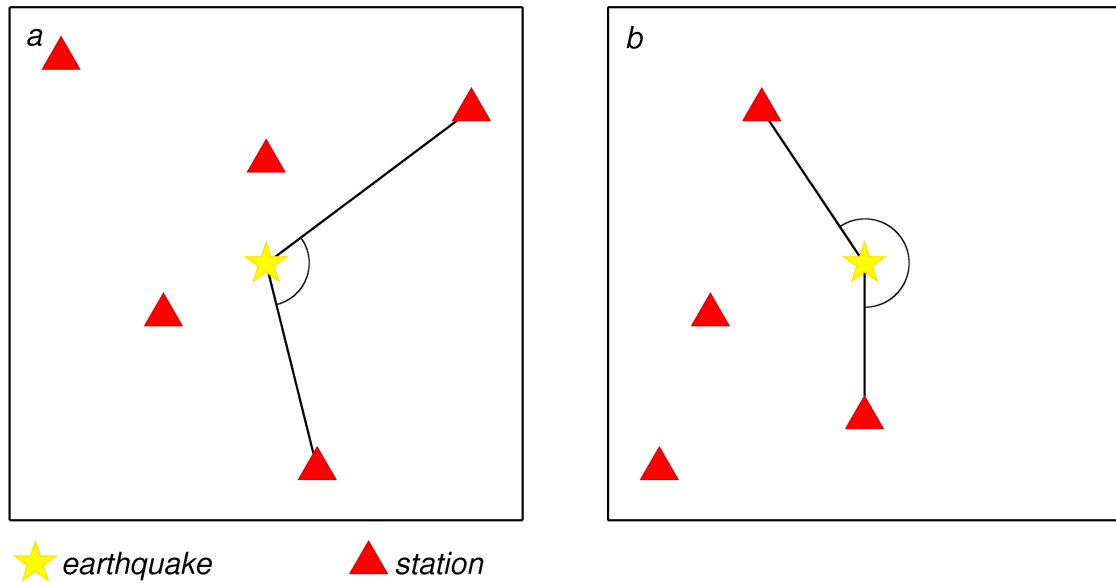


Figure 7.1: Sketch to illustrate the GAP value. The yellow stars are the hypocenters of an earthquake and the red triangles are stations which recorded this earthquake. In (a) a GAP value of about 110° is displayed. (b) shows a value of 210° where information from just one side of the hypocenter is provided for the location of the earthquake and the minimum 1D velocity model.

A minimum depth of the pre-located (in SEISAN located) earthquakes is chosen to remove earthquakes which are located as too shallow. This could be due to inaccurate picking of phases or just too few stations with recordings for a better location. A recording on minimum 6 stations with picked phases is required to develop a qualitative minimum 1D velocity model. The GAP describes the maximal azimuthal gap in degree between two neighbouring recording stations (sketch in figure 7.1). Is the GAP value too high (figure 7.1(b)), information from just one side of the hypocenter is provided for further data processing. This can result in a wrong location of the hypocenters and therewith an error in the minimum 1D velocity model. In figure 7.1(a) the GAP is smaller than 180° . Data for the hypocenter is provided from all sides of the earthquake.

The earthquakes which fulfill the minimum criteria are used for the next step to model an average velocity profile for the area. This is the minimum 1D model.

7.2 Minimum 1D Model

A minimum 1D model is computed with the VELEST software package (section 2.2.2). It describes an average velocity model of the researched area. The Alboran Sea is a relatively narrow area which is about 170 km wide in its north-south direction. The norther part continues into the Betic mountains on the Iberian peninsula and in the southern direction are the Rif mountains. All these geologically very different areas are included in the earthquake data because stations which recorded the earthquake are located in the whole region (figure 7.2).

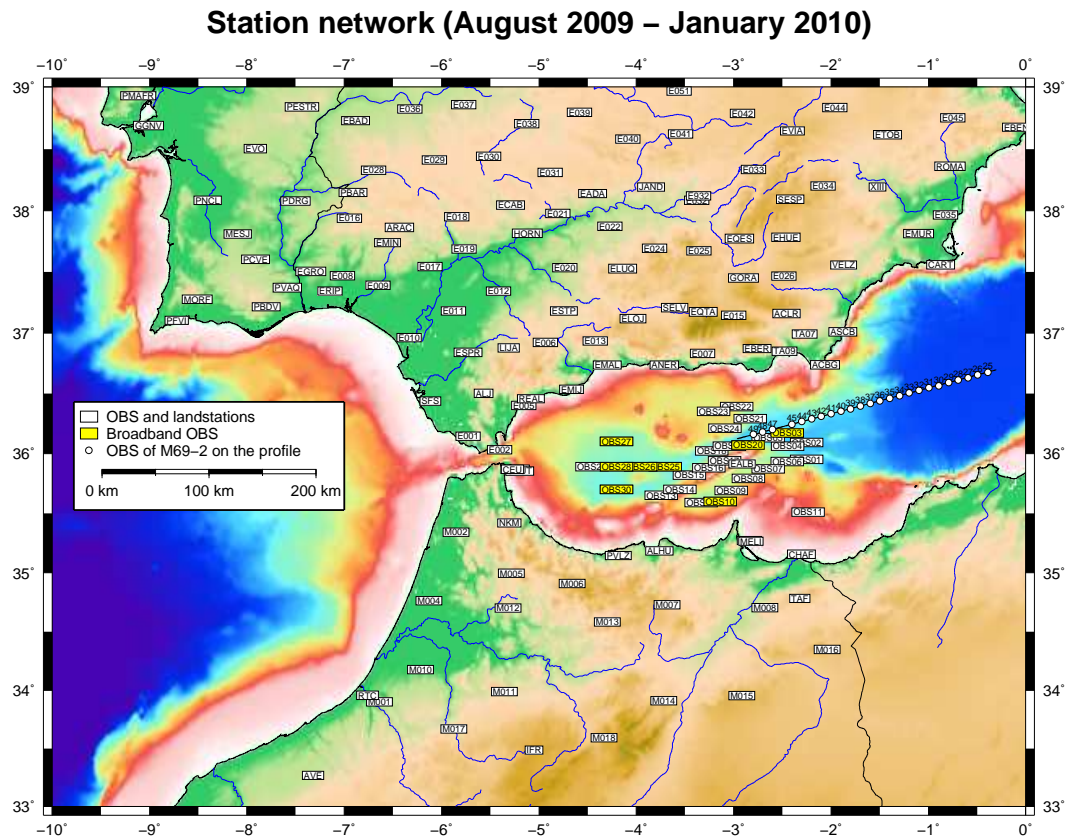


Figure 7.2: Network of the TOPO-MED project (rectangles) and stations of the refraction wide-angle profile 2 of M69-2 (circles).

The hypocenters of the earthquakes which are used to derive the minimum 1D model are almost all located in the Alboran Sea. This is the matter because it is the center of the network. The requirement of the GAP and the minimum number of recording stations excludes most of the non local (regional and distant) earthquakes which lie outside the Alboran Sea. Local earthquakes from outside the Alboran Sea are mostly not recorded by the OBS and thus not part of the used dataset selected with a trigger algorithm (see section 3.2.3).

Initially the velocity profile from the westernmost part of the refraction analysis (chapter 6) is chosen for the upper part of the model, the crust. The lower part of the model is completed with the lower part of a velocity profile for the Alboran region from *Stich et al.* (2003a). This model is in this study named “Alboran model”. For the modeling OBS 9 was chosen as the reference station. This is due to the fact that it is located close to the center of the network and is a reliable station with clear recordings. There was no station in the center region of the network which is not close to a lithological structure. Stations on land are influenced by the mountains and are far away from the network center. OBS in the westernmost Alboran Sea are seated ontop a thick sedimentary layer (*Comas et al.*, 1992,

1999). The eastern part of the network is close to the Alboran Ridge and other structures (see figure 1.5). The vicinity of the reference station to lithological changes will influence the results and the error estimation but in this study it is not possible to get around this problem. The reference station is chosen to calculate station corrections relative to it, which is part of the minimum 1D model calculation. Station correction compensates differences in elevation and subsurface geology.

Station elevation is neglected in this study. Differences in elevation are up to 3.6 km. The highest situated station lies in 1690 m (EBER) and the deepest one is OBS 2 at 1876 m depth. Not to use the station elevation is due to the fact that the number of earthquakes is relatively low and for this reason the model resolution will not be the best. The differences in elevation are then compensated with the station correction additional to the subsurface geology.

The “Alboran model” shows a finer layering in the upper part and a very rough differentiation of velocity layers in the lower part of the model. The resulting minimum 1D velocity model is compared to other different starting models. *Stich et al.* (2003a) presented in their publication three different velocity models. Each of their models is constructed for a tectonic setting in the Betic-, Rif- and Alboran-region. In this study the models are named Stich-A, Stich-B and Stich-C. Stich-A describes the western Mediterranean and particularly the Alboran Sea and is generally meant for the offshore regions. The mountains of the Iberian and Maghreb region are part of the Stich-B model. Hercynian (late Palaeozoic) basement and Mesozoic platforms are described with the Stich-C model. All three models of *Stich et al.* (2003a) have a relatively coarse velocity profile with a maximum of six layers in the profile. Most of these layers are in the upper 25 km of each model.

Additional to the so far mentioned models other models are tested and compared among each other.

7.2.1 Minimum 1D P-Velocity Model

The first step of the modeling is done just with picked P-phases. This results in a minimum 1D P-velocity model. The selection of earthquakes which is done with the in section 7.1 mentioned criteria results in 40 to 80 analysable earthquakes from the 229 picked earthquakes, depending on the starting model. This small number of analysable earthquakes is the result of many earthquakes with just few readings or earthquakes which originate at the edge of the research area.

The ray coverage and depth distribution of selected events for one starting model is shown in figure 7.3. Most events lie in the eastern part of the research area of the Alboran Sea (2.5°W - 3.5°W) in a depth of 5 to 20 km. Just few of the analysable events are deeper than 25 km and few epicenters are lying outside of the Alboran Sea. The fact that only a hand full of earthquakes occur outside of the Alboran Sea depends on the selection criteria of earthquakes which had to be picked. All the earthquakes are selected with an algorithm (section 3.2.3) which was for this study applied to the OBS data. The OBS mostly recognized just the earthquakes of the Alboran region and not further landward events.

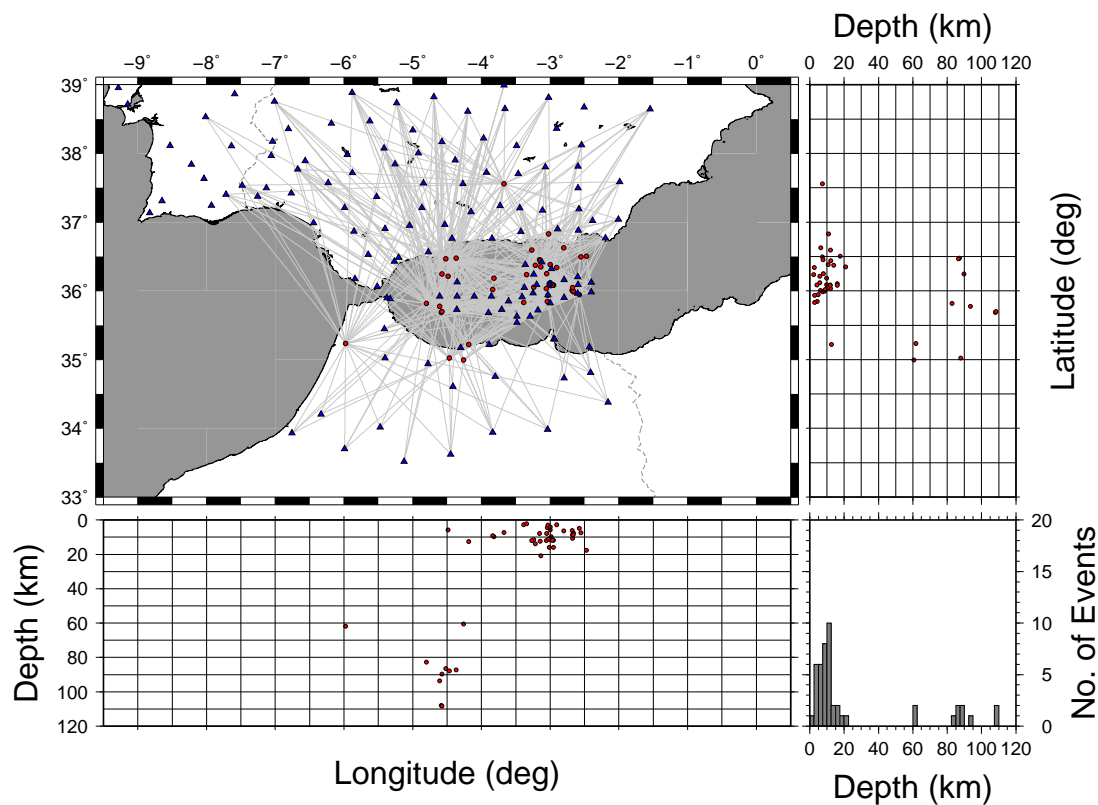


Figure 7.3: Example for selected earthquakes of a velocity model with the criteria enumerated in section 7.1. Blue triangles show the stations and red circles the events. Light grey lines illustrate the ray coverage by connecting each event with the stations that recorded this event. Right is a depth distribution of the earthquakes projected along a N-S oriented line. In the lower plot a projection of earthquakes along an E-W oriented line is shown. The histogram in the lower right corner shows the number of earthquakes for depth intervals of 2.5 km.

Tested velocity models are displayed in figure 7.4. Most velocity models have depth steps around 3.5, 12.5, 20 and 120 km. Very different models are tested to analyse the behaviour of the velocity models in the VELEST routines. Some are quite far away from a possible solution and the reality with very slow or very fast velocities.

The first tested model, the Alboran model, has a slow upper part which is the sedimentary layer of the refraction analysis with just 2.5 km/s. A steep velocity gradient for the upper crust and a slight gradient in the lower crust result in a mantle velocity of 8 km/s in the starting model. Through the modeling, the upper part did not change very much. The two depth intervals between 7 and 25 km result in one thicker layer with a velocity of 6.7 km/s, which is the average of the starting velocity of both layers, and the mantle velocity slightly increases to 8.05 km/s. The RMS error for the Alboran model has a value of 0.403979 s. This relatively high value has its origin in the complexity of the region the starting model is ment for. The Alboran model is derived from the westernmost part of the refraction profile. However, the minimum 1D model is an average for the whole Alboran region and the surrounding land region. The Alboran Sea differs in its structure from

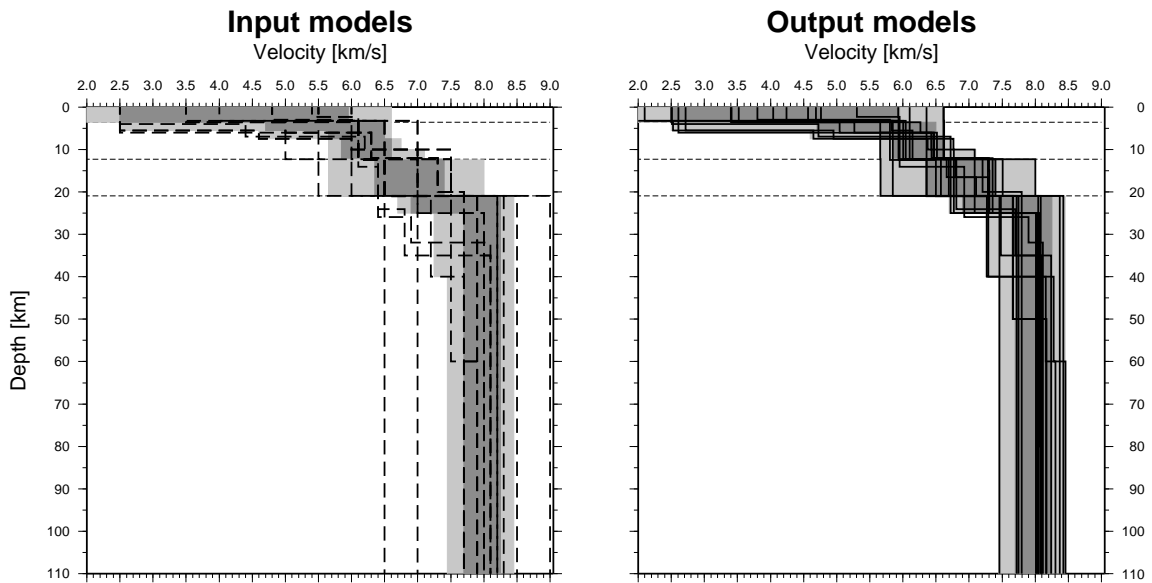


Figure 7.4: Tested starting velocity models (left) and their results (right). Light grey shaded is the range of resulting velocities (except some transition zones where the depth step is different to the most other models). Dark grey shows the velocity range where more than 75 % of the resulting velocity models are included.

the West to the East. The easternmost part of the seismic studied area is described by the western end of the refraction analysis, which is the upper part of the starting Alboran model but differs from the West Alboran Sea. And especially the Betic and Rif mountains have a very different subsurface compared to the Alboran region. The Alboran model is therefore too far away from the most reasonable minimum 1D P-velocity model for the whole studied region.

The test with the first starting model results is a trial and error approach with many different models. The upper layer of each model (2.5 to 5.5 km thick) is not well defined by the existing earthquake data. An insufficient number of earthquakes originate in this layer to identify a narrow band of possible velocities. The resulting velocity models include velocities from lower than 2 km/s up to 6.6 km/s. The layer is quite thin in comparison to the depth range of the model. Most rays pass this layer vertically because the hypocenter is located much deeper and the fastest way through the upper layer to the recording station is the vertical path. Hence, the thinness of the layer and therewith the velocity in this layer has not so much influence on velocities in deeper layers. This results in a not definable upper layer velocity which can be fixed with the damping values in SEISAN to a probable velocity for further modeling of the minimum 1D velocity model. This value is set to an average value of the tested models. A sedimentary velocity of 2.5 km/s is too low for a 1D velocity model of the Alboran-Betic-Rif region and the fastest modeled velocity of 6.6 km/s is too high. The velocity of this layer is set to 4.25 km/s, which is the resulting velocity of an inversion with the Stich-A model and it is close to the average of all modelings.

The next layer reach down to a depth of ~12 km, depending on the starting model. After

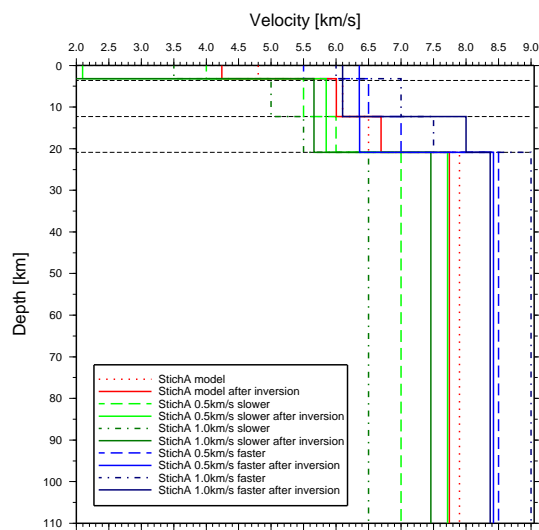


Figure 7.5: Results of the inversion with extremely slow and fast starting models. More information see text.

inversion of different models, velocities between 5.6 and 6.6 km/s are the result. More than 75 % of the models lie in the range of 5.85 to 6.5 km/s. Until the depth of ~ 20 km the solutions are scattered between 5.6 and 8 km/s where more than 75 % lies between 6.35 - 7.4 km/s. Between ~ 20 and 120 km more than 75 % of the models have velocities between 7.7 and 8.25 km/s. The velocity profiles are displayed in figure 7.4, where the light grey area marks all models and dark grey defines the array where more than 75 % of the modeled velocity profiles are within this range.

The Stich-B and Stich-C models result in comparison to other tested velocity profiles in models with a higher RMS error. Stich-B gains a RMS error of 0.437485 s, similar to the RMS error of Stich-C with 0.431798 s. Both velocity profiles were ment for on land with geologically uniform regions (*Stich et al., 2003a*). These profiles do not show a close approximation to a minimum 1D P-velocity model for the researched region.

The Stich-A model results in a lower RMS error of 0.398120 s. The model is ment for the region of the Alboran Sea and includes onshore parts of the lithosphere. The error still is not very good, which would be an RMS error of 0.15 s, but one of the best gained results. This is due to the regional very different lithosphere below the Alboran-Betic-Rif region. Offshore is combined with different onshore structures into one model. Additionally to these sturctural differences, just few analysable earthquakes suffice the minimum criteria (see page 77) for further calculation of the minimum 1D P-velocity model.

The result of the P-velocity modeling with the Stich-A model is compared to extrem models with very low or very high velocities (figure 7.5). Therefore values of 0.5 and 1 km/s are added or subtracted to or from the Stich-A model and inverted. The results show in most cases a convergence to the inversion result of the Stich-A inversion.

The upper layer between 0 and 3.2 km is very inconsistent and does not show a convergence to one velocity. This behaviour is discussed before and was expected. Between 3.2 and 12.3 km the velocities converge to the velocities of the Stich-A inversion of 6 km/s:

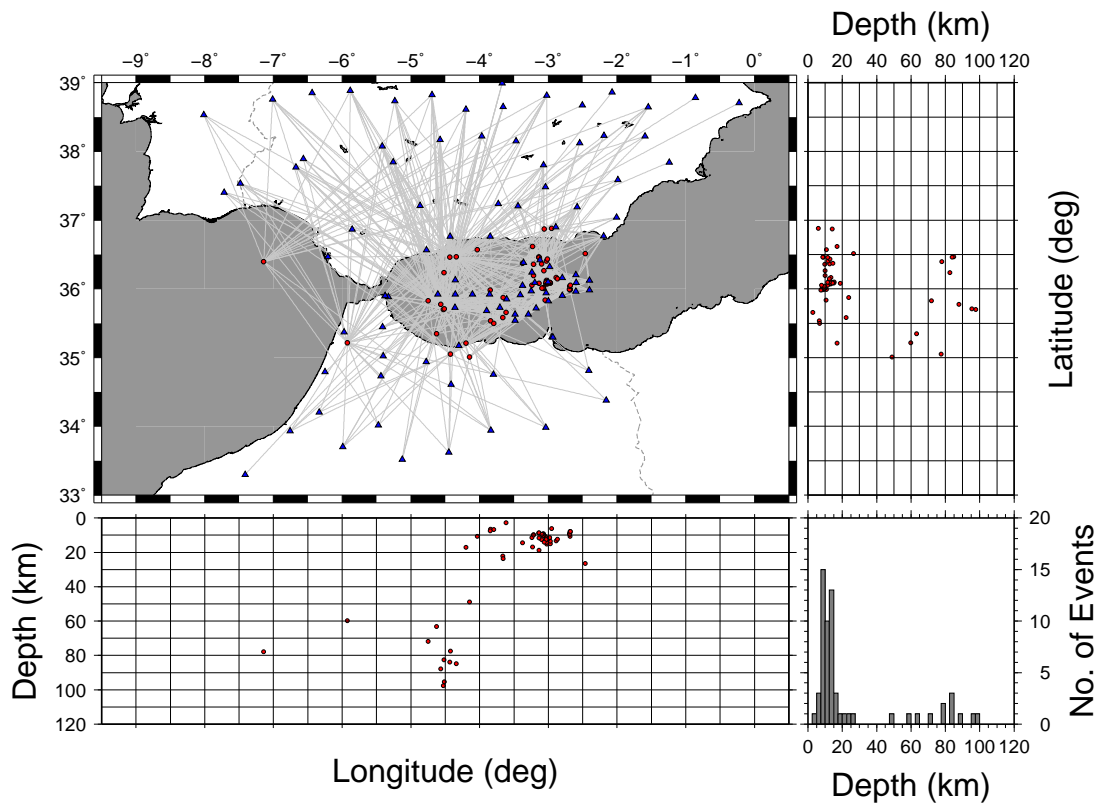


Figure 7.6: The resulting ray coverage for the final minimum 1D P-velocity model with 61 analysed events. Subfigures and symbols are explained in figure 7.3.

the faster velocities in the starting model compared to Stich-A get slower and the slower models increase the speed through the inversion. One layer deeper, 12.3 to 20.9 km depth, the inversion of the slower models tend to form one layer with the overlying layer. The faster models behave in different ways: the slower version forms also one layer with the layer above, but the faster version increases the speed through the inversion to compensate the lower velocities in the over- and underlying layer. Between 20.9 and 120 km the results of the inversion converge to the Stich-A inversion with a value of 7.75 km/s.

The test with extreme velocity profiles as the starting models shows a convergence to a velocity profile which is similar to the result of the Stich-A inversion. This test and the different tested starting models result in a kind of frame of possible solutions for the minimum 1D P-velocity profile which is displayed in figure 7.4. Light grey surrounds the range of modeled velocities and dark grey defines the more than 75 % boundary for reasonable and possible P-velocity profiles.

The resulting ray coverage of the final minimum 1D P-velocity model is displayed in figure 7.6. The ray coverage shows a best resolution in the central Alboran Sea. Most epicenters originate in the eastern Alboran Sea in a depth above 30 km, mainly up to a depth of ~15 km. In the central western Alboran Sea, the hypocenters are mainly located between 50 and 100 km depth. The number of recorded earthquakes is higher in the eastern part of the Alboran Sea. In the West and therewith in a higher depth, there are just

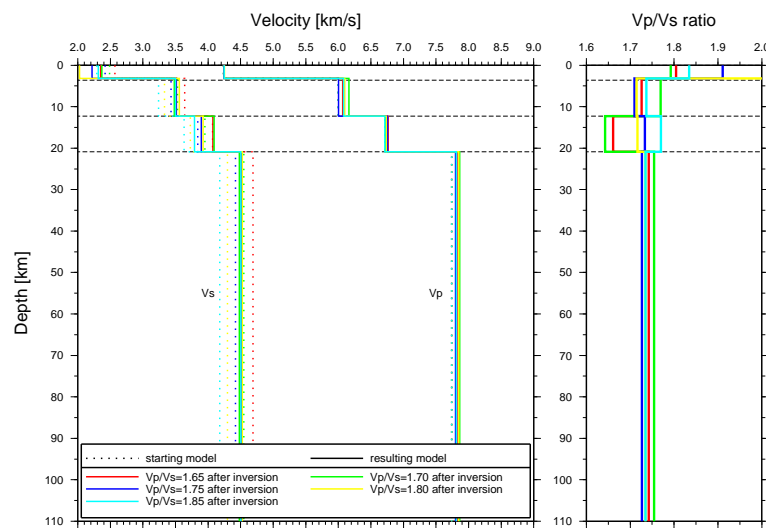


Figure 7.7: Resulting velocity profiles with different starting v_p/v_s -ratios.

few events which satisfy the requirements of analysable earthquakes which are listed in section 7.1.

7.2.2 Inversion with P- and S-Phases

After the minimum 1D P-velocity model is calculated, the S-arrivals are included into the inversion. The SEISAN package includes a calculation of the v_p/v_s -ratio. The average value of the v_p/v_s -ratio for 146 earthquakes with P- and S-arrivals is 1.70. For the minimum 1D P-velocity profile different values of the v_p/v_s -ratio is included into the model and compared among each other. Values between 1.60 and 1.85 in steps of 0.05 are used (figure 7.7).

With the defined P-velocity model and the v_p/v_s -ratio the S-velocities are calculated by including the v_p/v_s -ratio into the velocity model. During the inversion the P-velocities are overdamped to fix them to the calculated values of the minimum 1D P-velocity model. The S-velocities are not damped to adjust the S-velocities to a low RMS error of the whole model (P- and S-velocities). The uppermost layer (0 - 3.2 km) is damped with a low damping value because of the same reason in the inversion of the P-velocities: there are too few earthquakes in this layer to result through the inversion in a narrow band of reasonable velocities. The influence to deeper layers is little. The resulting S-velocities of the upper thin layer with the slight damping are 2 - 2.4 km/s, which is a slight reduction of the starting velocities during the inversion. The second layer (3.2 - 12.3 km) shows very similar results of all five models. The S-velocities in this layer are around 3.5 km/s. Between 12.3 and 20.9 km the inversions of the models with the different v_p/v_s -ratios result in slightly different values between 3.75 and 4.1 km/s. But the deepest and thickest layer of the model (20.9 to 120 km) shows a behaviour like the second layer: all models result in a S-velocity close to 4.5 km/s.

The resulting v_p/v_s -ratios of the different starting models are in most parts of the models

very similar. In the depth between 3.2 and 12.3 km, the v_p/v_s -ratio is 1.7 to 1.74. Just one model has a higher value of 1.77, which is compensated in the layer below with a very low value of 1.64. This layer has for all models very different v_p/v_s -ratios between 1.64 and 1.77. The thick layer from 20.9 to 120 km has very similar v_p/v_s -ratios between 1.72 to 1.76 for all different starting models.

7.2.3 Final Minimum 1D Velocity Model

The final minimum 1D velocity profile is listed in table 7.1. During the inversion the RMS error of P- and S-arrivals is calculated and gains in the final model a value of 0.444063 s. This high error is the result of an attempt to form one 1D velocity profile for geologically very different regions. Although the center of the region is the Alboran Sea and the dataset only contains earthquakes which are at least recorded by three stations in the Alboran Sea (requirement in the trigger algorithm, section 3.2.3), the impact of the crust and mantle below the southernmost Iberian Peninsula and northern Morocco is high. Stations on Iberia and in Morocco give additional information for the localization of earthquakes. Without onshore stations, the evaluable dataset would be too small to invert a velocity profile and result in a reasonable model for the geology of the Alboran region.

Depth [km]	v_p [km/s]	v_s [km/s]	v_p/v_s -ratio
0	4.25	2.37	1.79
3.2	6.16	3.48	1.77
12.3	6.72	4.09	1.64
20.9	7.86	4.48	1.75
120	8.20	4.82	1.70

Table 7.1: The final minimum 1D velocity profile showing the result of the inversion with a starting v_p/v_s -ratio of 1.70.

After inversion for the final minimum 1D velocity model, a v_p/v_s -ratio is calculated (table 7.1). The resulting v_p/v_s -ratio is mainly lying for the different layers between 1.7 and 1.8. This indicates that no large-scale serpentinization is present in the Alboran region. For a high grade of serpentinization a higher v_p/v_s -ratio as determined in this study would be needed.

With the resulting velocity profil (table 7.1), station corrections are calculated for all stations which recorded the analysed earthquakes. In figure 7.8, station corrections are shown on a map. Compared to the reference station (OBS 09, south of the Alboran Ridge), a negative station correction is calculated for the stations in the Alboran Sea East of the reference station. In the central part of the Alboran Sea, station corrections are relatively low. The westernmost stations show a positive station correction. These differences are the result of different subsurface structures. In the West, a thicker sedimentary cover is present (up to 7 km thick) compared to the Eastern Alboran Sea with just a thin sedimentary layer (e.g. *Comas et al.*, 1992, 1999; *Polyak et al.*, 1996), which makes it necessary

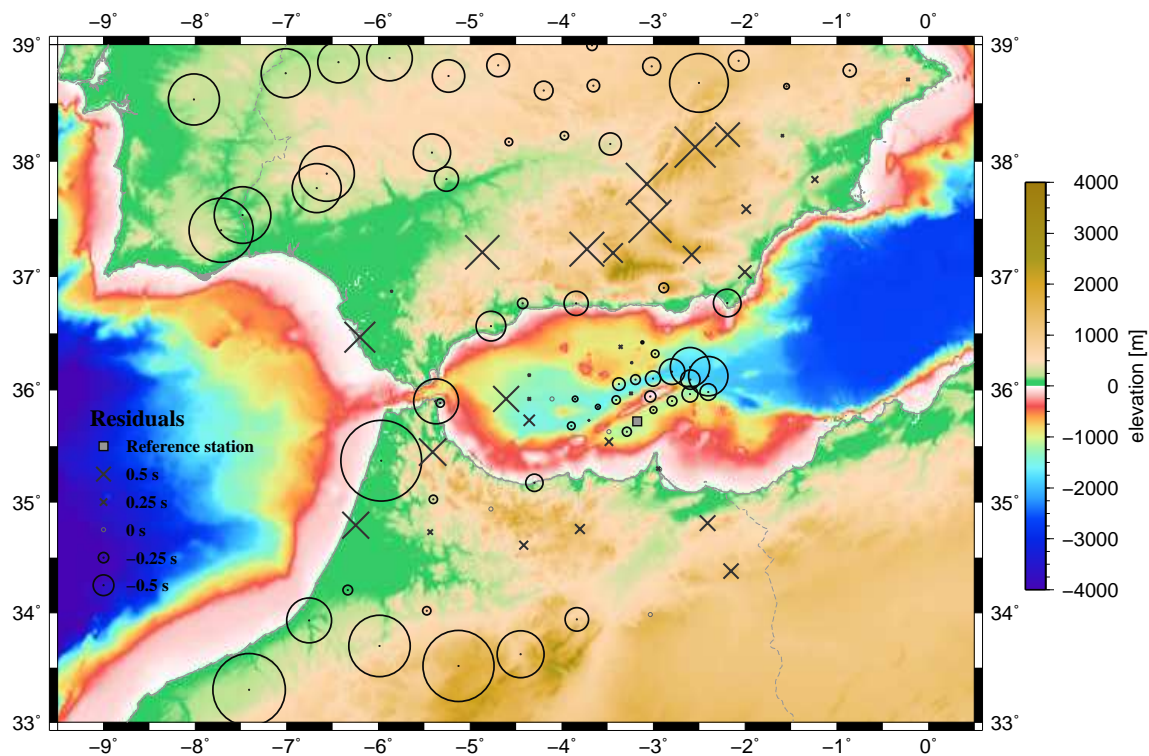


Figure 7.8: A regional map with the station correction for all used stations for the calculation of the minimum 1D velocity profile is shown. The reference station is marked as a grey square (OBS 09). Stations with crosses have a positive station correction compared to the reference station. Circles denote negative station corrections. The size of the symbols describe the magnitude of station correction.

to result in different algebraic signs for the station corrections when the reference station lies between these two regions. Land stations are influenced by the different crustal structure compared to station in the Alboan Sea and by the elevation of the station. In the Betic mountain chain, station corrections are positive. The higher the station elevation, the higher the station correction. North of the Betics, stations in the Sierra Morena result in negative station corrections. On the African continent stations in the Rif mountain chain have low values for station correction. In the Middle Atlas, negative station correction are needed to correct the different elevation and crustal structure compared to the reference station in the Alboran Sea.

In figure 7.9, a graph is shown with a comparison of station elevation and station correction. A correlation between station elevation and correction is identifiable. The higher the station on a continent is, the higher the resulting station correction is for the calculated velocity profile and further earthquake location. The northern- and southernmost stations (in figure 7.9 the last stations in the right and first stations in the left, respectively) do not show a correlation as good as for station which lie in the Betic or Rif mountain chain or the Alboran Sea. Those are stations in the Sierra Morena and Middle Atlas which are far away from the center of the network and the located earthquakes. But the trend cor-

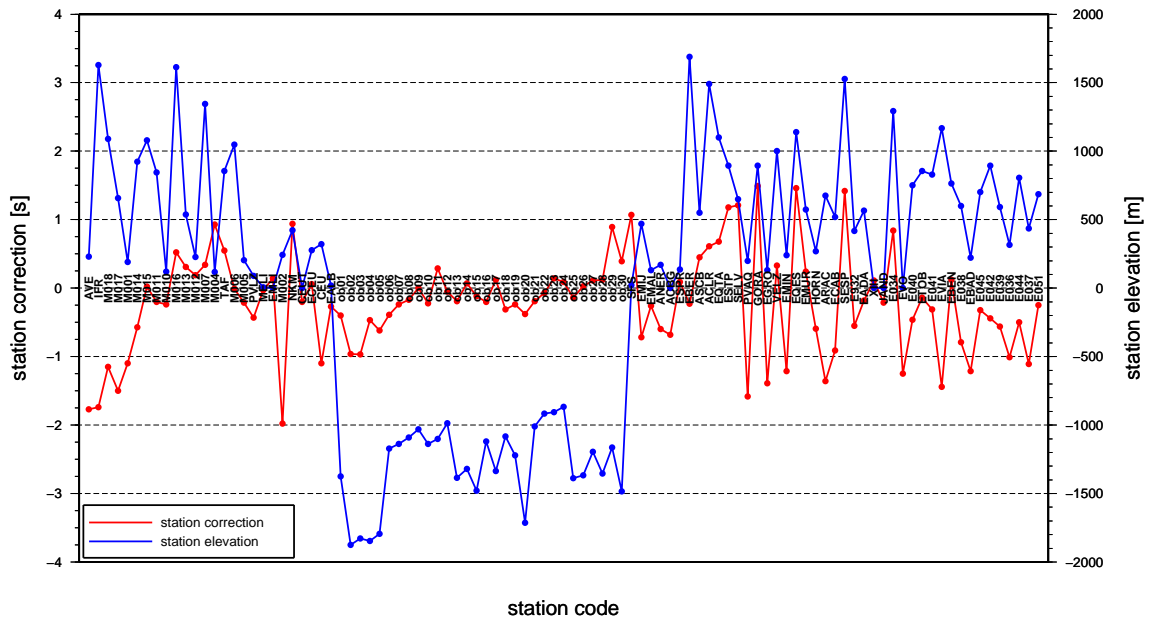


Figure 7.9: Station correction (red line) of all used recording stations are plotted for comparison together with the station elevation (blue line) in a graph. Landstations are sorted from South to North (left to right).

relates: the higher the station in these two regions, the higher is the station correction compared to another station correction of a station which is also located in this region. The ray coverage of all recorded and localized earthquakes of the whole dataset where the hypocenter is located below 2 km depth is presented in figure 7.10. Additionally to the events which are used for the determination of the minimum 1D velocity model, the earthquakes which did not satisfy the criteria for the modeling of a minimum 1D velocity profile are shown. Station corrections are used for this final earthquake location to correct the existing differences in elevation and subsurface structure. Comparing figure 7.10 to figure 7.6, also earthquakes with a GAP (see figure 7.1) higher than 180° are included. The location of all earthquakes is done with the final minimum 1D velocity model. The ray coverage in the Alboran Sea, on the southern Iberian Peninsula and in northern Morocco is improved. Many epicenters with a GAP higher than 180° are located in northern Morocco and offshore Morocco close to the coast in a depth range from near the surface up to a depth of ~ 50 km. These earthquakes are in a depth interval where just few information was available for the modeling.

7.3 Results of the Seismological Analysis

The final minimum 1D velocity model for the Alboran region including the Alboran Sea surrounding continental parts (South Iberia and North Morocco) show after location a distinct distribution of the hypocenters for the analysed earthquakes (figure 7.10). The depth distribution of all located earthquakes can be separated in deep earthquakes (in

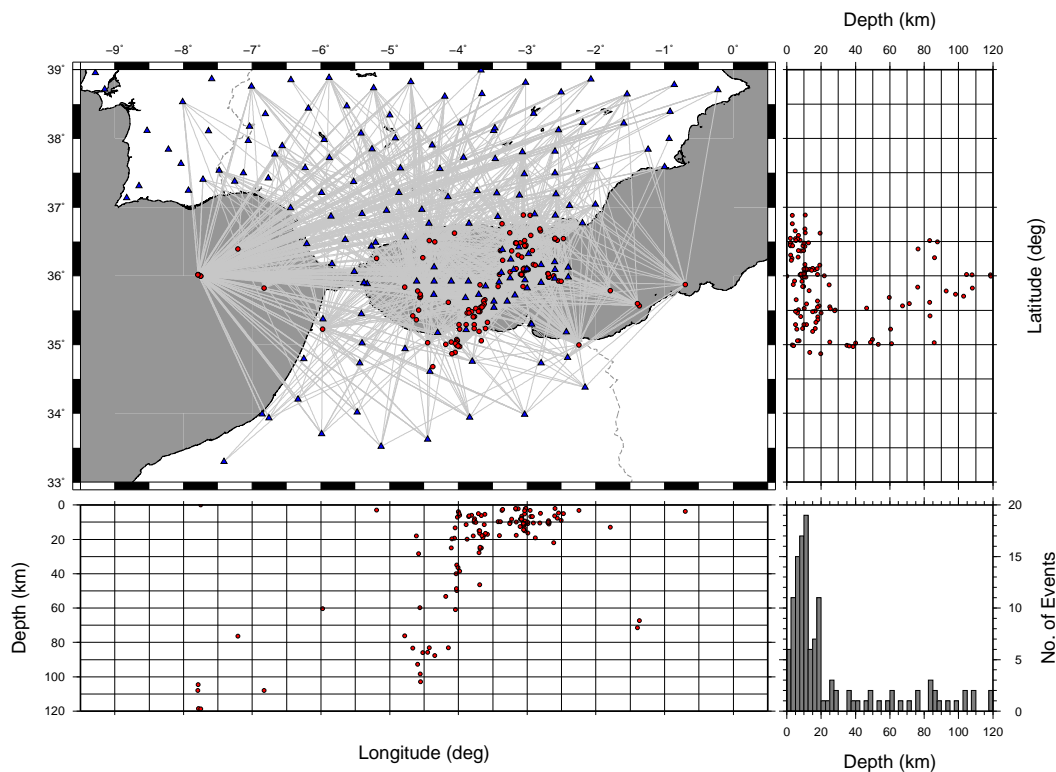


Figure 7.10: The ray coverage of all earthquakes in the dataset with a hypocenter deeper than 2 km. Subfigures and symbols are explained in figure 7.3.

this study ~70 to 120 km deep) and shallow ones (up to ~30 km depth). Between 30 and 70 km there are some earthquakes located in this intermediate depth.

Figure 7.10 shows in the subfigure at the right a depth distribution of the hypocenters projected along a North-South profile. A distinct distribution, where the deeper and the shallower earthquakes are occurring is not distinguishable. Contrary to this, along the West-East profile, the projected earthquake hypocenters (figure 7.10 lower subfigure) can be divided into regions with earthquake hypocenters in different depth positions. Most of the shallow earthquakes (up to 30 km depth) are located in the East Alboran Basin (EAB) and in the South Alboran Basin (SAB) and in the East of the West Alboran Basin (WAB). Earthquakes within the intermediate depth (30 to 70 km) are rare and occur in the SAB and onshore Morocco. The deepest earthquakes located in this study (70 to 120 km) are released in the WAB and in northern Morocco.

Polyak et al. (1996) analysed the heat flow in the Alboran Sea. Their result is shown in figure 7.11. There exist obvious differences of heat flow between the WAB and EAB/SAB. In the WAB, heat flow increases from West to East. Over this region, an average heat flow of 69 ± 6 mW/m² was measured. In contrast to this, heat flow in the EAB and SAB was measured nearly twice as high as in the WAB with an average value of 124 ± 8 mW/m². In this region, the heat flow is nearly constant with just some local anomalies.

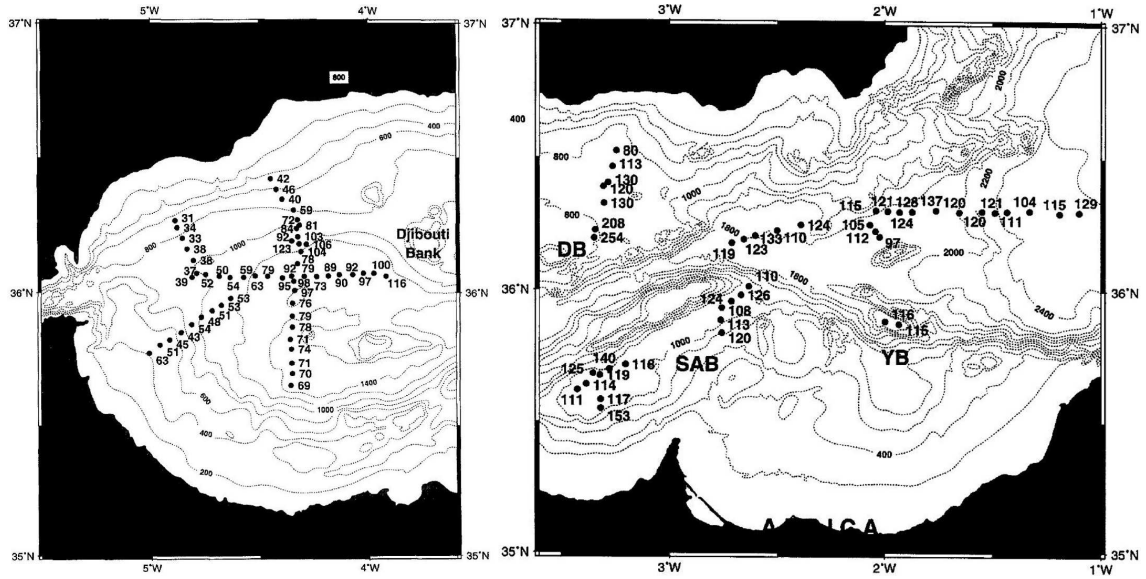


Figure 7.11: Heat flow measurements analysed by Polyak *et al.* (1996) in mW/m^2 . Left: West Alboran Basin, right: East and South Alboran Basin. Isolines of the bathymetry are in an interval of 200 m. DB = Djibouti Bank, SAB = South Alboran Basin, YB = Yusuf Basin.

Comparing the resulting pattern of heat flow measurements of Polyak *et al.* (1996) to the hypocenter distribution in this region, a correlation is visible. In the WAB, where heat flow values are low, deeper earthquakes are detected during the recording time of the network. Only where low heat flow values were measured by Polyak *et al.* (1996), deeper earthquakes were located. Contrary to this, in the EAB and SAB where high heat flow was measured most shallow earthquakes and some earthquakes in an intermediate depth are located.

Doser and Kanamori (1986) compared heat flow measurements to hypocenter depths for the Imperial Valley and Peninsular Ranges (USA). They also found a correlation between both values. Shallower earthquakes appear in the Imperial Valley compared to those in the Peninsular Ranges where concomitant the heat flow is nearly twice as high in the Imperial Valley as in the Peninsular Ranges. The lowest heat flow was measured where the hypocenters are deepest.

Taking the heat flow measurements of Polyak *et al.* (1996), an estimation of maximum depth for occurrence of earthquakes can be made. A simple estimation for conductive heat flow is computed. With the formular for calculation of simple geotherms

$$T(z) = -\frac{A}{2k}z^2 + \frac{Q_0}{k}z + T_0, \quad (7.1)$$

the maximum depth for earthquakes can be calculated after reorganization of equation 7.1:

$$z = \frac{Q_0}{A} \pm \sqrt{\frac{Q_0^2}{A^2} - 2\frac{kdT}{A}}. \quad (7.2)$$

Q_0 is the surface heat flow measured by Polyak *et al.* (1996), A the heat production, k the thermal conductivity and $dT = T(z) - T_0$ the temperature difference between the seafloor

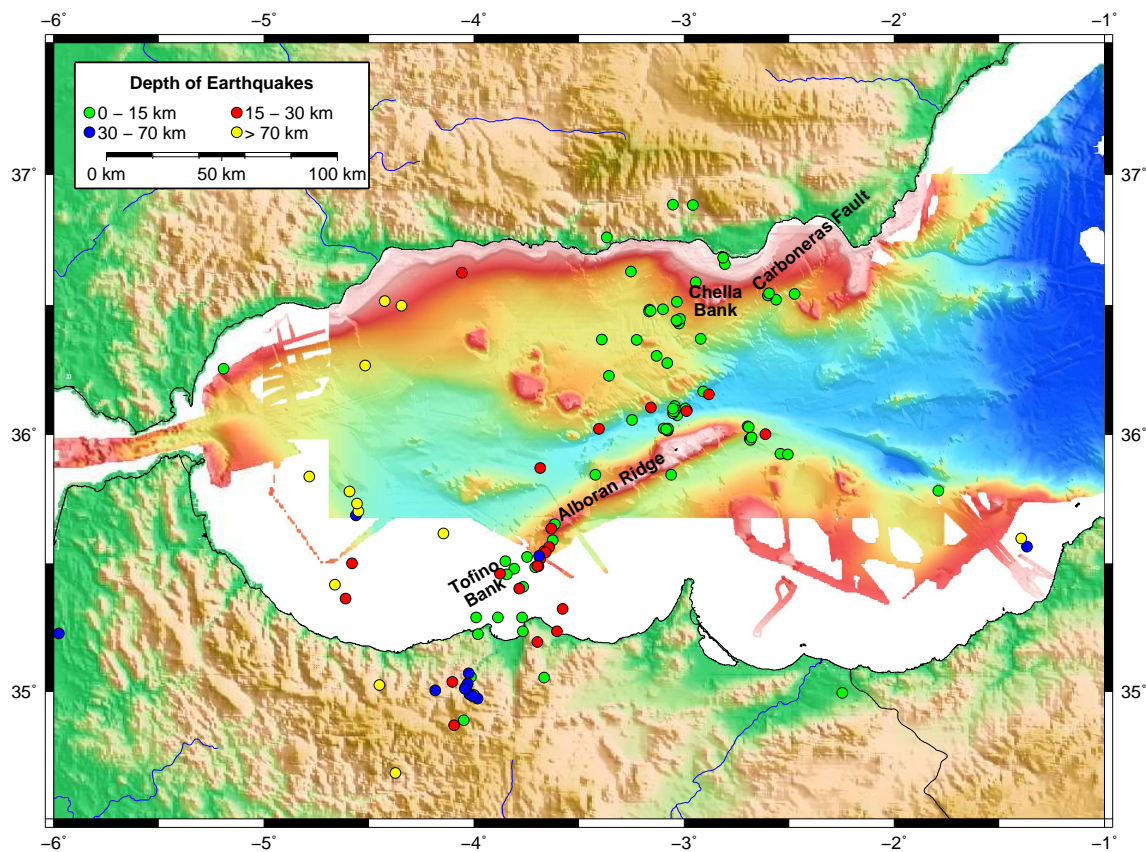


Figure 7.12: The depth distribution for the Alboran Basin of the in this study localized earthquakes.

and temperature in depth.

In a depth where $600\text{ }^{\circ}\text{C}$ is reached, no earthquakes occur anymore in the lithosphere. At the seafloor $\sim 0\text{ }^{\circ}\text{C}$ are present. An estimation for heat production and thermal conductivity is made. Values for the heat production and the thermal conductivity are taken from *Fullea et al.* (2007) who analyse the Gibraltar Arc system. With $A = 1.25\text{ }\mu\text{W}/\text{m}^3$ and $k = 2.5\text{ W}/(\text{m K})$, a maximum depth for earthquakes in the EAB and SAB ($Q_0 = 124\text{ mW}/\text{m}^2$) is calculated with 13 km. For the WAB ($Q_0 = 69\text{ mW}/\text{m}^2$) a depth of 30 km is calculated. The calculated depths for the $600\text{ }^{\circ}\text{C}$ isotherm below which no earthquakes occur in the lithosphere fit to the resulting earthquake location of this study (figure 7.10). In the EAB, a maximum depth of $\sim 15\text{ km}$ can be determined (figure 7.10 and 7.12) for located earthquakes which is close to the calculated maximum depth of 13 km with equation 7.2. In the WAB where the heat flow is about half of the heat flow in the EAB, the calculated maximum depth of 30 km is the same as lithospheric earthquakes are located in this region. Even when equation 7.1 describes an a lot simplified estimation of geotherm calculation, the resulting depths for the $600\text{ }^{\circ}\text{C}$ isotherm, and therewith the maximum earthquake depth, fit to the maximum depth of the in this study located earthquakes.

Deeper located events (figure 7.10 and 7.12; events below $\sim 30\text{ km}$) can be related to the old remnant slab in this region and not to the lithospheric earthquakes. Those earthquakes

only occur in the western part of the studied area, in the WAB and beneath Morocco on the African continent.

Having a look at the epicenters of the located earthquakes, the distribution shows two clusters as the different depths of lithospheric earthquakes are referred to with the comparison to the heat flow measurements. One in the EAB and the other in the WAB.

In the EAB, in the surrounding of the Carboneras Fault (figure 7.12) in the North of the Alboran Sea a number of events are released during the recording time of the seismic network. Those are the shallow located earthquakes up to a depth of ~15 km.

The second cluster of located earthquakes lies in the East of the WAB close to the coast of Morocco and onshore Morocco (figure 7.12). The offshore events are mainly those in a depth up to ~30 km. Onshore Morocco, the main earthquakes occur in a depth between 30 and 70 km but also in a shallower depth.

The location of the two clusters of earthquakes can be referred to topographic features (figure 7.12). Events in the WAB occur close to the Tofino Bank and along the Alboran Ridge. The northernmost events in the Alboran Sea are located close to the Chella Bank and the Carboneras Fault. Deeper earthquakes are located in the West of the WAB and are not related to lithospheric earthquakes. Those are the events which can be related to the remnant slab.

In the region of the Tofino Bank and the Alboran Ridge, recorded seismicity with higher magnitudes are for example two events close to Al Hoceima in northern Morocco. In 1994, a $M_W = 5.9$ earthquake ruptured in the region on 26 May. Ten years later, a $M_W = 6.3$ on 24 February 2004 ruptured close to Al Hoceima (Stich *et al.*, 2005). These earthquakes and the associated aftershocks are mainly strike-slip events in a depth between 10 and 16 km (Stich *et al.*, 2005).

Around the Chella Bank and the Carboneras Fault, predominantly strike-slip events occur. In the vicinity of Adra and Almeria (southern Spain), many devastating earthquakes ruptured. Offshore Adra, a historic strike-slip-to-normal faulting event ruptured on 16 June 1910 (figure 7.13; Stich *et al.*, 2003b) with a magnitude of $M_W = 6.1$. Almeria, which lies next to the onshore continuation of the Carboneras Fault, was hit in the past by a number of historic events with destructive dimensions: 1487, 1522 (IX MSK), 1658 (VIII MSK), and 1804 (IX MSK) (Gràcia *et al.*, 2006).

By Stich *et al.* (2003a, 2006, 2010), different time periods with recorded local seismicity in the Alboran region were analysed. In the periods of the three publications (November 1995 - March 2002, beginning 2002 - May 2005 and mid 2005 - end 2008, respectively), moment tensor solutions were defined. These solutions show mainly strike-slip faulting in the Alboran region (figure 7.13). Those strike-slip events occur in the two clustering regions, as defined by the in this study analysed local seismicity, roughly along the Alboran Ridge and the Carboneras Fault. The localized earthquake activity along the Alboran Ridge and the Carboneras Fault is defined as the Trans Alboran Shear Zone (e.g. Stich *et al.*, 2006).

The focal mechanisms also show that the Alboran Basin is not merely dominated by strike-slip motion. Also a combination with normal and reverse faulting is present

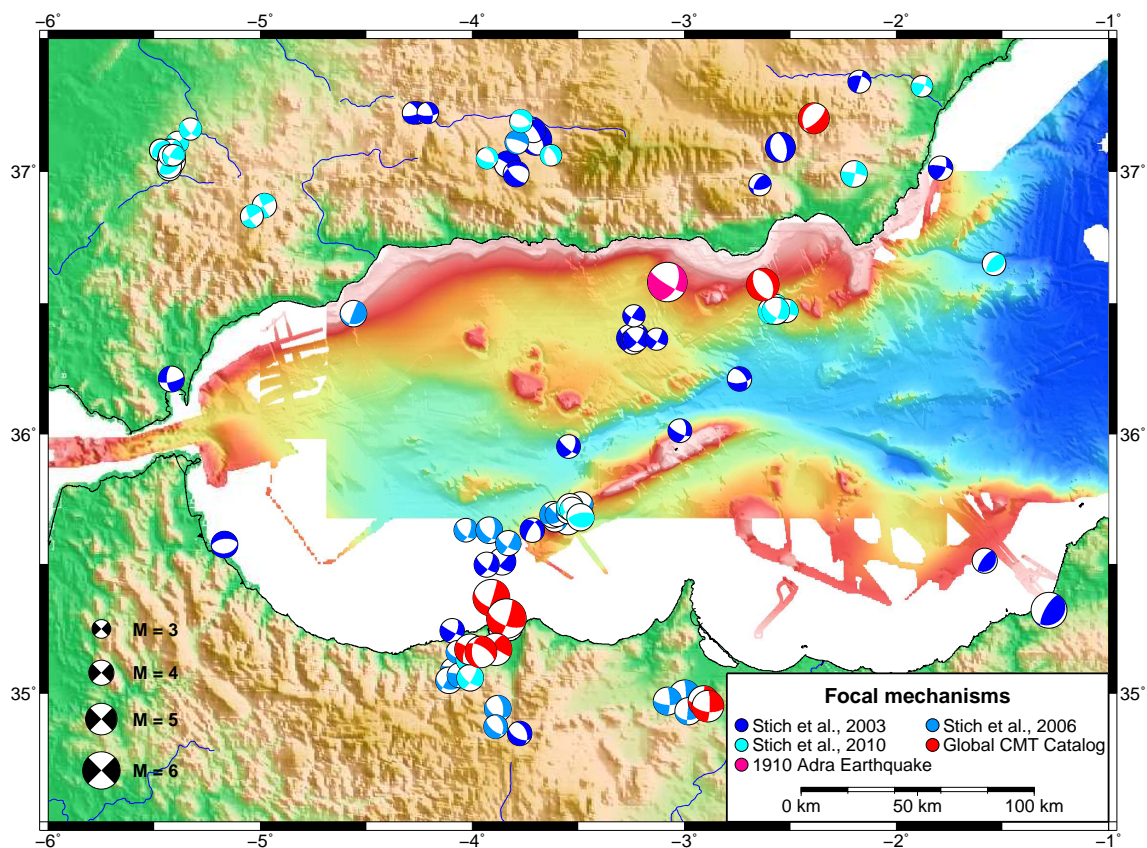


Figure 7.13: Focal mechanisms in the Alboran Basin. Data of different studies are shown (see legend).

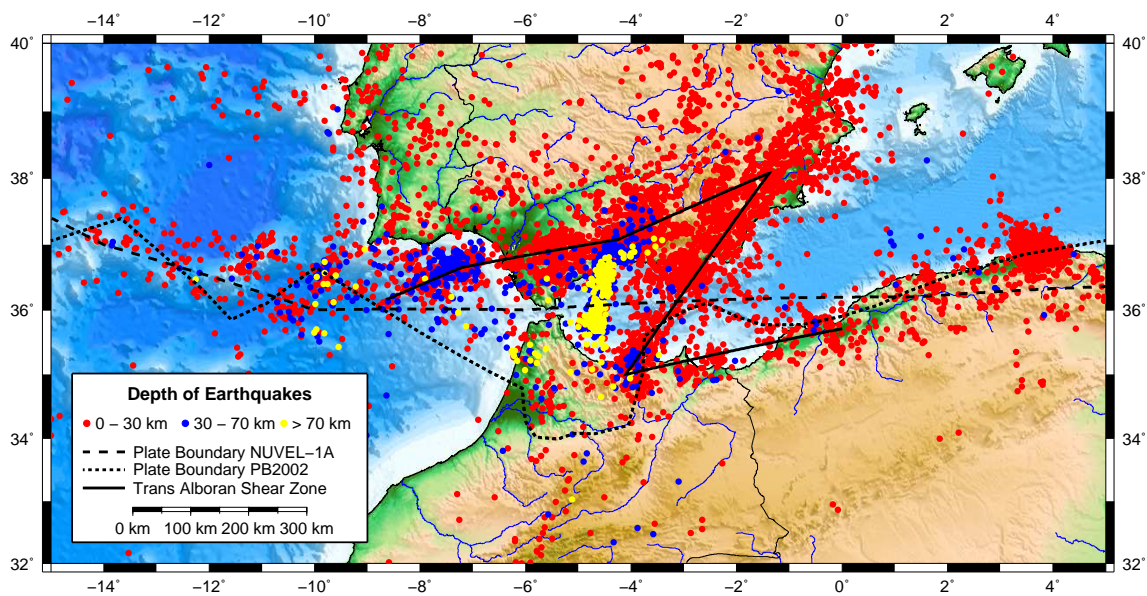


Figure 7.14: Earthquakes of the NEIC Catalog (1990 - 2012). Additionally, three different possible plate boundaries are shown for the Alboran region: NUVEL-1A model (DeMets et al., 1990, 1994), PB2002 (Bird et al., 2002; Bird, 2003) and the Trans Alboran Shear Zone (simplified illustration).

(figure 7.13).

Regional seismicity is displayed in figure 7.14 (data of the NEIC Catalog from 1990 to 2012). Most events, like the in this study localized earthquakes (figure 7.10 and 7.12), occur in a shallow depth up to 30 km (red dots in figure 7.14 and red and green dots in figure 7.12). Deeper events occur mainly in the West of the WAB.

The distribution of the shallow regional events form a z-shaped structure running along the Betics, crossing the Alboran Sea mainly along the the Carboneras Fault and the Alboran Ridge (Trans Alboran Shear Zone) and continuing eastwards on the African continent along the coast (figure 7.14). Some studies analyse this as the possible plate boundary between the Eurasian and African continents (straight line in figure 7.14; e.g. *Gutscher et al.*, 2009). A rough model of the plate boundary in the Alboran region is presented by the NUVEL-1A model (dashed line in figure 7.14; *DeMets et al.*, 1990, 1994). The PB2002 model of the plate boundaries runs mainly along the African coast (dotted line in figure 7.14; *Bird et al.*, 2002; *Bird*, 2003). By the analysed data, a plate boundary model can not be verified (see earthquake distribution in figure 7.12). The localized earthquakes of the local half-year period of seismic recording coincide with the main regional earthquake distribution (figure 7.14). Those events were recorded along the Trans Alboran Shear Zone in the Alboran Sea (figure 7.10 and 7.12). The recording period was too short and the located events are too few to analyse the present location of the plate boundary in the Alboran region. The events rupture along a zone of faults in the Alboran Basin which is not running parallel to the Alboran Ridge as a main topographic structure in the Alboran Sea but along the Trans Alboran Shear Zone. Some events occur at the Alboran Ridge but most events within the latitudes of the Alboran Ridge originate few kilometers further to the West.

The magnitude of the located earthquakes are in general relatively low. Moment magnitudes are in almost all earthquakes smaller than 3. The number of located earthquakes is relatively small to analyse the release of seismic energy. Including earthquakes of the NEIC catalog to consider the release of seismic energy in this region, the main release is continuously. There exist some historic events with higher magnitudes. These are e.g. the 6.1 Adra earthquake in 1910 (*Stich et al.*, 2003b), the 7.8 Granada Earthquake in 1954 (*Chung and Kanamori*, 1976) and the 6.2 Granada earthquake in 2010 (*Bufo et al.*, 2011). But the main release of seismic energy is in the Alboran region continuously.

The distribution of the located earthquakes which are mainly from low magnitude ($M_W \leq 3$) shows a regional separation which is consistent with heat flow measurements and other studies which analyse the local and regional seismicity in the Alboran region. A plate boundary is not clear visible as in subduction zones. This was expected. But the regional separation shows also differences in lithospheric thicknesses. In the WAB, events occur in a higher depth than in the EAB. This describes, that the lithosphere is thicker in the WAB than in the EAB. A drastic decrease in lithospheric and crustal thickness from the WAB to the EAB was analysed, parallel to the heat flow measurements and including those into their calculations, by *Polyak et al.* (1996). This supports the in this study first analysed dataset, where a thinning of the crust was analysed from the EAB in the transi-

tion to the Algerian Basin (chapter 6).

Chapter 8

Conclusion

In this study, the structure of the Alboran Sea was surveyed with seismic refraction and wide-angle data (eastern Alboran Basin in transition to the Algerian Basin) and local earthquake data (whole Alboran Basin and surrounding onshore domains). The aim was to analyse the available datasets and provide further data for the support of a formation history hypothesis for the Alboran Basin. What kind of crust is present along the recorded transect and how is the local earthquake distribution and what does this imply for the formation history of the Alboran Basin.

The refraction and wide-angle data were recorded along a pre-existing MCS profile (*Comas et al.*, 1995; *Booth-Rea et al.*, 2007). On 24 stations, refracted and wide-angle reflected arrivals were traced through the subseafloor. The resulting seismic velocity structure shows a segmentation of the profile into three parts.

The first 40 km of the profile, the westernmost kilometers, consist of continental crust. The crustal velocities in this segment are similar to typical continental crust and too slow for oceanic crust. This part is with respect to typical continental crust with a thickness of 6 - 7 km extremely thinned.

Continuing to the East, the second segment is present. It includes km 40 - 140 of the seismic profile. This segment is crossing the Maimonid Ridge diagonally. It describes a transition zone between the first, the westernmost, and the third, the easternmost, segment. Due to the topographic feature, the Maimonid Ridge, the crustal thickness of this part is the thickest along the refraction profile. An up to 12 km thick crust is modeled along this part of the profile. It looks like a root-like structure. Thinnest at both ends of the segment and the highest thickness in the central part where the highest part of the Maimonid Ridge is ontop. The velocity structure is similar to continental crust, but, as the westernmost segment, extremely thinned compared to typical continental crust.

In the third segment, the easternmost part of the seismic profile from km 140 - 250, a completely different velocity structure is present. This part resembles oceanic crust. Also the thickness is typical for oceanic crust with 6 - 7 km.

Overall, the refraction seismic profile indicates extremely thinned continental crust in the eastern Alboran Sea. The two westernmost segments have a velocity structure similar to

that of typical continental crust. Both segments mainly differ in their crustal thicknesses. The transition to a completely different velocity structure occurs in the central segment of the analysed seismic profile where the Maimonid Ridge is crossed. It is the transition from the East Alboran Basin to the Algerian Basin. In relatively few kilometers, the crustal velocities change to that of oceanic crust. This is the style of the third, the easternmost, segment which lies in the Algerian Basin.

The structure of the Moho is affected by the topographic feature Maimonid Ridge where a root-like structure is formed. In the other two segments, the westernmost and easternmost part of the profile, a relatively flat continuous structure of the Moho is existent.

Upper mantle velocities are especially in the western part of the recorded profile with ~ 7.0 km/s extremely low compared to typical upper mantle velocities in regions of continental crust. In the East, upper mantle velocities of ~ 7.6 km/s are also lower compared to expected values in oceanic lithosphere.

The segmentation of the profile and the velocity structure, also the slow upper mantle velocities beneath all three segments show similarities to arc-back-arc structures (e.g. Mariana Arc (*Takahashi et al.*, 2007, 2008) and Tonga Arc (*Contreras-Reyes et al.*, 2011)). These similarities support, together with the velocity structure, the analysis of the Alboran Basin as a back-arc basin formed while westward slab rollback. The westernmost segment describes the thinned remnant continental crust which was thinned due to the westward slab rollback. The easternmost segment is the western end of a back-arc basin consisting of oceanic crust and continuing to the East. The transition from continental to oceanic crust and therewith from the thinned continental crust to the back-arc basin floored with oceanic crust is present along a few kilometers in the eastern part of the central segment.

Additional to the support of the slab rollback theory as formation history, the seismic data show a low velocity zone at the bottom of the sedimentary layer of easternmost segment. This can be attributed to fast evaporites compared to the sediments lying on top of the LVZ. Those evaporites are deposited while the Messinian salinity crisis (e.g. *Duggen et al.*, 2003; *Booth-Rea et al.*, 2007).

The analysed earthquake dataset results in a rough velocity profile describing the Alboran Basin and the surrounding onshore domains. Therefore offshore and additional onshore stations were used to locate earthquakes which were recorded in the Alboran Sea.

The v_p/v_s -ratio was determined as 1.7 - 1.8 for the different layers of the velocity model. This implies that no largescale serpentinization is present in the researched region, which would result in a higher v_p/v_s -ratio.

A second result of the earthquake analysis is that mainly low magnitude earthquakes are recorded while the network was established in this region. Events with higher magnitudes are rare but occur (e.g. 6.1 Adra earthquake in 1910 (*Stich et al.*, 2003b), 7.8 Granada Earthquake in 1954 (*Chung and Kanamori*, 1976) or 6.2 Granada earthquake in 2010 (*Bufoern et al.*, 2011)) and were not recorded while the station network was deployed. A continuous release of the seismic energy is present in the Alboran region.

The distribution of the located earthquake hypocenters shows a distinct pattern. In the Alboran Basin, most earthquakes are shallow. Deeper earthquakes are located in the western part of the West Alboran Basin (WAB).

The shallow earthquakes can be separated in two areas: the WAB and the East and South Alboran Basin (EAB and SAB). In the WAB, earthquakes occur until a depth of ~30 km. In the EAB and SAB, the maximum depth of the hypocenters are ~15 km. This is consistent with heat flow measurements by *Polyak et al.* (1996) and a rough assessment of the maximum earthquake depth with the formula for calculation of simple geotherms, using the heat flow measurements of *Polyak et al.* (1996). The earthquakes in the Alboran Basin occur mostly in the lithosphere. The results of the maximum earthquake depths show the decreasing lithospheric thickness in the Alboran Basin from West to East. In the WAB, a thicker crust and lithosphere is present, thinning to the East.

Deep earthquakes occurring mainly in the western part of the WAB can be related to the remnant subducted slab in the West of the analysed region.

The two areas where the shallow events occur can be related to topographic expressions in the Alboran Basin. Earthquakes rupture mainly close to the Alboran Ridge and the Corboneras Fault. This is consistent to previous analysis, e.g. *Stich et al.* (2003a, 2006, 2010), where moment tensor solutions were determined with mainly strike-slip faulting in the Alboran region. The analysed events were mainly located along the Alboran Ridge and the Corboneras Fault.

The earthquake distribution shows the same result as the wide-angle refraction data show: a crustal and lithospheric thinning from West to East. Together with the occurrence of the deep earthquakes, the depth distribution of the recorded seismicity fits to the theory of westward slab rollback as formation history of the Alboran Basin. The two analysed datasets give additional information for the Alboran region and the interpretation of slab rollback as the formation history.

Appendix A

Enlarged Plots

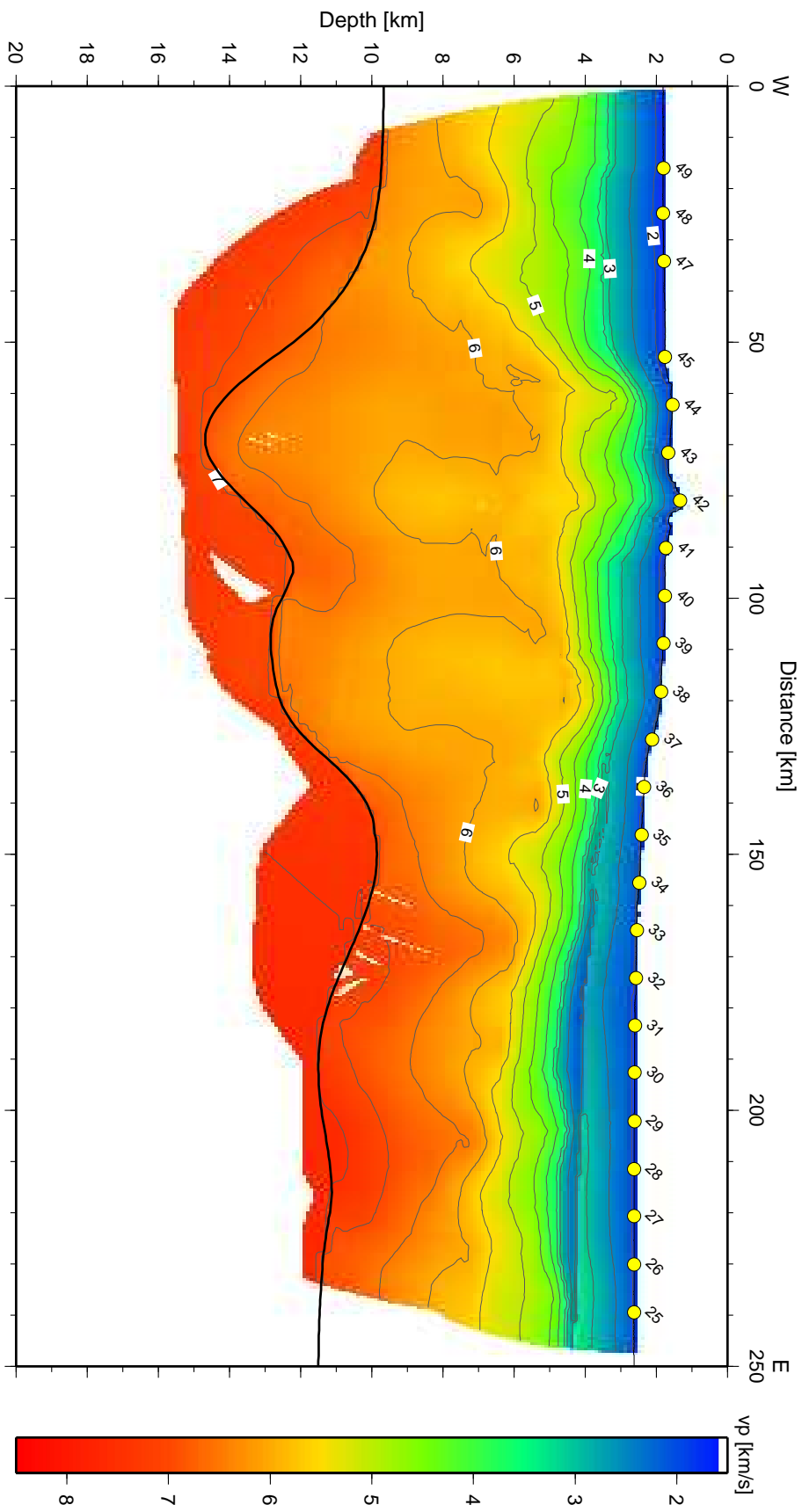


Figure A.1: The final inversion model. Isolines are every 0.5 km/s. Left = West, right = East. This is an enlarged plot of figure 4.14.

Appendix B

Data Fit and Seismograms of the Recorded Seismic Refraction Data

Figure B.1: *Observed and calculated traveltimes. The observed traveltimes are the picked traveltimes with errorbars in grey. Red are the calculated traveltimes of refractions and blue are reflected calculated traveltimes. OBH/OBS are enumerated from the westernmost (OBH49) to the easternmost station (OBS25).*

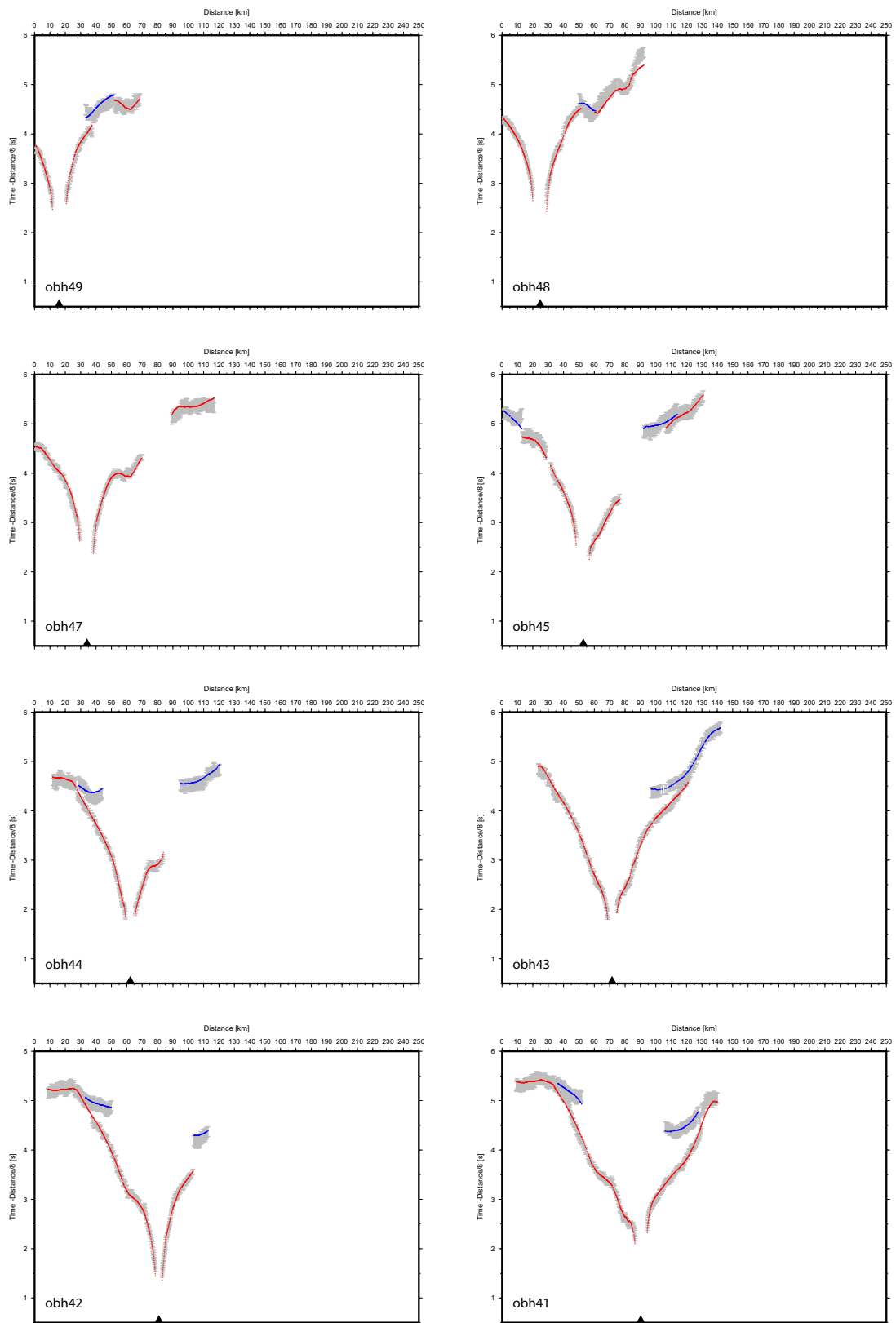


Figure B.1

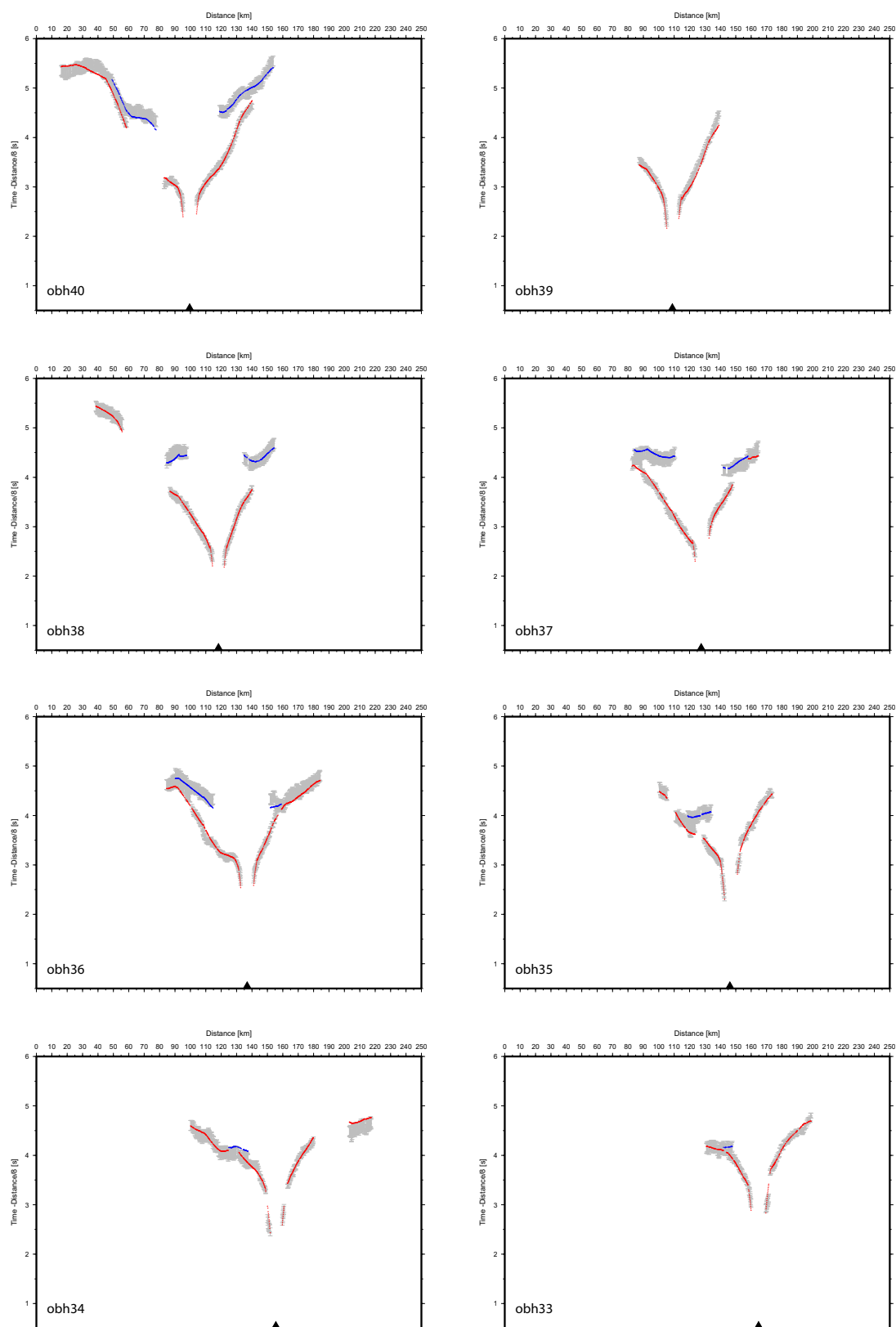


Figure B.1: (continued)

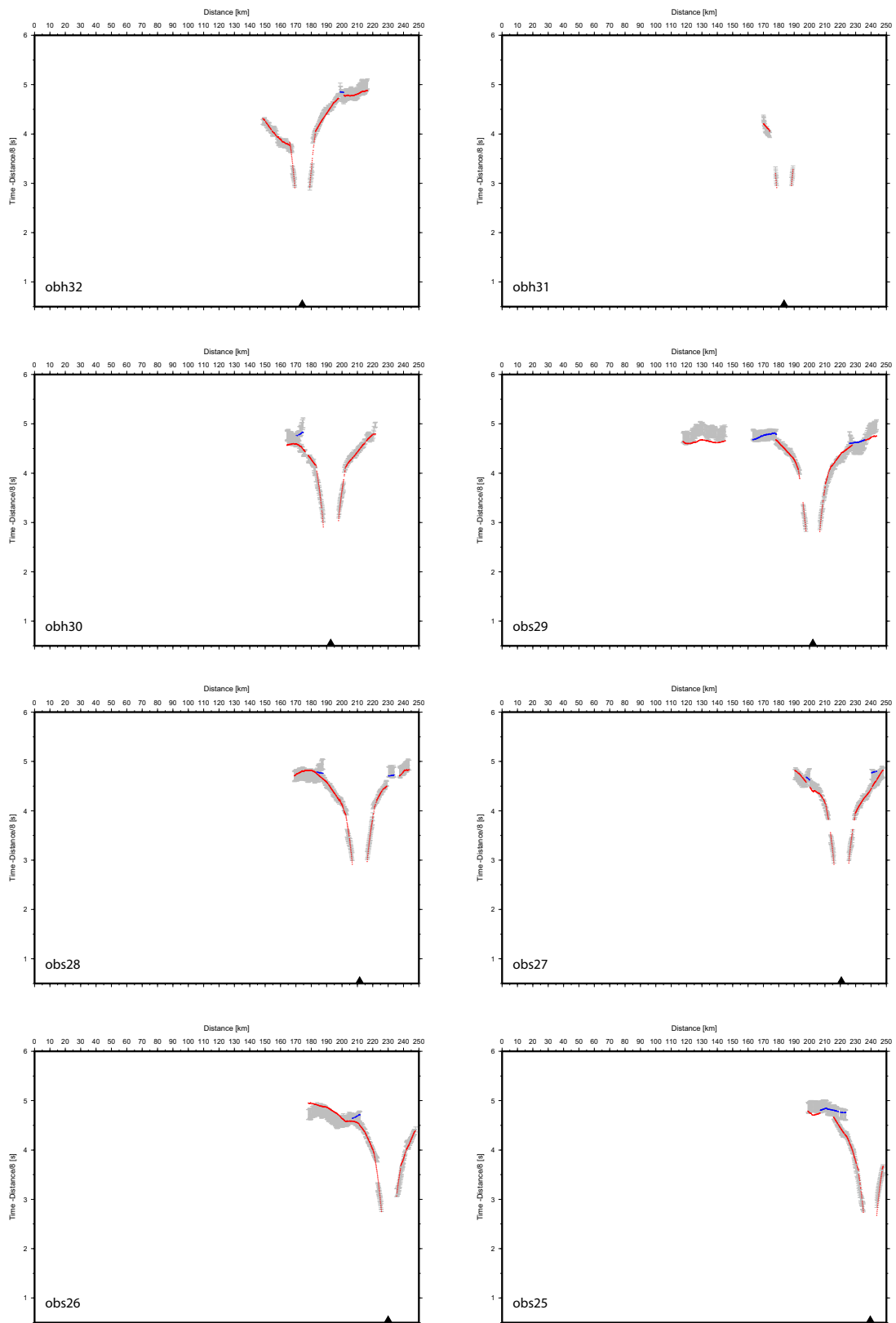


Figure B.1: (continued)

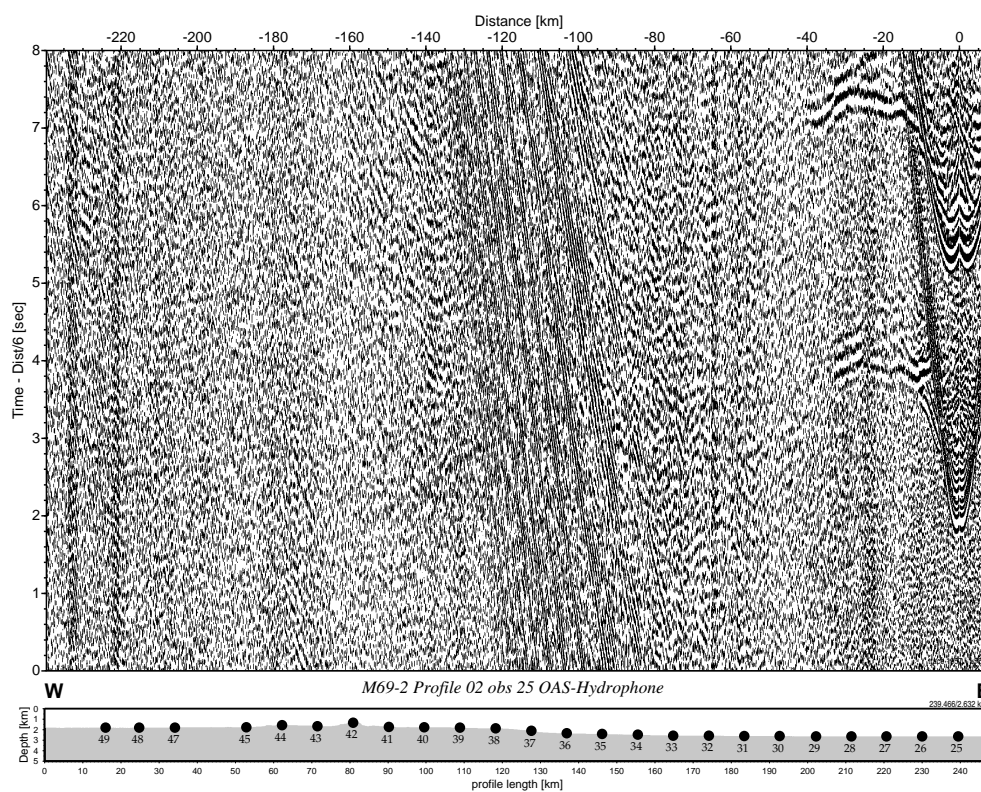


Figure B.2: Seismogram of OBS 25, channel 1

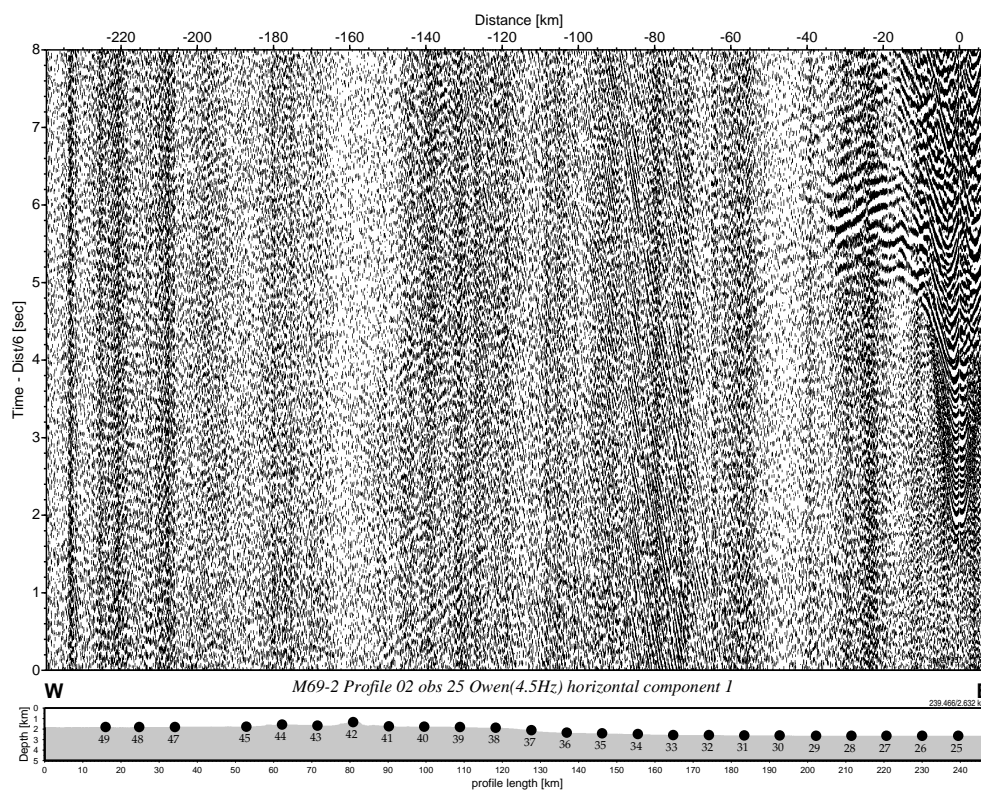


Figure B.3: Seismogram of OBS 25, channel 2

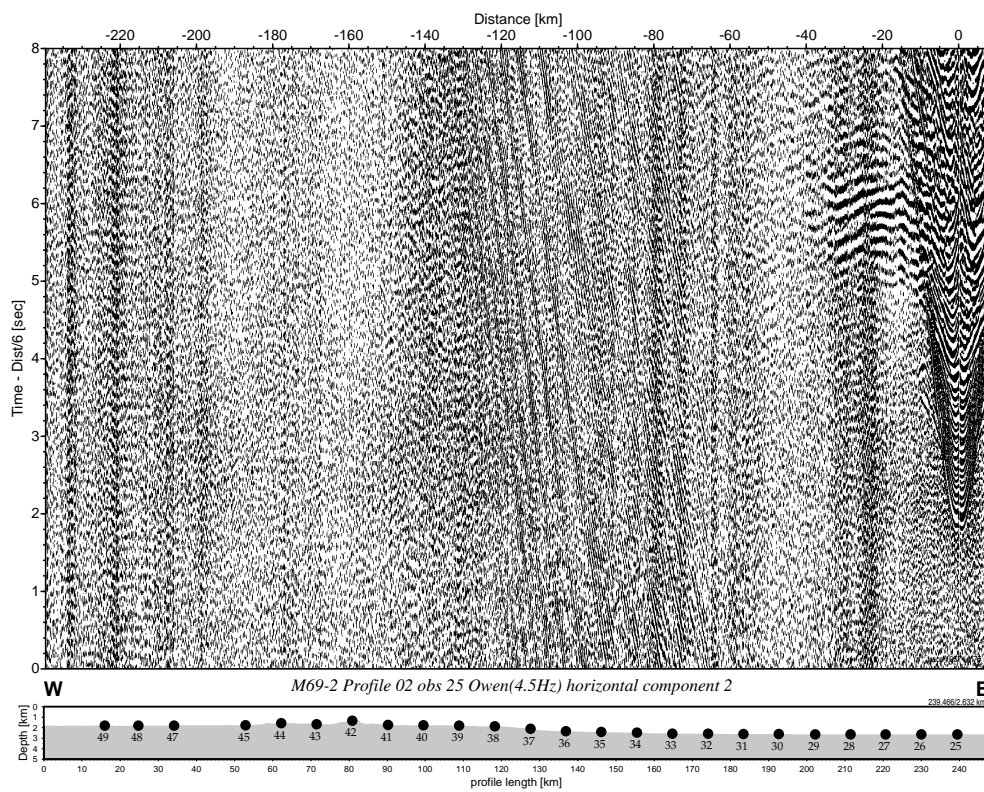


Figure B.4: Seismogram of OBS 25, channel 3

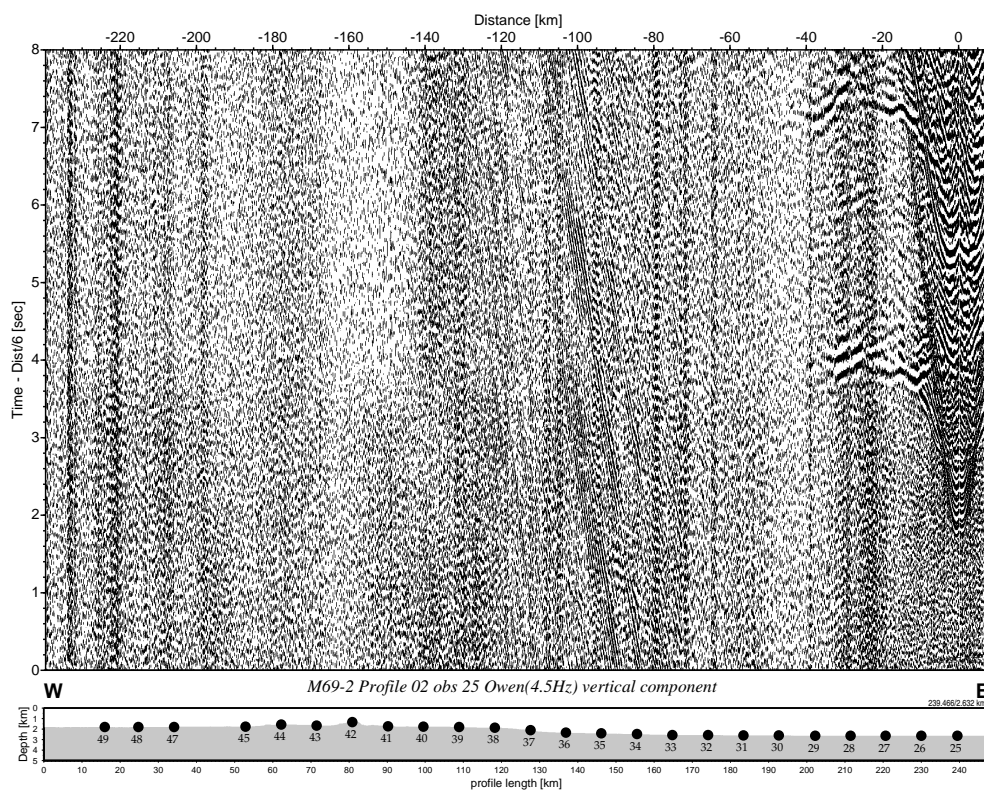


Figure B.5: Seismogram of OBS 25, channel 4

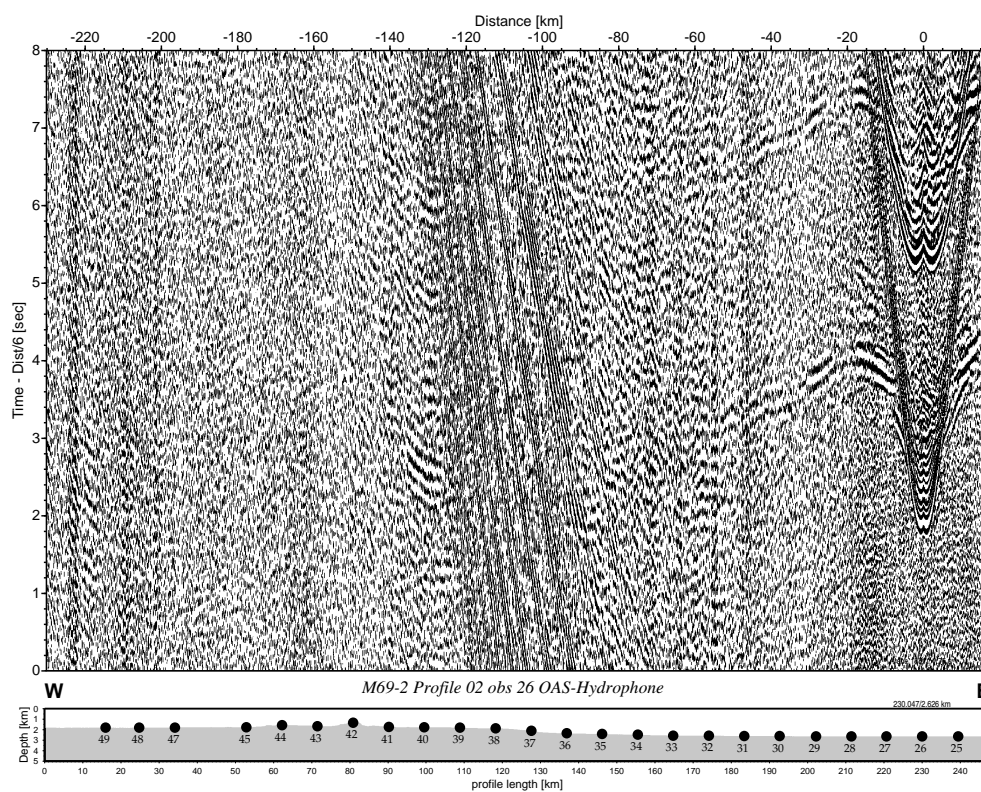


Figure B.6: Seismogram of OBS 26, channel 1

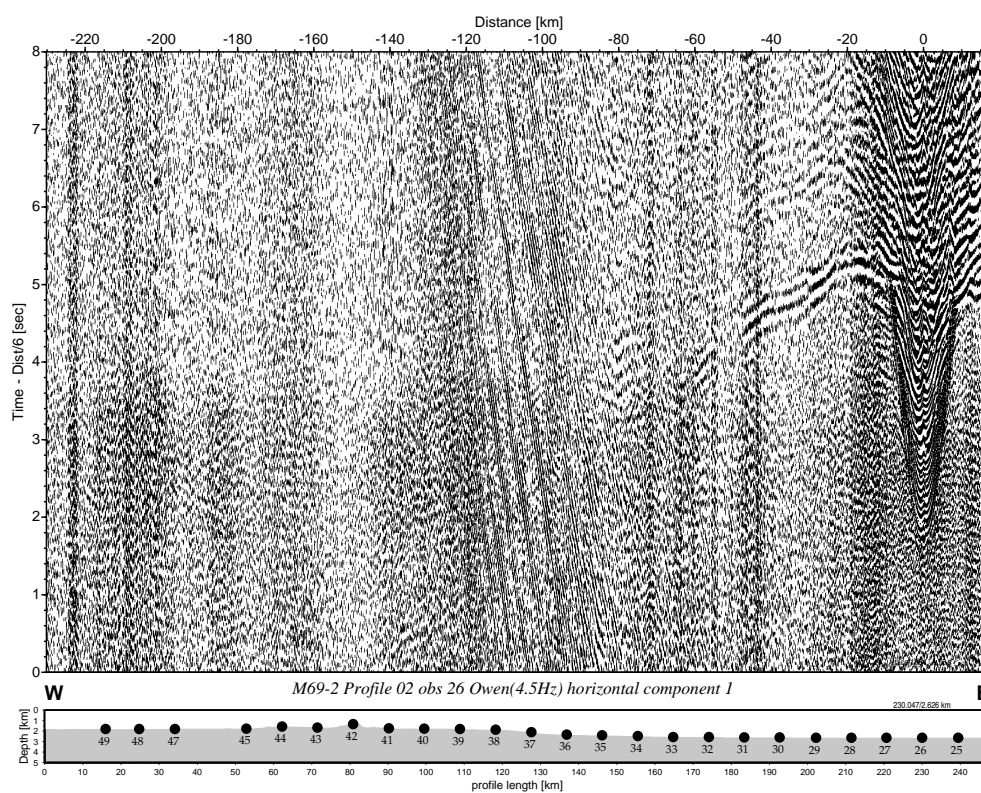


Figure B.7: Seismogram of OBS 26, channel 2

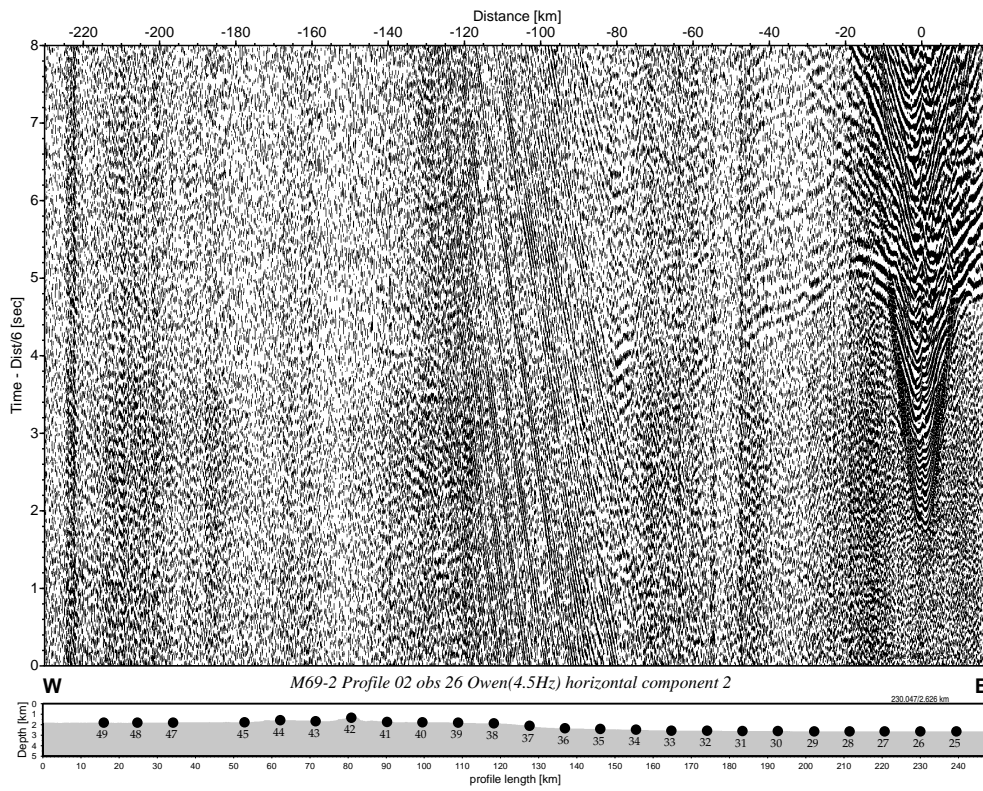


Figure B.8: Seismogram of OBS 26, channel 3

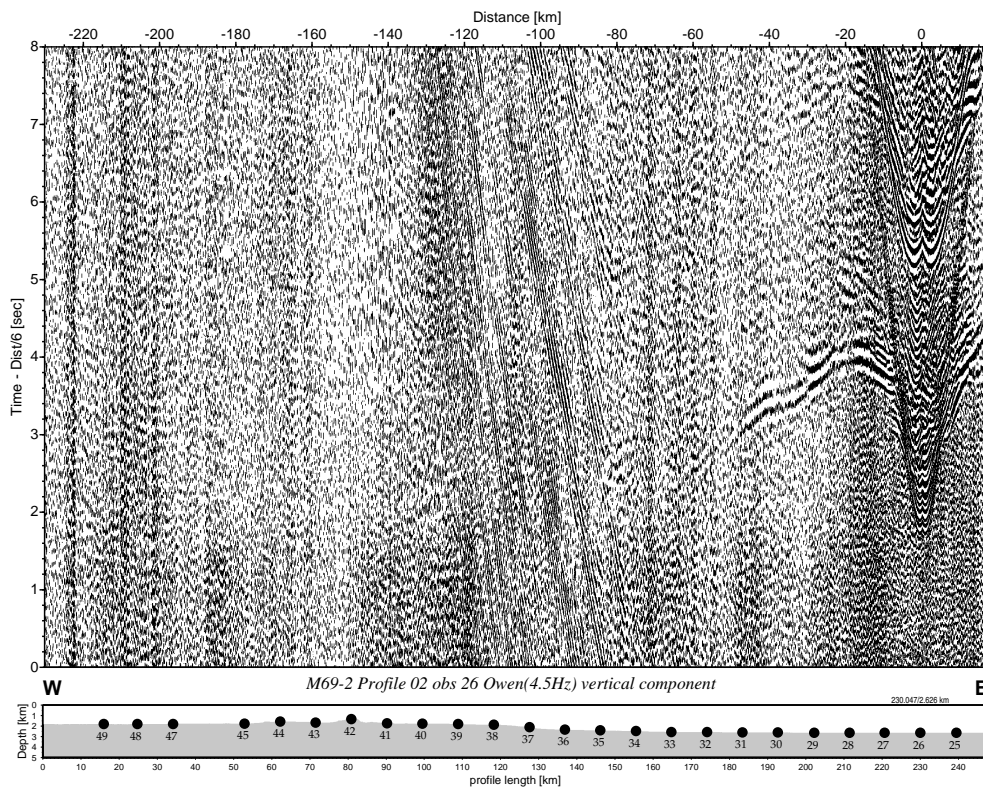


Figure B.9: Seismogram of OBS 26, channel 4

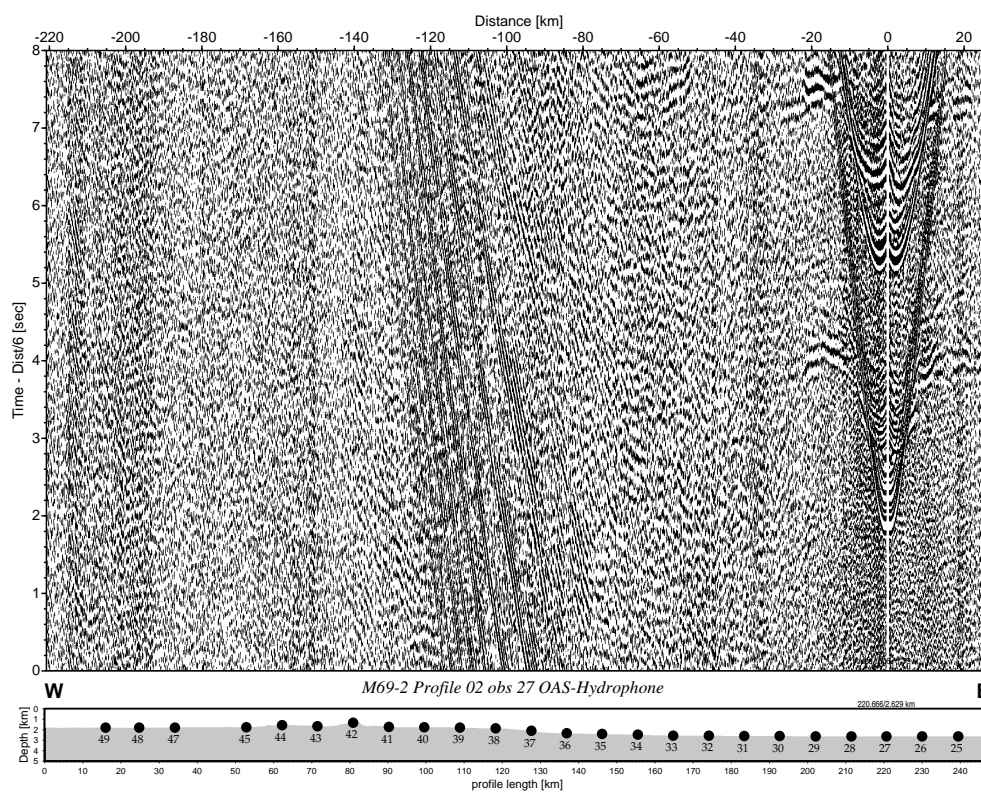


Figure B.10: Seismogram of OBS 27, channel 1

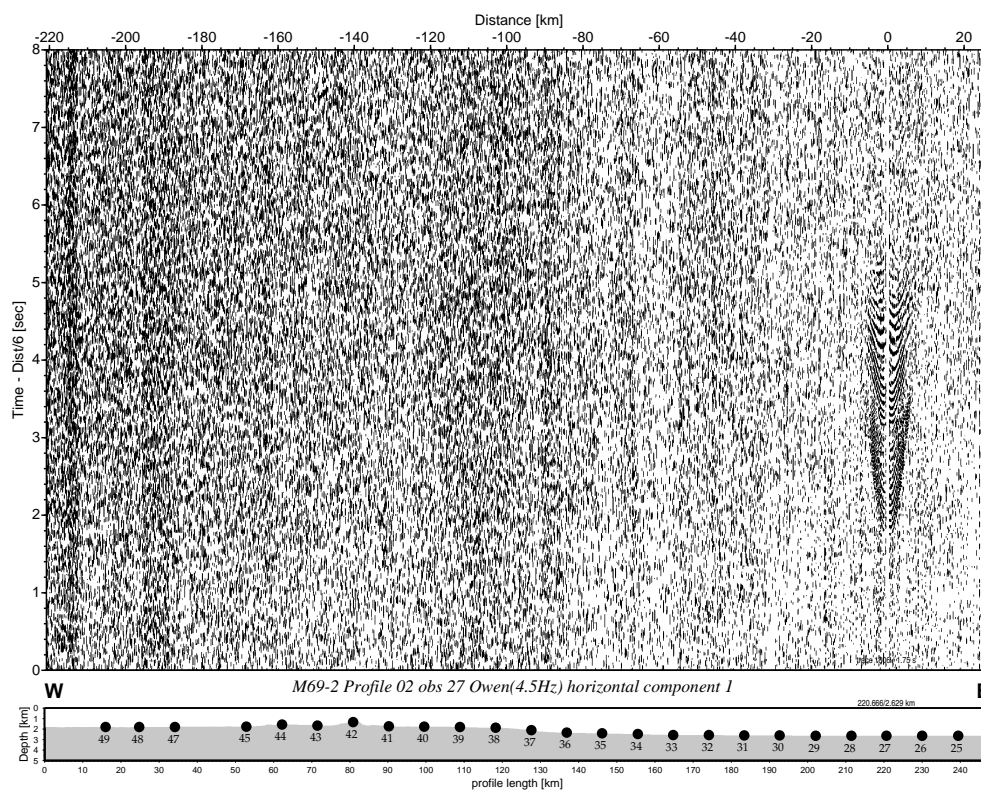


Figure B.11: Seismogram of OBS 27, channel 2

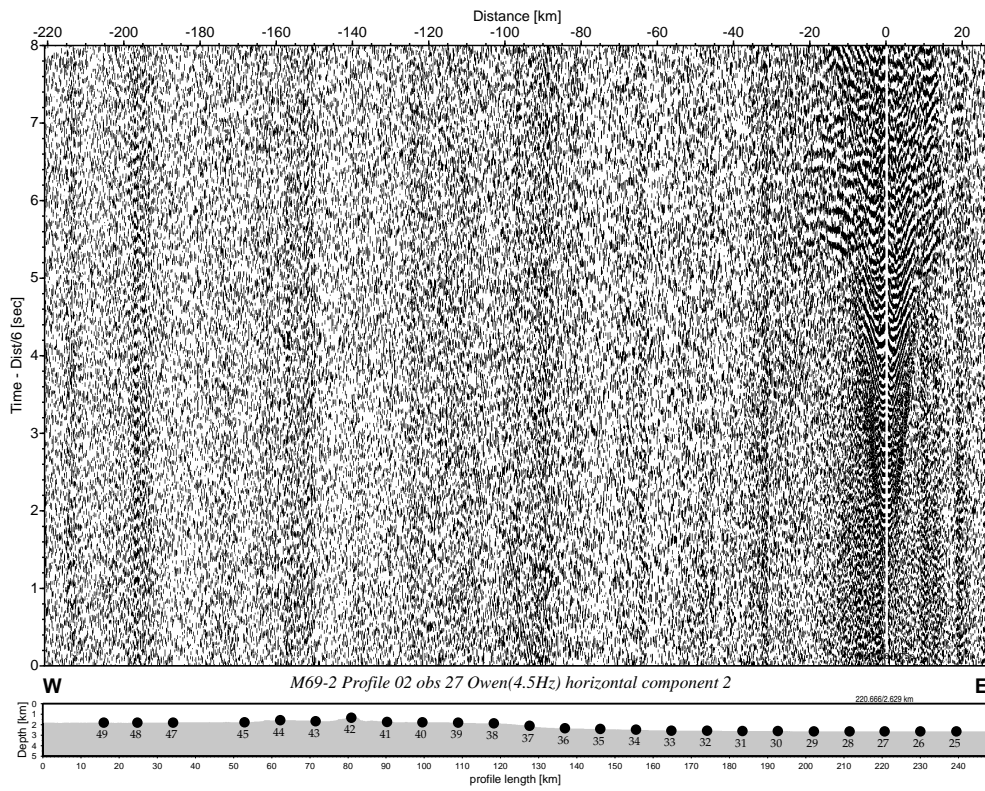


Figure B.12: Seismogram of OBS 27, channel 3

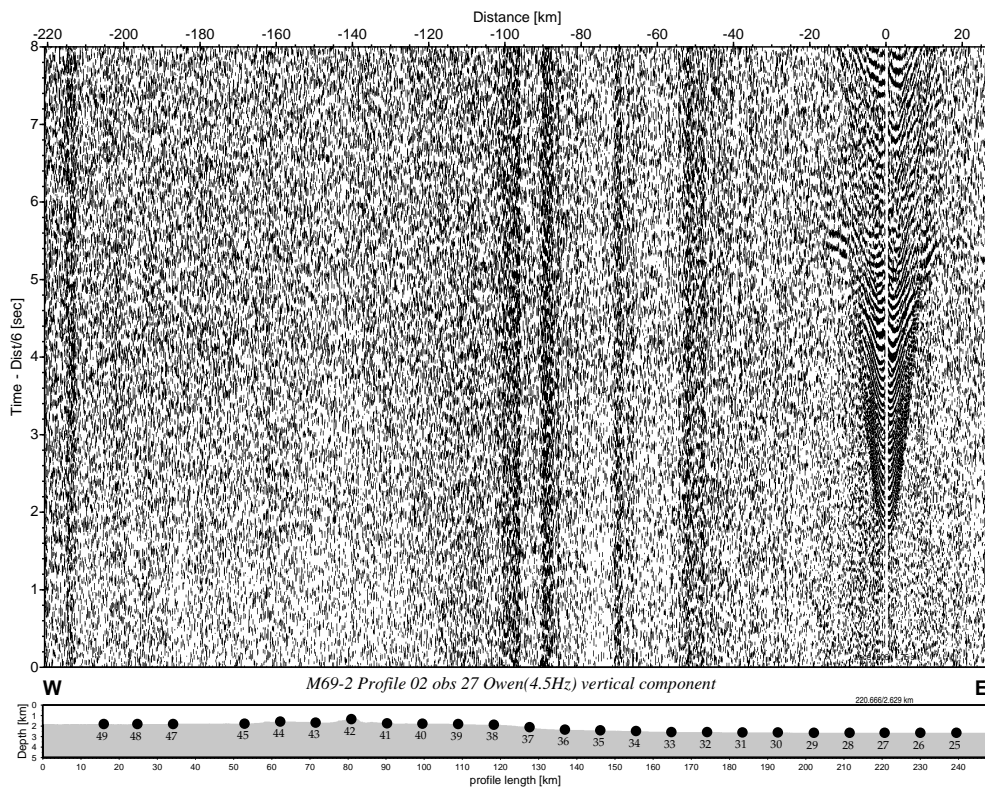


Figure B.13: Seismogram of OBS 27, channel 4

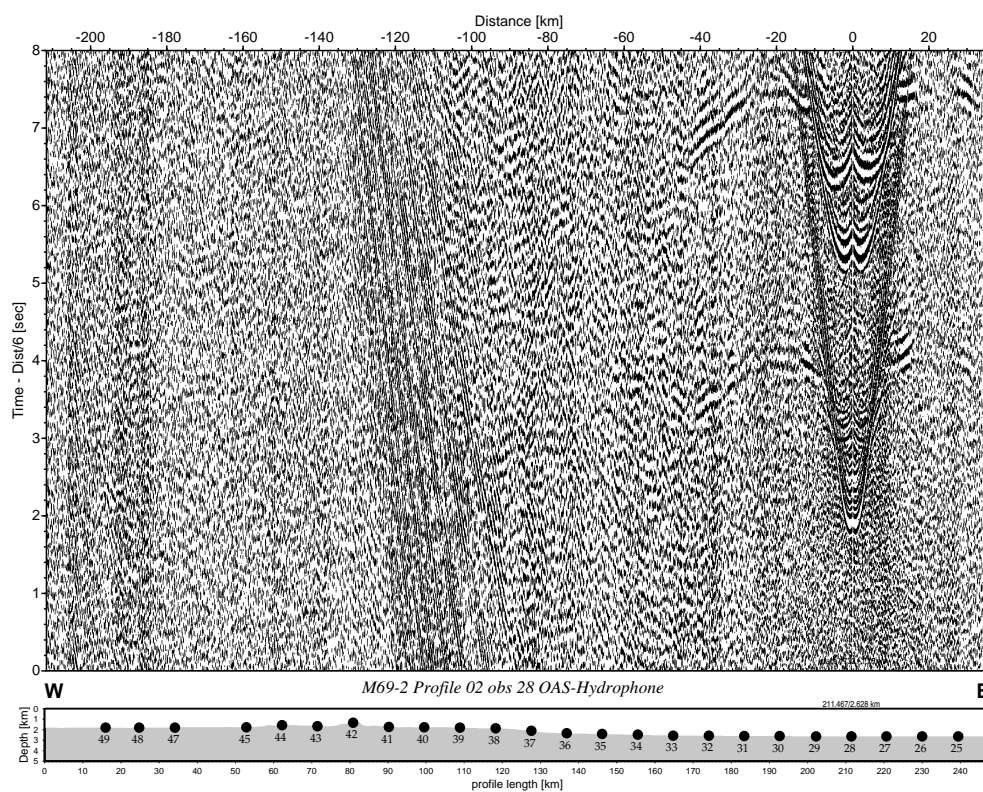


Figure B.14: Seismogram of OBS 28, channel 1

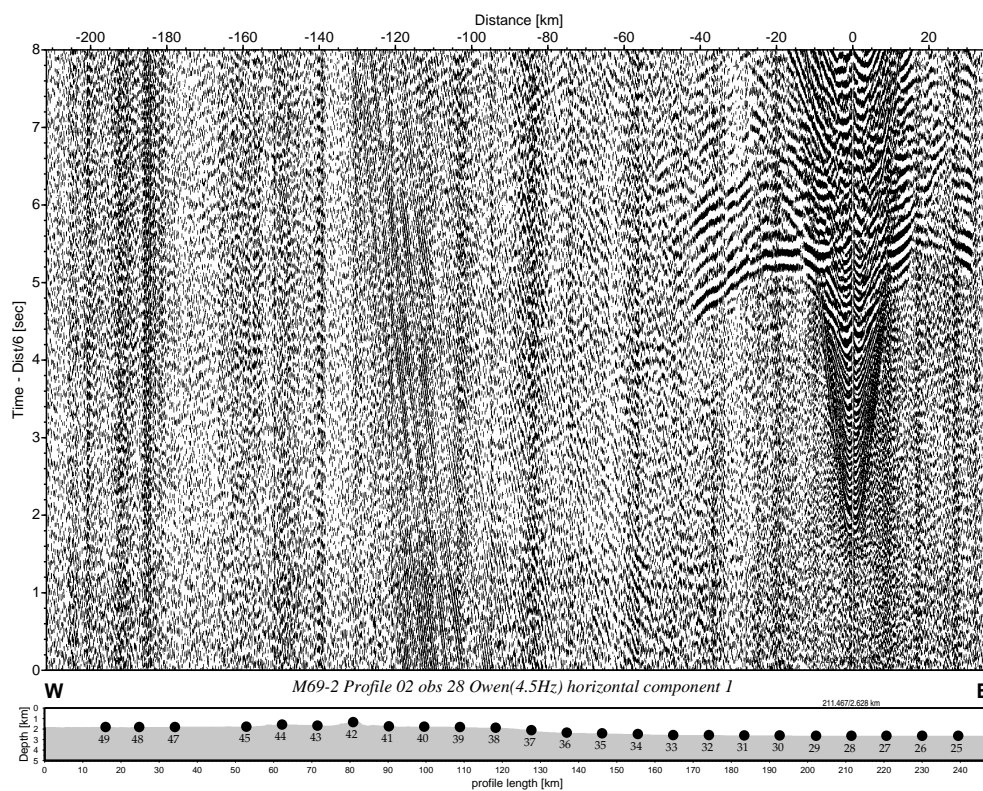


Figure B.15: Seismogram of OBS 28, channel 2

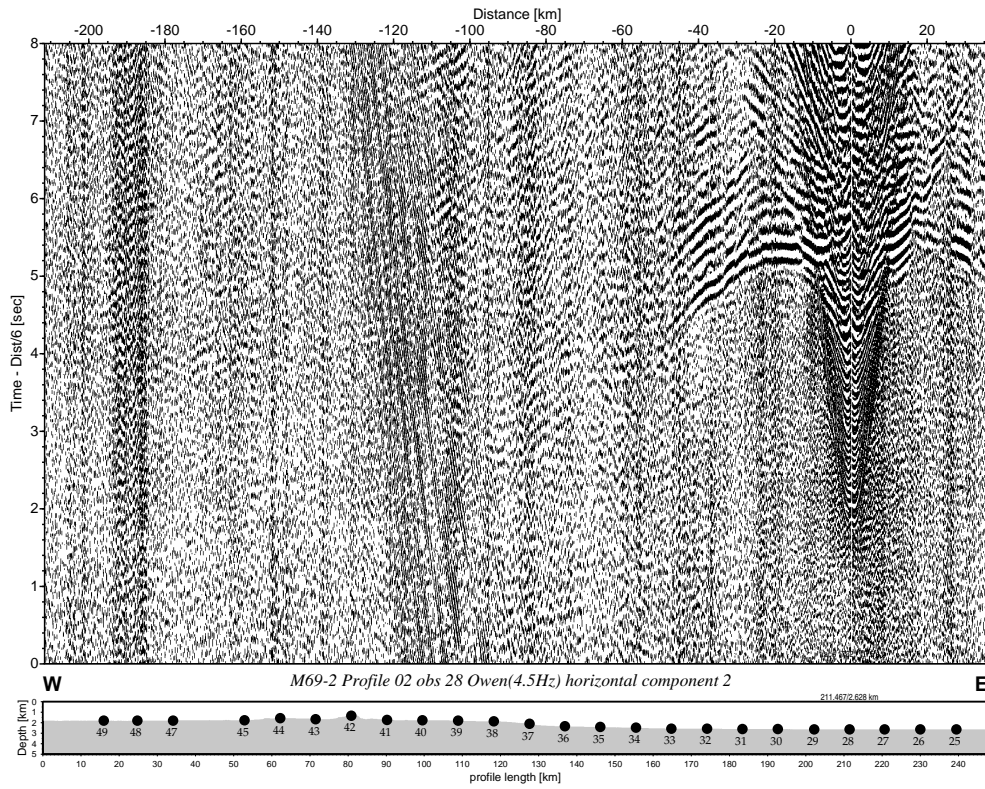


Figure B.16: Seismogram of OBS 28, channel 3

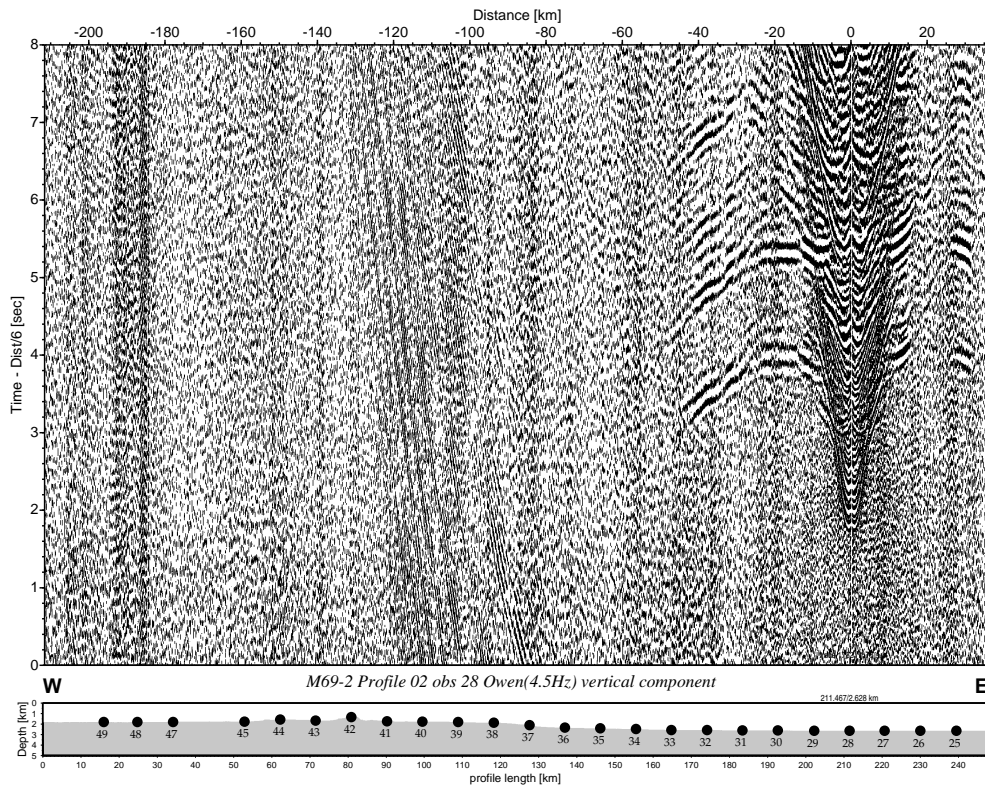


Figure B.17: Seismogram of OBS 28, channel 4

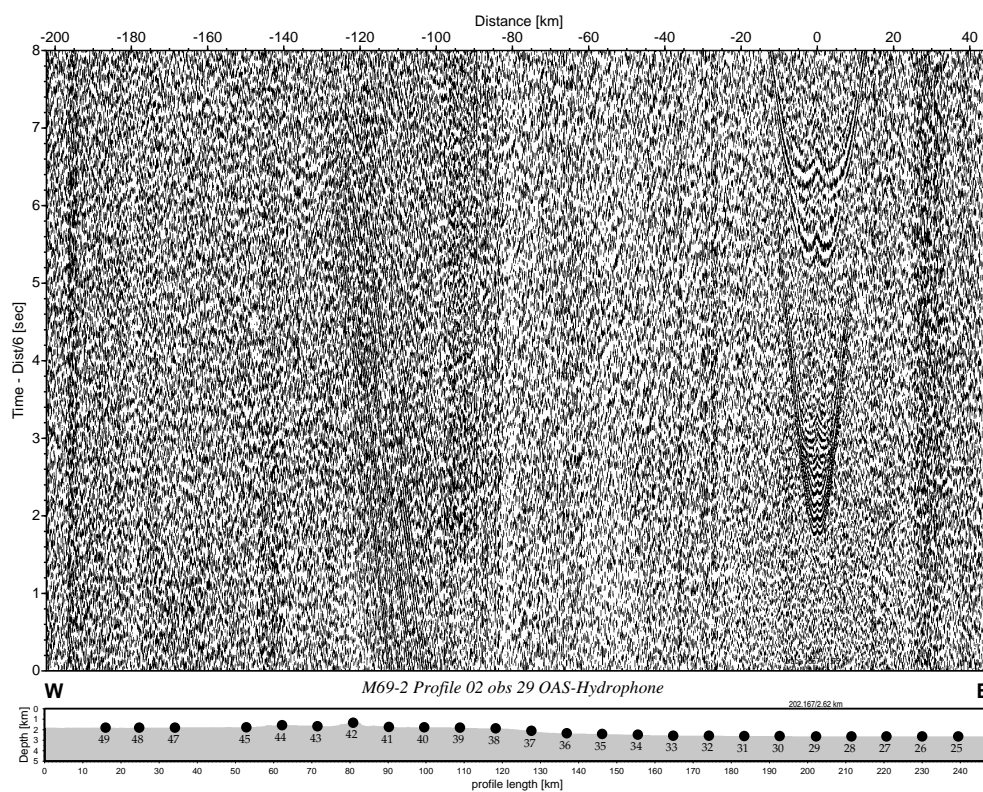


Figure B.18: Seismogram of OBS 29, channel 1

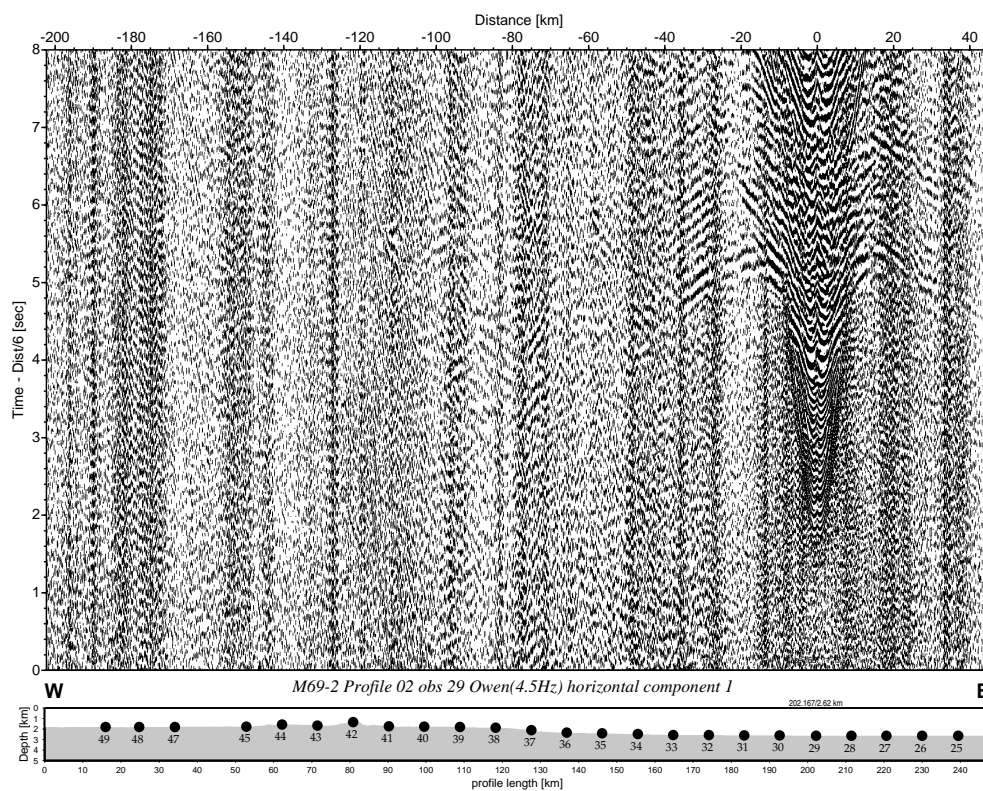


Figure B.19: Seismogram of OBS 29, channel 2

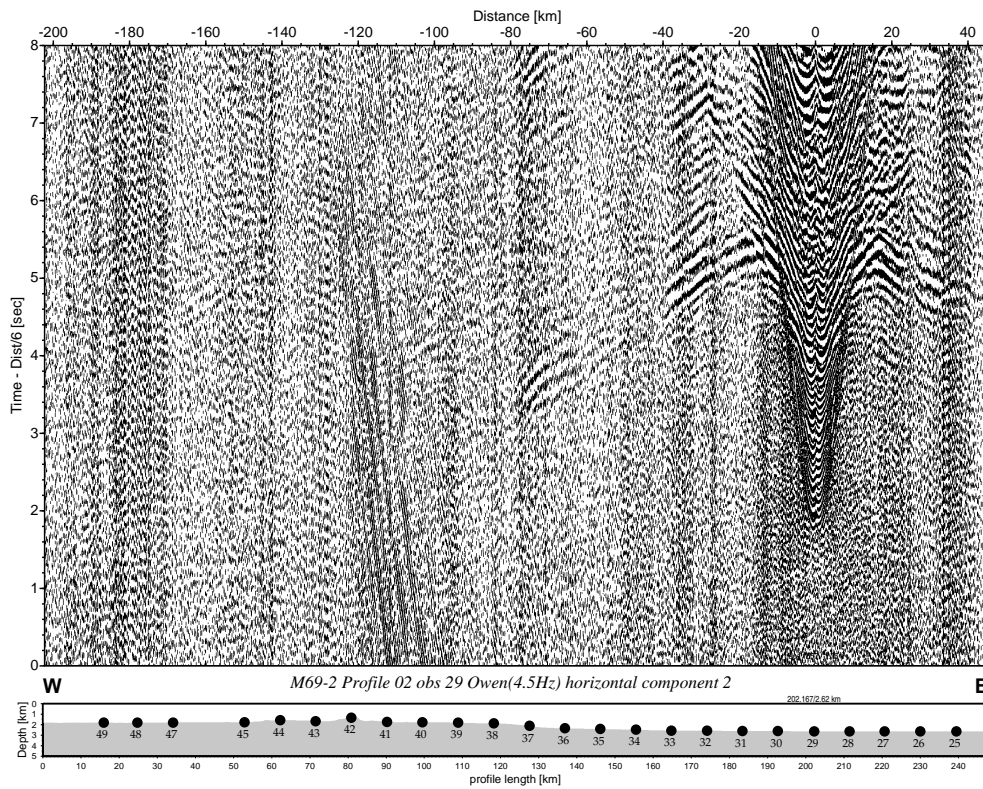


Figure B.20: Seismogram of OBS 29, channel 3

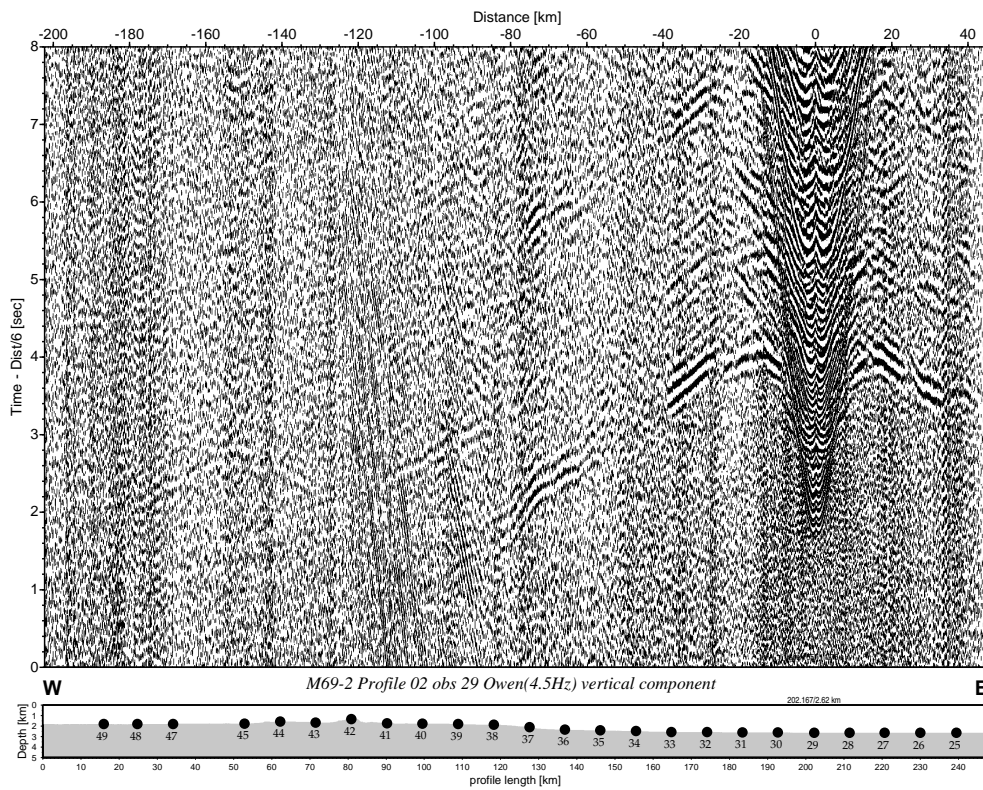


Figure B.21: Seismogram of OBS 29, channel 4

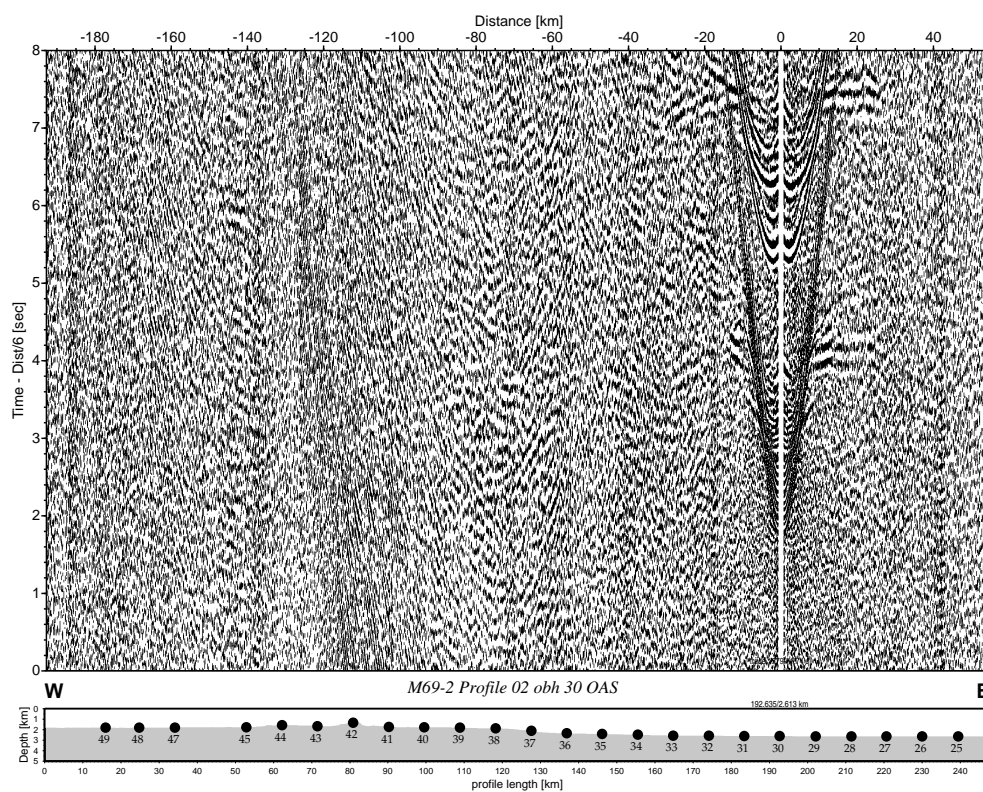


Figure B.22: Seismogram of OBH 30

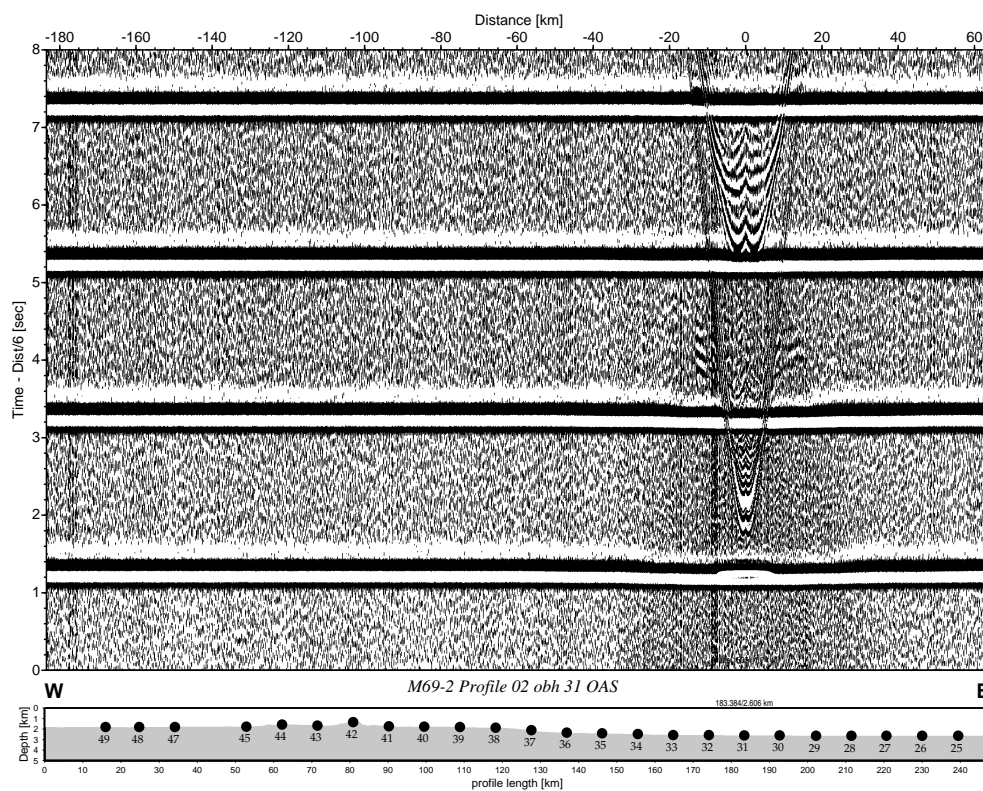


Figure B.23: Seismogram of OBH 31

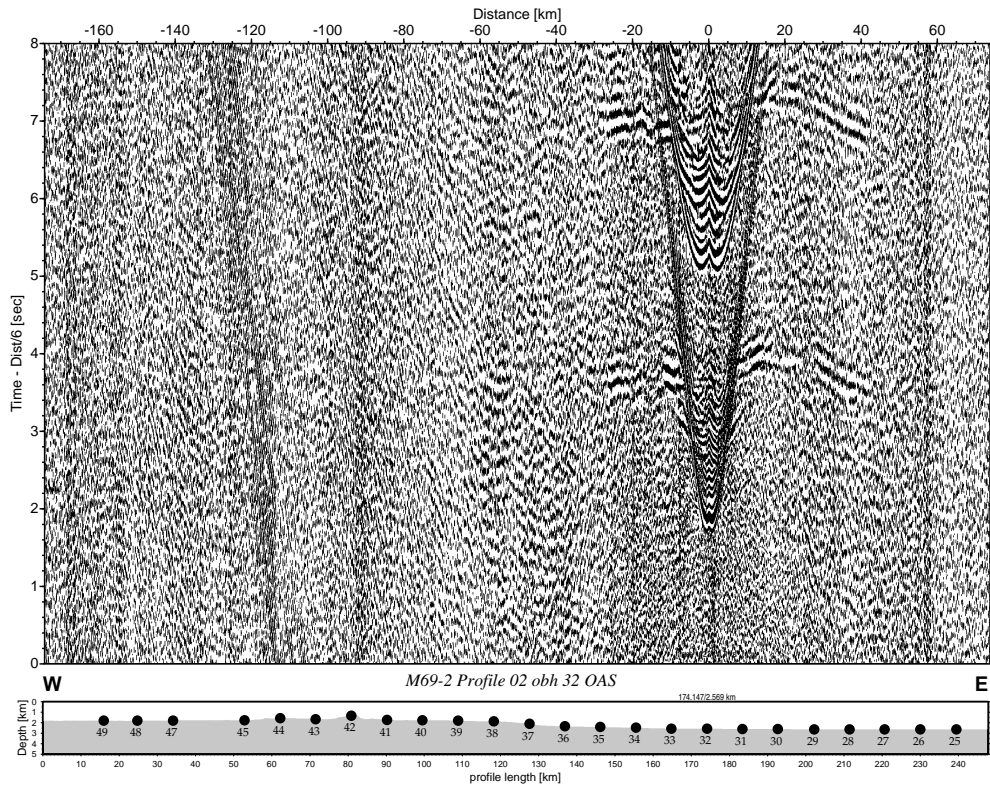


Figure B.24: Seismogram of OBH 32

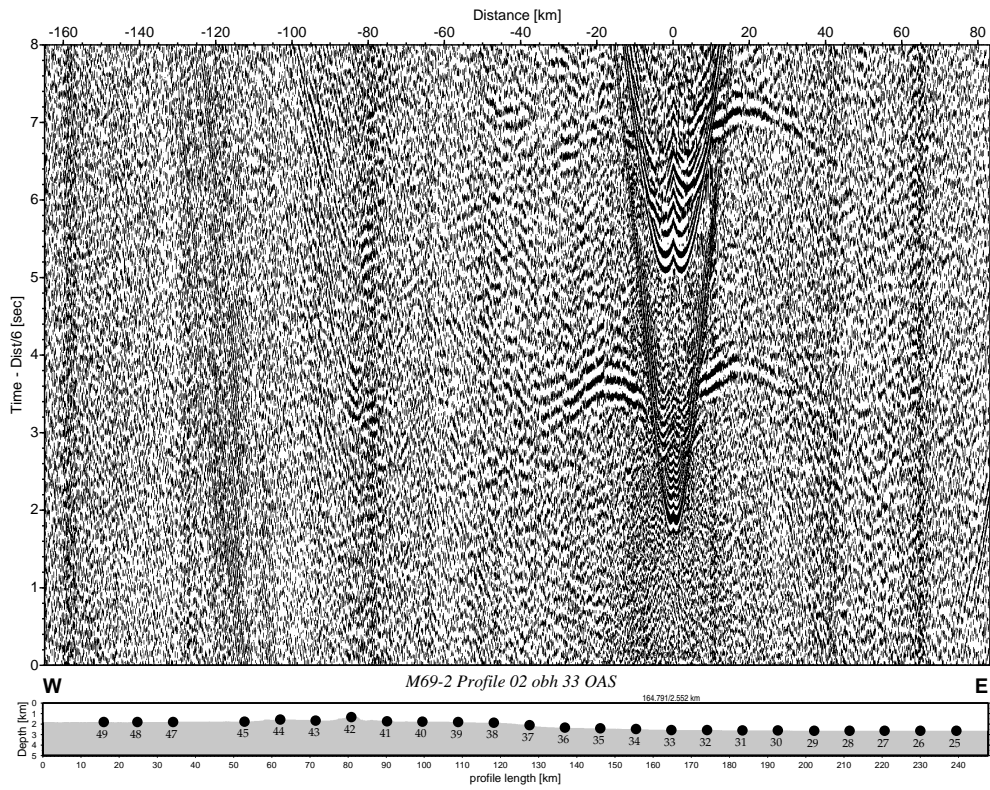


Figure B.25: Seismogram of OBH 33

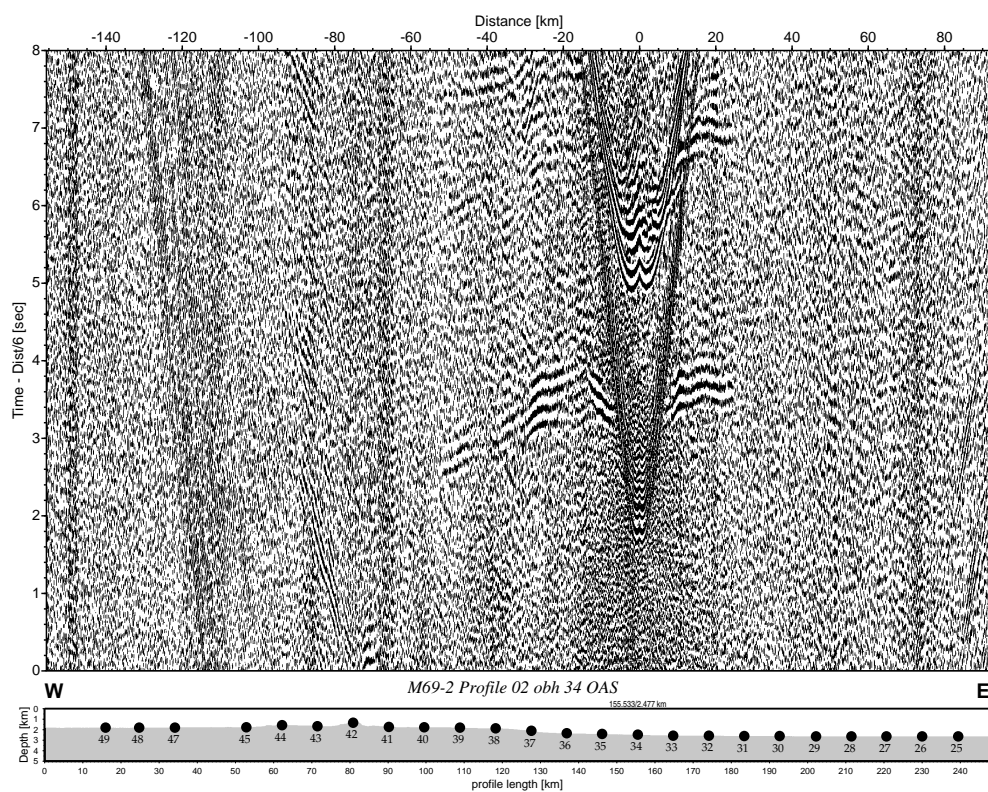


Figure B.26: Seismogram of OBH 34

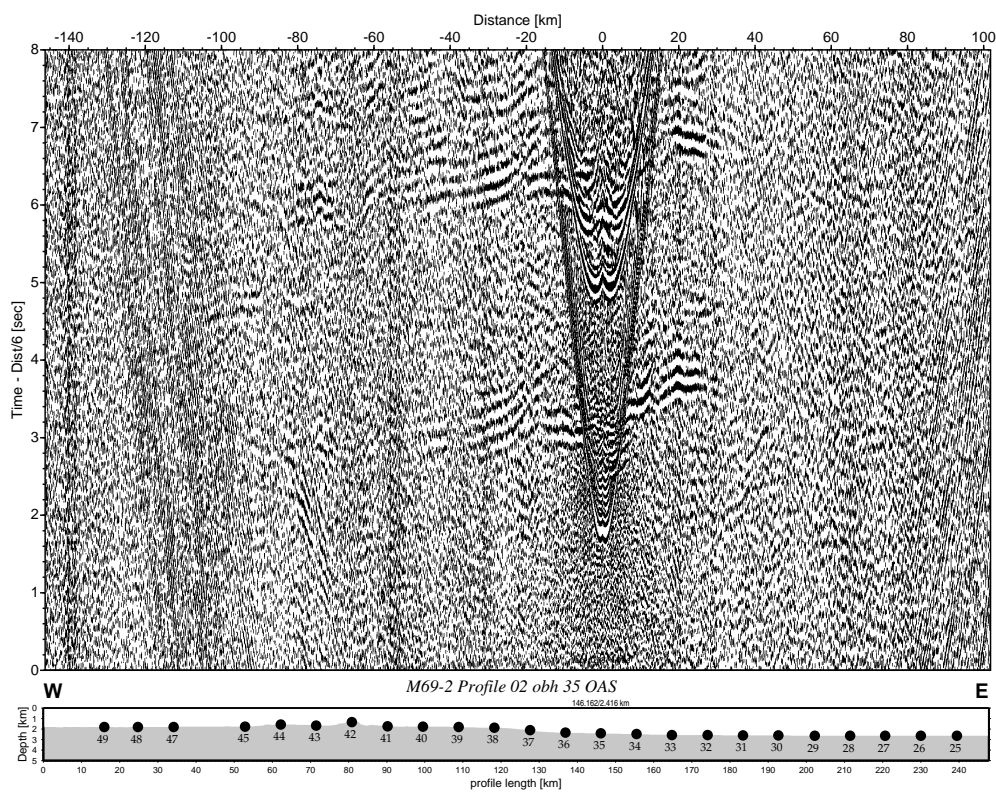


Figure B.27: Seismogram of OBH 35

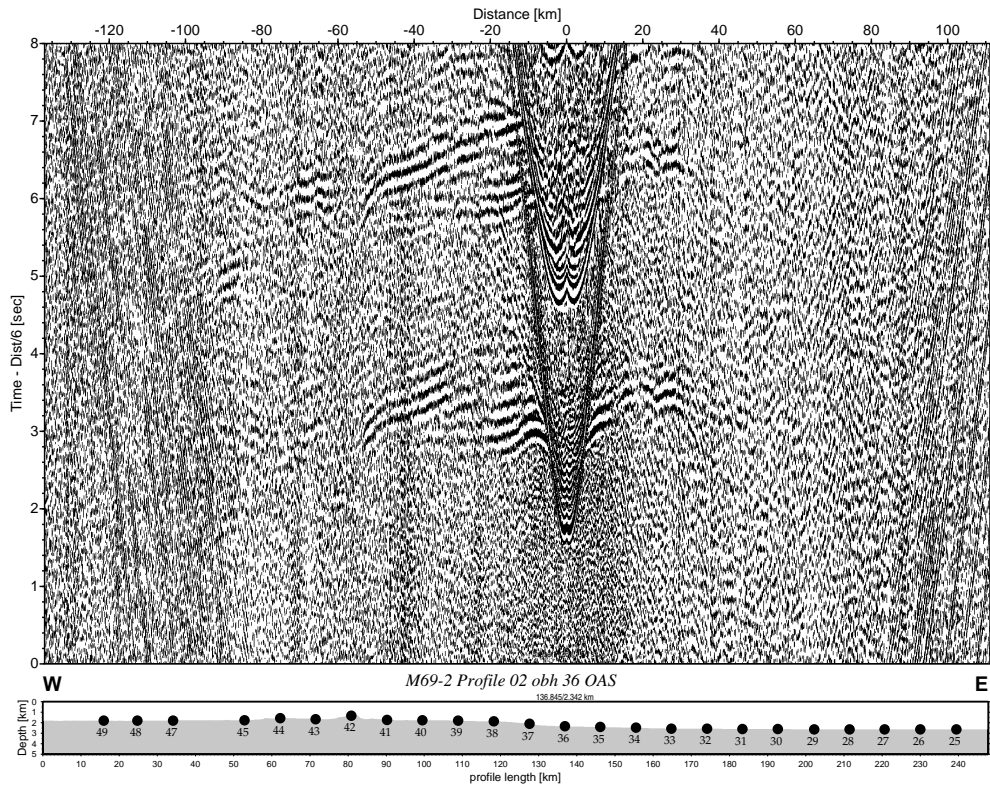


Figure B.28: Seismogram of OBH 36

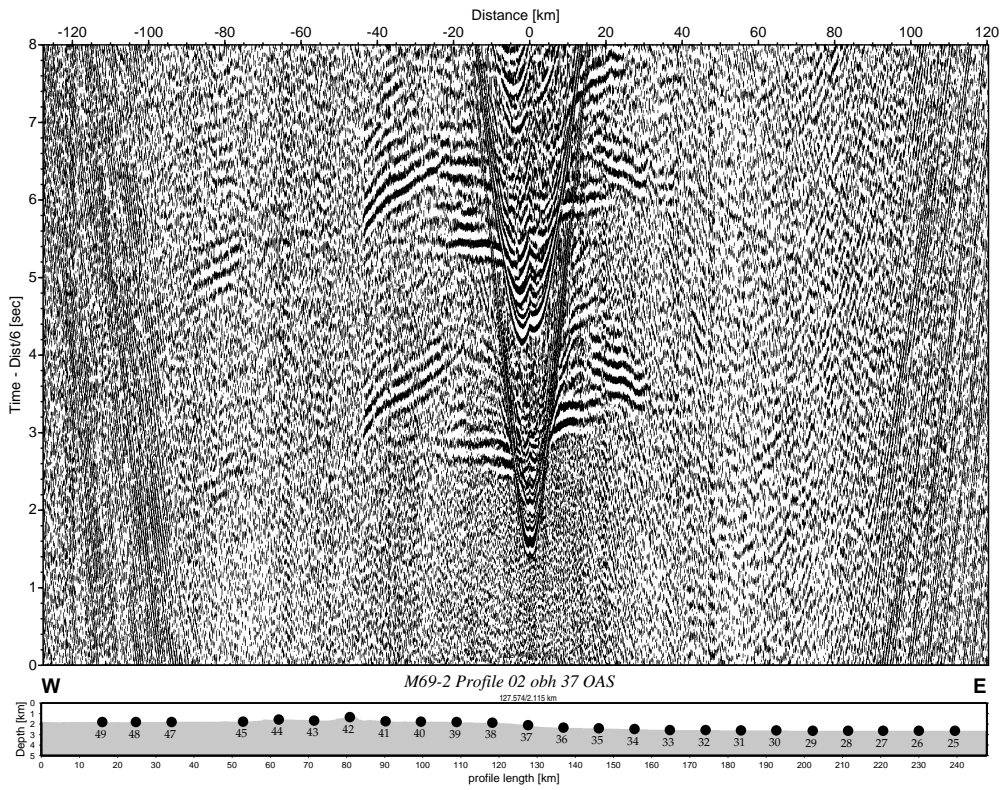


Figure B.29: Seismogram of OBH 37

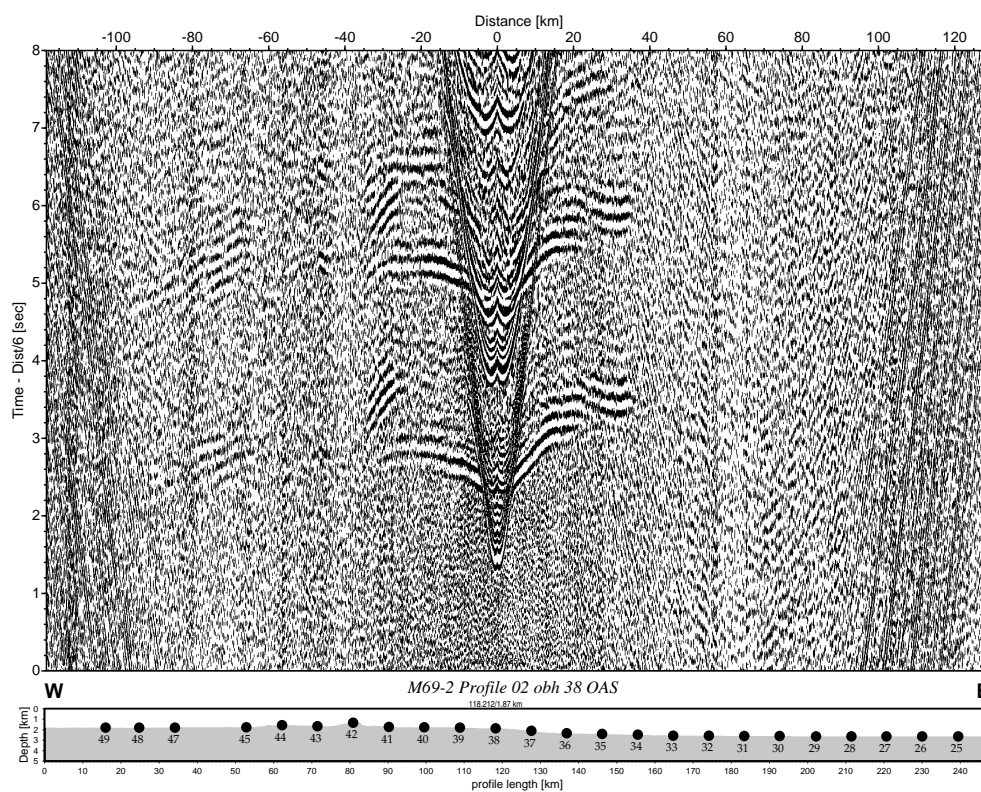


Figure B.30: Seismogram of OBH 38

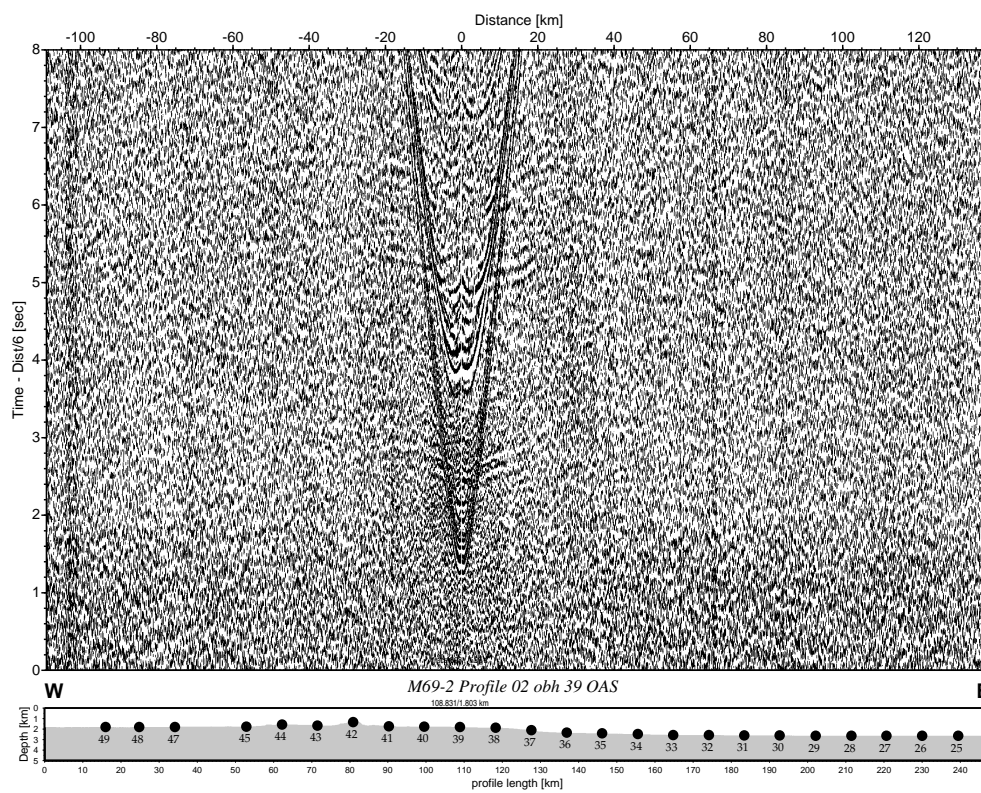


Figure B.31: Seismogram of OBH 39

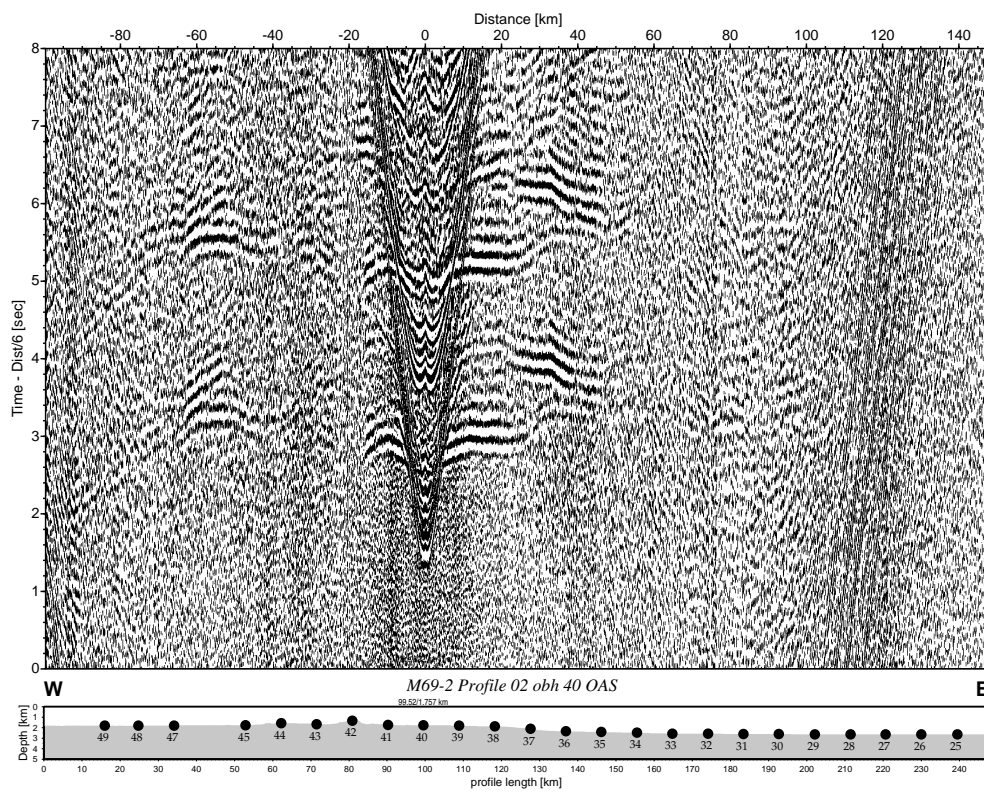


Figure B.32: Seismogram of OBH 40

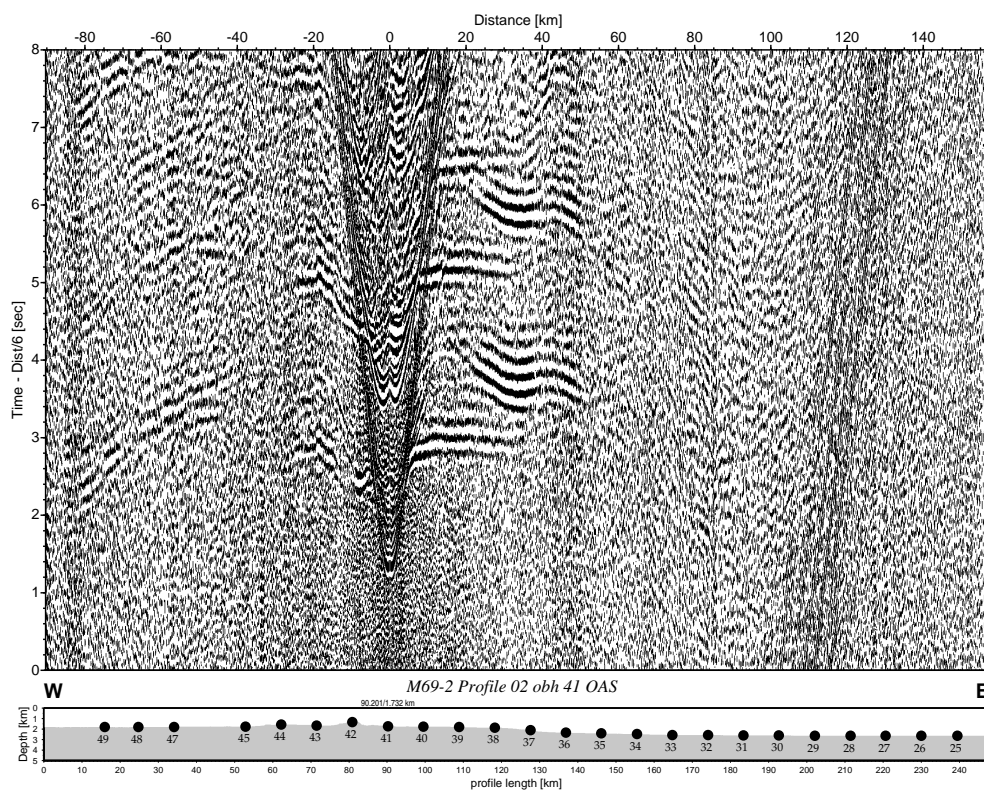


Figure B.33: Seismogram of OBH 41

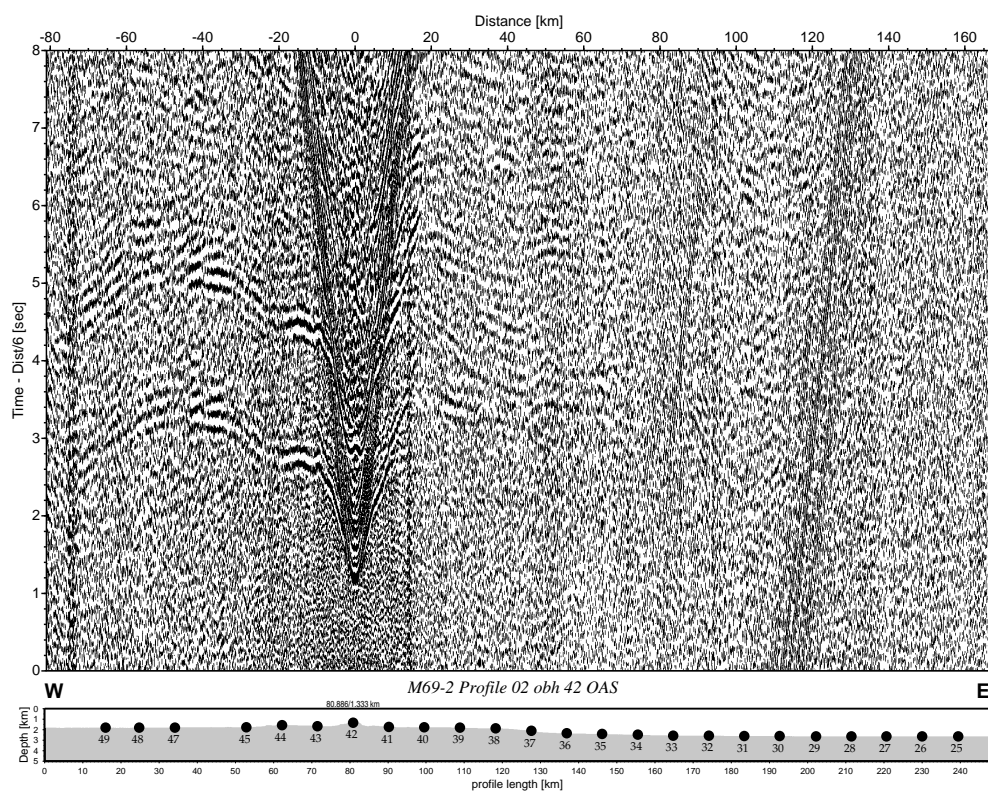


Figure B.34: Seismogram of OBH 42

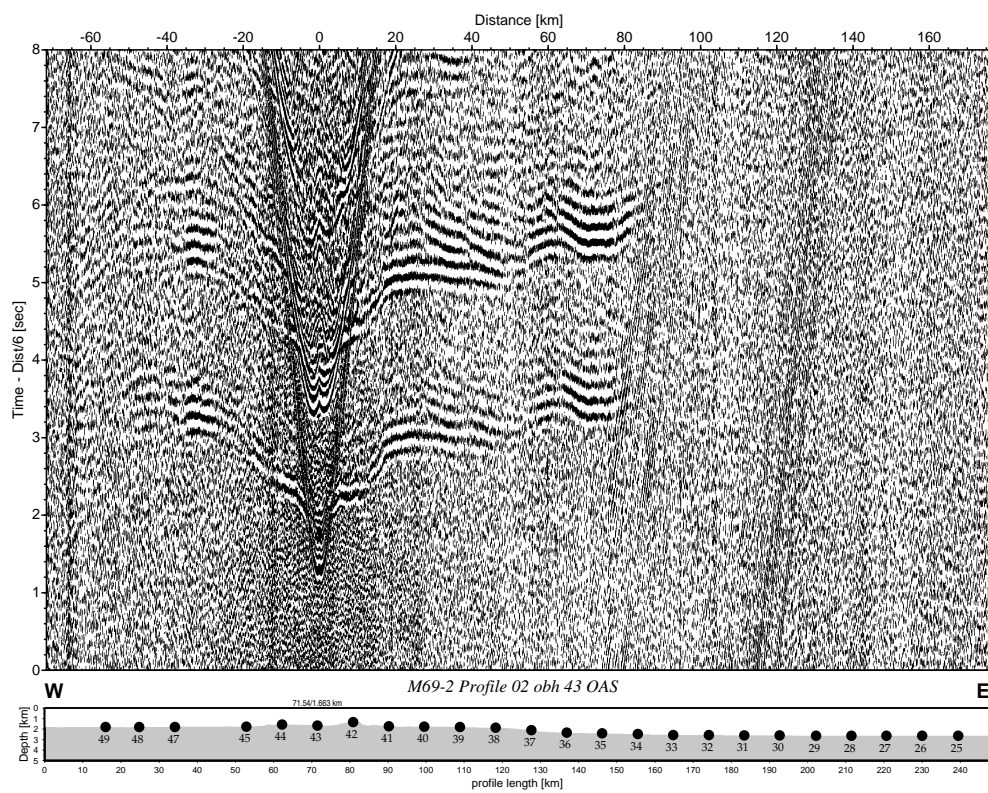


Figure B.35: Seismogram of OBH 43

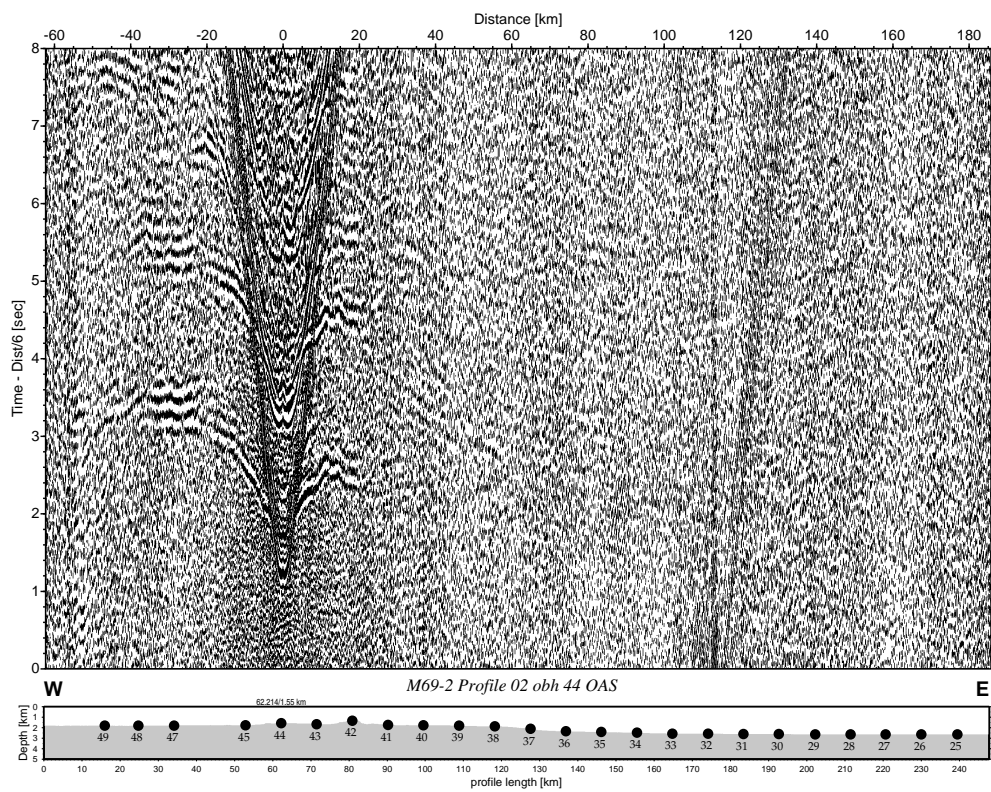


Figure B.36: Seismogram of OBH 44

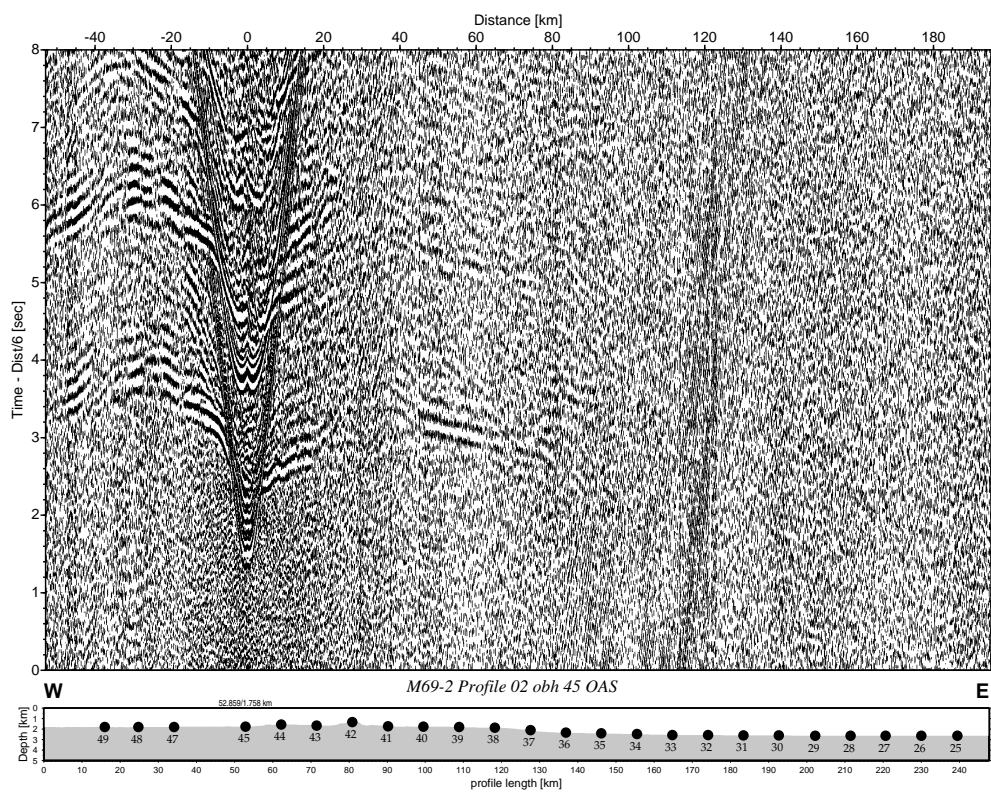


Figure B.37: Seismogram of OBH 45

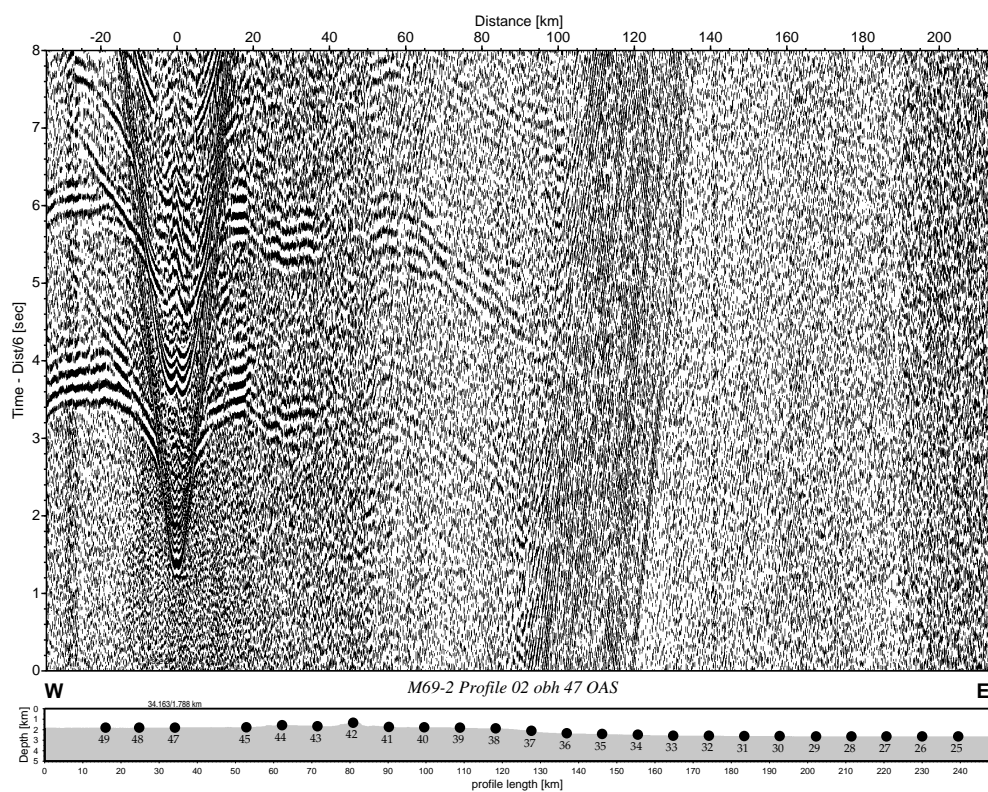


Figure B.38: Seismogram of OBH 47

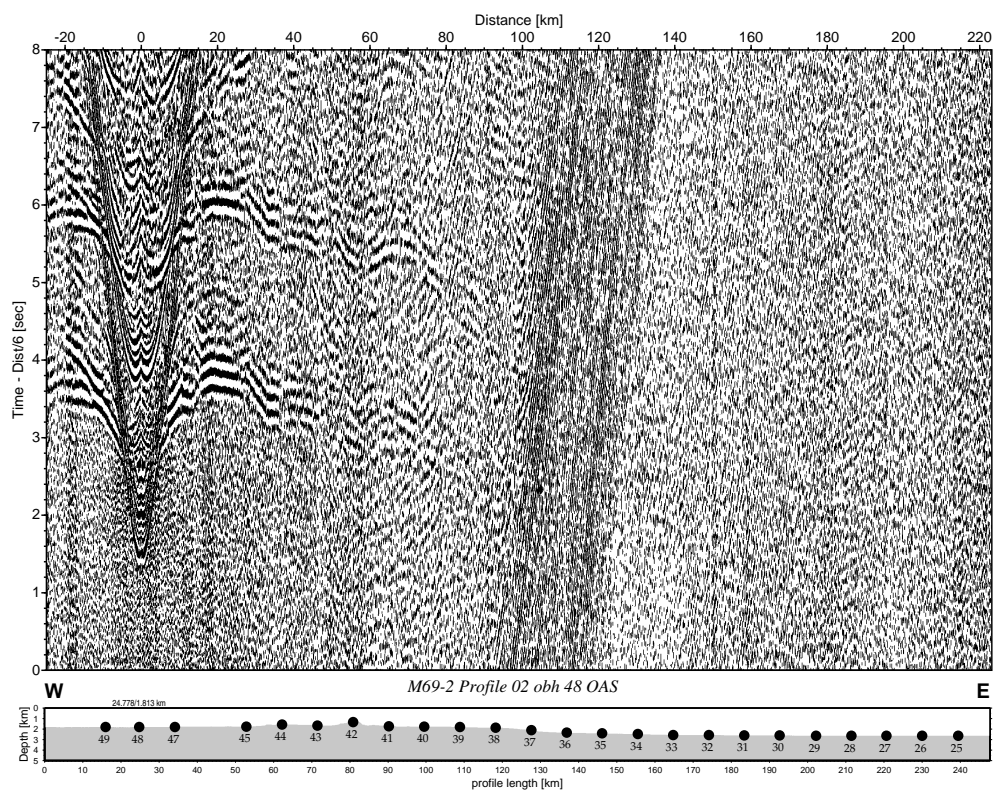


Figure B.39: Seismogram of OBH 48

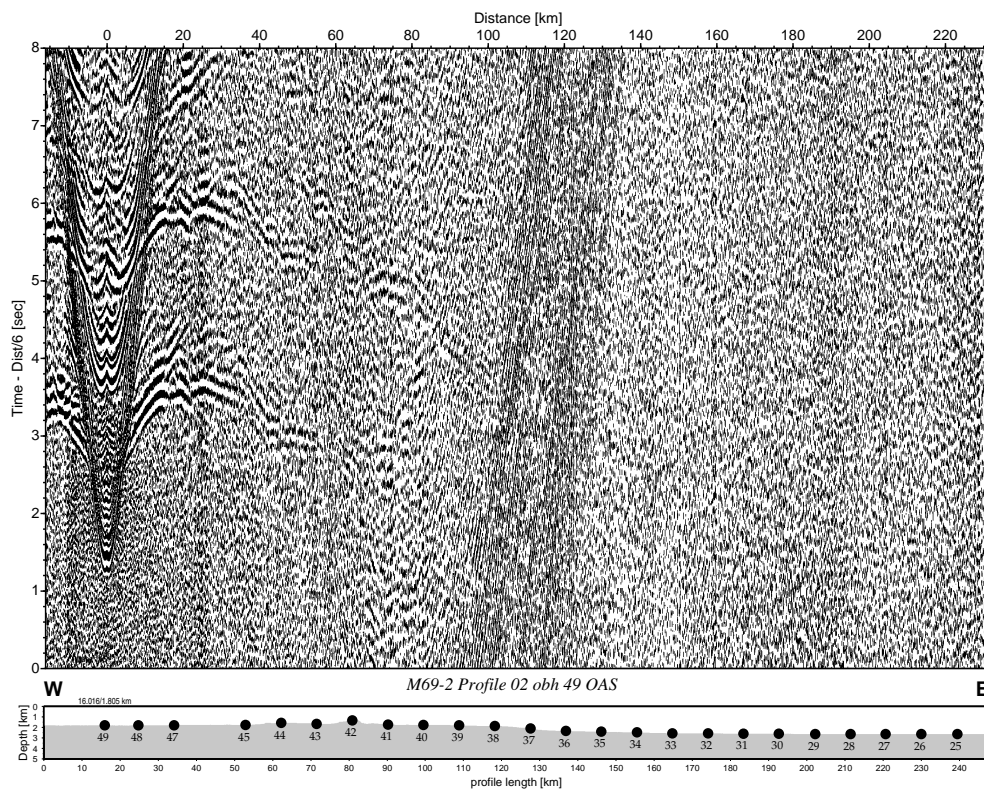


Figure B.40: Seismogram of OBH 49

Abbreviations

EAB	East Alboran Basin
LSQR	Least Squares
LVZ	Low Velocity Zone
MCS	MultiChannel Seismic data
OBS	Ocean Bottom Seismometer
OBH	Ocean Bottom Hydrophone
Pg	Seismic compressional wave refracted in the crust
PmP	Seismic compressional wave reflected from the crust-mantle boundary
Pn	Seismic compressional wave refracted in the upper mantle
Ps	Seismic compressional wave refracted in the sedimentary layer
Pu	Seismic compressional wave refracted in the upper crust
RMS	Root Mean Square
SAB	South Alboran Basin
WAB	West Alboran Basin

List of Figures

1.1	Tectonic map of present plate boundaries of the main plates (http://pubs.usgs.gov/gip/dynamic/slabs.html).	2
1.2	Map of the Mediterranean Sea. The red rectangle denotes the Alboran Sea.	3
1.3	Two types of subduction: the Chilean or Andean subduction in a compressional regime (top) and the Mariana type subduction with an extensional back-arc basin (bottom). The figure is taken from <i>Stern</i> (2002) after <i>Uyeda and Kanamori</i> (1979).	4
1.4	Compilation of figures of <i>Rosenbaum et al.</i> (2002) for the evolution of the western Mediterranean. (a) Beginning of the evolution of the western Mediterranean in Oligocene. (b) First stage of extension and formation of the Valencia Trough and the Gulf of Lion in Late Oligocene. (c) Formation of the Provençal Basin in Early Burdigalian. (d) Opening of the Algerian Basin in Late Burdigalian. (e) Collision of the Kabylies Block with the African margin and first stage of opening the Alboran Basin in Middle Miocene. (f) Accretion of Betic and Rif on Iberia and Africa (respectively) in Tortonian. (g) Start of formation of the Northern Tyrrhenian Sea in Messinian. (h) Further opening of the Tyrrhenian Sea in the South in Late Pliocene.	6
1.5	(a) Geological map of the Alboran Sea and surrounding onshore (after <i>Comas et al.</i> (1999)). Black circles show location of ODP Leg 161 sites and DSDP Site 121. (b) Topographic map of the Alboran Sea. Main structural features are shown. EAB = East Alboran Basin; SAB = South Alboran Basin; SBB = South Balearic Basin; WAB = West Alboran Basin; YB = Yusuf Basin.	10
1.6	Sketch of convective removal (after <i>Platt and England</i> , 1993). (a) The initial state with the initial thermal profile in equilibrium. (b) Thickened lithosphere with a reduced thermal gradient. (c) Convective removal thinned the lithosphere and replaced removed lithosphere by asthenospheric mantle. The thermal gradient was induced with a step at the lithosphere-asthenosphere boundary. (d) Extension results and the thermal gradient due to lithospheric thinning increases. Through time the thermal gradient gets back to its equilibrium.	13

1.7	Sketch of the evolution of slab rollback (<i>Rosenbaum et al., 2002</i> after <i>Loneragan and White, 1997</i>). (a) The vertical negative buoyant force F of the subducting slab has the two components P (slab pull) and R (slab retreat). If R is big enough and the asthenospheric mantle cannot support the overlying cold and dense slab anymore, the slab starts to retreat. (b) Extension starts and opens a back-arc basin when the velocity of the retreating slab v_r exceeds the velocity of the plate convergence v_c	14
1.8	Seismic map of <i>Bufo</i> <i>et al.</i> (2011). Epicenters in the Alboran region from 1990-2010 with a magnitude larger than 3.0 (catalog of Instituto Geográfico Nacional (IGN), Spain). Circles: earthquake shallower than 40 km, squares: earthquakes between 40 and 150 km depth, triangles: earthquakes deeper than 150 km and star: 2010 Granada earthquake.	16
2.1	Example for a model layering from <i>rayinvr</i> (<i>Zelt and Ellis, 1988</i>).	20
2.2	Grid structure of a velocity model. A mesh is hanging below the seafloor with a spacing increasing with depth. The used grid spacing of the x-axis for this study is 0.5 km, which is due to distinguishability not visualised in this grid.	21
2.3	Forward star of 5 x 10 nodes used in the graph method. Circles mark grid nodes of the used mesh.	22
2.4	Comparison of a ray path with the graph method (a) and with a combination of graph method and ray bending (b). A hybrid method results in a smoother ray and higher accuracy of travelttime with a lower RMS error.	23
3.1	Location of profile 2 of the Meteor cruise M69-2. Yellow circles are the OBH and OBS positions.	30
3.2	An OBS (left) and OBH (right) while deployment. The hydrophone on the photo with the OBH is not visible.	31
3.3	This diagram illustrates the steps for data pre-processing. The steps are run on board the vessel. The final output is a dataset in SEG-Y format which is used to pick the phases of the seismic waves (section 3.1.4).	33
3.4	Data of OBH 36 in the program <i>zplot</i> . In this program for phase picking, different parameters can be adjusted for a better view on the data and therewith better picks of phases.	34
3.5	Location of the OBS, LOBSTER and landstation of the seismic network from August 2009 to January 2010. OBS and LOBSTER are marked with numbers and landstations with name shortcut of the station.	35

- 3.6 An example of the STA/LTA trigger algorithm: (a) The filtered seismic signal. (b) STA and LTA average amplitude of the seismic signal. (c) STA/LTA ratio with the window of trigger activity between the trigger ratio (left dotted line) and the de-trigger ratio (right dotted line). The pre-event time (PEM, dotted rectangle) and the post-event time (PET, dashed rectangle) complete the by this algorithm selected event. (d) The selected seismic signal of the event. From *Trnkoczy* (2002). 38
- 3.7 Examples of records of an event for (a) good and (b) bad data quality. Filtering while picking can help to identify phases which are hidden in the noise. (c) is the filtered record of (b). 40
- 3.8 The waveforms show a zoom into a P- and a S-arrival on OBS08 for the event on 30 October 2009 at 07:01 am. (a) A clear P-arrival is shown with low noise on the station. (b) The S-arrival is also well identifiable. 40
- 4.1 Distribution of the (a) depth nodes and (b) velocity nodes in the forward model. (a) Squares define the position of depth nodes. The upper layer, which simulates the seafloor, has a fine spacing of 0.5 km because of measured bathymetry data. Below the seafloor a spacing of 3 to 10 km is defined through the modeling phase. (b) Triangles define the velocity nodes. Those triangles with apex down are velocity nodes which define the velocity at the top of a layer. Apex up triangles show the position of nodes which define the velocity at the bottom of a layer. The distance between velocity nodes is 30 km. In addition to the node spacing the layering of the final forward model is illustrated (left = West, right = East). 44
- 4.2 The final forward model. Isolines are every 0.5 km/s between 2 and 7 km/s and every 0.1 km/s between 7 and 8 km/s. Left = West, right = East. . . . 45
- 4.3 Closeup of the seismogram of OBH33. Reflections of the bottom of the low velocity zone and the bottom of the basement are recorded (red arrows). . . 46
- 4.4 Top: Coverage of the resulting model with the forward modeling method. Bottom: Fitting of the data (colored bars are the error bars for the different phases) on the resulting velocity model. Left = West, right = East. 47
- 4.5 Testing of the velocity smoothing (SV) for the modeling step with PmP-phase. (a) χ^2 and corresponding horizontal and vertical roughnesses for different SV values. (b) RMS and corresponding horizontal and vertical roughnesses for different SV values. Chosen parameter was for the PmP-phase the value 30 because of a low error and low roughness. 50
- 4.6 An example for the “step” in the refraction arrivals of OBH32 as indication of a LVZ (red circles). 51

- 4.7 Different starting models with a velocity gradient below the basement. Isolines are every 0.5 km/s and from 7 km/s onward every 0.1 km/s. The thick black line shows one of different tested Mohos inverted with this starting model. 51
- 4.8 Different starting models with a velocity structure below the basement. Isolines are every 0.5 km/s and from 7 km/s onward every 0.1 km/s. The thick black line shows one of different tested Mohos inverted with this starting model. 52
- 4.9 Different starting models. Top: Result of the forward modeling. Center: Forward model with a 0.5 km thick velocity transition zone between layers. Bottom: Forward model with a 2 km thick velocity transition zone between crust and mantle and a 0.5 km thick velocity transition zone between other layers. Isolines are every 0.5 km/s and from 7 km/s onward every 0.1 km/s. The thick black line shows one of different tested Mohos inverted with this starting model. 53
- 4.10 Resulting models after inversions of different starting models. Top: Inversion result with a starting model with a velocity gradient below the basement (figure 4.7, top). Center: Inversion result of a starting model with structure below the basement (figure 4.8, bottom). Bottom: Inversion result with the forward model result as starting model (figure 4.9, bottom). Isolines are every 0.5 km/s and from 7 km/s onward every 0.1 km/s. The thick black line shows the resulting Moho. 54
- 4.11 Top: Average of Tomo2D inversions of Ps, Pu, Pg and PmP. The average Moho is shown as a black line. Grey shaded is the standard deviation of the Moho. Isolines are every 0.5 km/s. Bottom: Standard deviation of the crustal inversions. 57
- 4.12 The histograms show the traveltimes residuals for two different modelings. (a) Residuals for a starting model with a velocity gradient (figure 4.7, top). (b) Resulting residuals after 5 inversion iterations. (c) Residuals for the starting model of forward modeling result with an inserted velocity gradient between sedimentary layer and crust and between crust and mantle (figure 4.9, bottom). (d) Resulting residuals after 5 inversion iterations. . . 58
- 4.13 DWS of the inversion result. 58
- 4.14 Velocity model after inversion of Ps, Pu, Pg, PmP and Pn phases. Isolines are every 0.5 km/s. (Enlarged plot is in the appendix: figure A.1.) 59
- 4.15 Data example for (a) OBH38 and (b) OBH41. 61

4.16	Checkerboard test with an anomaly of 5%. (a), (c) and (e) are the inserted anomalies, (b), (d) and (f) the results of the checkerboard test, respectively. (a) Checkerboard grid size of 10 km × 2 km. (b) Recovery of the 10 km × 2 km checkerboard grid. In the upper ~3 to 5 km the resolution of the velocity model is fine enough to resolve the checkerboard structure. This includes the sedimentary layer and the upper crust. Only the westernmost part of the model does not resolve the checkerboard structure. (c) Checkerboard grid size of 20 km × 3 km. (d) The larger grid cells are resolved in the sedimentary layer and the crust. Only in the thicker crust the lower crust is not resolved very good. (e) Checkerboard grid size of 50 km × 5 km. (f) Huge grid cells of the checkerboard are resolved in the whole crust.	62
5.1	Velocity-depth profile for v_p and v_s and damping values with depth (Q_p and Q_s). A high Q describes a low damping and vice versa.	64
5.2	Recorded seismogram of OBS26.	65
5.3	Recovered seismogram after amplitude modeling for OBS26.	65
6.1	Comparison of velocity profiles of the western half of the seismic section with the velocity structure of typical continental crust after <i>Christensen and Mooney</i> (1995) (grey shaded).	67
6.2	Comparison of velocity profiles of the eastern half of the seismic section with the velocity structure of typical oceanic crust in the Atlantic ocean (59 - 127 Ma old) after <i>White et al.</i> (1992) (grey shaded).	69
6.3	The interpretation of <i>Booth-Rea et al.</i> (2007) of the in 1992 recorded MCS data plotted over the resulting velocity profile of this study (figure 4.14 / A.1), illuminated with the MCS data.	70
6.4	Section of the by <i>Booth-Rea et al.</i> (2007) analysed MCS profile. Arrows denote identified faults. I to III are the defined sedimentary units and MCR is the mid crustal reflector. White and grey dots define the unit boundaries and black dots the acoustic basement. (<i>Booth-Rea et al.</i> , 2007)	71
6.5	Illustration of the resulting velocity profile. The crust can be separated in three different parts. From West to East the crustal styles are of continental crust, transitional crust with more similarities in the crustal velocities to continental crust and oceanic crust. The two westernmost segments can also be seen as one part because both have a crustal velocity structure similar continental crust. The transition to oceanic crustal velocities is relatively abrupt at the end of the central segment (km 40 - 140).	73
7.1	Sketch to illustrate the GAP value. The yellow stars are the hypocenters of an earthquake and the red triangles are stations which recorded this earthquake. In (a) a GAP value of about 110° is displayed. (b) shows a value of 210° where information from just one side of the hypocenter is provided for the location of the earthquake and the minimum 1D velocity model.	78

7.2	Network of the TOPO-MED project (rectangles) and stations of the refraction wide-angle profile 2 of M69-2 (circles).	79
7.3	Example for selected earthquakes of a velocity model with the criteria enumerated in section 7.1. Blue triangles show the stations and red circles the events. Light grey lines illustrate the ray coverage by connecting each event with the stations that recorded this event. Right is a depth distribution of the earthquakes projected along a N-S oriented line. In the lower plot a projection of earthquakes along an E-W oriented line is shown. The histogram in the lower right corner shows the number of earthquakes for depth intervals of 2.5 km.	81
7.4	Tested starting velocity models (left) and their results (right). Light grey shaded is the range of resulting velocities (except some transition zones where the depth step is different to the most other models). Dark grey shows the velocity range where more than 75 % of the resulting velocity models are included.	82
7.5	Results of the inversion with extremely slow and fast starting models. More information see text.	83
7.6	The resulting ray coverage for the final minimum 1D P-velocity model with 61 analysed events. Subfigures and symbols are explained in figure 7.3.	84
7.7	Resulting velocity profiles with different starting v_p/v_s -ratios.	85
7.8	A regional map with the station correction for all used stations for the calculation of the minimum 1D velocity profile is shown. The reference station is marked as a grey square (OBS 09). Stations with crosses have a positive station correction compared to the reference station. Circles denote negative station corrections. The size of the symbols describe the magnitude of station correction.	87
7.9	Station correction (red line) of all used recording stations are plotted for comparison together with the station elevation (blue line) in a graph. Landstations are sorted from South to North (left to right).	88
7.10	The ray coverage of all earthquakes in the dataset with a hypocenter deeper than 2 km. Subfigures and symbols are explained in figure 7.3.	89
7.11	Heat flow measurements analysed by <i>Polyak et al.</i> (1996) in mW/m^2 . Left: West Alboran Basin, right: East and South Alboran Basin. Isolines of the bathymetry are in an interval of 200 m. DB = Djibouti Bank, SAB = South Alboran Basin, YB = Yusuf Basin.	90
7.12	The depth distribution for the Alboran Basin of the in this study localized earthquakes.	91
7.13	Focal mechanisms in the Alboran Basin. Data of different studies are shown (see legend).	93
7.14	Earthquakes of the NEIC Catalog (1990 - 2012). Additionally, three different possible plate boundaries are shown for the Alboran region: NUVEL-1A model (<i>DeMets et al.</i> , 1990, 1994), PB2002 (<i>Bird et al.</i> , 2002; <i>Bird</i> , 2003) and the Trans Alboran Shear Zone (simplified illustration).	93

A.1	The final inversion model. Isolines are every 0.5 km/s. Left = West, right = East. This is an enlarged plot of figure 4.14.	102
B.1	Observed and calculated traveltimes. The observed traveltimes are the picked traveltimes with errorbars in grey. Red are the calculated traveltimes of refractions and blue are reflected calculated traveltimes. OBH/OBS are enumerated from the westernmost (OBH49) to the easternmost station (OBS25).	103
B.2	Seismogram of OBS 25, channel 1	107
B.3	Seismogram of OBS 25, channel 2	107
B.4	Seismogram of OBS 25, channel 3	108
B.5	Seismogram of OBS 25, channel 4	108
B.6	Seismogram of OBS 26, channel 1	109
B.7	Seismogram of OBS 26, channel 2	109
B.8	Seismogram of OBS 26, channel 3	110
B.9	Seismogram of OBS 26, channel 4	110
B.10	Seismogram of OBS 27, channel 1	111
B.11	Seismogram of OBS 27, channel 2	111
B.12	Seismogram of OBS 27, channel 3	112
B.13	Seismogram of OBS 27, channel 4	112
B.14	Seismogram of OBS 28, channel 1	113
B.15	Seismogram of OBS 28, channel 2	113
B.16	Seismogram of OBS 28, channel 3	114
B.17	Seismogram of OBS 28, channel 4	114
B.18	Seismogram of OBS 29, channel 1	115
B.19	Seismogram of OBS 29, channel 2	115
B.20	Seismogram of OBS 29, channel 3	116
B.21	Seismogram of OBS 29, channel 4	116
B.22	Seismogram of OBH 30	117
B.23	Seismogram of OBH 31	117
B.24	Seismogram of OBH 32	118
B.25	Seismogram of OBH 33	118
B.26	Seismogram of OBH 34	119
B.27	Seismogram of OBH 35	119
B.28	Seismogram of OBH 36	120
B.29	Seismogram of OBH 37	120
B.30	Seismogram of OBH 38	121
B.31	Seismogram of OBH 39	121
B.32	Seismogram of OBH 40	122
B.33	Seismogram of OBH 41	122
B.34	Seismogram of OBH 42	123
B.35	Seismogram of OBH 43	123
B.36	Seismogram of OBH 44	124

B.37 Seismogram of OBH 45	124
B.38 Seismogram of OBH 47	125
B.39 Seismogram of OBH 48	125
B.40 Seismogram of OBH 49	126

List of Tables

3.1	STA/LTA parameter used in this study. s = length of short term window, l = length of long term window, m = mean removal window length, t = trigger ratio, d = de-trigger ratio, S = minimum number of stations with detected events, M = network trigger time window length. S and M are typical used values. The other parameters are determined for this study.	39
4.1	Thickness and depth of the layers in the final forward velocity model.	46
4.2	Chosen parameters for different phases. The tested modeling steps are named after the last added phase (e.g. parameter test for sedimentary layer, upper and lower crust refractions and mantle reflections (Ps, Pu, Pg and PmP) is named PmP). Parameter abbreviations are explained in the text.	48
6.1	The thicknesses of the sediment and the crust after seismic inversion are listed in this table for profiles below each seismic station. Sedimentary thickness is calculated by subtracting the water depth from the basement depth, which is taken from the forward modeling. Due to damping in the sedimentary layer while inversion with the program Tomo2D, the basement depth does not change between forward modeling and inversion. For the crustal thickness, the basement depth is subtracted from the Moho depth, which is a result of the inversion.	68
7.1	The final minimum 1D velocity profile showing the result of the inversion with a starting v_p/v_s -ratio of 1.70.	86

Bibliography

- Bailey, D. K. (1992), Episodic alkaline igneous activity across Africa: implications for the causes of continental break-up, *Magma Generation and Break-Up Processes. Geological Society, London. Special Publications*, 68, 91–98, doi:10.1144/GSL.SP.1992.068.01.06.
- Ballesteros, M., J. Rivera, A. Muñoz, A. Muñoz-Martín, J. Acosta, A. Carbó, and E. Uchupi (2008), Alboran Basin, southern Spain – Part II: Neogene tectonic implications for the orogenic float model, *Marine and Petroleum Geology*, 25, 75–101, doi:10.1016/j.marpetgeo.2007.05.004.
- Bickel, S. H. (1990), Velocity-depth ambiguity of reflection traveltimes, *Geophysics*, 55(3), 266–276, doi:10.1190/1.1442834.
- Birch, F. (1961), The Velocity of Compressional Waves in Rocks to 10 Kilobars, Part 2, *Journal of Geophysical Research*, 66(7), 2199–2224, doi:10.1029/JZ066i007p02199.
- Bird, P. (2003), An updated digital model of plate boundaries, *Geochemistry Geophysics Geosystems*, 4(3), 1027, doi:10.1029/2001GC000252.
- Bird, P., Y. Y. Kagan, and D. D. Jackson (2002), Plate Tectonics and Earthquake Potential of Spreading Ridges and Oceanic Transform Faults, *Plate Boundary Zones, Geophys. Monogr. Ser.*, 30, 203–218, doi:10.1029/030GD12.
- Bishop, T. N., K. P. Bube, R. T. Cutler, R. T. Langan, P. L. Love, J. R. Resnick, R. T. Shuey, D. A. Spindler, and H. W. Wyld (1985), Tomographic determination of velocity and depth in laterally varying media, *Geophysics*, 50, 903–923, doi:10.1190/1.1441970.
- Booth-Rea, G., C. R. Ranero, J. M. Martínez-Martínez, and I. Grevemeyer (2007), Crustal types and Tertiary tectonic evolution of the Alborán sea, western Mediterranean, *Geochemistry Geophysics Geosystems*, 8(10), doi:10.1029/2007GC001639, Q10005.
- Bourgeois, J., A. Mauffret, A. Ammar, and A. Demnati (1992), Multichannel Seismic Data Imaging of Inversion Tectonics of the Alboran Ridge (Western Mediterranean Sea), *Geo-Marine Letters*, 12, 117–122.
- Brun, J.-P., and C. Faccenna (2008), Exhumation of high-pressure rocks driven by slab rollback, *Earth and Planetary Science Letters*, 272, 1–7, doi:10.1016/j.epsl.2008.02.038.

- Bufo, E., M. Bezzeghoud, A. Udías, and C. Pro (2004), Seismic Sources on the Iberia-African Plate Boundary and their Tectonic Implications, *Pure and Applied Geophysics*, 161, 623–646, doi:10.1007/s00024-003-2466-1.
- Bufo, E., C. Pro, S. Cesca, A. Udías, and C. del Fresno (2011), The 2010 Granada, Spain, Deep Earthquake, *Bulletin of the Seismological Society of America*, 101(5), 2418–2430, doi: 10.1785/0120110022.
- Burke, K. (1996), The African Plate, *South African Journal of Geology*, 99(4), 341–409.
- Burrus, J. (1984), Contribution to a geodynamic synthesis of the Provençal Basin (north-western Mediterranean), *Marine Geology*, 55, 247–269.
- Calvert, A., E. Sandvol, D. Seber, M. Barazangi, S. Roecker, T. Mourabit, F. Vidal, G. Alguacil, and N. Jabour (2000), Geodynamic evolution of the lithosphere and upper mantle beneath the Alboran region of the western Mediterranean: Constraints from travel time tomography, *Journal of Geophysical Research*, 105(B5), 10,871–10,898, doi: 10.1029/2000JB900024.
- Cavazza, W., F. Roure, and P. A. Ziegler (2004), The Mediterranean Area and the Surrounding Regions: Active Processes, Remnants of Former Tethyan Oceans and Related Thrust Belts, in *The TRANSMED Atlas – The Mediterranean Region from Crust to Mantle*, edited by W. Cavazza, F. M. Roure, W. Spakman, G. M. Stampfli, and P. A. Ziegler, Springer, Berlin Heidelberg, ISBN 978-3-540-22181-4.
- Christensen, N. I., and W. D. Mooney (1995), Seismic velocity structure and composition of the continental crust: A global view, *Journal of Geophysical Research*, 100(B7), 9761–9788.
- Chung, W.-Y., and H. Kanamori (1976), Source process and tectonic implications of the Spanish deep-focus earthquake of March 29, 1954, *Physics of the Earth and Planetary Interiors*, 13, 85–96.
- Comas, M. C., V. García-Dueñas, and M. J. Jurado (1992), Neogene tectonic evolution of the Alborán Sea from MCS data, *Geo-Marine Letters*, 12, 157–164.
- Comas, M. C., J. J. Dañobeitia, J. Álvarez-Marrón, and J. I. Soto (1995), Crustal reflections and structure in the Alborán basin: preliminary results of the ESCI-Alborán survey, *Revisita de la Sociedad Geológica de España*, 8(4), 529–542.
- Comas, M. C., J. P. Platt, J. I. Soto, and A. B. Watts (1999), The origin and tectonic history of the Alboran Basin: Insights from Leg 161 results, *Proceedings of the Ocean Drilling Program, Scientific Results*, 161, 555–579.
- Contreras-Reyes, E., I. Grevemeyer, A. B. Watts, E. R. Flueh, C. Peirce, S. Moeller, and C. Papenberg (2011), Deep seismic structure of the Tonga subduction zone: Implications for mantle hydration, tectonic erosion, and arc magmatism, *Journal of Geophysical Research*, 116, doi:10.1029/2011JB008434, B10103.

- Coward, M., and D. Dietrich (1989), Alpine tectonics – an overview, *Geological Society, London, Special Publications*, 45(1), 1–29, doi:10.1144/GSL.SP.1989.045.01.01.
- DeMets, C., R. G. Gordon, D. F. Argus, and S. Stein (1990), Current plate motions, *Geophysical Journal International*, 101(2), 425–478, doi:10.1111/j.1365-246X.1990.tb06579.x.
- DeMets, C., R. G. Gordon, D. F. Argus, and S. Stein (1994), Effect of recent revisions to the geomagnetic reversal time scale on estimates of current plate motions, *Geophysical Research Letters*, 21(20), 2191–2194.
- Dewey, J. F., W. C. Pitman III, W. B. F. Ryan, and J. Bonnin (1973), Plate Tectonics and the Evolution of the Alpine System, *Geological Society of America Bulletin*, 84, 3137–3180.
- Dietz, R. S. (1961), Continent and Ocean Basin Evolution by Spreading of the Sea Floor, *Nature*, 190, 854–857.
- Docherty, C., and E. Banda (1995), Evidence for the eastward migration of the Alboran Sea based on regional subsidence analysis: a case for basin formation by delamination of the subcrustal lithosphere?, *Tectonics*, 14(4), 804–818, doi:10.1029/95TC00501.
- Doglioni, C., E. Gueguen, F. Sàbat, and M. Fernandez (1997), The Western Mediterranean extensional basins and the Alpine orogen, *Terra Nova*, 9(3), 109–112, doi:10.1046/j.1365-3121.1997.d01-18.x.
- Doser, D. I., and H. Kanamori (1986), Depth of Seismicity in the Imperial Valley Region (1977-1983) and its Relationship to Heat Flow, Crustal Structure, and the October 15, 1979, Earthquake, *Journal of Geophysical Research*, 91(B1), 675–688.
- Duggen, S., K. Hoernle, P. van den Bogaard, L. Rüpke, and J. Phipps Morgan (2003), Deep roots of the Messinian salinity crisis, *Nature*, 422, 602–606, doi:10.1038/nature01553.
- Duggen, S., K. Hoernle, P. van den Bogaard, and C. Harris (2004), Magmatic evolution of the Alboran region: The role of subduction in forming the western Mediterranean and causing the Messinian Salinity Crisis, *Earth and Planetary Science Letters*, 218, 91–108, doi:10.1016/S0012-821X(03)00632-0.
- Duggen, S., K. Hoernle, A. Klügel, J. Geldmacher, M. Thirlwall, F. Hauff, D. Lowry, and N. Oates (2008), Geochemical zonation of the Miocene Alborán Basin volcanism (westernmost Mediterranean): geodynamic implications, *Contributions to Mineralogy and Petrology*, 156, 577–593, doi:10.1007/s00410-008-0302-4.
- Faccenna, C., C. Piromallo, A. Crespo-Blanc, L. Jolivet, and F. Rossetti (2004), Lateral slab deformation and the origin of the western Mediterranean arcs, *Tectonics*, 23, doi:10.1029/2002TC001488, TC1012.
- Fernández-Ibáñez, F., and J. I. Soto (2008), Crustal rheology and seismicity in the Gibraltar Arc (western Mediterranean), *Tectonics*, 27, doi:10.1029/2007TC002192, TC2007.

- Frizon de Lamotte, D., A. Crespo-Blanc, B. Saint-Bèzar, M. Comas, M. Fernández, H. Zeyen, P. Ayarza, C. Robert-Charrue, A. Chalouan, M. Zivi, A. Teixel, M.-L. Arboleya, F. Alvarez-Lobato, M. Julivert, and A. Michard (2004), TRANSMED Transect I: Iberian Meseta - Guadalquivir Basin - Betic Cordillera - Alboran Sea - Rif - Moroccan Meseta - High Atlas - Sahara Platform, in *The TRANSMED Atlas – The Mediterranean Region from Crust to Mantle*, edited by W. Cavazza, F. M. Roure, W. Spakman, G. M. Stampfli, and P. A. Ziegler, Springer, Berlin Heidelberg, ISBN 978-3-540-22181-4.
- Fuchs, K. (1968), The Reflection of Spherical Waves from Transition Zones with Arbitrary Depth-dependent Elastic Moduli and Density, *Journal of Physics of the Earth*, 16, 27–41, Special Issue.
- Fuchs, K., and G. Müller (1971), Computation of Synthetic Seismograms with the Reflectivity Method and Comparison with Observations, *Geophysical Journal of the Royal Astronomical Society*, 23(4), 417–433, doi:10.1111/j.1365-246X.1971.tb01834.x.
- Fullea, J., M. Fernández, H. Zeyen, and Vergés (2007), A rapid method to map the crustal and lithospheric thickness using elevation, geoid anomaly and thermal analysis. Application to the Gibraltar Arc System, Atlas Mountains and adjacent zones, *Tectonophysics*, 430, 97–117, doi:10.1016/j.tecto.2006.11.003.
- Gallart, J., J. Díaz, N. Vidal, and J. J. Dañobeitia (1995), The base of the crust at the Betics-Alborán Sea transition: evidence for an abrupt structural variation from wide-angle ESCI data, *Revisita de la Sociedad Geológica de España*, 8(4), 519–527.
- García-Dueñas, V., E. Banda, M. Torné, D. Córdoba, and ESCI-Béticas Working Group (1994), A deep seismic reflection survey across the Betic Chain (southern Spain): first results, *Tectonophysics*, 232, 77–89, doi:10.1016/0040-1951(94)90077-9.
- Goldstein, P. (1999), SAC user's manual, *Tech. rep.*, Lawrence Livermore Laboratory, University of California.
- Govers, R. (2009), Choking the Mediterranean to dehydration: The Messinian salinity crisis, *Geology*, 37(2), 167–170, doi:10.1130/G25141A.1.
- Gràcia, E., R. Pallàs, J. I. Soto, M. Comas, X. Moreno, E. Masana, P. Santanach, S. Diez, M. García, and J. Dañobeitia (2006), Active faulting offshore SE Spain (Alboran Sea): implications for earthquake hazard assessment in the Southern Iberia Margin, *Earth and Planetary Science Letters*, 241, 734–749, doi:10.1016/j.epsl.2005.11.009.
- Grevemeyer, I. (2011), RV Poseidon POS389 & POS393 & RV Maria S. Merian MSM15/5 – Topographic, structural and seismotectonic consequences of plate re-organization in the Gulf of Cadiz and Alboran Sea, *IFM-GEOMAR Report*, No. 45.
- GSETT-3 (1997), Provisional GSE 2.1 - Message Formats & Protocols - Operations Annex 3, *Tech. rep.*

- Gurría, E., and J. Mezcua (2000), Seismic tomography of the crust and lithospheric mantle in the Betic Cordillera and Alboran Sea, *Tectonophysics*, 329, 99–119.
- Gutscher, M.-A., J. Malod, J. P. Rehault, I. Constucci, F. Klingelhoefer, L. Mendes-Victor, and W. Spakman (2002), Evidence for active subduction beneath Gibraltar, *Geology*, 30(12), 1071–1074.
- Gutscher, M.-A., S. Dominguez, G. K. Westbrook, and P. Leroy (2009), Deep structure, recent deformation and analog modeling of the Gulf of Cadiz accretionary wedge: Implications for the 1755 Lisbon earthquake, *Tectonophysics*, 475, 85–97, doi:10.1016/j.tecto.2008.11.031.
- Havskov, J., and L. Ottemöller (1999), SeisAn Earthquake Analysis Software, *Seismological Research Letters*, 70(5), 532–534, doi:10.1785/gssrl.70.5.532.
- Hess, H. H. (1962), History of Ocean Basins, in *Petrological Studies: A Volume in Honor of A. F. Buddington*, edited by A. E. J. Engel, H. L. James, and B. F. Leonard, pp. 599–620, Geological Society of America.
- Hoernle, K., P. van den Bogaard, S. Duggen, B. Mocek, and D. Garbe-Schönberg (1999), Evidence for Miocene subduction beneath the Alboran Sea: $^{40}\text{Ar}/^{39}\text{Ar}$ dating and geochemistry of volcanic rocks from Holes 997A and 978A, *Proceedings of the Ocean Drilling Program, Scientific Results*, 161, 357–373.
- IRIS Consortium (1993), *Standard for the Exchange of Earthquake Data*, Federation of Digital Seismographic Network, Incorporated Research Institutions for Seismology, United States Geological Survey, SEED Format Version 2.3.
- Jolivet, L., and C. Faccenna (2000), Mediterranean extension and the Africa-Eurasia collision, *Tectonics*, 19(6), 1095–1106.
- Jolivet, L., D. Frizon de Lamotte, A. Mascle, and M. Séranne (1999), The Mediterranean Basins: Tertiary Extension within the Alpine Orogen - an Introduction, in *The Mediterranean Basins: Tertiary Extension within the Alpine Orogen, Special Publications*, vol. 156, pp. 1–14, Geological Society, London.
- Kissling, E. (1995), *Program VELEST User's Guide - Short Introduction*, Institute of Geophysics, ETH Zuerich, Switzerland, 5 ed.
- Kissling, E., W. L. Ellsworth, D. Eberhart-Phillips, and U. Kradolfer (1994), Initial reference models in local earthquake tomography, *Journal of Geophysical Research*, 99(B10), 19,635–19,646.
- Korenaga, J., W. S. Holbrook, G. M. Kent, P. B. Kelemen, R. S. Detrick, H.-C. Larsen, J. R. Hopper, and T. Dahl-Jensen (2000), Crustal structure of the southeast Greenland margin from joint refraction and reflection seismic tomography, *Journal of Geophysical Research*, 105(B9), 21,591–21,614.

- Korenaga, J., W. S. Holbrook, R. S. Detrick, and P. B. Kelemen (2001), Gravity anomalies and crustal structure at the southeast Greenland margin, *Journal of Geophysical Research*, 106(B5), 8853–8870.
- Lienert, B. R. E., and J. Havskov (1995), A computer program for locating earthquakes both locally and globally, *Seismological Research Letters*, 66(5), 26–36, doi:10.1785/gssrl.66.5.26.
- Lonergan, L., and N. White (1997), Origin of the Betic-Rif mountain belt, *Tectonics*, 16(3), 504–522, doi:10.1029/96TC03937.
- Maldonado, A., and M. C. Comas (1992), Geology and Geophysics of the Alboran Sea: An Introduction, *Geo-Marine Letters*, 12, 61–65.
- Maldonado, A., A. C. Campillo, A. Mauffret, B. Alonso, J. M. Woodside, and J. Campos (1992), Alboran Sea Late Cenozoic Tectonic and Stratigraphic Evolution, *Geo-Marine Letters*, 12, 179–186.
- Mezcua, J., and J. Rueda (1997), Seismological evidence for a delamination process in the lithosphere under the Alboran Sea, *Geophysical Journal International*, 129(1), F1–F8, doi:10.1111/j.1365-246X.1997.tb00934.x.
- Moser, T. J. (1991), Shortest path calculation of seismic rays, *Geophysics*, 56(1), 59–67, doi:10.1190/1.1442958.
- Moser, T. J., G. Nolet, and R. Snieder (1992), Ray Bending Revisited, *Bulletin of the Seismological Society of America*, 82(1), 259–288.
- Müller, G. (1985), The reflectivity method: a tutorial, *Journal of Geophysics*, 58, 153–174.
- Nakanishi, I., and K. Yamaguchi (1986), A numerical experiment on nonlinear image reconstruction from first-arrival times for two-dimensional island arc structure, *Journal of Physics of the Earth*, 34, 195–201.
- Ottmøller, L., P. Voss, and J. Havskov (2010), *SEISAN: The Earthquake Analysis Software for Windows, Solaris, Linux and MacOSX*, University of Bergen, Norway, 8.3 ed.
- Paige, C. C., and M. A. Saunders (1982), LSQR: An Algorithm for Sparse Linear Equations and Sparse Least Squares, *ACM Transactions on Mathematical Software*, 8(1), 43–71.
- Platt, J. P., and P. C. England (1993), Convective Removal of Lithosphere beneath Mountain Belts: Thermal and Mechanical Consequences, *American Journal of Science*, 293, 307–336.
- Platt, J. P., and R. L. M. Vissers (1989), Extensional collapse of thickened continental lithosphere: A working hypothesis for the Alboran Sea and Gibraltar arc, *Geology*, 17, 540–543.

- Platt, J. P., J. I. Soto, M. J. Whitehouse, A. J. Hurford, and S. P. Kelley (1998), Thermal evolution, rate of exhumation, and tectonic significance of metamorphic rocks from the floor of the Alboran extensional basin, western Mediterranean, *Tectonics*, 17(5), 671–689, doi:10.1029/98TC02204.
- Polyak, B. G., M. Fernández, M. D. Khutorskoy, J. I. Soto, I. A. Basov, M. C. Comas, V. Y. Khain, B. Alonso, G. V. Agapova, I. S. Mazurova, A. Negredo, V. O. Tochitsky, J. de la Linde, N. A. Bogdanov, and E. Banda (1996), Heat flow in the Alboran Sea, western Mediterranean, *Tectonophysics*, 263, 191–218.
- Rosell, O., A. Martí, À. Marcuello, J. Ledo, P. Queralt, E. Roca, and J. Campanyà (2011), Deep electrical resistivity structure of the northern Gibraltar Arc (western Mediterranean): evidence of lithospheric slab break-off, *Terra Nova*, 23(3), 179–186, doi:10.1111/j.1365-3121.2011.00996.x.
- Rosenbaum, G., G. S. Lister, and C. Duboz (2002), Reconstruction of the tectonic evolution of the western Mediterranean since the Oligocene, *Journal of the Virtual Explorer*, 8, 107–126.
- Royden, L. H. (1993), Evolution of retreating subduction boundaries formed during continental collision, *Tectonics*, 12(3), 629–638, doi:10.1029/92TC02641.
- Seber, D., M. Barazangi, A. Ibenbrahim, and A. Demnati (1996), Geophysical evidence for lithospheric delamination beneath the Alboran Sea and Rif-Betic mountains, *Nature*, 379, 785–790, doi:10.1038/379785a0.
- Serrano, I., J. Morales, D. Zhao, F. Torcal, and F. Vidal (1998), P-wave tomographic images in the Central Betics-Alborán sea (South Spain) using local earthquakes: contribution for a continental collision, *Geophysical Research Letters*, 25(21), 4031–4034.
- Stern, R. J. (1998), A Subduction Primer for Instructors of Introductory-Geology Courses and Authors of Introductory-Geology Textbooks, *Journal of Geoscience Education*, 46, 221–228.
- Stern, R. J. (2002), Subduction Zones, *Reviews of Geophysics*, 40(4), doi:10.1029/2001RG000108, 1012.
- Stich, D., C. J. Ammon, and J. Morales (2003a), Moment tensor solutions for small and moderate earthquakes in the Ibero-Maghreb region, *Journal of Geophysical Research*, 108(B3), doi:10.1029/2002JB002057, 2148.
- Stich, D., J. Batlló, J. Morales, R. Macià, and S. Dineva (2003b), Source parameters of the $M_w = 6.1$ 1910 Adra earthquake (southern Spain), *Geophysical Journal International*, 155, 539–546.
- Stich, D., F. d. L. Mancilla, D. Baumont, and J. Morales (2005), Source analysis of the M_w 6.3 2004 Al Hoceima earthquake (Morocco) using regional apparent source time functions, *Journal of Geophysical Research*, 110, doi:10.1029/2004JB003366, B06306.

- Stich, D., E. Serpelloni, F. d. L. Mancilla, and J. Morales (2006), Kinematics of the Iberia-Maghreb plate contact from seismic moment tensors and GPS observations, *Tectonophysics*, 426, 295–317, doi:10.1016/j.tecto.2006.08.004.
- Stich, D., R. Martín, and J. Morales (2010), Moment tensor inversion for Iberia-Maghreb earthquakes 2005-2008, *Tectonophysics*, 483, 390–398, doi:10.1016/j.tecto.2009.11.006.
- Takahashi, N., S. Kodaira, S. L. Klemperer, Y. Tatsumi, Y. Kaneda, and K. Suyehiro (2007), Crustal structure and evolution of the Mariana intra-oceanic island arc, *Geology*, 35(3), 203–206, doi:10.1130/G23212A.1.
- Takahashi, N., S. Kodaira, Y. Tatsumi, Y. Kaneda, and K. Suyehiro (2008), Structure and growth of the Izu-Bonin-Mariana arc crust: 1. Seismic constraint on crust and mantle structure of the Mariana arc-back-arc system, *Journal of Geophysical Research*, 113, doi: 10.1029/2007JB005120, B01104.
- Thiebot, E., and M.-A. Gutscher (2006), The Gibraltar Arc seismogenic zone (part 1): Constraints on a shallow east dipping fault plane source for the 1755 Lisbon earthquake provided by seismic data, gravity and thermal modeling, *Tectonophysics*, 426, 135–152, doi:10.1016/j.tecto.2006.02.024.
- Toomey, D. R., S. C. Solomon, and G. M. Purdy (1994), Tomographic imaging of the shallow crustal structure of the East Pacific Rise at 9°30'N, *Journal of Geophysical Research*, 99(B12), 24,135–24,157.
- Trnkoczy, A. (2002), *IASPEI New Manual of Seismological Observatory Practice (NMSOP)*, GeoForschungsZentrum Potsdam, peter bormann ed., Information Sheets 8.1 - Understanding and parameter setting of STA/LTA trigger algorithm.
- Turner, S. P., J. P. Platt, R. M. M. George, S. P. Kelley, D. G. Pearson, and G. M. Nowell (1999), Magmatism Associated with Orogenic Collapse of the Betic-Alboran Domain, SE Spain, *Journal of Petrology*, 40(6), 1011–1036.
- Uyeda, S., and H. Kanamori (1979), Back-Arc Opening and the Mode of Subduction, *Journal of Geophysical Research*, 84(B3), 1049–1061.
- van Avendonk, H. J. A., A. J. Harding, J. A. Orcutt, and J. S. McClain (1998), A two-dimensional tomographic study of the Clipperton transform fault, *Journal of Geophysical Research*, 103(B8), 17,885–17,899, doi:10.1029/98JB00904.
- van Avendonk, H. J. A., A. J. Harding, J. A. Orcutt, and W. S. Holbrook (2001), Hybrid shortest path and ray bending method for traveltimes and raypath calculations, *Geophysics*, 66(2), 648–653, doi:10.1190/1.1444955.
- Wegener, A. (1912), Die Entstehung der Kontinente, *Geologische Rundschau*, 3(4), 276–292, doi:10.1007/BF02202896.

- White, R. S., D. McKenzie, and R. K. O'Nions (1992), Oceanic Crustal Thickness from Seismic Measurements and Rare Earth Element Inversions, *Journal of Geophysical Research*, 97(B13), 19,683–19,715.
- Wiener, N. (1949), *Extrapolation, Interpolation, and Smoothing of Stationary Time Series*, New York: Wiley, ISBN: 0-262-73005-7.
- Wilson, M., and G. Bianchini (1999), Tertiary-Quaternary magmatism within the Mediterranean and surrounding regions, in *The Mediterranean Basins: Tertiary Extension within the Alpine Orogen, Special Publications*, vol. 156, pp. 141–168, Geological Society, London.
- Working Group for Deep Seismic Sounding in the Alboran Sea 1974 (1978), Crustal Seismic Profiles in the Alboran Sea – Preliminary Results, *Pure and Applied Geophysics*, 116, 167–180, doi:10.1007/BF00878991.
- Zeck, H. P. (1996), Betic-Rif orogeny: subduction of Mesozoic Tethys lithosphere under eastward drifting Iberia, slab detachment shortly before 22 Ma, and subsequent uplift and extensional tectonics, *Tectonophysics*, 254(1-2), 1–16, doi:10.1016/0040-1951(95)00206-5.
- Zeck, H. P. (1997), Mantle peridotites outlining the Gibraltar Arc - centrifugal extensional allochthons derived from the earlier Alpine, westward subduction nappe pile, *Tectonophysics*, 281(3-4), 195–207, doi:10.1016/S0040-1951(97)00067-X.
- Zelt, C. A. (1997), *Documentation for ZPLOT & XZPLOT*.
- Zelt, C. A., and R. M. Ellis (1988), Practical and efficient ray tracing in two-dimensional media for rapid traveltimes and amplitude forward modelling, *Canadian Journal of Exploration Geophysics*, 24(1), 16–31.
- Zelt, C. A., and R. B. Smith (1992), Seismic traveltimes inversion for 2-D crustal velocity structure, *Geophysical Journal International*, 108, 16–34, doi:10.1111/j.1365-246X.1992.tb00836.x.

Acknowledgements

First and particularly I would like to thank Ingo Grevemeyer for his support over the years from the first to the last day of this work. Helpful discussions, advises and guidance through the whole work were a key to clarify aspects of the work and the seismic modeling.

I would like to thank Heidrun Kopp to act as the coreferee for this work.

Many thanks to Ivonne Aden-Arroyo for her support with the seismological data and the discussions about those.

Thank you to all members of the Marine Geodynamic department for assistance through the last years.

For the nice working condition I would like to thank especially all colleagues of floor 8B. They made the work more comfortable in this separated part of the building.

I also want to thank all participants of the cruises M69-2, POS389 and POS393 for collecting the data for this work.

Last but not least, I want to thank my whole family and especially my husband Holger for the support through the last years.

Eidesstattliche Erklärung

Hiermit bestätige ich, dass ich die vorliegende Arbeit abgesehen von der Beratung durch meinen Betreuer selbständig verfasst und keine anderen als die angegebenen Quellen und Hilfsmittel verwendet habe. Ich versichere, dass diese Arbeit noch nicht zur Erlangung eines Doktorgrades an anderer Stelle vorgelegen hat. Die Arbeit ist unter Einhaltung der Regeln guter wissenschaftlicher Praxis der Deutschen Forschungsgemeinschaft entstanden.

Kiel,

(Wiebke Leuchters)

Curriculum Vitae

Name: Wiebke Leuchters

Date of Birth: 12. July 1981
Place of Birth: Ahaus
Citizenship: German

Address: Stuthagen 27
24113 Molfsee

1988 - 1991: Alfred-Delp-Schule, Geseke

1991 - 1992: Pestalozzischule, Ahaus

1992 - 2001: Alexander-Hegius-Gymnasium, Ahaus
May 2001: Abitur

2001 - 2007: Study of Meteorology at the Christian-Albrechts-University of Kiel
September 2007: Diploma (equivalent M. Sc.) in Meteorology

Since October 2007: PhD student in Geophysics at GEOMAR – Helmholtz Centre for Ocean Research, Kiel